Computation and Measurements of Flows in Rooms

by

Alexandre Jouvray

A thesis submitted for the partial fulfilment

of the requirements for the degree of

Doctor of Philosophy in Engineering

Fluid Dynamics Research Centre, School of Engineering,

University of Warwick, U.K.

July, 2003

Contents

1 Introduction **1**

2 Literature review **8**

2.1 Introduction to room-ventilation processes 8

2.1.1 Air quality 12

2.1.2 Thermal comfort 16

2.1.3 Ventilation efficiency and energy consumption 18

2.2 Advances in CFD for room ventilation 19

2.2.1 Advanced RANS models for room ventilation 20

2.2.2 Large Eddy Simulation for room ventilation 23

3 Turbulence modelling **26**

3.1 The RANS approach 26

3.1.1 Prandtl's mixing-length model 29

3.1.2 The transport equation of turbulent kinetic energy 30

3.1.3 The $k - l$ model 30

3.1.4 The $k - \epsilon$ model 31

3.1.5 Passive scalar, temperature and buoyancy modelling 32

3.1.6 High and low Reynolds number turbulence models 34

3.1.7 Wall damping function 37
3.2 Advanced turbulence models 40
3.2.1 Reynolds stress models, algebraic stress models and explicit algebraic stress models 41
3.2.2 Non-linear eddy-viscosity models 45
3.2.3 Large Eddy Simulation: A brief overview 48
3.2.4 Zonal and hybrid RANS/LES models 50

4 Numerical methods and code optimisation **54**
4.1 Spatial and temporal discretisation methods 54
4.2 General solution procedure: The SIMPLE algorithm 57
4.3 The TDMA solver 58
4.4 Optimisation of the code 60
4.4.1 Multigrid method 60
4.4.2 Parallel processing 63
4.4.3 Results and discussion on the optimised code 64

5 Turbulence models' validation **69**
5.1 Introduction 69
5.2 Two-dimensional turbulent channel flow 70
5.2.1 Results and discussion 70
5.2.2 Variants of the EASM 73
5.3 Side-injection channel flow 76
5.3.1 Numerical modelling 78
5.3.2 Results and discussion 78
5.4 Backward-facing step flow configuration 83

5.5 Secondary motion in a square duct 85
5.6 Conclusions 89

6 Experimental work: Layout and setup **91**
6.1 Introduction 91
6.2 Experimental model 92
6.2.1 Overall layout and furnishing of the room 92
6.2.2 Ventilation aspects 94
6.2.3 Thermal aspects 98
6.3 Measurement Methods 102
6.3.1 Temperature and velocity measurements of air flows 102
6.3.2 Temperature measurements for walls 104
6.3.3 Gas tracer device 107

7 Experimental results **112**
7.1 Introduction 112
7.2 Gas tracer analysis 113
7.3 Time considerations 117
7.4 Surface temperature 118
7.5 Velocity and air temperature analysis 120
7.6 DIN man area 122
7.7 Conclusions 125

8 Modelling of a jet-ventilated room **128**
8.1 Numerical modelling 128
8.2 Results and discussion 130
8.2.1 Jet centerline decay analysis 130

8.2.2 Near-wall behaviour 137
8.3 Conclusions 141

9 Modelling of gas tracer decay in an office **143**
9.1 Numerical modelling 146
9.2 Results and discussion 148
9.3 Conclusions 153

10 Modelling of a displacement-ventilated office **154**
10.1 Numerical modelling 156
10.1.1 Thermal aspects 156
10.2 Results and discussion 159
10.3 Conclusions 165

11 Modelling of the CFD idealised office **168**
11.1 Numerical modelling 168
11.1.1 Surface temperature 170
11.1.2 DIN-man modelling 171
11.1.3 Gas tracer decay 172
11.2 Results and discussion 172
11.2.1 Thermal stratification 172
11.2.2 Air velocities 175
11.2.3 Gas tracer decay 178
11.3 Conclusions 181

12 Conclusions and recommendation for future work **182**

13 References **188**

A An assessment of a range of tubulence models when predicting room ventilation 211

B Typical calibration certificate of the DANTEC anemometers 218

C Wall temperature for cases 01 to 06 221

D Velocity and airflow temperature of the Dantec anemometers 224

List of Figures

1.1 Leonardo da Vinci's sketches on turbulence. 2

2.1 Naturally ventilated buildings: Computational model of the Hall of Still Thought in Taiwan. (http://www.architectureweek.com/). 9

2.2 Typical ventilation layouts: (a) Mixed-ventilation and (b) displacement-ventilation layout. 11

3.1 Typical turbulent flow and Reynolds decomposition. 27

3.2 Near-wall velocity profile: Experimental data of Laufer (1951) in a 2-D channel flow. 36

3.3 Three-dimensional growth of streaks in the turbulent boundary layer. . . 51

4.1 Typical control volume: (a) Two-dimensional control volume with volume faces and (b) three-dimensional representation of the computational grid with scalar quantities (at grid nodes) and velocities. 55

4.2 (a) Principle of the multigrid method on a one-dimensional grid and (b) multigrid V cycle. 62

4.3 Schematic of the Red-Black method using the TDMA solver. 64

4.4 (a) Test case 1: Heated wall configuration and (b), Test case 2: Recirculating flow configuration. 65

4.5 Residuals as a function of the number of iterations for various solvers. . . 66

5.1 Near-wall velocity profile. (a) EASM $k-l$ model and (b) cubic $k-\epsilon$ model. 71

5.2 Comparison of non-linear Reynolds stresses in a $k-l$ framework with measurements: (a) EASM model and (b) cubic model. 74

5.3 Comparison of non-linear Reynolds stresses in a $k-\epsilon$ framework with channel flow measurements: (a) EASM model and (b) Cubic model. . . . 75

5.4 (a) Distribution of α_i across half of the channel and (b), influence of the $C_{\mu i}$ approximation on the Reynolds stresses. 77

5.5 Schematic of the side-injection driven channel. 78

5.6 Comparison of linear, EASM and cubic $k-l$ models with measurements (symbols). Profiles located at $x = 0.031m$: $\circ$; $x = 0.031m$: $\triangle$; $x = 0.120m$: $\square$; $x = 0.220m$: $\diamond$; $x = 0.500m$: $*$. 80

5.7 Comparison of normal Reynolds stress profiles: (a) and (b) τ_{xx} at a distance of 570 mm along x; 81

5.8 Comparison of normal Reynolds stress profiles: (a) τ_{xx} at a distance of 450 mm along x and (b) τ_{yy} at a distance of 570 mm along x. 82

5.9 Backward-facing step: geometry and flow profile. 83

5.10 Secondary motions in a square duct using the EASM $k-l$ model: (a) Full view and (b) zoom on the top right corner. 86

5.11 Secondary motion in a square duct using the cubic eddy-viscosity model: (a) Full view and (b) zoom on the top right corner. 87

5.12 Scalar trajectory in a 40 m long square duct. 88

6.1 Overall view of the test room: (a) Top and (b) side view of the room layout. 1: Filing cabinet, 2 & 3: desks, 4: DIN man, 5 & 6: Inlet ducts, 7: Door and 8: Outlet. Dimensions in mm. 93

6.2 Ventilation layout and expected airflow pattern for the (a) displacement-ventilation and (b) mixed-ventilation layout. 94
6.3 Various diffusers.(a,b):"www.price-hvac.com", (c):"www.airtechproducts.com" and (d): "www.poltech.com.au". 95
6.4 (a) Inlet duct system and (b) details of the orifice plate. 96
6.5 Schematic of the test facility. 99
6.6 DIN man; (a) Standard cylindrical DIN man and (b) square cover. 101
6.7 Dantec 54R10 transducer. 103
6.8 Location of the Dantec 54R10 transducers in the room. (a) Top view and (b) side view of the room. Dimensions in *mm*. 105
6.9 (a) Overview of the probes in the din man area with (b) projected view. Dimensions in *mm*. 106
6.10 Layout of the thermocouple in the room (marked by o); (a) Back wall, (b) Front wall and door, (c) Left wall, (d) Right wall, (e) Floor and (f) Ceiling. The hatched areas represent the room's furniture. Dimensions in *mm*. 108
6.11 Gas tracer analyser. 109
6.12 Probe layout for the gas tracer analysis marked by o: (a) Overview and (b) top view of the room. Dimensions in *mm*. 111

7.1 Gas concentration in the room for Case 01. 114
7.2 Time-decay of gas concentration in the room for (a) Case 01, (b) Case 02 and (c) Case 03. 115
7.3 Time-decay of gas concentration in the room for (a) Case 04, (b) Case 05 and (c) Case 06. 116

7.4 Wall temperatures for Case 01: (a) back wall, (b) left wall, (c) right wall, (d) floor, (e) ceiling and (f) door. 119
7.5 Thermal stratification in the room for Cases 01, 02 and 03. 121
7.6 Thermal stratification in the room for Cases 04, 05 and 06. 121
7.7 Inlet velocity measurements from the Dantec anemometers for Case 01. . 124

8.1 Room geometry and position of vertical measurement axes (Dimensions in mm). Distance from inlet along x: $A1 = 190\ mm$; $A2 = 515mm$; $A3 = 965\ mm$; $A4 = 1555\ mm$; $A5 = 2355\ mm$; $A6 = 3155\ mm$; $A7 = 3945\ mm$; $A8 = 4395\ mm$; $A9 = 4720\ mm$. 129
8.2 Comparison of predicted velocities with measurements (m/s). 131
8.3 Centerline velocity decay of the inlet jet: Comparison of measurements with linear eddy-viscosity models. 132
8.4 Centerline velocity decay of the inlet jet: Comparison of measurements with non-linear eddy-viscosity models. 134
8.5 Centerline velocity decay of the inlet jet: Comparison of measurements with LES and LNS models. 134
8.6 Normal Reynolds stresses τ_{xx}/ρ along the jet centerline. 136
8.7 Normal Reynolds stresses τ_{yy}/ρ along the jet centerline. 136
8.8 Normal Reynolds stresses τ_{zz}/ρ along the jet centerline. 137
8.9 Centerline distribution of α for the LNS model. 138
8.10 Streaklines in the room. (a) Linear $k-\epsilon$, (b) cubic, (c) LES (Smagorinsky) and (d) LNS models. 139
8.11 Velocity profile in the lower part of the room. (a) Profile A2, (b) profile A4, (c) profile A6 and (d) profile A8. 140

8.12 Contour plot of velocity at $y^+ \simeq 30$ in the lower part of the room. (a) Cubic model and (b) EASM $k-\epsilon$ model. 141

9.1 Shaw's room layout: 1: Partition; 2: Two desks; 3: Bookcase; 4: Filing cabinet; 5: Inlet; 6 & 7: Outlets. 144

9.2 Time-decay of SF_6 in the room. Measurements and predictions of eddy-viscosity models in a $k-l$ framework. 148

9.3 Velocity contour plots in the breathing zone ($y = 1.6\ m$) for (a) $k-l$, (b) cubic $k-l$, (c) $k-\epsilon$ and (d) EASM $k-\epsilon$ models. 151

10.1 Room layout. (a) Three-dimensional view and (b) top view with location of measurement points. 155

10.2 Comparison of measured velocity profiles (a) M1, (b) M3, (c) M7 and (d) M9 with predictions of the linear, EASM and cubic $k-\epsilon$ models. 160

10.3 Comparison of measured velocity profiles (a) M1, (b) M3, (c) M7 and (d) M9 with predictions of the linear, EASM and cubic $k-l$ models. 161

10.4 Velocity contour plots in the room for (a) the linear and (b) EASM $k-\epsilon$ models. 162

10.5 Comparison of measured temperature profiles (a) M3, (b) M5, (c) M6 and (d) M8 with predictions of the linear, EASM and cubic $k-\epsilon$ models. 164

10.6 Comparison of measured temperature profiles (a) M3, (b) M5, (c) M6 and (d) M8 with predictions of the linear, EASM and cubic $k-l$ models. 166

11.1 Room layout: 1: Filing cabinet; 2: Large desk; 3: Desk; 4: DIN man; 5: Outlet; 6: Door; 7: Light; 8: Mixed-ventilation inlet; 9: Displacement-ventilation inlet. 169

11.2 Averaged temperature stratification in the room for Case 01. 173

11.3 Averaged airflow temperature stratification in the room for Case 06. . . . 174
11.4 Comparison of measured and predicted airflow velocities for Case 01. . . 175
11.5 Comparison of measured and predicted airflow velocities for Case 06. . . 176
11.6 Velocity contour plots in the DIN man's mid-plane for Case 01. (a) $k-\epsilon$ model and (b), instantaneous Smagorinsky LES. 177
11.7 Velocity contour plots in the DIN man's mid-plane for Case 06. (a) linear and (b) EASM $k-\epsilon$ model. 177
11.8 Averaged concentration decay for Case 01. 179
11.9 Averaged concentration decay for Case 06. 179

List of Tables

4.1 Alternate sweeping method for the TDMA solver. 60

4.2 Number of iteration and computing time to reach convergence for test case 2 and the simply ventilated room of He *et al.* (1999). 67

5.1 Non-dimensional wall shear stress ($\tau_w/(\rho U_0^2) \times 10^4$). 72

5.2 Specifications of the backward-facing step flow. 84

5.3 Specifications of the square duct used to obtain secondary motion. 85

6.1 Inlet velocity and temperature used during the experiments. 98

6.2 Specifications of the Dantec 54R10 anemometer and requirements of the ASHRAE and ISO 7726 (1985) standards. 103

7.1 Location, mean temperature and velocity of the Dantec anemometers for Case 01 (dimensions in *mm*). 123

7.2 Mean temperature and velocity of the Accusense thermistors for cases 01, 02 and 03. 125

7.3 Mean temperature and velocity of the Accusense thermistors for cases 04, 05 and 06. 126

7.4 Temperature of the Accusense thermistors taken as: $T - T_{inlet}$. 126

8.1 Averaged prediction error at the jet centerline. 133

9.1 Room dimensions (m). Label 1-a to 1-d corresponds to the four sides of the partition. Label 2-a ands 2-b are the two desks. 145
9.2 Relative prediction error (%) of concentration decay for the models tested. 150
9.3 Ventilation efficiency index E_f at the time $t = 20$ *mins*. 152

10.1 Dimensions of the room configuration (dimensions in m). 157
10.2 Relative velocity error for each of the nine measured profiles. 163
10.3 Relative temperature error for each of the nine measured profiles. 167

11.1 Averaged wall temperatures for Case 01 and Case 06. 171
11.2 Coefficients of the polynomial fit for wall temperature of Case 01. 171
11.3 Averaged temperature error (%) of the models for Case 01 and 06. 175
11.4 Averaged velocity errors (%). 178
11.5 Relative averaged error (%) of the models compared with measurements. 180
11.6 Contaminant-removal index. 181

C.1 Surface temperature in the room for the displacement ventilation layout. Dimensions in *mm*. 222
C.2 Surface temperature in the room for the mixed ventilation layout. Dimensions in *mm*. 223

D.1 Location, mean temperature and velocity of the Dantec anemometers for Case 02 (dimensions in *mm*). 224
D.2 Location, mean temperature and velocity of the Dantec anemometers for Case 03 (dimensions in *mm*). 225
D.3 Location, mean temperature and velocity of the Dantec anemometers for Case 04 (dimensions in *mm*). 226

D.4 Location, mean temperature and velocity of the Dantec anemometers for Case 05 (dimensions in mm). 227
D.5 Location, mean temperature and velocity of the Dantec anemometers for Case 06 (dimensions in mm). 228

Nomenclature

a	Cross section area
A	General coefficient solution of the discretised equations
$A1$ to $A12$	Label for Accusense thermistors
A_ϵ, A_μ	$k-l$ turbulence model constants
B	Wall roughness constant
$B_{(i,j,k)}$	Spatial notation of grid points (Back)
C_1 to C_7	Non-linear eddy-viscosity model constants
C_s	Smagorinsky model constant
C_μ, $C_{\epsilon 1}$, $C_{\epsilon 2}$	$k-\epsilon$ model constants
$C_{\mu 0}$, $C_{\epsilon 0}$, A_ϵ, A_μ	$k-l$ model constants
$C_{\mu 1}$, $C_{\mu 2}$, $C_{\mu 3}$	EASM coefficients
c_w	Yap factor constant
d	Length scale
$D1$ to $D19$	Label for Dantec anemometers
D_c	Discharge coefficient for orifice flowmeters
E	Wall roughness constant
$E_{(i,j,k)}$	Spatial notation of grid points (East)
$F_{(i,j,k)}$	Spatial notation of grid points (Front)
f_μ, f_1, f_2	Damping functions

$G1$ to $G5$, GS, GR	Label of gas tracer sampling points
G_k	Buoyancy source term
H	Step height in backward-facing step flow
k	Turbulent kinetic energy
L	Length scale
l_e, l_{yc}	Yap factor constants
l_m	Mixing length
l_{sgs}	Subgrid-scale length scale
l_ϵ	Dissipation length scale
l_μ	Eddy length scale
MW	Molecular weight
$N_{(i,j,k)}$	Spatial notation of grid points (North)
p	Average, or mean, pressure
P	Instantaneous pressure
p'	Fluctuating pressure
p^*	Guessed pressure for SIMPLE algorithm
p^c	Correction pressure for SIMPLE algorithm
P_k	Production term
Pr	Prandtl number
$P_{(i,j,k)}$	Spatial notation of grid points (Point)
R	Ideal gas constant
$[R]$	Matrix of residual error
Re	Reynolds number
Re_t, Re_y	Turbulent Reynolds numbers
S	Source term
S_e	Extra source term for the $\tilde{\epsilon}$ equation

S_{ij}	Mean strain rate
S^*_{ij}	Non-dimensional strain rate
$\tilde{S}_{ij}$	Resolved mean strain rate (LES)
$S_{(i,j,k)}$	Spatial notation of grid points (South)
T	Temperature
$T01$ to $T30$	Label for thermocouples
t	Time
t_i	Turbulence time scale
U, V, W	Instantaneous velocities
u, v, w	Averaged, or mean, velocities
u', v', w'	Fluctuating velocities
$\overline{u}$, $\overline{v}$, $\overline{w}$	Time averaged velocities
$\tilde{u}$, $\tilde{v}$, $\tilde{w}$	Filtered velocities (for LES)
u^*, v^*, w^*	Guessed velocities for SIMPLE method
u^c, v^c, w^c	Corrected velocities for SIMPLE method
u^+	Non-dimensional velocity
V	Volume flow rate
V^*	Velocity scale
$W_{(i,j,k)}$	Spatial notation of grid points (West)
W_{ij}	Mean vorticity rate
$\tilde{W}_{ij}$	Resolved vorticity rate (LES)
W^*_{ij}	Non-dimensional vorticity rate
x, y, z	spatial coordinates
y_c	Yap correction factor
y^+, y^*	Non-dimensional wall distance
α	RANS damping coefficient for LNS

α_1, α_2, α_3, g	EASM constants
β	Temporal discretisation parameter
Δ	Grid size or filter width for LES
δ	Boundary-layer thickness
δt	Time step
δ_x, δ_x, δ_x	Local grid spacing
δ_{ij}	Krondeker delta
η, ζ	Invariance coefficients
ϵ, $\tilde{\epsilon}$	Rate of dissipation of turbulent kinetic energy
ϵ_{ij}	Dissipation rate tensor
ϵ_s	Material emissivity
Γ_k, Γ_ϵ	Diffusion coefficients for k and ϵ
γ_1, γ_2, γ_3	EASM constants
κ	Von Karman constant
μ	Dynamic viscosity
μ_t	Turbulent viscosity
μ_{t1}, μ_{t2}, μ_{t3}	Turbulent viscosity for EASM
μ_{sgs}	Subgrid-scale turbulent viscosity
ν	Kinematic viscosity
Ω	LNS parameters
Π_{ij}	Pressure-strain correlation tensor
ρ	Fluid density
$-\rho\overline{u_i'\phi'}$	Turbulent scalar transport term
σ	Stefan-Boltzman constant
σ_k, σ_ϵ	Diffusion Prandtl numbers for k and ϵ

$\tau_{ij} = -\rho\overline{u_i' u_j'}$	Reynolds stress tensor
τ_{ij}^{R}	Residual stress tensor (LES)
τ_{ij}^{sgs}	Subgrid-scale stress tensor (LES)
τ_w	Wall Shear stress
Φ	Instantaneous flow property
ϕ	Mean flow property
$\tilde{\phi}$	Resolved flow property for LES
ϕ'	Fluctuating flow property
ϕ^{sgs}	Subgrid-scale flow property
ϕ^{*}	Guessed flow property used for SIMPLE method
ϕ^{c}	Corrected flow property for SIMPLE method

Subscripts

i, j, k	Tensorial notation related to the spatial direction
l, m, n	Tensorial notation
g	Multigrid level
nb	Spatial notation of neigbouring grid points
x, y, z	Spatial coordinates

Superscipts

sgs	Subgrid-scale property
f	Finer multigrid level

Acknowlegments

I would like to thank my supervisor Paul Tucker for his kind help, guidance and advice throughout the course of my PhD.

Special thanks to my dear friends Reza and Pascal who have always been there for help, support, and of course the occasional cheeky pint. As well as all the people I had the chance to meet and work with during my stay in Warwick, I would like to thank my friends Rai, Dr. Jason, Ross, Gianni and Helen, Rich, Karen, Yan and Mark who made the office a special place to work. I will never forget those friday afternoon coffees with Ross and Pascal nor will I forget the numerous CFD boys Ruby nights out.

Finally, I would like to thank my family and especially my parents whose unconditional support carried me through the difficult, and the not so difficult, times of this PhD.

Declaration

I declare that the work presented in this thesis is my own work. This thesis or no part of this thesis has been submitted for a degree at another University.

As part of the research, the following papers have been published:

- **Jouvray A.** and Tucker P. G., (2003), "On non-linear RANS, hybrid and LES models applied to complex flows.", *Proceedings of the* 4^{th} *International Symposium on Turbulence, Heat and Mass Transfer*, pp. 665-670, Ed. Hanjalic K., Nagano Y. and Tummers M., Begell House Inc., New-York, Swansea (UK).

- Tucker P. G., Liu Y., Chung Y-M. and **Jouvray A.**, (2003), "Computation of an unsteady complex geometry flow using novel non-linear turbulence models", *International journal for numerical methods in fluids*, Vol. 43, No. 9, pp. 979-1001.

- Liu Y., Tucker P.G., **Jouvray A.** and Carpenter P.W., (2003), "Computation of a non-isothermal complex geometry flow using non-linear URANS and Zonal LES modelling", *Proceedings of the* 3^{rd} *International Symposium on Turbulence and Shear Flow Phenomena*, Vol. 1, pp. 87-91, Ed. Kasagi N., Eaton J.K., Friedrich R., Humphrey J.A.C., Leschziner M.A. and Miyauchi T., Sendai, Japan, June, 2003.

- Holmes S. H., **Jouvray A.** and Tucker P. G., (2000), "An assessment of a range of turbulence models when predicting room ventilation", *Proc. Healthy Buildings 2000*, Vol. 2, pp. 401-406, ISBN 952-5236-09-9.

Abstract

This thesis contributes to the numerical modelling of flows in ventilated rooms. A range of advanced turbulence models (non-linear low Reynolds number Reynolds Averaged Navier-Stokes (RANS), Large Eddy Simulation (LES) and hybrid LES/RANS models) are used to model the flow in four ventilated rooms. These describe the flow in a more physically consistent manner than the commonly used linear RANS models.

The performances of Explicit Algebraic Stress Model (EASM) and, cubic eddy-viscosity RANS model are first analysed on four benchmark flow configurations. They show significant accuracy improvements when compared to their linear equivalents.

Flows in ventilated rooms are complex. Their numerical modelling required an accurate definition of the various boundary conditions. This is often lacking in the literature and hence, as part of this work, measurements in a controlled ventilated office (optimised for Computational Fluid Dynamics (CFD) modelling) have been done. The measurements comprise airflow velocities, temperatures, concentration decay and, a careful description of the room's boundary conditions under six ventilation settings. This room data is thus seen as ideal for validating of CFD codes when applied to room ventilation problems.

The numerical investigations show that the predictions with zero- or, one-equation ($k-l$) RANS models (commonly used in room ventilation modelling) are less accurate than those using two-equation $k-\epsilon$ models. The study shows that the accuracy improvements of the EASM and cubic models are of lesser magnitude when applied to room ventilation modelling than when applied to the benchmark flow configurations. The cubic model in particular, besides being more numerically unstable than the other RANS models, does not always improve flow predictions when compared with its linear equivalent. The EASM, about 20 to 30% more computationally demanding than its linear equivalent, improves solution accuracy for most flow considered in this work. LES predictions have highest level of agreement with measurements. LES is however too computationally expensive to be used for practical engineering applications. The novel hybrid RANS/LES model presented appears promising. It has similar accuracy to LES at lower computational costs.

Chapter 1

Introduction

The research is concerned with airflows in ventilated spaces such as rooms and offices. Ventilation is used to control and maintain a specified air quality, air temperature, moisture content, etc..., in a given space. To design an adequate ventilation system in a building or a room, some knowledge of the airflow pattern is desired. Until the advent of Computational Fluid Dynamics (CFD) airflows in rooms were ascertained from analytical methods, measurements or a-priori knowledge from similar flow configurations. With the growth of computer power, CFD methods have been applied to the modelling of complex engineering flows. In the last decade, CFD methods have been used as a design tool in the building industry to predict airflows. However, like in most engineering flows, flows in ventilated areas are of a turbulent nature and cannot be easily modelled. This work mostly contributes to the numerical modelling of turbulent flows in rooms.

Turbulence is a three-dimensional complex unsteady phenomenon. Turbulent flows are characterised by the presence of large eddies which are created by the mean flow. Another characteristic of turbulent flows pointed out by Leonard (1974), known as the energy cascade, is that the energy of the large eddies of the flow is successively dissipated

Figure 1.1: Leonardo da Vinci's sketches on turbulence.

by smaller eddies. It is found that the smaller eddies of the flow, near the Kolmogorov scale, are universal whereas, the larger eddies are highly dependent on the flow configuration itself (geometry, Reynolds number, etc...). The modelling of the various eddy scales is critical to ensure the correct energy transfer within the fluid and hence predict accurately flow fields.

From a historical perspective, Leonardo da Vinci (1452-1519) is considered by many as the first to study turbulence as illustrated by his many drawings (see for example Figure 1.1). Despite the efforts of many scientists such a Newton (1643-1727) and Bernoulli (1700-1782) no mathematical models describing the turbulent motion of a viscous fluid have been found until the nineteenth century with the derivation of the Navier (1785-1836) Stokes (1819-1903) equations. The Navier-Stokes (N-S) equations remain the fundamental mathematical model of turbulent fluid motion. More recently

Reynolds (1842-1912) and Prandtl (1875-1953) have contributed to the development of turbulence modelling techniques based on averaging methods. Another key contribution of Reynolds (1842-1912) is the introduction of non-dimensional quantities, in particular the Reynolds number, to determine the state of fluid flows. The Reynolds number is defined as $Re = \rho u d/\mu$ where ρ is the density of the fluid, u a characteristic velocity, d a characteristic length scale and μ the viscosity of the fluid. The Reynolds number expresses the ratio of inertial forces to viscous forces and is used to define the laminar state (at low Reynolds number) or turbulent state (at high Reynolds number) of a fluid. The transition from laminar to turbulent flow, which typically occurs at $Re_x \simeq 1.3 \times 10^5 \ - \ 1.3 \times 10^6$ for a flat plate boundary layer, is complex and governed by the growth in space and time of Tollmien-Schlichting instabilities. Further details on transition processes is extensively covered in the literature (*i.e.* Schlichting and Gersten (2000), Tritton (1988)).

The contribution of the many researchers over centuries has given rise to a mathematical expression of fluid motion as the conservation of three physical quantities: Momentum, mass and energy. These equations are the governing equations of fluid flows and are expressed here in their incompressible form as:

$$\frac{\partial U_i}{\partial t} + \frac{\partial U_i U_j}{\partial x_j} = -\frac{1}{\rho}\frac{\partial p}{\partial x_i} + \frac{\mu}{\rho}\frac{\partial}{\partial x_j}\left(\frac{\partial U_i}{\partial x_j} + \frac{\partial U_j}{\partial x_i}\right) \tag{1.1}$$

$$\frac{\partial U_j}{\partial x_j} = 0 \tag{1.2}$$

$$\frac{\partial(\rho T)}{\partial t} + \frac{\partial(\rho T U_j)}{\partial x_j} = \frac{\partial}{\partial x_j}\left(\frac{\mu}{P_r}\frac{\partial T}{\partial x_j}\right) \tag{1.3}$$

The momentum equation (Equation 1.1) is commonly referred as the N-S equation and is the expression of Newton's second law. Equation 1.2 is commonly referred as the continuity equation and express the conservation of mass of a fluid. Equation 1.3 is

the energy equation and embodies (via the Reynolds transport theorem) the first law of thermodynamics.

The computation of turbulent flows using the governing equations can be achieved using either of the three following methods: Direct Numerical Simulation (DNS), LES or the RANS method.

DNS is the resolution (through the use of extremely fine grids and time steps) of the full N-S equations for all time scales and spatial scales of a given flow. As a result, DNS provides highly accurate results but suffers greatly from being computationally expensive. DNS requires a grid resolution of the order of the Kolmogorov scales and needs a grid resolution of the order of $\simeq 10^{13}$ for airflows in rooms (Zhang and Chen (2000)). Due to the limitations of computing power and because the computational cost of DNS increase as Re^3 (Pope(2000)), DNS is still limited to the resolution of low Reynolds numbers flows and is thus not considered in this work.

To reduce computational cost and resolve more complex flows at higher Reynolds numbers, methods to approximate the consequences of turbulence are used. LES and RANS methods are currently the two most popular methods for computing practical turbulent flows. The numerical work presented here focuses on RANS, LES and hybrid RANS/LES approaches. A brief overview of these methods is given below and further discussed in Chapter 3.

In LES, a separation of scales is assumed for the flow eddies. The larger are computed, and the smaller (called sub-grid-scale components) modelled. Early work on LES

(*i.e.* Smagorinsky (1963), Deardorff (1974)) was aimed towards meteorological applications and atmospheric boundary layers. An extensive overview of LES and its applications to atmospheric modelling can be found in Galperin and Orzag (1993). With recent increases in computing power, LES has become increasingly popular for the modelling of flows at low to medium Reynolds numbers. LES for ventilated rooms is presented as part of this work.

The third and most popular method for computing turbulent flows is based on a form of time averaging of the governing equations. The averaging of the governing equations introduced by Reynolds (1895) (further described in Section 3.1) yields the RANS equations. These can be solved for most flow configurations and Reynolds numbers. The averaging of the governing equations, however, removes some of the key information on the time dependent fluctuations of the flow itself. Therefore, predictive accuracy can be relatively low. However, RANS solutions are relatively inexpensive. A wide range of RANS models is found in the literature (see Wilcox (1995)). Linear eddy-viscosity models such, as the $k - \epsilon$ model (see Chapter 3), have been widely validated but have limitated prediction accuracy. Their application to the modelling of ventilated rooms is reviewed in Chapter 2. The numerical prediction of flows in rooms using RANS here focuses on models that include a more consistent description of turbulent flow physics (*i.e.* non-linear eddy viscosity models and those derived from Reynolds stress models). Part of this work aims to assess the range of applicability and accuracy of these advanced RANS models. To do so, they are first validated using known data of four benchmark problems. The models are then applied to room ventilation cases where again, comparison is made with measurements.

To enhance flow predictions and keep computational cost to a minimum, zonal and hybrid RANS/LES methods are tested. In zonal models, computational expense is reduced by solving the computationally demanding near-wall areas using RANS. This region is demanding using LES since it contains fine streak-like structures needing an especially fine grid to resolve (see Chapter 3). The remainder, or core, of the flow is solved using LES. In hybrid models the transition between RANS and LES can occur at any point of the domain. Hybrid models are discussed in Chapter 3.

To fully assess the performances of numerical models, comparison with experimental data in a realistic ventilated spaces is required. It is often found in the literature that measurements in ventilated rooms are not well suited for CFD modelling. These often have missing boundary condition definition and hence cannot be used for the evaluation of numerical models. Thus, as part of this work, measurements in a ventilated office idealised for CFD modelling are made. For these, the boundary conditions are carefully defined.

Layout of the thesis

A general introduction to room ventilation processes and a review of CFD modelling applied to room ventilation is presented in Chapter 2. Chapter 3 presents the RANS, LES, zonal and hybrid RANS/LES models (equations and physical underlying principles) used. An overview of the numerical methods used is given in Chapter 4. In Chapter 5, the advanced RANS models as implemented in the code are assessed in terms of accuracy and range of applicability for four benchmark problems. Chapter 6 and 7 focus on the experimental set-up and results for the CFD idealised ventilated

office. Finally, Chapter 8 to 11 present the numerical investigation of four ventilated rooms. In Chapter 8, a wide range of turbulence models is applied to a simple empty jet-ventilated room. The performances of RANS models for the time-decay predictions of a scalar quantity in a mixed-ventilated room are assessed in Chapter 9. Chapter 10 presents the investigation of a complex non-isothermal displacement-ventilated office. Finally Chapter 11 presents the investigation of the CFD idealised room.

Chapter 2

Literature review

2.1 Introduction to room-ventilation processes

Until recently (early 1970's), the vast majority of offices and buildings in the U.K. were naturally ventilated (Awbi (1996)). The increased interest in improving ventilation systems in buildings, rooms and offices, in the last decades, has been driven by three key elements, namely the availability of relatively inexpensive energy sources, the increased need for improving comfort and well being in working places and the increased awareness of the impact of air quality on the health of people. These factors remain key in the definition of modern ventilation systems which aim to provide occupants a suitable air quantity, air quality and thermal comfort at low energy costs.

From a practical point of view, the ventilation of rooms can be grouped under two main categories: Natural ventilation and mechanical (or forced) ventilation. It is often found that in real buildings, a combination of the two techniques is used.

The growing awareness of environmental issues is leading to tremendous changes in

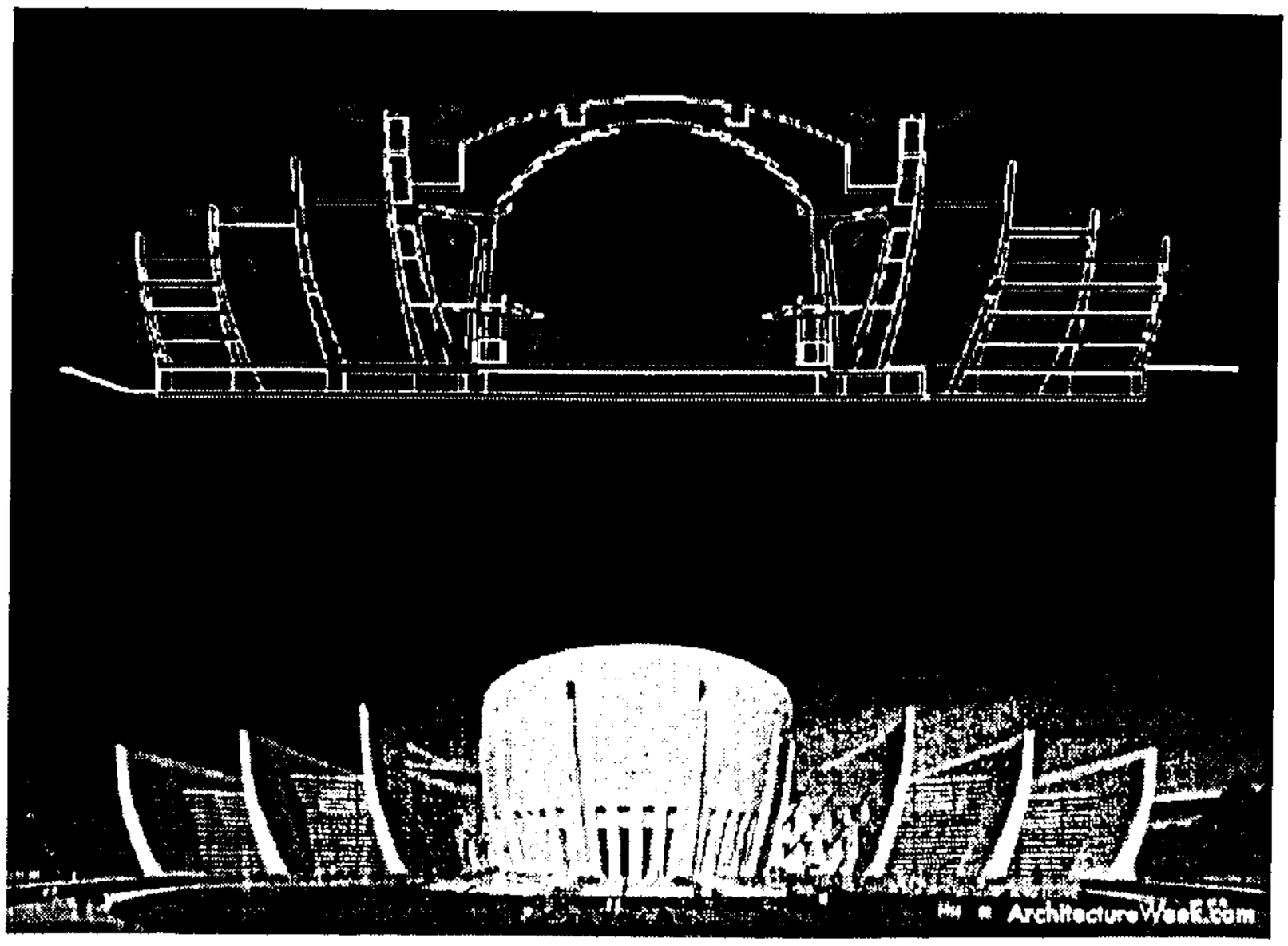

(a)

Figure 2.1: Naturally ventilated buildings: Computational model of the Hall of Still Thought in Taiwan. (http://www.architectureweek.com/).

building architecture in modern cities. Naturally ventilated buildings are becoming a popular choice. They have the main advantage of being highly energy efficient and so, environmentally friendly. Natural ventilation in buildings is caused by external winds or buoyancy forces between the inside and the outside of the building (Croome and Roberts (1981)). Naturally ventilated buildings or rooms are, however, not as versatile nor as stable as mechanically ventilated buildings. In order to be efficient, their design, as illustrated by Figure 2.1, is often found to be of a complex nature. Mechanical ventilation systems provide a better controlled indoor climate than natural ventilation systems. Natural ventilation is often used for large-scale ventilation (*i.e.* a building as a whole) and mechanical ventilation systems are often used for the specific needs of a room or an office.

Mechanical ventilation systems are mainly composed of a fan, a temperature regulation unit, an air-filtering device, a fresh air supply and, of inlet and outlet diffusers placed in the room. This study is only concerned with the ventilation processes occurring inside rooms or offices and further details on the various components constituting a mechanical ventilation unit can be found in McQuiston and Parker (1994) and Jones (1997). The mechanical ventilation of rooms is found under many forms that mainly differ from each other by the layout and shape of the various inlets and outlets in the room. The influence of the diffuser on the airflow pattern in a room is illustrated by Hu, Barber and Chuah (1999) who studied numerically, using the $k-\epsilon$ turbulence model with a condensation and thermal comfort model, the indoor environment provided by three diffusers. The airflow pattern in the room as well as the thermal comfort analysis is found to be highly dependent on the diffuser. Further discussion on inlet diffusers is found in Chapter 6.

The two dominant ventilation layouts illustrated by Figure 2.2 are displacement- and mixed-ventilation. A mixed-ventilation layout (Figure 2.2 (a)) consists in the supply and exhaust of air in the ceiling area of the room. In mixed-ventilation, the air is supplied at higher velocity than in displacement-ventilation and creates a uniform (mixed) indoor environment. The presence of an extraction fan on the mixed-ventilation device ensures an adequate air renewal in the room. In a typical displacement-ventilation layout, as illustrated by Figure 2.2 (b), cold air is supplied at low level and returned in the ceiling area. The airflow pattern of displacement ventilated areas is governed by convection phenomena. When the cool supplied air encounters heat sources, (such as a working person, a personal computer (PC), etc...) convection occurs. The renewal of air in the

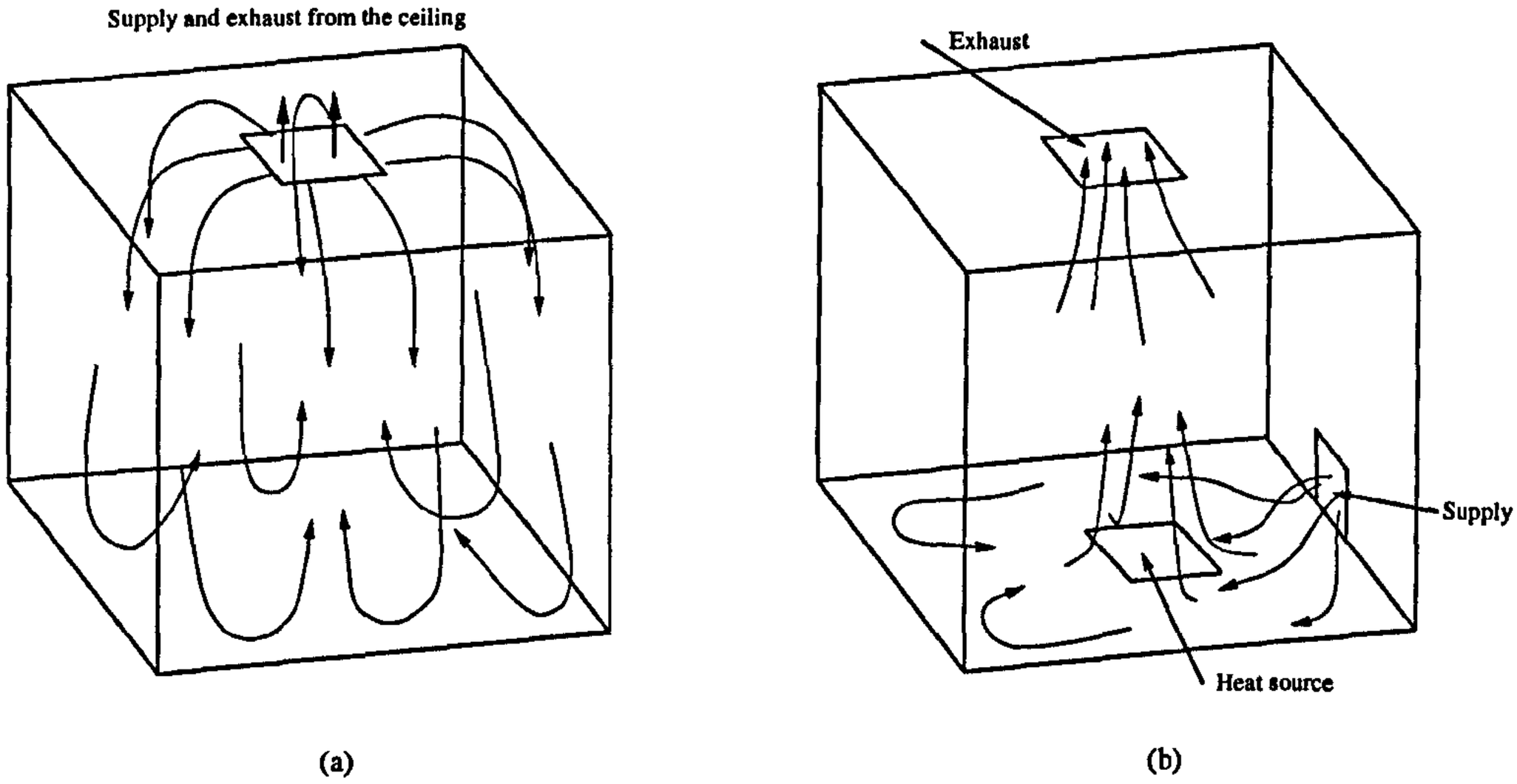

Figure 2.2: Typical ventilation layouts: (a) Mixed-ventilation and (b) displacement-ventilation layout.

room is thus driven by the rise of air from the lower part to the higher part of the room.

Mundt's (2000) investigation in a displacement ventilated room shows that particles introduced at a low level, and therefore subject to convection, do not increase drastically the risk of polluting the breathing zone of a standing or walking individual. However, the motion of an individual is found to increase the concentration of particles in the breathing zone and outside the convective area. It is also found that the decay rate of larger particles ($> 10\mu m$) is mostly independent of the convective flow.

Xing, Hatton and Awbi (2001) compare the overall air quality in a displacement ventilated room, equipped with various heat load and a thermal manikin, with the air quality in the breathing zone. Both numerical predictions (standard $k - \epsilon$ model) and

measurements are used. The investigation shows that the air quality in the breathing zone is better than the overall air quality in the room (up to 50% better for a seated manikin and up to 20% better for a standing manikin) and highlights the advantages of the displacement-ventilation layout.

The next sections place greater emphasis on CFD work in relation to air quality issues, thermal comfort and ventilation effectiveness in rooms. Recent developments in CFD methods allows better flow predictions but, the trade-off between prediction accuracy and computational expenses remains crucial in the industrial world. Thus, most of the CFD work undertaken for room ventilation, and presented here, is carried out using linear eddy viscosity RANS approach and in particular the standard $k-\epsilon$ turbulence model (see Chapter 3). Only recently the use of more advanced approaches for the modelling of turbulence, such as variants of the standard models or LES, have been applied to simply ventilated room or offices. These novel CFD techniques as applied to room ventilation are reviewed in Section 2.2.

2.1.1 Air quality

Air quality issues in ventilated areas has become a topic of great interest in the last decades with studies revealing the association between indoor air quality and numerous health complaints. In particular the Sick Building Syndrome (SBS) which can be traced back to 1970 (Hart (1970), LaVerne (1970)) has been extensively covered in the recent years (*i.e.* Sundell (1996), Hedge (1992), Molhave (1989)). The SBS as defined by the World Health Organization (WHO (1983)) includes a range of symptoms such as skin, nose and throat irritation, headaches, nausea, dizziness and, seems to be partly assimi-

lated with ventilation rate, air quality and airflow patterns in a room (Sundell (1994)). Besides the SBS, air quality issues in rooms and offices are often related to the diffusion, containment and extraction of pollutant sources. A typical list of pollutant sources in rooms such as CO_2, smoke, radon, etc... is given by Hodgson (2000).

The control of the diffusion of contaminant sources (*i.e.* Environmental Tobacco Smoke (ETS), airborne viruses, etc...) is one example where ventilation is needed. The extraction and control of ETS in public places has become a greater problem in the last decades as illustrated by the new amendments to the Norwegian Smoking Law of 1988. The latter stipulates that at least one-half of the tables in a restaurant are to be kept free of smoke. Some of the basic ventilation rules and strategies to adopt where both smoking and non-smoking people share a common space is reviewed by Krühne and Fitzner (2000). One of the problem induced by investigating the diffusion of ETS products is that it is constituted by a range of particles sizes which, as showed by Mundt (2000), have a different distribution in a ventilated area.

Mundt's (2000) work on particle distribution is further supported by Timmer and Zeller's (2000) investigation. The numerical simulation of Timmer and Zeller (2000) compares predicted deposition of particles in the vicinity of the outlet of a ceiling inlet, floor outlet ventilation system with the experimental data of Rauer (1996). Rechnagel *et al.* (1999) estimate that one million solid particles are contained in 1 m^3 of air in an average European city. 98% of these particles have a diameter of less than 1 μm and represents only 3% of the total mass load. The numerical modelling of Timmer and Zeller (2000), using the commercial code FLUENT/4.48^{TM} with a particle load of 1000 g/m^3, shows that the number of particles hitting the ceiling increases by five for

particles sizes in the range 0.1 to 40 μm. The increase of particle load from 800 to 1400 g/m^3 increases particle deposition from 1% to 2.4%. A rise in the inlet velocity from 2.4 to 4.7 m/s increases the amount of deposited particles from 0.1% to 2.5%. Finally, the increase of the outlet turbulence intensity from 2 to 80 also increases the amount of particles reaching the ceiling from 0.5% to 3.3%. These results are found to be in good agreement with the experimental data of Rauer (1996) and emphasise the importance of the turbulence level, velocity and particle size on the deposition of particles in a ventilated room.

Thus, to analyse accurately the diffusion of complex pollutants such as ETS in ventilated spaces, experimental data on the size and quantity of these particles are required. Experimental data such as those of Cumo *et al.* 's (2000) which relate the nature and variation of the concentration of ETS in the house of parliament in Rome can be used to validate numerical methods. Other studies on particles distributions in rooms can be found in Nazaroff *et al.* (1990), Lu (1995) and Lu and Howarth (1999) who investigate numerically, using the $k - \epsilon$ model, the particle distribution in a multizone ventilated room.

One of the most efficient way to contain the diffusion of smoke in a given space is to install obstacles or partitions. Air curtains, as often seen in commercial buildings and warehouse, are designed to maintain thermal comfort at low energy expenses. Air curtains can also be used as an obstacle or partition that separates smoking and non-smoking areas. Rydock *et al.*'s (2000) investigation is based on the design and evaluation of an air curtain that aims to isolate smoking and non-smoking areas in a restaurant. It is found that the air curtain provide significantly improved air quality in the non-

smoking area but, a completely smoke-free area could not be achieved.

Changes in legislation in recent years also affect ventilation rates required in public places. Among the many changes, ventilation rates in classrooms have been affected as illustrated by the amendment of building regulations in the U.K. (2001) which imposes a minimum of 3 litres of fresh air per second per occupant.

The recent interest in classroom ventilation can be illustrated by the work of Zeng *et al.* (2000) who investigate experimentally and numerically the flow behaviour inside a typical Canadian portable classroom equipped with a single high-mount supply and a single low-mount exhaust ventilation device. The experimental data (flow visualisation and SF_6 measurements) are used for the implementation of the boundary conditions of the three-dimensional CFD simulation (standard $k-\epsilon$ model). The unsteady CFD model is used to predict the mean age of air and CO_2 concentration in the room. The latter, since stagnation zones with high CO_2 concentrations are observed at the front of the classroom, underlines the need for improvement of the ventilation unit.

Karimipanah *et al.* (2000) study the efficiency of four ventilation strategies (displacement-ventilation, mixed-ventilation, impinging jet and textile diffuser) in a mock-up of a full-size classroom under the extreme external temperature conditions found in Sweden. Both experimental analysis and CFD modelling ($k-\epsilon$ model of the VORTEX code) are made. CFD and experimental data are found to agree well. The minor discrepancies observed are partly explained by the strong buoyancy effects induced by the ventilation device and, by the lack of accuracy of the CFD model especially in the near-wall areas. It is concluded that for a all-year use none of the four system is more efficient than another.

2.1.2 Thermal comfort

Ventilation also aims to increase thermal comfort in rooms and offices in order to increase the level of productivity of its occupants (Awbi (1991)). Since the sensation of comfort depends on the individual thermal comfort is a difficult topic to address scientifically. To understand and study thermal comfort, a series of parameters or indices have been introduced over the years to define the level of satisfaction of the room's occupants (Fanger *et al.* (1988)). The Predicted Percentage of Dissatisfied (PPD) and Predicted Mean Vote (PMV) are among the standard indices used. Thermal comfort in a room depends on a multitude of parameters such as ventilation strategy, clothing, body activity, etc... . The ISO 7730 (1994) and ASHRAE (1993) standards offer some guidelines on indoor temperature settings based on ideal experimental conditions. These guidelines are often found to be misleading when considering real rooms (Awbi (1998)).

Thermal problems in ventilated rooms can mostly be assimilated as thermal plumes rising from sources such as lighting, electrical equipment, etc... . Using the water tank analogy, Hunt *et al.* (2000) investigate the variations in the mixing process of a non-zero momentum buoyancy point source. This problem, commonly referred as the filling box, is carefully described by Baines and Turner (1968) and includes most of the physical behaviour of thermal problems encountered in rooms. Hunt *et al.*'s (2000) experimental analysis reveals that buoyancy effect alone leads to a stable flow stratification in the room. The combination of buoyancy and momentum sources (or jet) leads to a more traditional jet flow, to unsteadiness and, drastically affect the overall thermal behaviour of the room.

Park and Holland (2000) perform a two-dimensional numerical simulation ($k-\epsilon$ model) of a heat source in a displacement ventilated room. The investigation aims to determine the influence of the position of the heat source on the performances of the ventilation system. As expected the CFD results show that, since both buoyancy forces and momentum effects are present (c.f. Hunt *et al.* (2000)), the thermal plume generated by the heat source is affected by the displacement-ventilation inlet. It is found that the height of thermal stratification reduces as the heat source rises. The temperature gradient observed near the ceiling is found to increase as the heat sources rises. This also increase the cooling load required to maintain the room's temperature.

Thermal comfort in displacement ventilated areas is difficult to achieve. This is illustrated by Melikov and Nielsen (1989) who analysed thermal comfort in 18 displacement ventilated spaces. They found that up to 15% of occupants are dissatisfied due to draught problems. Also, about 40% of the locations considered have a thermal gradient $> 3K$ between the head and feet of the occupants. To enhance predictions of thermal stratification and thermal comfort in displacement ventilated rooms, Yuan *et al.* (1999) created a large database of air temperature and contaminant distribution in various rooms. This is further discussed in Chapter 10. Using this database, Yuan, Chen and Glicksman (1999) developed simple models that aim to determine the temperature stratification in typical displacement ventilated offices.

Trzeciakiewicz *et al.* (2000) show the importance of radiant effects in rooms. To show this, they use numerical simulation (standard $k-\epsilon$ model) and experimental data to investigate long-wave radiant heat source emitted from a 600 W circular plate of 0.15 m

in diameter in a displacement ventilated room. The implementation as a boundary condition of an emission coefficient at the wall, given by experimental measurement, ensure the modelling of the long-wave radiation induced by the heat source. The comparison of CFD and experimental data reveals that only qualitative data can be extracted from the CFD analysis. It also appears that the modelling of heat sources as convective and radiant source is required to model accurately heat sources in displacement ventilated areas.

2.1.3 Ventilation efficiency and energy consumption

To quantify ventilation efficiency in removing pollutants from given spaces, criteria such as the mean age of air, the local concentrations of pollutant are commonly used. The development of indices to evaluate ventilation efficiency is ongoing as illustrated by the recent work of Hayashi *et al.* (2002) who introduce two new indices (IEVC and IECI). These characterise the effectiveness of pollutant removal and the effect of contaminant inhalation.

Collignan and Riberon (2000) used the two-dimensional experimental test case of Nielsen *et al.* (1978) to conduct a series of numerical test that aim to assess the efficiency of pollutant removal from a room. PHOENICS CFD code predictions, testing four variants of the $k-\epsilon$ model (Launder and Spalding (1974); Chen and Kim (1987); Lam and Bremhorst (1981) and a two-layer model), shows that the Lam and Bremhorst (1981) model gives best agreement with measurements in terms of velocity distribution and turbulence intensity. A parametric study of the position of the contaminant source with respect to the location of the exhaust of the ventilation system reveals that the

use of the contaminant removal effectiveness index ϵ_p, defined as $\epsilon_p = C_m/C_e$, where C_m is the mean concentration of pollutant in a given zone and C_e is the mean concentration of pollutant at the exhaust, can be used to grade the efficiency of pollutant removal in a room. High-efficiency ventilation devices would return a value of ϵ_p below 1.

Akabayashi *et al.* (2000) use numerical modelling and a full-scale experimental set-up to investigate the influence of three ventilation layouts and efficiencies in a working office. The time decay of SF_6 gas tracer, in 27 sampling locations in the $5 \times 3.6 \times 2.45$ metres room containing numerous heat sources, is used for the CFD calculations provided by the STREAM (Cradle Co. ltd. (1990)) code and a high Reynolds number $k-\epsilon$ model. The ventilation efficiency for the three layouts presented is calculated according to the model of Kato and Murakami (1986). The numerical analysis emphasises the deficiency of the numerical model in predicting accurately heat transfer and airflow in near-wall areas. Kuwahara *et al.* (2000) investigate ventilation efficiency of an atrium space and also emphasise the deficiency of numerical models in predicting accurately near-wall flows.

2.2 Advances in CFD for room ventilation

A review of the recent advances in CFD techniques applied to room-ventilation problems is presented here. Improvements can be seen in two of the mainstream areas of current CFD which are based on RANS and LES methods.

2.2.1 Advanced RANS models for room ventilation

As discussed previously, the standard linear $k-\epsilon$ model is the most popular method for computing flows in ventilated spaces but is known to give unsatisfactory predictions for a number of flow configurations. Limitations of the $k-\epsilon$ model for room ventilation are reviewed by Chen (1997). Peng, Davidson and Holmberg (1996) investigate performances of three two-equations models for prediction of room airflows. It is found that a modified version of the $k-\omega$ model (Peng, Davidson and Holmberg (1997)) gives similar predictive accuracy to the $k-\epsilon$ but has faster convergence.

Variants of the $k-\epsilon$ model such as the Re-Normalisation Group (RNG) of Yakhot and Orzag (1986), the model of Kim, Kato and Murakami (2001) which includes radiant effect or the model of Jacobsen and Nielsen (1993) which includes buoyancy effects, have been introduced to increase the predictive accuracy of the standard $k-\epsilon$ model. A range of variants of the $k-\epsilon$ models applied to room ventilation is given by Chen (1996).

Kim, Kato and Murakami (2001) present a novel method to analyse the heating/cooling load in a ventilated room. In the numerical model, the standard $k-\epsilon$ model is coupled with a radiation model (Gebhart (1959)). The numerical model is also coupled with the control system of an HVAC unit which gives the boundary conditions of the numerical model. This new method, which allows the study of cooling/heating loads under various conditions, has been successfully applied to the testing of two HVAC systems.

Jacobsen and Nielsen (1993) investigate the ability of three variants of the $k-\epsilon$ model to predict flows in displacement-ventilated rooms. The three models (standards $k-\epsilon$,

$k-\epsilon$ with buoyancy term and the low Reynolds number model of Chikamoto, Murakami and Kato (1992)) are compared with temperature and velocity measurements. Despite their differences, all three models are found to give overall similar level of agreement with measurements.

To model more accurately the near-wall behaviour, low Reynolds number turbulence models can be used. Low Reynolds number $k-\epsilon$ models, further discussed in Section 3.1.6 use wall damping functions. To model near-wall effects, Xu and Chen (2001-a) propose a zonal model for the evaluation of indoor air flows. In this model, the one-equation model of Rodi, Mansour and Michelassi (1993) is used in the near wall region ($y^+ < 80$) and the standard $k-\epsilon$ is used otherwise. The model is validated for natural and mixed convection in cavity flows as well as real room configurations (Xu and Chen (2001-b)) and is found to be stable. It also shows good agreement with measurements or DNS data.

Owing to recent increases in affordable computing power transient-flow calculation of ventilated spaces is now possible. For example, Hyun and Kleinstreuer (2000) investigate the effect of transient breathing on the concentration of ambient tracer gas in a non-isothermal room. The use of transient mode, instead of the steady-state mode, reveals significant concentration differences when compared with the measurements of Brohus (1997). Concentrations at the steady state are found to be higher than those in the transient mode.

Besides the need for increased accuracy, solution speed is a key factor in CFD investigations of ventilated rooms. To reduce computational expense, Chen and Xu (1998) present a zero-equation model aiming to predict velocity, temperature and contami-

nant concentration in rooms. The new model is found to be less accurate than the standard $k - \epsilon$ model for natural, forced and mixed convection problems but convergence times are a factor of ten lower. The model is further validated on four fully furnished ventilated-room configurations containing various heat sources (Srebric, Chen and Glicksman (1999)). The model, despite being less accurate than the $k - \epsilon$ model, allows the simulation of a ventilated room in less than 7 mins on a PC (350 MHz) using a $27 \times 22 \times 20$ grid points.

Owing to its flexibility and to increases in computing power, CFD is becoming a widely used tool in the design of ventilation units. Some of the recent case studies where CFD has been used as a tool to design or to improve the design of ventilation units or ventilation layouts without the backup of experimental data are presented below.

Among recent projects, Yoon *et al.* (2000) use the RNG model in the PHOENICS code to predict airflow, temperature and CO_2 concentration in the great hall of the Inchon international airport in Korea. The use of CFD reveal in this case that natural ventilation methods give a better thermal distribution in the hall (34^oC) than the HVAC unit considered (up to 80^oC).

Lin *et al.* (1999) also use a RNG model to model a typical workshop in Hong-Kong. The CFD model aims to evaluate radon, CO_2 and moisture concentrations in the ventilated area. Also, Sinai *et al.* (2000) use the CFX commercial code to design and implement HVAC system in the Greenwich millennium dome opened in London in December 1999. The three-dimensional CFD analysis of the dome includes both convective and radiative effects and parameters such as, wind and seasonal parameters

(clouds...), heat loads corresponding to a populated dome and, a general layout of the interior of the dome. The results obtained from the CFD study drove the selection of the ventilation design and layout currently being use in the dome.

2.2.2 Large Eddy Simulation for room ventilation

In LES, the large scales are resolved and the small scale eddies are modelled by a SubGrid-Scale (SGS) model. The SGS should ensure the correct transfer of energy between the resolved and modelled scales of the flow and is key to the accuracy of the simulation. Since the first LES model proposed by Smagorinsky (1963), various SGS models have been proposed. Among the most popular models are the dynamic SGS model of Germano *et al.* (1991) or Lilly (1992) and the one-equation SGS of Yoshizawa (1993) in which all the local dynamic information of the flow are included in the transport equation of kinetic energy. A review of SGS models is presented by Lesieur and Metais (1996) and is further discussed in Chapter 3.

Emmerich and McGrattan (1998) used the Smagorinsky (1963) model to predict the airflow in an isothermal three-dimensional room. The results, strongly dependent on the grid resolution and on the Smagorinsky constant, partly highlight the need for better SGS models.

The potential of LES for room ventilation can be illustrated using the investigations of Nielsen *et al.* (2000) and Davidson *et al.* (2000) based on the analysis of the low Reynolds (Re) number effect commonly observed in ventilated rooms. Nielsen *et al.* (2000) investigate an isothermal low Re number flow coming from an inlet boundary condition slot. Slot inlets are devices commonly found in mixed or natural ventilation

systems such as airflow from the bottom of hung windows (Svidt *et al.* (2000)). Experimental data have shown that the velocity profile induced by the inlet boundary condition does not match exactly the universal wall-jet profile for fully developed flow for low Reynolds numbers as defined by ASHRAE (1997). The difference observed between universal profile and measurements is found to reduce as the Reynolds number is increased. Davidson *et al.*'s (2000) two-dimensional numerical investigation, at an inlet Reynolds number of 600, aims to verify the experimental observations of Nielsen *et al.* (2000) using a low Reynolds number RANS model (the $k-\omega$ model of Peng, Davidson and Holmberg (1997)). This method is found to be inadequate since RANS models have been developed to deal with the near-wall regions where viscous effects are dominant. In the present analysis, and more generally in ventilated rooms and buildings, low Reynolds number effect are observed in regions far-off the wall, where viscous effect are negligible and thus lead to mispredictions of the RANS models. The dynamic subgrid model of Davidson (1997) in this case has shown a real improvement in the prediction of an accurate velocity profile compared with experimental data (Davidson *et al.* (2000)).

Peng and Davidson (2000) applied the one-equation SGS of Davidson (1997) to three flow configurations (Rayleigh-Benard convection, buoyant cavity flow and mixed-ventilation flow) to demonstrate the potential of LES for room ventilation. In the three test cases, the LES gives good agreement with DNS or experimental data. The investigation for the mixed ventilated room at low Reynolds number emphasise the importance of the near-wall treatment.

Müller and Davidson (2000) use the two-dimensional test case of Nielsen (1990) to investigate the performances of two SGS stress models. The one-equation SGS model

of Davidson (1997) and the one-equation SGS model of Menon and Kim (1996). The implementation of boundary conditions for LES requires extra fluctuating information (transient information) not required for RANS simulations. The use of a random multiplicating number that changes the inlet at every time step and, transient data from channel flow investigations are tested on the Menon and Kim (1996) SGS model. Better predictions are found when transient inlet conditions are used.

The SGS model of Joubert *et al.* (2000) derived from the mixed scale model of Sagaut *et al.* (1996) allows the separate computation of the subgrid viscosity and the subgrid thermal diffusivity. This model has been developed for the specific application of non-isothermal flows in cavities and is found to agree well with the two-dimensional DNS investigation of a heated cavity at a Rayleigh (Ra) number of 5.10^{10} (Xin and Le Quere (1995)). The new LES model is also found to perform well when applied to two-dimensional non-isothermal partitioned cavities.

Zhang and Chen (2000), present a novel SGS model based on a double filtering of the coefficients of the dynamic SGS model of Germano *et al.* (1991). This model (FDSM) allows the modelling of a range of complex flows and is tested on natural, forced, and mixed convection in rooms. It is found that the FDSM gives better predictions than the standard Smagorinsky (1963) model when compared with measurements. The FDSM is found to be more accurate in predicting mean airflows components than in predicting turbulent quantities or heat transfer.

Chapter 3

Turbulence modelling

As discussed previously, turbulence can be accounted for using either of the following methods: DNS, LES or RANS. This chapter is focused on the modelling of turbulent flows using RANS, LES and hybrid RANS/LES methods.

3.1 The RANS approach

The RANS method, introduced by Reynolds (1895), is based on a time-averaging of the governing equations. The instantaneous flow property $\Phi(t)$ (see Figure 3.1) can be decomposed as the sum of a fluctuating component $\phi'(t)$ and of an averaged (or mean) component ϕ ($\Phi(t) = \phi'(t) + \phi$). Considering a sufficiently long time period t_l such as $t_l >> t_i$ (where t_i is the turbulence time scale), the time average (or mean) of $\Phi(t)$ can be expressed as:

$$\overline{\Phi(t)} = \frac{1}{t_l} \int_0^{t_l} \Phi(t)\, dt\ . \tag{3.1}$$

The overbar symbolises the time-averaging process. Since $t_l >> t_i$ the averaging of the mean flow component over the time t_l ($\overline{\phi}$) is found to be equal to the same mean flow component ϕ ($\overline{\phi} = \phi$). Also, by definition, the time average of the fluctuating flow

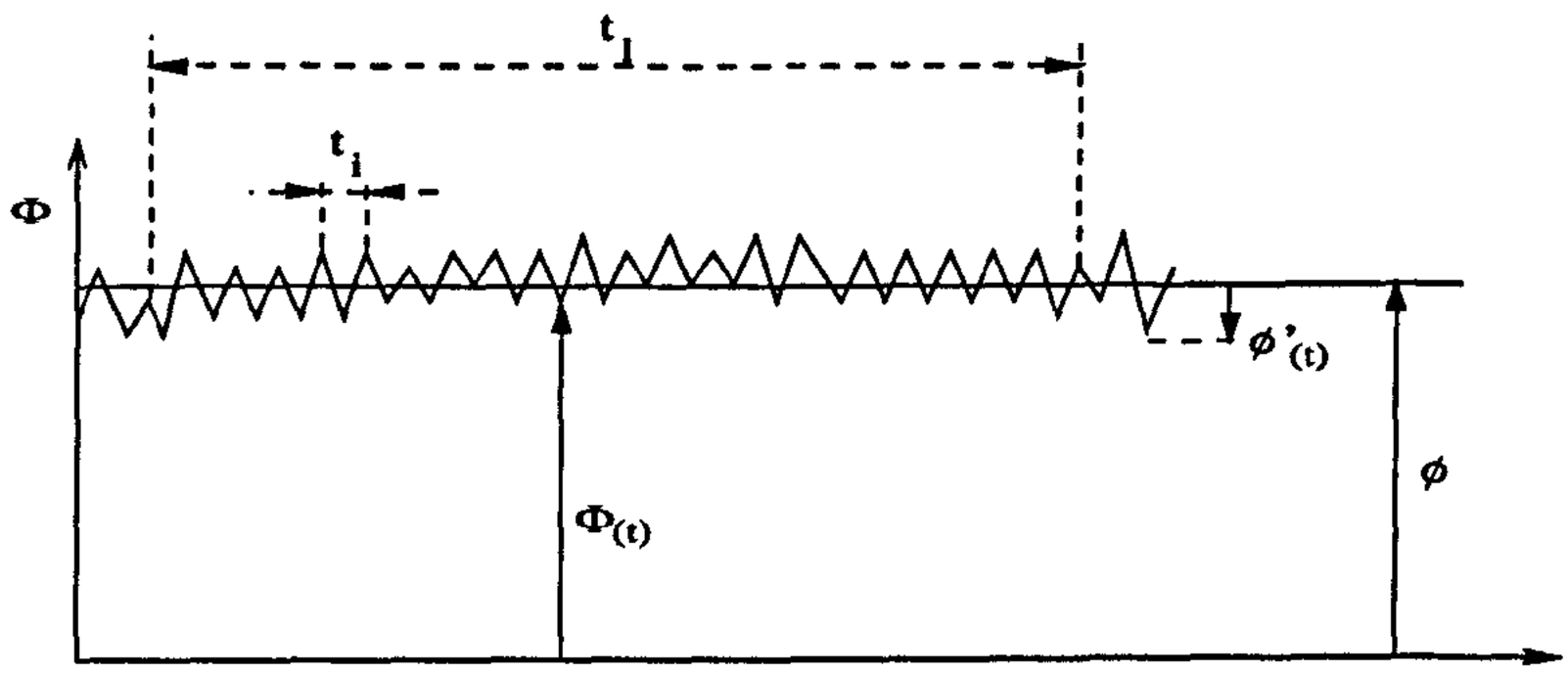

Figure 3.1: Typical turbulent flow and Reynolds decomposition.

component $\overline{\phi'(t)}$ is zero (see Figure 3.1).

The substitution of the definition of $\Phi(t) = \phi'(t) + \phi$ into the N-S equations followed by the time averaging yield the following:

$$\frac{\partial \rho u_i}{\partial t} + u_j \frac{\partial \rho u_i}{\partial x_j} = -\frac{\partial p}{\partial x_i} + \mu \frac{\partial}{\partial x_j}\left(\frac{\partial u_i}{\partial x_j} + \frac{\partial u_j}{\partial x_i}\right) + \frac{\partial}{\partial x_j}\left(-\rho \overline{u_i' u_j'}\right) \tag{3.2}$$

$$\frac{\partial u_j}{\partial x_j} = 0. \tag{3.3}$$

$$\frac{\partial (\rho \phi)}{\partial t} + \frac{\partial (\rho \phi u_j)}{\partial x_j} = \frac{\partial}{\partial x_j}\left(\frac{\mu}{P_r}\frac{\partial \phi}{\partial x_j}\right) + \frac{\partial}{\partial x_j}\left(-\rho \overline{u_j' \phi'}\right) \tag{3.4}$$

The RANS equations introduce the new quantities $-\rho\overline{u_i' u_j'}$ and $-\rho\overline{u_i' \phi'}$ known as Reynolds stress tensor (also noted τ_{ij}) and the turbulent scalar transport term. These are the only components in Equation 3.2 and 3.4 which contain turbulent flow information. The RANS equations form a system of five equations with eleven unknowns (u, v, w, p, $\overline{\rho u_i' \phi'}$ and six Reynolds stresses) and so cannot be solved. This difficulty, known as the closure problem, is overcome by introducing turbulence models. A turbulence model

is simply a way to close the system of RANS equations by approximating τ_{ij} and $-\overline{\rho u_i' \phi'}$.

One turbulence modelling concept was introduced by Boussinesq (1877) who related the Reynolds stress tensor to the rate of deformation of the fluid. By analogy with Newton's law of viscosity, Boussinesq (1877) proposed to evaluate the turbulent Reynolds stress tensor using:

$$\tau_{ij} = 2\mu_t S_{ij} \tag{3.5}$$

where the term μ_t is introduced as an eddy, or turbulent, viscosity. S_{ij} is the mean strain rate and is often used for turbulence modelling purposes along with W_{ij}, the vorticity. They are defined as:

$$S_{ij} = 0.5\left(\frac{\partial u_i}{\partial x_j} + \frac{\partial u_j}{\partial x_i}\right) \tag{3.6}$$

$$W_{ij} = 0.5\left(\frac{\partial u_i}{\partial x_j} - \frac{\partial u_j}{\partial x_i}\right) \tag{3.7}$$

A generalised form of the Boussinesq assumption remains a key assumption in many turbulence models and is given by:

$$\tau_{ij} = -\frac{2}{3}\rho k \delta_{ij} + 2\mu_t S_{ij} \tag{3.8}$$

where δ_{ij} is known as the Krondeker delta equal to 0 if $i \neq j$ and equal to 1 if $i = j$ and, k is the turbulent kinetic energy (see Section 3.1.2).

Turbulence models are often classified by the number of extra partial differential equations (Pde) used to close the RANS equations. The next sections present the zero-, one- and two-equations linear eddy-viscosity models used.

3.1.1 Prandtl's mixing-length model

Prandtl's (1925) mixing-length model is based on the simple concept, from a dimensional analysis, that the turbulent viscosity μ_t can be expressed as the product of an eddy length scale l_μ and, of a velocity scale V^*.

$$\mu_t = \rho c_1 l_\mu V^* \ , \tag{3.9}$$

c_1 being a constant. Research in two-dimensional shear flows shows that the only velocity gradient having a significant effect on the flow is $\partial u/\partial y$ (where u is the main flow direction and y its normal). This suggest the velocity scale V^* should be expressed as:

$$V^* = c_2 l_\mu \frac{\partial u}{\partial y} \tag{3.10}$$

where c_2 is a constant. Combining equations 3.9 and 3.10 allows the turbulent viscosity μ_t to be written as:

$$\mu_t = \rho c_1 c_2 l_\mu^2 \frac{\partial u}{\partial y} = \rho l_m^2 \frac{\partial u}{\partial y} \tag{3.11}$$

where l_m, the mixing length, includes the effect of the coefficients c_1 and c_2. The mixing length (l_m) is obtained from empirical methods and depends on the flow configuration. Some of the common mixing length definitions can be found in Wilcox (1995). In this work, the standard mixing length model uses $l_m = \kappa y f_\mu$ where κ is the von Karman (1931) constant (= 0.41) and y the normal wall distance. The high Reynolds number model uses $f_\mu = 1$. The low Reynolds number model uses the Wolfshtein (1969) damping function (see Section 3.1.6). In Chapter 8, the mixing-length model is tested on a jet-ventilated room. To model a round jet (such as the one seen in Chapter 8) the mixing length l_m is taken as:

$$l_m = C_m L \tag{3.12}$$

where $0.075 < C_m < 0.09$ and L is taken as the half width of the jet. Further discussion on the effect of C_m is discussed in Chapter 8. The model uses the Boussinesq approx-

imation (Equation 3.5) to evaluate the Reynolds stress tensor. Since no extra Pde are used, the mixing length model is known as a zero-equation model.

3.1.2 The transport equation of turbulent kinetic energy

To hopefully enhance turbulence predictions, the non-zero-equation turbulence models (*i.e.* $k-\epsilon$, $k-l$) use extra partial differential equations (Pde). The turbulent kinetic energy k is commonly used to gain a turbulence velocity scale. It is defined as:

$$k = \frac{1}{2}\overline{u_i' u_j'} = \frac{1}{2}\left(\overline{u'^2} + \overline{v'^2} + \overline{w'^2}\right) \tag{3.13}$$

A transport equation for k can be derived by taking the trace of the Reynolds stress equation (see Section 3.2.1). Assuming incompressible flow, the k equation can be written as (Tennekes and Lumley (1972)):

$$\frac{\partial k}{\partial t} + \frac{\partial u_j k}{\partial x_j} = \frac{1}{\rho}\frac{\partial}{\partial x_j}\left(\Gamma_k \frac{\partial k}{\partial x_j}\right) + \overline{u_i' u_j'}\frac{\partial u_i}{\partial x_j} - \epsilon \tag{3.14}$$

where ϵ is the rate of dissipation of turbulent kinetic energy and $\Gamma_k = \mu + (\mu_t/\sigma_k)$. The diffusion Prandtl's number for k, $\sigma_k = 1$. The popular one-equation $k-l$ and two-equation $k-\epsilon$ linear models are described below.

3.1.3 The $k-l$ model

In the $k-l$ model, only one extra Pde is used (the k equation) and ϵ (in the inner part of the boundary layer) is evaluated by equations based on wall distances. In the $k-l$ model of Wolfshtein (1969), originally introduced by Van Driest (1956), which contains damping functions and allows the model to be used in a low Reynolds number form, ϵ is defined as:

$$\epsilon = \frac{k^{3/2}}{l_\epsilon} \tag{3.15}$$

where l_ϵ is a dissipation length scale:

$$l_\epsilon = C_{\epsilon 0}\ y(1 - e^{-A_\epsilon y^+/C_\mu^{1/4}}) \tag{3.16}$$

The turbulent viscosity μ_t is defined as a function of the turbulent kinetic energy k and the length scale l_μ by:

$$\mu_t = \rho l_\mu k^{0.5} \tag{3.17}$$

l_μ is defined by:

$$l_\mu = C_{\mu 0}\ y(1 - e^{-A_\mu y^+/C_\mu^{1/4}})\ . \tag{3.18}$$

The following constants are used in the model: $C_{\epsilon 0} = 2.4$, $C_{\mu 0} = 2.4$, $A_\mu = 0.016$ and $A_\epsilon = 0.263$. y and y^+ are the wall distance and the non-dimensional wall distance respectively (see Section 3.1.6). The term $(1 - e^{-A_i y^+/C_\mu^{0.25}})$ found in Equation 3.16 and 3.18 is the damping function of Wolfshtein (1969) and can be set to one to allow the use of the high Reynolds number model. To model the outer part of the turbulent boundary layer, a limit is placed on l_μ and l_ϵ. Here the limit used is $0.4857 \times Hgap$. $Hgap$ being half the normal distance between the closest and farthest wall.

Variants of the $k - l$ model such as the Chen and Patel (1988) model have been found to be successful in predicting curved and separated flows. The Chen and Patel (1988) model uses the following constants: $C_{\epsilon 0} = 2.495$, $C_{\mu 0} = 2.495$, $A_\mu = 0.014$ and $A_\epsilon = 0.200$.

3.1.4 The $k-\epsilon$ model

This model was introduced by Jones and Launder (1972). Despite the recent advances in many areas of CFD, the two equations $k - \epsilon$ model remain the most widely used in industry. The high Reynolds number model of Launder and Spalding (1974) is referred

here as the standard $k-\epsilon$ model and is presented below. The Low Reynolds Number (LRN) version uses damping functions. The Launder and Sharma (1974) and the Lam and Bremhorst (1981) models are among the most popular LRN versions of the $k-\epsilon$ model and are discussed in Section 3.1.6. In the $k-\epsilon$ model, the turbulent kinetic energy k is approximated using Equation 3.14 and ϵ is evaluated by:

$$\frac{\partial \epsilon}{\partial t} + \frac{\partial u_j \epsilon}{\partial x_j} = \frac{1}{\rho}\frac{\partial}{\partial x_j}\left(\Gamma_\epsilon \frac{\partial \epsilon}{\partial x_j}\right) + f_1 C_{\epsilon 1}\frac{\epsilon}{k}P_k - f_2 C_{\epsilon 2}\frac{\epsilon^2}{k} \tag{3.19}$$

where P_k is known as the production term defined by:

$$P_k = -\overline{u_i' u_j'}\frac{\partial u_i}{\partial x_j} \tag{3.20}$$

The Boussinesq approximation (Equation 3.8) is used to evaluate the Reynolds stress tensor and, the turbulent viscosity is expressed, from a dimensional analysis, by:

$$\mu_t = \rho f_\mu C_\mu \frac{k^2}{\epsilon} \tag{3.21}$$

In the standard model, the constants C_μ, $C_{\epsilon 1}$ and $C_{\epsilon 2}$ are equal to 0.09, 1.44 and 1.92 respectively. The diffusion coefficient $\Gamma_\epsilon = \mu + (\mu_t/\sigma_\epsilon)$ where σ_ϵ is the diffusion Prandtl's number for ϵ $(= 1.3)$. In the standard (high Reynolds number) model, $f_\mu = f_1 = f_2 = 1$. For LRN models, those parameters allow the introduction of near-wall turbulence damping.

3.1.5 Passive scalar, temperature and buoyancy modelling

To model an arbitrary scalar quantity (C), such as the SF_6 tracer gas (see Chapters 9 and 11) using RANS, the following transport equation is used:

$$\frac{\partial C}{\partial t} + \frac{\partial u_j C}{\partial x_j} = \frac{1}{\rho}\frac{\partial}{\partial x_j}\left(\Gamma_C \frac{\partial C}{\partial x_j}\right) \tag{3.22}$$

where the diffusion coefficient $\Gamma_C = \mu + \mu_t/\sigma_C$. The diffusion Prandtl for an arbitrary scalar $\sigma_C = 1$ (see Tucker (2001)). This equation uses a standard linear gradient approach and is used for all RANS models. The use of a scalar transport equation that include a more physically consistent description of the turbulent processes (*i.e.* contribution from the non-linear part of the Reynolds stress tensor) is left as future work.

For non-isothermal studies, neglecting frictional, compressive and radiant heat, the following equation is used to model the transport of thermal energy (see Tucker (2001)):

$$\frac{\partial T}{\partial t} + \frac{\partial u_j T}{\partial x_j} = \frac{1}{\rho}\frac{\partial}{\partial x_j}\left(\Gamma_T \frac{\partial T}{\partial x_j}\right) \tag{3.23}$$

The diffusion coefficient Γ_T is defined as:

$$\Gamma_T = \frac{\mu}{Pr} + \frac{\mu_t}{Pr_t} \tag{3.24}$$

where Pr and Pr_t are the Prandtl and, turbulent Prandtl numbers.

To model buoyancy effects, extra source terms are used. The term $-g(\rho - \rho_0)$ is added to the appropriate vertical momentum equation (v). g being the acceleration due to gravity (9.81 m^2/s), ρ the local fluid density and ρ_0 the reference density of the fluid. The addition of this extra source term makes the momentum equation more unstable and it is often found that lower under-relaxation coefficients (0.1) have to be used to stabilise the solution. For one- and two-equation models an extra source term G_k that accounts for the production of buoyancy forces is also used. The modelling of the buoyancy term G_k is the subject of numerous studies (*i.e.* Peng (1998)). Here owing to its simplicity, the widely used standard gradient-diffusion hypothesis is used. In this approach,

$$G_k = -g\beta\frac{\mu}{\mu_t}\frac{\partial T}{\partial y} \tag{3.25}$$

where β is a volumetric expansion coefficient given as:

$$\beta = -\frac{1}{\rho}\frac{\partial \rho}{\partial y} \tag{3.26}$$

For the $k-l$ and $k-\epsilon$ models, the source term G_k is added to the k equation. In the ϵ equation, the term $f_1 C_{\epsilon 1}\frac{\epsilon}{k}P_k$ is re-written to include buoyancy effects as follows:

$$f_1 C_{\epsilon 1}\frac{\epsilon}{k}(P_k + G_k)(1 + C_3 R_f) \tag{3.27}$$

where R_f is the Richardson number. In flows dominated by vertical shear layers, $R_f \simeq 0$. In flows dominated by horizontal shear layers like in ventilated rooms R_f is defined as:

$$R_f = -\frac{G_k}{G_k + P_k} \tag{3.28}$$

and $C_3 \simeq 0.8$ (Rodi (1975)). Further discussion on the effect of buoyancy can be found in Turner (1973).

3.1.6 High and low Reynolds number turbulence models

The turbulent boundary layer near a solid wall is assumed to be constituted by two layers: The viscous sublayer and the log-law layer. The viscous sub-layer, closest to the wall is thin and characterised by the predominance of viscous forces over turbulent forces (Reynolds stresses). The thickness of the viscous sub-layer is about five "wall units", a dimensionless distance defined as below:

$$y^+ = \frac{y\rho(\tau_w/\rho)^{0.5}}{\mu} \tag{3.29}$$

From a practical point of view, the dimensionless wall unit y^* is preferred to y^+. y^* behaves like y^+ in near-wall areas where damping effect occurs. It is defined as:

$$y^* = \frac{y\rho k^{1/2} C_\mu^{1/4}}{\mu} \tag{3.30}$$

In the viscous sub-layer:

$$u^+ = y^+ \tag{3.31}$$

where u^+, the non-dimensional velocity is defined by:

$$u^+ = \frac{u}{(\tau_w/\rho)^{0.5}} \tag{3.32}$$

τ_w being the wall shear stress. In the log-law layer, turbulent forces are much greater than viscous forces. A relationship between y^+ and u^+, known as the log law, can be derived from Prandtl's (1925) mixing-length assumption as:

$$u^+ = \frac{1}{\kappa}\log y^+ + B = \frac{1}{\kappa}\log(Ey^+) \tag{3.33}$$

In the above, B and E are constants related to the wall roughness. For a smooth wall they are equal to 5.5 and 9.8 respectively. The transition between the viscous sublayer and the log-law layer occurs at $y^+ \simeq 11.63$. The outer limit of the log law layer is found to be close to $y^+ \simeq 500$ (Versteeg and Malalasekera (1995)).

The computation of the near-wall flows can be undertaken using either of the two following methods:

- Use of wall functions (high Reynolds number model) and
- Use of damping function (LRN model).

The choice between low and high Reynolds number model depends on the computational resources and flow physics. If the position of the first node off the wall is above $y^+ \simeq 30$ a high Reynolds number version of the turbulence model is used and, the flow at the first node is approximated by wall functions (Equations 3.31 and 3.32). If the position of the first off-wall node is $y^+ \simeq 1$, LRN models are used. Since the grid has

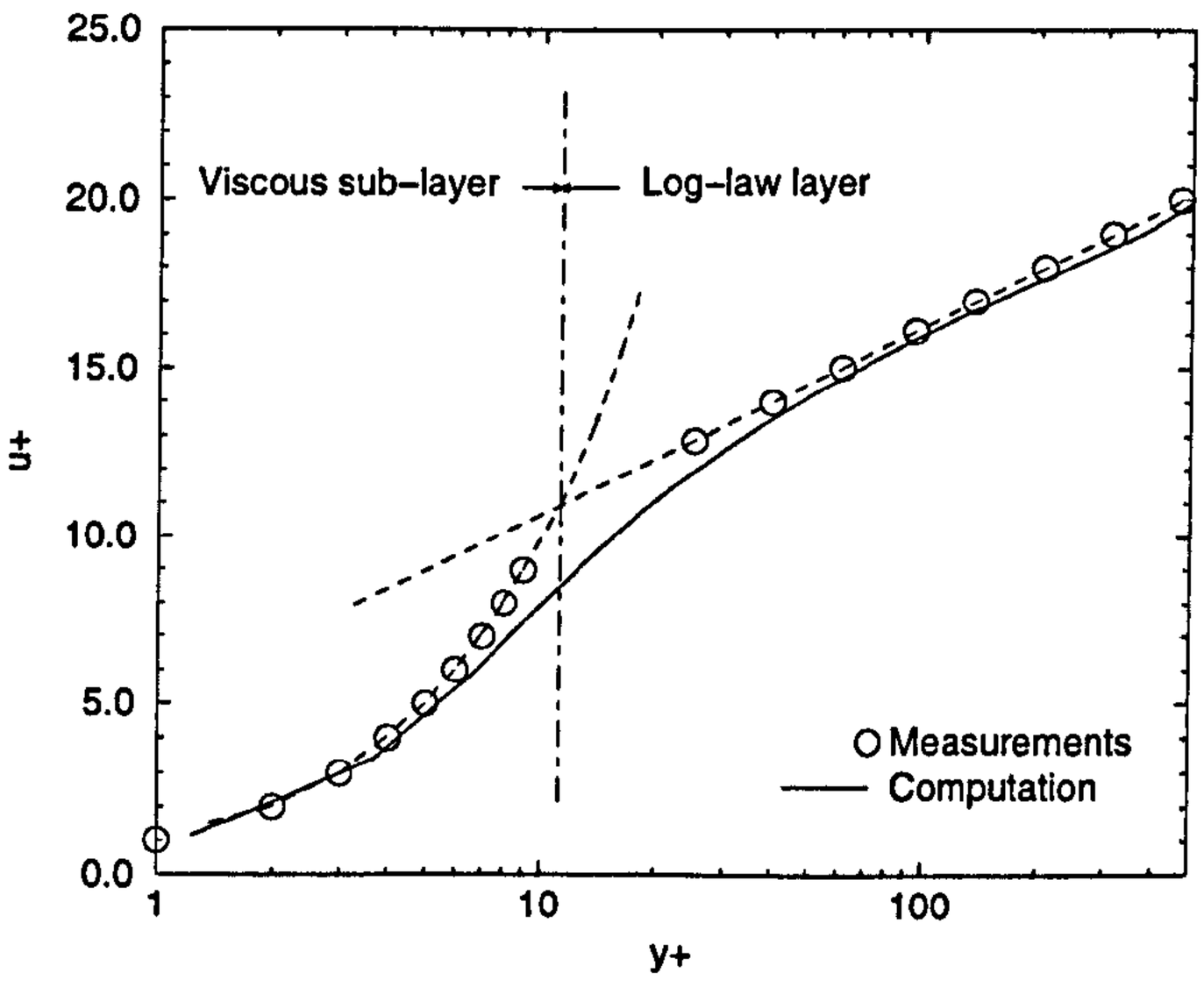

Figure 3.2: Near-wall velocity profile: Experimental data of Laufer (1951) in a 2-D channel flow.

to be fine enough to ensure $y^+ \simeq 1$ LRN models are computationally more expensive than their high Reynolds number equivalents. LRN models are well suited to room-ventilation modelling where average near-wall y^+ values tends to be smaller than in typical engineering flows. The contour plot of y^+ values in a typical ventilated office can be found in Holmes, Jouvray and Tucker (2000) (see Appendix A) and perfectly illustrates the need for LRN in modelling room-ventilation problems. LRN modelling involves damping functions. These ensure correct physical behaviour of the flow at the solid boundaries.

3.1.7 Wall damping function

This section presents a selection of LRN $k-\epsilon$ models used in this work. Unless otherwise specified, the $k-l$ based models use the Wolfshtein (1969) damping function (see Section 3.1.3). The definition of the damping functions f_μ, f_1 and f_2 often involves the turbulent Reynolds numbers Re_t and Re_y defined by:

$$Re_t = \frac{\rho k^2}{\mu \epsilon} \tag{3.34}$$

$$Re_y = \frac{\rho k^{0.5} y}{\mu} \tag{3.35}$$

Van Driest damping function

The Van Driest (1956) damping function improves flow predictions by acting on the turbulent viscosity μ_t alone. This simple-to-implement function has the following form:

$$f_\mu = 1 - e^{y^+/26} \tag{3.36}$$

while as in the high Reynolds number version of the model $f_1 = f_2 = 1$.

Mompean damping function

Mompean (1998), based on DNS data, proposed a variant of the original Van Driest (1956) damping function. The key concept introduced by Mompean (1998) is that near a corner, the flow is influenced not only by the closest wall but by the proximity of several walls. As discussed in Section 5.5, the Mompean (1998) damping function is successful at predicting secondary motions in straight square duct. The functions f_1 and f_2 remains equal to unity and, the turbulent viscosity is damped by:

$$f_\mu = [1 - e^{(-0.08y^+)}][1 - e^{(-0.08z^+)}] \tag{3.37}$$

where y^+ and z^+ are the non-dimensional distances from two separate orthogonal walls.

Launder and Sharma model with Yap correction

The Launder and Sharma (1974) model is one of the oldest LRN $k-\epsilon$ model form. This model with the Yap (1987) correction is used for the LRN cubic eddy viscosity model (see Section 3.2.2). The damping functions f_μ, f_1 and f_2 are defined as:

$$f_\mu = e^{\left(-3.4/\left(1+\frac{Re_t}{50}\right)^2\right)} \tag{3.38}$$

$$f_1 = 1 \tag{3.39}$$

$$f_2 = 1 - 0.3e^{-Re_t^2} \tag{3.40}$$

The Launder and Sharma (1974) model solves a transport equation for $\tilde{\epsilon}$ instead of ϵ. Conveniently $\tilde{\epsilon}$ vanishes at the walls and thus increases the solution stability. It is defined by:

$$\epsilon = \tilde{\epsilon} + 2\frac{\rho}{\mu}\left(\frac{\partial k^{0.5}}{\partial x_i x_j}\right)^2 \tag{3.41}$$

When using $\tilde{\epsilon}$ instead of ϵ, an extra source term S_e is added to the ϵ transport equation as:

$$S_e = 2\frac{\rho}{\mu\mu_t}\left(\frac{\partial^2 u_i}{\partial x_i \partial x_j}\right) \tag{3.42}$$

To further improve the model's predictive accuracy the Yap (1987) correction factor (y_c) can also be used as an extra additive source term in the ϵ equation. The Yap (1987) correction factor intends to correct the over-dissipative behaviour of the ϵ equation in near-wall areas.

$$y_c = c_w \frac{\epsilon^2}{k} max\left([\frac{l_{yc}}{l_e} - 1][\frac{l_{yc}}{l_e}]^2; 0.0\right) \tag{3.43}$$

where $c_w = 0.83$, $l_{yc} = \frac{k^{1.5}}{\epsilon}$ and $l_e = 2.55y$.

Lam-Bremhorst damping function

The Lam-Bremhorst (1981) (or L-B) damping function has been widely validated. It is used in many commercial CFD codes. The damping functions f_μ, f_1 and f_2 are defined as:

$$f_\mu = \left(1 - e^{-0.0165 Re_y}\right)^2 \left(1 + \frac{20.5}{Re_t}\right) \tag{3.44}$$

$$f_1 = 1 + \left(\frac{0.05}{f_\mu}\right)^3 \tag{3.45}$$

$$f_2 = 1 - e^{-Re_t^2} \tag{3.46}$$

To be consistent with the physical behaviour of the flow at the wall, the L-B model uses the following wall boundary condition on ϵ:

$$\epsilon_{wall} = \nu \frac{\partial^2 k}{\partial y^2} \tag{3.47}$$

A simpler alternative to this boundary condition (used in this work) is:

$$\frac{\partial \epsilon}{\partial y_{wall}} = 0 \tag{3.48}$$

Abe Kondoh Nagano damping function

The Abe Kondoh Nagano (1996) (or AKN) damping function, which has proven to be particularly successful when used with the explicit algebraic stress model (Rokni (1998)), has the following form:

$$f_\mu = \left(1 - e^{-(y^\times/14)}\right)^2 \left(1 + \frac{5}{Re_t^{0.75}} e^{-(Re_t/200)^2}\right) \tag{3.49}$$

$$f_1 = 1 \tag{3.50}$$

$$f_2 = \left(1 - e^{-(y^\times/3.1)}\right)^2 \left(1 - e^{-(Re_t/6.5)^2}\right) \tag{3.51}$$

The AKN model uses the Kolmogorov velocity scale $((\mu\epsilon/\rho)^{0.25})$ to define the non-dimensional wall distance $y^\times$ as:

$$y^\times = \left(\frac{\mu\epsilon}{\rho}\right)^{0.25} \frac{\rho y}{\mu} \tag{3.52}$$

The Prandtl numbers σ_k and σ_ϵ are both set to 1.4. For optimum results the AKN should be used with a first off-wall y^+ value $\simeq 10^{-2}$.

3.2 Advanced turbulence models

In previous sections, a description of linear eddy viscosity RANS models is given. These have a limited predictive accuracy. In an attempt to improve prediction accuracy, advanced turbulence models which describe the flow in a more physically consistent manner have been developed. The following advanced models are considered here:

- Models derived from the Reynolds Stress Model (RSM): The Explicit Algebraic Stress Model (EASM) of Gatski and Speziale (1993) discussed in Section 3.2.1.

- Non-linear eddy-viscosity models: The non-linear (quadratic) eddy-viscosity model of Speziale (1987) and the cubic eddy-viscosity model of Craft *et al.* (1996).

- LES: The Smagorinsky (1963) model and the one-equation model of Yoshizawa (1993) (see Section 3.2.3).

- Hybrid RANS/LES models.

3.2.1 Reynolds stress models, algebraic stress models and explicit algebraic stress models

By multiplying the N-S equations by a fluctuating component, a general equation for the Reynolds stress tensor can be derived. The Reynolds stress equation or RSM can be written as:

$$\frac{\partial \overline{u_i' u_j'}}{\partial t} + \frac{\partial}{\partial x_k}\left(u_k \overline{u_i' u_j'}\right) = -\overline{u_i' u_k'}\frac{\partial u_j}{\partial x_k} - \overline{u_j' u_k'}\frac{\partial u_i}{\partial x_k} + \Pi_{ij} - \epsilon_{ij} \ , \tag{3.53}$$

where the pressure strain correlation tensor (Π_{ij}) and dissipation rate tensor (ϵ_{ij}) are expressed as:

$$\Pi_{ij} = \overline{-p'\left(\frac{\partial u_i'}{\partial x_j} + \frac{\partial u_j'}{\partial x_i}\right)} \ , \tag{3.54}$$

$$\epsilon_{ij} = 2\frac{\mu}{\rho}\overline{\frac{\partial u_i'}{\partial x_k}\frac{\partial u_j'}{\partial x_k}} \ . \tag{3.55}$$

Π_{ij} can be physically interpreted as the transport of Reynolds stresses due to turbulent pressure strain interaction.

One of the major RSM drawback is that they require seven extra Pdes (one for each Reynolds stress and one for a turbulent length scale such as ϵ) and hence are computationally expensive (Craft and Launder (1996)). Using Kolmogorov's assumption of local isotropy ($\epsilon_{ij} = \frac{2}{3}\epsilon\delta_{ij}$) and neglecting the convective and diffusive transport, Rodi (1975) showed that the RSM (Equation 3.53) can be reduced to an implicit system of equations known as the Algebraic Stress Model (ASM) where:

$$(P_k - \epsilon)\frac{\overline{u_i'u_j'}}{k} = -\overline{u_i'u_k'}\frac{\partial u_j}{\partial x_k} - \overline{u_j'u_k'}\frac{\partial u_i}{\partial x_k} + \Pi_{ij} - \frac{2}{3}\epsilon\delta_{ij} \ . \tag{3.56}$$

ASM are an alternative to the computationally expensive RSM. However, the Reynolds stress tensor is found here on both side of the (implicit) ASM. Gatski and Speziale (1993) derived an explicit form of the ASM which is less computationally demanding. The EASM of Gatski and Speziale (1993) evaluates the Reynolds stress tensor as follows:

$$\begin{aligned} \tau_{ij} \ = \ & -\frac{2}{3}\rho k\delta_{ij} + 2\mu_{t_1}S_{ij} \\ & + 2\mu_{t_2}\frac{k}{\epsilon}(S_{ik}W_{kj} + S_{jk}W_{ki}) \\ & - 4\mu_{t_3}\frac{k}{\epsilon}\left(S_{ik}S_{kj} - \frac{1}{3}S_{mn}S_{mn}\delta_{ij}\right) \ , \end{aligned} \tag{3.57}$$

where S_{ij} and W_{ij} are the usual strain and vorticity rate. The turbulent viscosity μ_{t_i} appears here in a tensor form defined by:

$$\mu_{t_i} = \rho C_{\mu_i}\frac{k^2}{\epsilon} \ . \tag{3.58}$$

Recent trends in turbulence modelling seem to account for the fact that C_μ (= 0.09 for the standard $k - \epsilon$ model) is not a constant and depends on the flow itself (Pope (1975). The realizable $k - \epsilon$ model of Shih *et al.* (1995), the EASM and the cubic eddy

viscosity model (*c.f.* Section 3.2.2) are three examples in which C_μ varies. The original formulation of $C_{\mu i}$ by Gatski and Speziale (1993) is as follows:

$$C_{\mu 1} = \alpha_1 \left[\frac{3(1+\eta^2)}{3+\eta^2+6\zeta^2\eta^2+6\zeta^2} \right] , \tag{3.59}$$

$$C_{\mu 2} = \alpha_1\alpha_2 \left[\frac{3(1+\eta^2)}{3+\eta^2+6\zeta^2\eta^2+6\zeta^2} \right] , \tag{3.60}$$

$$C_{\mu 3} = \alpha_1\alpha_3 \left[\frac{3(1+\eta^2)}{3+\eta^2+6\zeta^2\eta^2+6\zeta^2} \right] , \tag{3.61}$$

where η and ζ are known as the invariance coefficients defined as:

$$\eta = \frac{1}{2}\frac{\alpha_3}{\alpha_1}\frac{k}{\epsilon}(S_{ij}S_{ij})^{\frac{1}{2}} , \tag{3.62}$$

$$\zeta = \frac{\alpha_2}{\alpha_1}\frac{k}{\epsilon}(W_{ij}W_{ij})^{\frac{1}{2}} . \tag{3.63}$$

The coefficients α_i and g are:

$$\alpha_1 = 0.5(\frac{4}{3} - C_1)g , \qquad \alpha_2 = 0.5(2 - C_2)g , \qquad \alpha_3 = 0.5(2 - C_3)g , \tag{3.64}$$

$$g = \left(0.5\, C_4 + \frac{P_k}{\epsilon} - 1 \right)^{-1} . \tag{3.65}$$

The following constants are used: $C_1 = 0.36$, $C_2 = 0.4$, $C_3 = 1.25$ and $C_4 = 6.8$.

Variants of the model

This section presents some of the variants of the EASM encountered in the literature. Rokni (2000) emphasises that the use of the term P_k/ϵ in the definition of g reduces the rate of convergence of the solution. When considering isotropic turbulence, P_k/ϵ is quasi-constant resulting in quasi-constant α_i. The α_i (constants) used by Rokni (2000-b) are:

$$\alpha_1 = 0.114 \qquad \alpha_2 = 0.187 \qquad \alpha_3 = 0.088 \tag{3.66}$$

As might be expected, the use of constant α_i increases numerical stability and hence the rate of solution convergence.

When η is far from equilibrium ($\gg$1) Speziale and Xu (1995) propose to evaluate $C_{\mu i}$ as:

$$C_{\mu 1} = \alpha_1 \left[\frac{(1+2\zeta^2)(1+6\eta^5) + \frac{5}{3}\eta^2}{(1+2\zeta^2)(1+2\zeta^2+\eta^2+6\gamma_1\eta^6)} \right] \tag{3.67}$$

$$C_{\mu 2} = \alpha_1\alpha_2 \left[\frac{(1+2\zeta^2)(1+\eta^4) + \frac{2}{3}\eta^2}{(1+2\zeta^2)(1+2\zeta^2+\gamma_2\eta^6)} \right] \tag{3.68}$$

$$C_{\mu 3} = \alpha_1\alpha_3 \left[\frac{(1+2\zeta^2)(1+\eta^4) + \frac{2}{3}\eta^2}{(1+2\zeta^2)(1+2\zeta^2+\gamma_3\eta^6)} \right] \tag{3.69}$$

where γ_1, γ_2 and γ_3 are equal to 7.0, 6.3 and 4.0 respectively.

Gatski's (1996) approximation of C_{μ_i} gives more accurate predictions of the turbulent viscosity in near wall regions (increases the asymptotic behaviour) but decreases solution stability. The Gatski's (1996) C_{μ_i} are defined as:

$$C_{\mu 1} = \alpha_1 \left[\frac{3(1+\eta^2) + 0.2(\eta^6+\zeta^6)}{3+\eta^2+6\zeta^2\eta^2+6\zeta^2+\eta^6+\zeta^6} \right] \tag{3.70}$$

$$C_{\mu 2} = \alpha_1\alpha_2 \left[\frac{3(1+\eta^2)}{3+\eta^2+6\zeta^2\eta^2+6\zeta^2+\eta^6+\zeta^6} \right] \tag{3.71}$$

$$C_{\mu 3} = \alpha_1\alpha_3 \left[\frac{3(1+\eta^2)}{3+\eta^2+6\zeta^2\eta^2+6\zeta^2+\eta^6+\zeta^6} \right] \tag{3.72}$$

3.2.2 Non-linear eddy-viscosity models

The turbulence models described in Sections 3.1 are based on a linear approximation of the Reynolds stress tensor. Assuming that the Boussinesq approximation is the leading term of an expansion series, a higher order expression of the Boussinesq approximation can be derived (Lumley(1970); Pope (1975)). Using this concept, a range of non-linear eddy-viscosity models have been proposed and have offered various flow prediction improvements.

For example, Speziale's (1987) quadratic eddy-viscosity model ($k-\epsilon$) which successfully predict secondary motion in square ducts (Tucker (2000)) has the major drawback of being highly unstable and often lead to divergent solutions (Tucker (2000), Apsley and Leschziner (1998)). The quadratic model of Speziale (1987), however, has the advantage over linear eddy-viscosity models of capturing the anisotropy of the Reynolds stress tensor.

Based on similar principles, Craft *et al.* (1996) presented a cubic eddy-viscosity model. The use of cubic terms has the distinct advantage over linear and quadratic terms of capturing streamline curvature. The cubic eddy-viscosity model of Craft *et al.* (1996) has been implemented and tested within the scope of the present work. The model derived by Craft *et al.* (1996) has the following form:

$$\begin{aligned}
\tau_{ij} \;=\; & -\frac{2}{3}\rho\delta_{ij} + 2\mu_t S_{ij} \\
& - 4C_1\frac{\mu_t k}{\tilde{\epsilon}}\left(S_{ij}S_{kj} - \frac{1}{3}S_{mn}S_{mn}\delta_{ij}\right) \\
& - 4C_2\frac{\mu_t k}{\tilde{\epsilon}}\left(W_{ik}S_{kj} + W_{jk}S_{ki}\right) \\
& - 4C_3\frac{\mu_t k}{\tilde{\epsilon}}\left(W_{ik}W_{jk} - \frac{1}{3}W_{mn}W_{mn}\delta_{ij}\right)
\end{aligned}$$

$$
\begin{aligned}
&- 8C_4\frac{\mu_t k^2}{\tilde{\epsilon}^2}\left(S_{ki}W_{lj}+S_{kj}W_{li}\right)S_{kl} \\
&- 8C_5\frac{\mu_t k^2}{\tilde{\epsilon}^2}\left(W_{il}W_{lm}S_{mj}+S_{il}W_{lm}W_{mj}-\frac{2}{3}\left[S_{lm}W_{mn}W_{nl}\delta_{ij}\right]\right) \\
&- 8C_6\frac{\mu_t k^2}{\tilde{\epsilon}^2}\left(S_{ij}S_{mn}S_{mn}\right)-8C_7\frac{\mu_t k^2}{\tilde{\epsilon}^2}\left(W_{ij}W_{mn}W_{mn}\right) \qquad (3.73)
\end{aligned}
$$

The coefficients C_i have been defined using empirical methods based on various shear flow configurations. They are defined as: $C_1 = -0.1$, $C_2 = 0.1$, $C_3 = 0.26$, $C_4 = -1.0$, $C_5 = 0.0$, $C_6 = -0.1$ and $C_7 = 0.1$. The turbulent viscosity μ_t is evaluated using the standard expression as for the $k-\epsilon$ model:

$$\mu_t = \rho C_\mu f_\mu \frac{k^2}{\epsilon} \qquad (3.74)$$

Here again, C_μ is introduced as a variable depending on the flow as:

$$C_\mu = \frac{0.3}{1.+0.35\left[Max(S^*;W^*)\right]^{\frac{3}{2}}}\left[1.-e[\frac{-0.36}{e(-0.75\ Max(S^*;W^*))}]\right] \qquad (3.75)$$

where S^* and W^* are the dimensionless strain and vorticity rate defined by:

$$S^* = \frac{k}{\tilde{\epsilon}}\left(2S_{ij}S_{ij}\right)^{0.5} \qquad (3.76)$$

$$W^* = \frac{k}{\tilde{\epsilon}}\left(2W_{ij}W_{ij}\right)^{0.5} \qquad (3.77)$$

The cubic model has been found to give satisfactory predictions of separating and re-attaching flows such as diffuser flows, or flows over backward-facing steps (Craft (1998)). As seen with Speziale's (1987) model, the use of non-linear relationship of the Reynolds stress tensor often lead to unstable numerical simulations. The cubic model of Craft *et al.* (1996) is no exception to this and is found in particular to be numerically unstable when applied to separated flows. Craft *et al.* (1999) propose a series of measures that aim to increase the stability of the cubic model. These are mostly focused on improving

the diagonal dominance of the system of discretized equations hence increasing the rate of convergence of the simulation (see Chapter 4 for more details on numerical methods). Also, to enhance flow predictions and numerical stability of the cubic model near sharp corners, Craft *et al.* (1999) propose the following new c_μ formulation:

$$c_\mu = Min\left(0.09, \frac{1.2}{(1 + 3.5Max(S^*; W^*) + F_{rs})}\right) \tag{3.78}$$

where

$$F_{rs} = 0.235\ (Max(0; Max(S^*; W^*) - 3.333))^2\ e^{(-R_{et}/400)} \tag{3.79}$$

In near-wall areas this C_μ approximation behaves similarly to the original of Craft *et al.* (1996) but gives smoother C_μ distribution away from the wall. Craft *et al.* (1999) also show that the use of an alternative form of the Yap (1987) correction factor free of wall distances (Iacovides and Raisee (1997)) does not increase the model's predictive accuracy. Therefore, the original Yap (1987) correction factor is used in this work. Although the original Yap (1987) form needs normal wall distances in the present work this is computed from a differential equation (see Tucker (2001)).

The use of a cubic $k-l$ model is also considered. This model is validated in Chapter 5 and applied to room-ventilation configurations in Chapter 8 to 11. It is an adaptation of the cubic $k-\epsilon$ model of Craft *et al.* (1996). In the cubic $k-l$ model, the Reynolds stress tensor is defined by Equation 3.73 as for the standard cubic $k-\epsilon$ model. The turbulent viscosity is defined in a similar manner to that of the linear $k-l$ model (Equation 3.17). In the LRN form, the Wolfshtein (1969) damping function is used. This formulation of the cubic $k-l$ model has the disadvantage of using constants from empirical methods in the definition of the turbulent viscosity. However, this model has the advantage over linear models of using the cubic expansion of the Reynolds stress tensor. Thus accuracy improvements can be expected between the cubic $k-l$ model and its linear equivalent.

3.2.3 Large Eddy Simulation: A brief overview

LES is based on the simple physical observations that the small eddies of the flow, near the Kolmogorov scales, are universal in nature and can thus be more easily modelled. The larger eddies, however, depend on the flow configuration and, have to be computed. The scale separation between the large and the small eddies of the flow is the key underlying principle of LES and is achieved by decomposing a flow property ϕ as the sum of two components: A resolved field $\tilde{\phi}$ (associated with the large flow-dependent eddies) and a residual ϕ^{sgs} associated with the smaller more universal eddies. The residual flow property ϕ^{sgs} is commonly referred to as a SubGrid Scale (SGS) property. To separate the resolved field $\tilde{\phi}$ from the SGS field ϕ^{sgs}, a filtering of the initial field ϕ is used. The filtering method itself is a mathematical operation applied to the initial flow field and is not discussed in this work but, details can be found in Leonard (1974), Pope (2000), etc ... . The use of any filter (Gaussian, top hat ...) effectively introduces the length scale Δ known as the filter width. Δ represents the smallest scales of turbulence allowed through the filter. After filtering, the N-S (momentum) and continuity equations can be re-written for LES purposes in terms of resolved and SGS field as:

$$\frac{\partial \rho \tilde{u}_i}{\partial t} + \frac{\partial \rho u_i \tilde{u}_j}{\partial x_j} = -\frac{\partial \tilde{p}}{\partial x_i} + \mu \frac{\partial}{\partial x_j}\left(\frac{\partial \tilde{u}_i}{\partial x_j} + \frac{\partial \tilde{u}_j}{\partial x_i}\right) \tag{3.80}$$

$$\frac{\partial \tilde{u}_j}{\partial x_j} = 0. \tag{3.81}$$

The convective term $u_i\tilde{u}_j$ is key to the LES methods since it is the only element in Equation 3.80 which contains the SGS informations of the flow. $u_i\tilde{u}_j$ is defined as:

$$u_i\tilde{u}_j = \tilde{u}_i\tilde{u}_j + \tau_{ij}^R \tag{3.82}$$

Using Equation 3.82, the momentum equation can then be re-written as:

$$\frac{\partial \rho \tilde{u}_i}{\partial t} + \frac{\partial \rho \tilde{u}_i \tilde{u}_j}{\partial x_j} = -\frac{\partial \tilde{p}}{\partial x_i} + \mu \frac{\partial}{\partial x_j}\left(\frac{\partial \tilde{u}_i}{\partial x_j} + \frac{\partial \tilde{u}_j}{\partial x_i}\right) - \frac{\partial \rho \tau_{ij}^R}{\partial x_j} \tag{3.83}$$

where term τ_{ij}^R is the residual stress tensor related to the SGS stress tensor by:

$$\tau_{ij}^R = \tau_{ij}^{sgs} + n_0 \frac{2}{3} k_{sgs} \delta_{ij} \tag{3.84}$$

where $n_0 = 0$ for the Smagorinsky (1963) model and $n_0 = 0$ for the Yoshizawa (1993) model. Establishing an adequate SGS stress model (τ_{ij}^{sgs}) is an active area of research and is key to the accuracy of the LES model. As in RANS modelling, unless an approximation of τ_{ij}^{sgs} is given, the system of LES equations (Equations 3.81 and 3.83) is not closed and cannot be resolved. The SGS model of Smagorinsky (1963) has been used in this work and is presented below.

The Smagorinsky model

The pioneering Smagorinsky (1963) model, was aimed towards meteorological applications and atmospheric boundary layers. Smagorinsky (1963) proposed that the contribution of the SGS to the resolved scales of the flow is similar to a diffusion term as in Prandtl's mixing-length model. Smagorinsky (1963) thus proposed to evaluate the SGS stress tensor as:

$$\tau_{ij}^{sgs} = 2\rho\mu_{sgs}\tilde{S}_{ij} \tag{3.85}$$

where $\tilde{S}_{ij}$ is the resolved strain rate:

$$\tilde{S}_{ij} = \frac{1}{2}\left(\frac{\partial \tilde{u}_i}{\partial x_j} + \frac{\partial \tilde{u}_j}{\partial x_i}\right) \tag{3.86}$$

μ_{sgs} being a turbulent viscosity related to the SGS. Again, by analogy with Prandtl's mixing-length model, Smagorinsky (1963) proposed to evaluate the SGS viscosity as:

$$\mu_{sgs} = \rho l_{sgs}^2 \tilde{S}_{ij} = \rho (C_s \Delta)^2 \tilde{S}_{ij} \tag{3.87}$$

l_{sgs} being a characteristic length scale of the SGS it is thus related to the filter width Δ. The Smagorinsky constant C_s depends on the flow configuration. Rogallo and Moin

(1984) showed that $0.1 < C_s < 0.24$. Typically, for three-dimensional flows, Δ, the filter's width is taken as:

$$\Delta = (\delta_x \delta_y \delta_z)^{1/3} \tag{3.88}$$

where $\delta_{x,y,z}$ is the local grid spacing.

The Smagorinsky (1963) model remains a popular LES model and is now optional in many commercial codes. This model is, however, limited owing to the rather simplistic formulation of τ_{ij}^{sgs} and due to excessive grid requirement in near-wall areas. A key problem with the Smagorinsky model is that it cannot account for backscatter where energy is transferred back from the subgrid to the resolved scales.

3.2.4 Zonal and hybrid RANS/LES models

The resolution of the boundary layer is a significant LES challenge (Rodi *et al.* (1997)). As illustrated by Figure 3.3 the turbulent boundary layer is governed by the cyclic growth and burst of three-dimensional streaks. In the streamwise direction, the streaks grow and are ejected from the turbulent boundary layer at a periodicity equivalent to four times the thickness of the boundary layer δ. In the spanwise direction, those streaks are of dimension $z^+ \simeq 100$. In the direction normal to the wall (y), the ejection burst process contributes most to turbulent production in the region $y^+ \simeq 10$ to 15 (Hinze (1975)). The streaks influence the mean velocity profile up to $y^+ \simeq 80$. Thus, to resolve the turbulent boundary layer using LES, a fine grid is required in all directions and not only in the normal wall direction as for RANS modelling. The grid requirement for near-wall LES is $\Delta x^+ \simeq 100$, $\Delta y^+ \simeq 1$ and $\Delta z^+ \simeq 20$ (Davidson (2001)). This grid requirement makes LES of near-wall flows computationally expensive. To reduce the computational cost and maintain the predictive accuracy of LES zonal LES/RANS

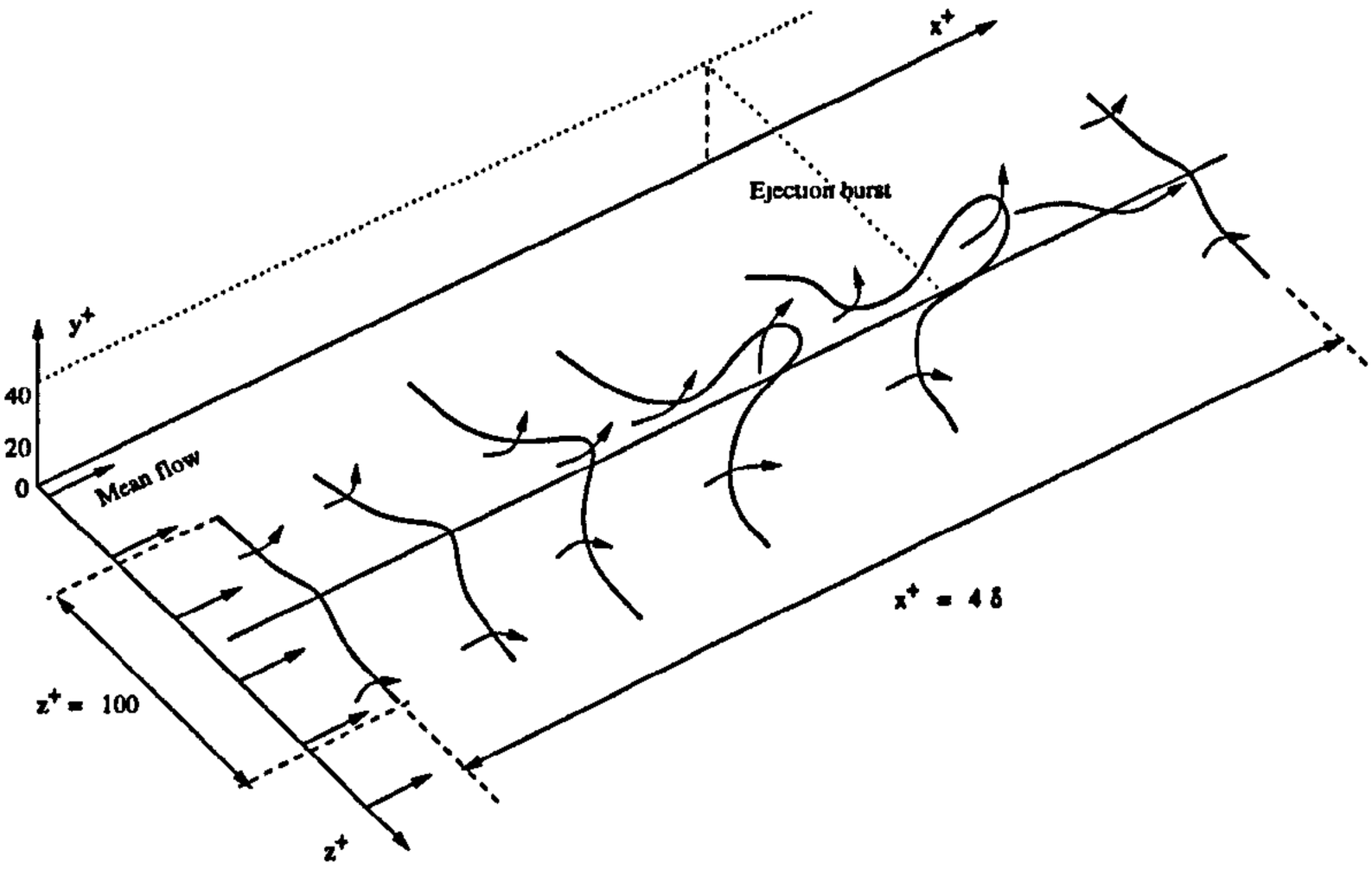

Figure 3.3: Three-dimensional growth of streaks in the turbulent boundary layer.

models and hybrid LES/RANS models are used.

Zonal models

In zonal models, a RANS simulation is adopted in the vicinity of the wall and LES is used for the reminder (or core) of the flow. Using this technique the grid requirement in near walls is identical to the grid requirements of RANS models ($100 < \Delta x^+ < 600$, $\Delta y^+ \simeq 1$ and $100 < \Delta z^+ < 300$) and thus allows faster flow resolution.

One of the key point of zonal methods is the determination of the interface between RANS and LES. In the Detached Eddy Simulation (DES) of Spalart (1999), a similar approach to zonal models, the turbulent boundary layer is modelled using RANS and, only the detached eddies in the outer boundary layer are modelled with LES. The DES approach is found to be particularly successful for the calculations of separated flows over aerofoils for which is was developed (Shur *et al.* (1999)). However, LES and hence

DES of non-separated flow is more challenging (Tucker (2004), Rollet-Miet *et al.* (1999)).

In the zonal model of Davidson (2001) and Peng and Davidson (2001) the RANS/LES interface is rigidly fixed at a specified y^+ value (typically $\simeq 60$) located within the logarithmic region of the turbulent boundary layer. In Davidson's (2001) investigation, a LRN RANS $k-\omega$ model is used near the wall ($y^+ < 60$) and the one-equation $k_{sgs}-l$ LES model of Yoshizawa (1993) is used for the reminder of the flow. The predictions of Davidson (2001) are found to be in good agreement with measurements of fully developed flows in a plane channel and of the flow over a two-dimensional hill. At the RANS/LES interface however, some undesirable kinks of the velocity field are found.

Tucker and Davidson (2003) use a zonal $k-l$ based model throughout the computational domain. The $k-l$ model of Wolfshtein (1969) and of Chen and Patel (1988) is used for the near-wall RANS simulations and the $k_{sgs}-l$ model of Yoshizawa (1993) and Fureby (1999) is used for the LES part. Using identical grid definition, the zonal model has higher predictive accuracy than RANS or LES methods for the simulation of a non-isothermal periodic ribbed-channel flows.

Hybrid models

Speziale (1998) on a different approach implies that zonal RANS/LES models can be implemented by damping the effect of the RANS turbulence model. Using this method, as the grid resolution gets finer, the solution tends towards LES (or DNS for sufficiently fine grids) and, as the grid get coarser, the solution tends to RANS. Using this approach, RANS areas can be found in the core of the flow aways from the wall unlike in zonal models.

The Limited Numerical Scale (LNS) model of Batten *et al.* (2002) is a hybrid RANS/LES method. In this method, a clear identification of the RANS or LES areas of the flow is crucial to obtain accurate results. The transition from RANS to LES is achieved by multiplying the turbulent viscosity of the RANS model by a parameter α taken between zero and one. α is defined as a function of a turbulent length scale (L) and velocity scale (V) for the LES and RANS as follows:

$$\alpha = \frac{Min(L_{LES}V_{LES}, L_{RANS}V_{RANS})}{L_{RANS}V_{RANS}} \tag{3.89}$$

When $\alpha = 1$ the model behaves like the equivalent RANS model. For the specific choice of a cubic eddy viscosity RANS model (Batten *et al.* (2000)) and of the Smagorinsky (1963) LES model α can be expressed as:

$$\alpha = \frac{Min(C_s(\Delta^2 S^*_{ij}, C_\mu k^2/\epsilon + \Omega))}{C_\mu k^2/\epsilon + \Omega} \tag{3.90}$$

where, C_s is the Smagorinsky constant (0.05), Δ the grid spacing (taken as $Max(\delta_x, \delta_y, \delta_z)$) and Ω a is small number used to avoid singularity.

An LNS model that uses the Smagorinsky (1963) LES model and the RANS cubic eddy viscosity model of Craft *et al.* (1996) has been applied to room-ventilation configurations discussed in Chapter 8 and 11. In this model, the damping of the turbulent viscosity of the RANS is done using α as defined in equation 3.90. The Smagorinsky constant $C_s = 0.05$ and C_μ is taken from the linear $k - \epsilon$ model (0.09).

Chapter 4

Numerical methods and code optimisation

This chapter presents an overview of the spatial and temporal discretisation of the governing equations used in the code. The general solution procedure (SIMPLE) as well as the solver (TDMA) are also briefly presented. Finally, Section 4.4 presents a multigrid method and a parallel processing strategy used to minimise computational costs.

4.1 Spatial and temporal discretisation methods

The governing equations can be written in a more general form in a cartesian coordinate system for the transported variable ϕ as:

$$\frac{\partial \rho\phi}{\partial t} + \frac{\partial}{\partial x_j}(\rho u_i \phi) = \frac{\partial}{\partial x_i}\left(\Gamma_{\phi x_i}\frac{\partial \phi}{\partial x_i}\right) + S_\phi \tag{4.1}$$

where ϕ is equal to either u, v, w or a scalar quantity. Equation 4.1 can be seen as a balance of transport processes acting on a fluid. The left-hand side terms of Equation

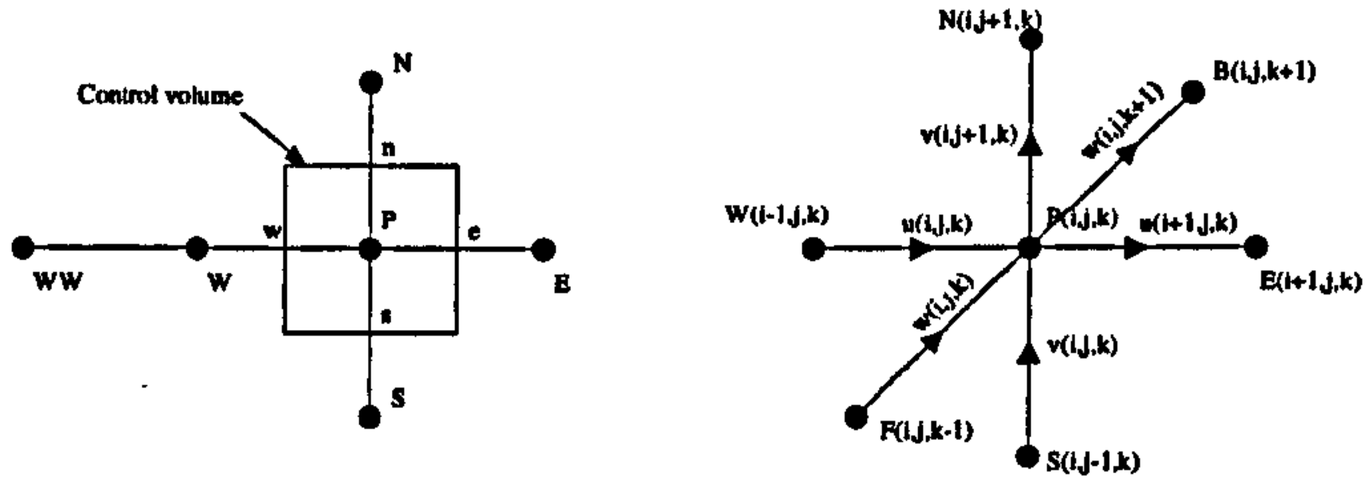

(a) (b)

Figure 4.1: Typical control volume: (a) Two-dimensional control volume with volume faces and (b) three-dimensional representation of the computational grid with scalar quantities (at grid nodes) and velocities.

4.1 comprise the time rate of change of fluid property ϕ (at a fixed point) and the transport of ϕ due to convection. The right-hand side of Equation 4.1 comprises the diffusive terms (where $\Gamma_{\phi i}$ is the diffusion coefficient) and the source terms are represented by S_ϕ.

In the code, the finite volume method (Patankar (1980)) is used with the staggered grid arrangement (Patankar (1980)) in which scalar quantities are evaluated at grid points and velocities are evaluated at control volume faces. A typical control volume with its geographic notation is shown in Figure 4.1. This staggered approach has better conservation properties and hence, is preferred for LES simulations which are carried out as part of the present work.

As part of the discretisation process, the transported variables need to be interpolated from the grid nodes, where they are evaluated, to the faces of the control volumes. A multitude of convective treatment are found in the literature (Tucker (2001)) but,

the simulations presented in this work have been obtained using a second-order central-difference scheme unless specified. The use of central difference schemes is found to create numerical instability under the form of oscillations or wiggles at high Reynolds numbers (Leonard (1979)). Due to this unstable behaviour, alternate schemes such as the HYBRID scheme of Spalding (1972) and the CONDIF scheme of Runchal (1987) have also been considered.

For the computation of unsteady flows in ventilated rooms (and for LES purposes) a two-level time-discretization scheme is used. The two-level scheme can be written for the general transported variable ϕ as:

$$\phi = \left(\frac{1+\beta\delta t}{2}\right)\phi^{new} + \left(\frac{1-\beta\delta t}{2}\right)\phi^{old} \tag{4.2}$$

Various time-discretisation schemes can be obtained by varying β as: $\beta = \pm 1/\delta t$: First-order forward and backward Euler; $\beta = 0$: Crank-Nicolson, etc... . Details on temporal discretization schemes is extensively covered by Tucker (2001). Here, the Crank-Nicolson method is used for LES purposes.

For unsteady flows, the code has been validated by comparison with an analytical solution of the propagation of the subcritical Tollmien-Schlichting wave in plane Poiseuille flow. Good agreement was found for both wave amplitude and phase components (see Tucker, Liu, Chung and Jouvray (2003)). Evidence of the code performance for LES can be found in Tucker and Davidson (2003) and also Lo Iaconno (2003). In the latter excellent agreement was found with DNS data and measurements for an $Re_t = 180$ plane channel flow.

The RANS simulations presented in this work are obtained using LRN models only.

The considered flows have relatively low Mach numbers and hence, compressibility effects are neglected. When modelling furniture blocks in Chapters 9 to 11 wall-roughness effects are also assumed negligible.

For the comparison of measurements with predictions in Chapters 8 to 11, relative errors are presented. These are evaluated as follows:

$$Error(\%) = \frac{|\phi_{CFD} - \phi_{Exp}|}{|\phi_{Exp}|} \times 100 \tag{4.3}$$

where ϕ_{CFD} and ϕ_{Exp} are predicted and measured flow variables, respectively. The average error is defined as:

$$Average = \sum_{i=1}^{n} \frac{Error}{n} \tag{4.4}$$

4.2 General solution procedure: The SIMPLE algorithm

The Semi Implicit Pressure Linked Equation (SIMPLE) algorithm of Patankar and Spalding (1972) is used in the code. It is based on the successive correction of an initially guessed pressure field. Once discretised, the momentum equation can be written at the point P as:

$$A_{P,\phi}\ \phi_P = \Sigma A_{nb,\phi}\ \phi_{nb} + \frac{\Delta p}{\Delta n_\phi} + S_\phi, \tag{4.5}$$

where the subscript nb indicates the neighbour grid points S_ϕ the source term and the term $(\Delta p)/(\Delta n_\phi)$ is the mean pressure gradient. In the SIMPLE algorithm, an initial pressure field p^* is guessed and Equation 4.5 is solved for the guessed velocities u^*, v^* and w^*. The correct pressure (p) and velocity (u, v and w) fields are then obtained by adding successive corrections (p^c, u^c, v^c and w^c) to the initially guessed fields. A

correction equation for momentum can be obtained by subtracting Equation 4.5 for the guessed values to Equation 4.5 for the calculated values. The correction equation for momentum can be written as:

$$A_{P,\phi}\ \phi^c_P = \Sigma A_{nb,\phi}\ \phi^c_{nb} + \frac{\Delta p^c}{\Delta n_\phi} \tag{4.6}$$

In the SIMPLE algorithm, $\Sigma A_{nb,\phi}\ \phi^c_{nb} = 0$. A correction equation for the pressure field can be derived from the continuity equation as:

$$A_{P,p}\ p^c_P = \Sigma A_{nb,p}\ p^c_{nb} + S_{p^c} \tag{4.7}$$

Once known, corrections are then added to the guessed values to give the resolved solution.

4.3 The TDMA solver

Once discretised, the governing equations of the flow constitute a system of linearised algebraic equations that needs to be simultaneously resolved. This system of linear equations can be solved directly (direct Gaussian elimination) or indirectly using iterative process such as the Jacobi, Gauss-Seidel or TDMA methods, etc ... (Ferziger and Peric (1999), Toro (1999))

The TDMA also known as Thomas algorithm is still widely used in CFD codes. The solution of the system of algebraic equations using the TDMA is obtained through two computational steps: The forward and the back substitution. To apply the TDMA, the system of linearised equations needs to be written in the form of a tridiagonal matrix system. Using Patankar's (1980) geographic notation (horizontal axis of Figure 4.1 (a))

the system of algebraic equations can be written as:

$$\begin{aligned}
A_W^j\phi_{j-1} + A_P^j\phi_j + A_E^j\phi_{j+1} &= D_j \\
A_W^{j+1}\phi_j + A_P^{j+1}\phi_{j+1} + A_E^{j+1}\phi_{j+2} &= D_{j+1} \\
\ddots \quad \ddots \quad \ddots &= \vdots \\
A_W^{n-1}\phi_{n-2} + A_P^{n-1}\phi_{n-1} + A_E^{n-1}\phi_n &= D_{n-1} \\
A_W^n\phi_{n-1} + A_P^n\phi_n + A_E^n\phi_{n+1} &= D_n
\end{aligned} \tag{4.8}$$

which could be written in a more general form for any j^{th} grid point as:

$$A_W^j\phi_{j-1} + A_P^j\phi_j + A_E^j\phi_{j+1} = D_j \ . \tag{4.9}$$

The forward substitution is simply a way of expressing ϕ_j as a function of ϕ_{j-1} and, the backward substitution is a general recurrence equation. The three-dimensional form of the TDMA used in the code is based on the same principle described above. The general discretised equations are written in a tri-dimensional form as:

$$A_P\phi_P = A_a\phi_a + A_b\phi_b + S \ , \tag{4.10}$$

where the source term S is defined as:

$$S = A_c\phi_c + A_d\phi_d + A_e\phi_e + A_f\phi_f \tag{4.11}$$

The subscripts a to f corresponds to the grid node locations . To improve the propagation of information using the TDMA, the alternative sweeping method is used. This consist in solving Equation 4.10 in three ways corresponding to the three main axis orientations (x, y and z) of the domain. The subscripts a to f are then assigned to the grid points for the three sweeps as shown in Table 4.1.

	a	b	c	d	e	f
Sweep 1: x axis	W	E	N	S	F	B
Sweep 2: y axis	S	N	W	E	F	B
Sweep 3: z axis	B	F	W	E	S	N

Table 4.1: Alternate sweeping method for the TDMA solver.

From a practical point of view, the TDMA is applied only to the main terms of Equation 4.10 (subscripts a and b and the source term). The source term S itself (Equation 4.11) is solved using a Gauss-Seidel method.

4.4 Optimisation of the code

Despites the recent advances in computing power, the trade-off between accuracy and computing time remains crucial in CFD. To numerically model ventilated rooms where both the Reynolds number and the physical dimensions of the studied domain are large, an optimisation of the computing time is desired. The following sections present the multigrid and parallel processing methods used in this investigation.

4.4.1 Multigrid method

The multigrid method, introduced by Brandt (1977) is based on a temporary coarsening of the computational grid. The principle of the multigrid method as illustrated by the one-dimensional grid of Figure 4.2 (a), is based on a progressive coarsening of the original grid. Once solved (quickly) on the coarse grid, the flow calculations are passed onto a less coarse multigrid level. The introduction of solved flow calculations on finer grid increases solution convergence. Considering that the equation to be solved can be written in a

form similar to Equation 4.10 as:

$$[A_g][\phi_g] = [S_g] \tag{4.12}$$

where, $[A]$ is the discretised coefficients array, $[\phi]$ a general transported property array and $[S]$ the source term array. The subscript g denotes the multigrid level (= 1 for the original grid). Equation 4.12 can be re-written in terms of guessed (ϕ^*) and correction terms (ϕ^c) as:

$$[A_g][\phi_g^* + \phi_g^c] = [R_g] + [A_g][\phi_g^*] \tag{4.13}$$

where $[R_g]$ is introduced as the residual error as:

$$[R_g] = [S_g] - [A_g][\phi_g^*] \tag{4.14}$$

At different multigrid level (coarser grids) Equation 4.13 becomes:

$$[A_{g+1}][\phi_{g+1}^{*,f} + \phi_{g+1}^c] = [R_{g+1}^f] + [A_{g+1}][\phi_{g+1}^{*,f}] \tag{4.15}$$

$m+1$ indicates the use of the next coarser multigrid level and, the superscript f indicates values taken on the finer multigrid level. By noting

$$[\phi_{g+1}^+] = [\phi_{g+1}^{*,f} + \phi_{g+1}^c] \tag{4.16}$$

and

$$[S_{g+1}^+] = [R_g^f] + [A_{g+1}][\phi_{g+1}^{*,f}] \tag{4.17}$$

Equation 4.15 can be re-written in a form similar to Equation 4.12 as:

$$[A_{g+1}][\phi_{g+1}^+] = [S_{g+1}^+] \tag{4.18}$$

Correction terms for coarser grid level can then be obtained by subtracting $[\phi_{g+1}^{*,f}]$ from $[\phi_{g+1}^+]$. Assuming that the equation to be solved is linear, the terms $[A_{g+1}][\phi_{g+1}^{*,f}]$ of Equation 4.15 vanishes and Equation 4.18 reduces to:

$$[A_{g+1}][\phi_{g+1}^c] = [R_{g+1}^f] \tag{4.19}$$

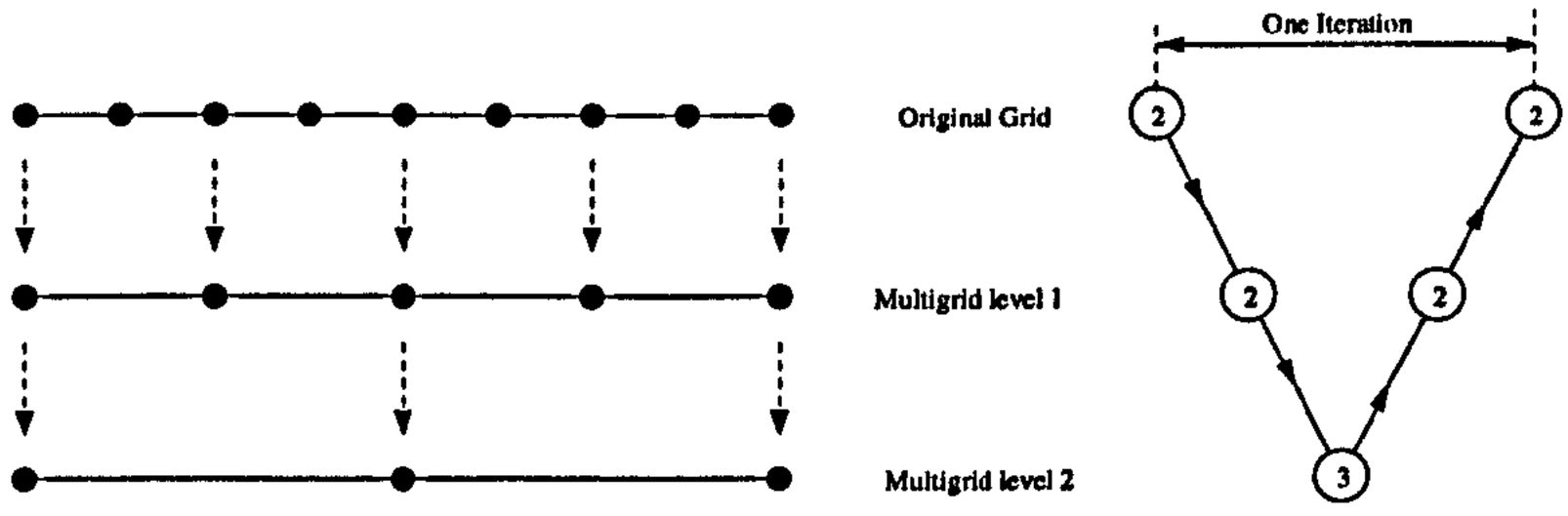

Figure 4.2: (a) Principle of the multigrid method on a one-dimensional grid and (b) multigrid V cycle.

The correction term $[\phi^c_{g+1}]$ can be interpolated to the multigrid level m using:

$$[\phi_g] = [\phi^{*,f}_g] + \lambda[\phi^c_{g+1}] \tag{4.20}$$

where λ is a relaxation factor. Since Equations 4.13 and 4.14 have the same form as Equation 4.12, a correction equation on a higher multigrid level $(m+2)$ can be derived. This procedure can be repeated until the grid cannot be further coarsened. The number of multigrid level to use for an optimum result depends on the original grid size and is discussed by Tucker (1998) and Tucker (2000). No more than three level of multigrid levels have been used in this work. In the code, the multigrid method is applied as an outer loop of the SIMPLE procedure in a V-cycle as illustrated by Figure 4.2 (b). In the V-cycle, the simulation starts from the initial grid $(g = 1)$ then passes through coarser grid levels $(g = 2, 3, ...)$ and returns progressively to the initial grid $(g = 1)$. The circled numbers of Figure 4.2 (b) represents the number of sweeps used to make corrections to the solution on the next multigrid level.

4.4.2 Parallel processing

Parallel processing of a CFD code can be done using various strategies. For example, block decomposition in which the computational domain is divided in sub-regions that are treated by different CPUs can be used. Without an existing multiblock solver, this technique requires a time-consuming coding phase and has therefore not been undertaken here.

The optimisation of the code has been done by applying local parallel processing directives (OPEN MP) on selected subroutines. The simultaneous equation solver subroutine being a primary target for optimisation due to its extensive cost during a CFD simulation ($\simeq 30\%$). To achieve an efficient level of parallel processing, some data independency within the selected subroutines is required. To have data independency, the computational loops have been split using a red-black method.

When considering a two-dimensional domain, the computational grid, in the red-black method, is viewed as a checker board where each node is coloured either red or black. Computationally, using a red-black method implies that a single "do" loop over the whole domain can be decomposed as a "do" loop over the red domain and, a "do" loop over the black domain. This method has the significant advantages of getting rid of some data dependency within a single loop and of splitting up a (large) loop into several (smaller) loops. Each of these smaller loops can then be processed by different CPUs. This method however reduces the propagation of informations throughout the whole computational domain.

As discussed in Section 4.3 the solver used is TDMA in which the source term S

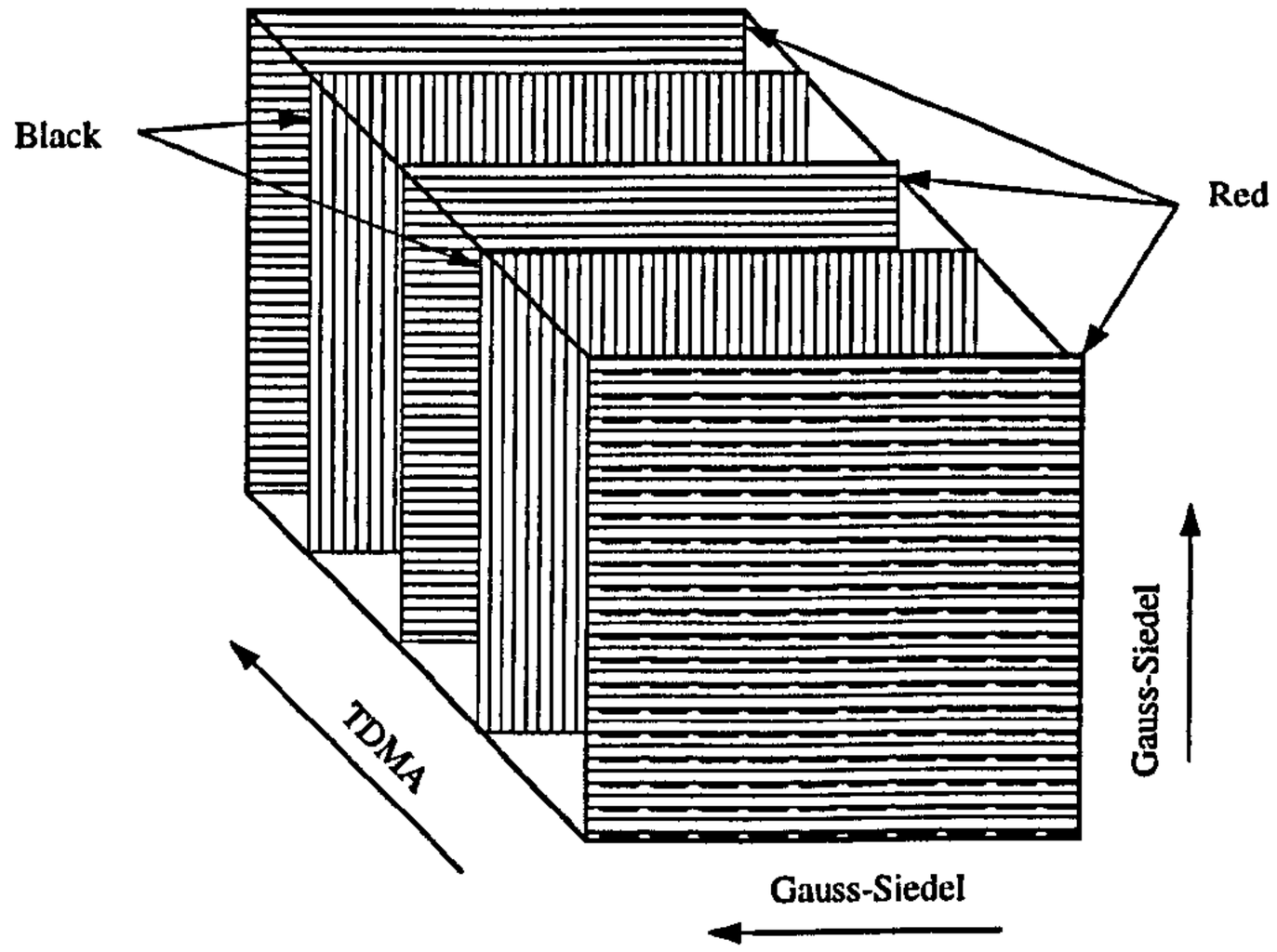

Figure 4.3: Schematic of the Red-Black method using the TDMA solver.

is solved using a Gauss-Seidel method. The Red-Black method is here applied to the outer loop of the solver and enable the use of parallel processing (see Figure 4.3). As mentioned previously, to enhance the propagation of information, alternate sweeping methods are used. The use of alternate sweeping methods implies higher computing requirements per iteration but increases the overall rate of convergence of the solution. To preserve the high rate of convergence given by the TDMA, the Red-Black splitting method is applied to each of the alternate sweeping directions.

4.4.3 Results and discussion on the optimised code

The optimised solver have been tested on 12 processors of an SGI Origin 2000. To test and analyse the improvements made on the code, two test cases (see Figure 4.4 (a) and (b)) and the room configuration of He *et al.* (1999) have been investigated.

Test case 1 (Figure 4.4 (a)) aims to validate the solver by analysing the temperature

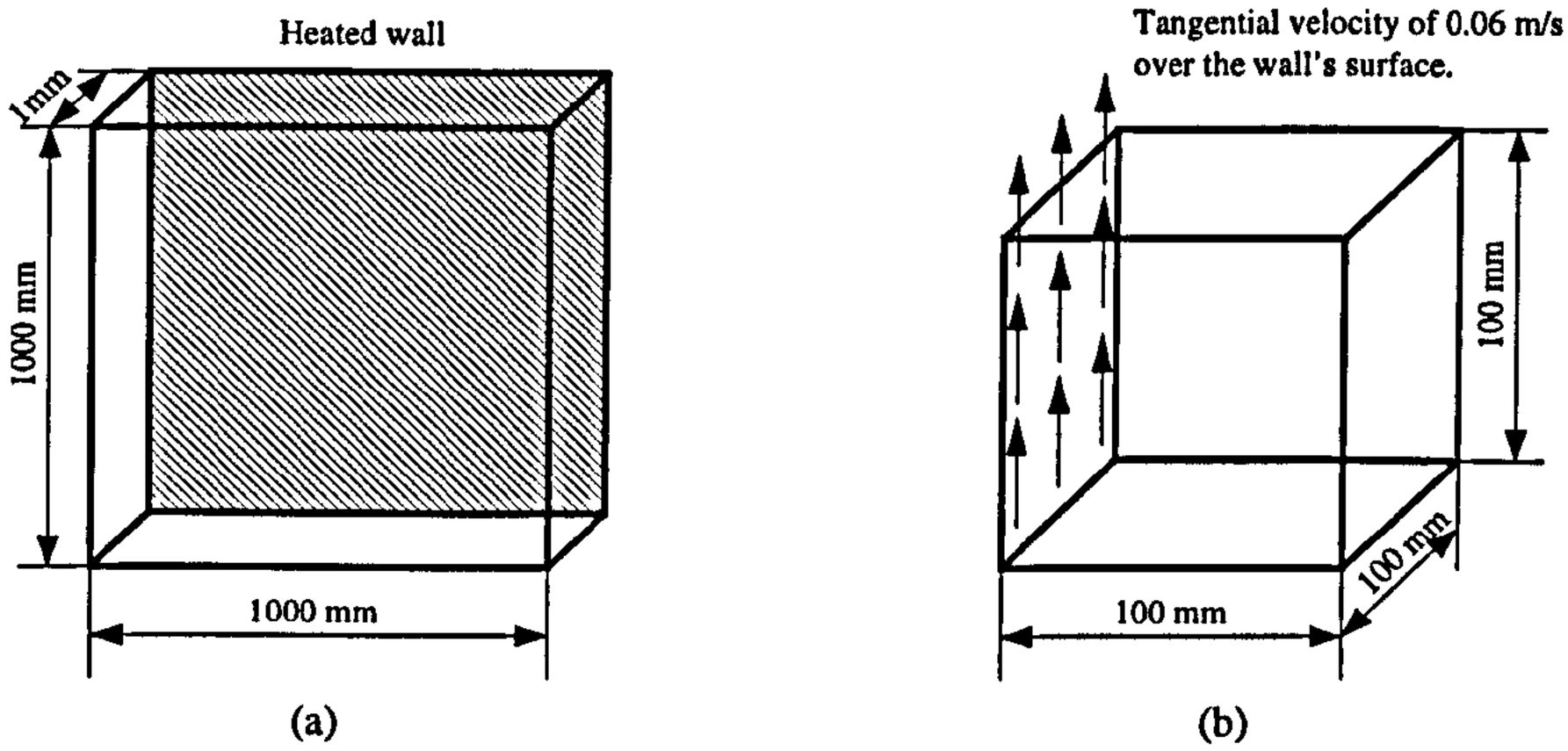

Figure 4.4: (a) Test case 1: Heated wall configuration and (b), Test case 2: Recirculating flow configuration.

drop between a hot and a cold wall. Assuming that the two walls are infinite, the temperature varies linearly between the hot and the cold wall. This case allows a simple validation of the improved code.

Test case 2 (Figure 4.4 (b)) has been set to have $Re = 400$ and a re-circulating flow induced by the tangential wall velocity. This test case has been chosen to assess the rate of convergence (in terms of residual drop and computing time) of the CFD simulations.

It is generally agreed that a drop of the residuals of three order of magnitude corresponds to $\simeq 0.1\%$ convergence error. The terms converged results is used in this work when the drop in residuals has reached a minimum of three orders of magnitude. The term converged is used in this section to indicate a drop in residuals down to machine round-off.

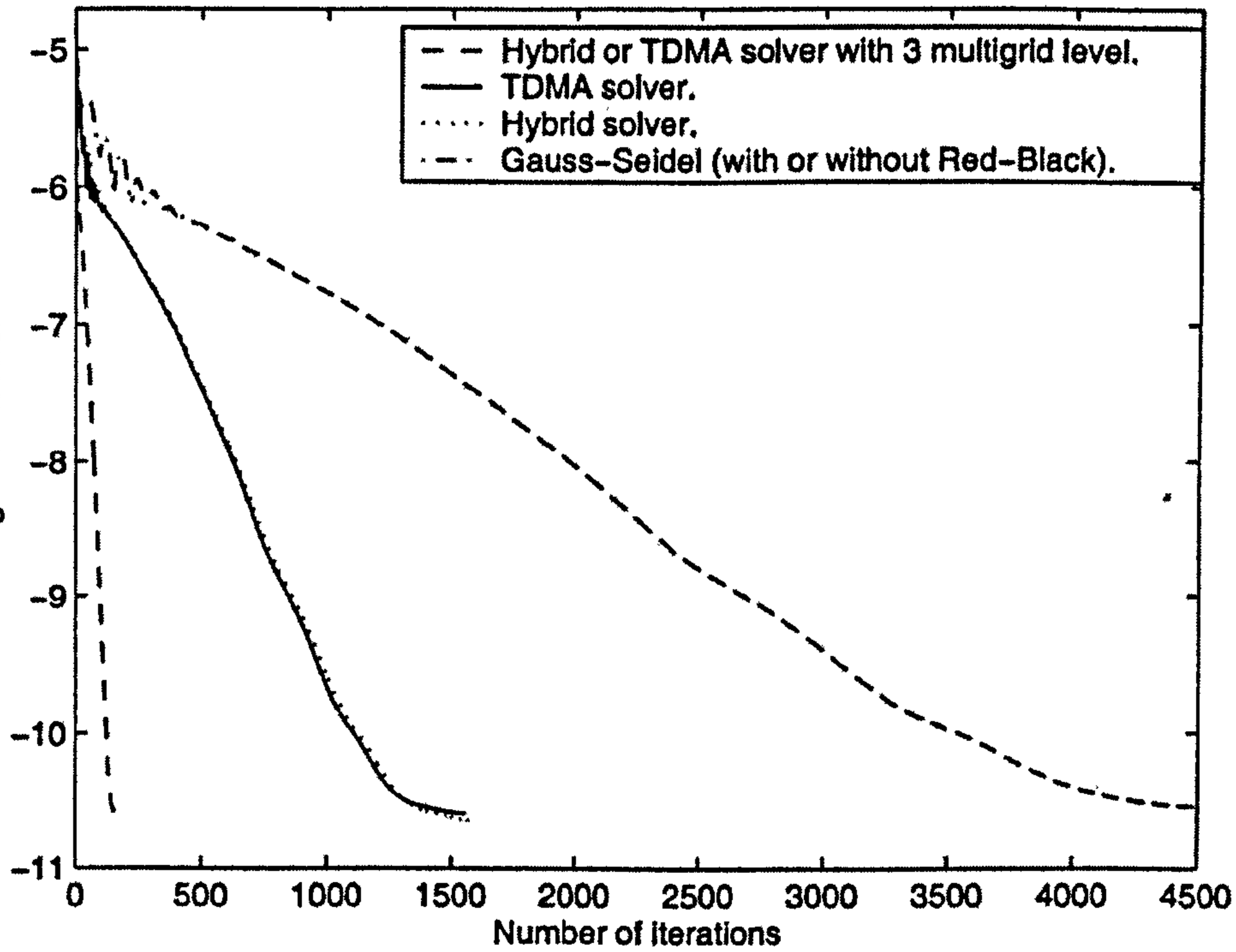

Figure 4.5: Residuals as a function of the number of iterations for various solvers.

Solver type	Test case 2		He *et al.*'s room	
	Iterations	Time	Iterations	Time
Gauss Seidel	4500	2h 39mins	-	-
TDMA	1549	2h 36mins	5483	54h 41 mins
with 3 multigrid level	70	28 mins 20 sec	-	-
Parallel solver	1556	1h 02 mins	5514	26h 16mins
with 3 multigrid level	74	8 mins 25 sec	-	-

Table 4.2: Number of iteration and computing time to reach convergence for test case 2 and the simply ventilated room of He *et al.* (1999).

Figure 4.5 shows the rate of residual drop of the various solvers for Test case 2. The Gauss-Seidel method requires over 4500 iterations to reach convergence on a $45 \times 45 \times 45$ computational grid. The TDMA and its parallel equivalent are found to require $\simeq$ 1550 iterations to reach convergence. The TDMA (or its parallel equivalent) used with three levels of multigrid reaches convergence in $\simeq$ 70 iterations. Since each type of solver has a different computing requirement per iteration, computing times are also required to assess the efficiency of the optimisation techniques.

Table 4.2 summarises the computing time and number of iterations required to reach convergence for the various optimisation methods when applied to Test case 2 and the more complex room geometry of He *et al.* (1999) (see Chapter 8 for details). The parallel computations were carried out using 12 processors of an SGI Origin 2000.

Table 4.2 shows that for Test case 2 a relative time savings of a factor of 2.57 is found between the Gauss-Seidel and the parallel TDMA solver. A relative time saving

factor of 2.52 is found between the TDMA and its parallel version. The combination of the parallel processing and multigrid methods is found to be the most economical strategy. The relative time savings observed between the TDMA solver and the TDMA solver with multigrid has been found to be smaller (5.51) than the relative time saving between the parallel TDMA and the parallel TDMA with multigrid (7.37). This result seems to indicate that the combined efficiency of multigrid method and parallel processing is greater than the efficiency of the separate methods. This result can be explained since, when combining multigrid and parallel processing, the coupling information lost by the red-black method (required for parallel processing) is retrieved by using coarser grids (multigrid method) which facilitates the propagation of informations throughout the domain.

The results obtained on the more complex ventilated room of He *et al.* (1999) reveal similar level of improvements. A relative time saving factor of 2.08 is found between the TDMA and its parallel equivalent.

Chapter 5

Turbulence models' validation

5.1 Introduction

To validate the turbulence models introduced in Section 3.2, in terms of accuracy and the extent of their applicability, four experimental benchmark flow configurations are considered. The four benchmark problems are:

- Two-dimensional turbulent channel flow;
- Side injection channel flow;
- Backward-facing step flow and;
- Secondary motion in a square duct.

All four test cases are well known and experimental or DNS data is available in the literature.

A grid independency analysis has been carried out for each case to ensure the validity of the results. Unless otherwise specified, the grids generated show an averaged first of

wall node $y^+ < 1$. The simulations assume isothermal flows.

5.2 Two-dimensional turbulent channel flow

The first test case considered to validate the turbulence models introduced in Section 3.2 is based on the experimental work of Laufer (1951) investigating turbulent flows in two-dimensional channels at $Re \simeq 32000$. The flow is assumed to be fully developed. Thus, the mean velocity gradients $\partial u/\partial x$, $\partial v/\partial y$ and $\partial w/\partial z = 0$. Because of this, the modelling of such a flow using a linear approximation of the Reynolds stress tensor ($\tau_{ij} = -\frac{2}{3}\rho k\delta_{ij} + 2\mu_t S_{ij}$) as used for the standard $k-\epsilon$ model, would imply that the three normal Reynolds stresses ($\tau_{xx}, \tau_{yy}, \tau_{zz}$) are all identical and equal to $-\frac{2}{3}\rho k$. The experimental work done on channel flows including the work of Laufer (1951) clearly reveals that the normal Reynolds stresses are not identical and emphasise the deficiency of linear eddy-viscosity turbulence models.

The use of advanced turbulence models in which the Reynolds stress tensor is described in a more physically consistent manner should reveal in this case a significant improvement in the prediction of the Reynolds stresses when compared with linear models.

5.2.1 Results and discussion

The $k-\epsilon$ and $k-l$ models have both been used to compare the EASM and cubic eddy-viscosity model predictions with their linear equivalents. Due to symmetrical properties of the flow, the results are only presented for half of the channel.

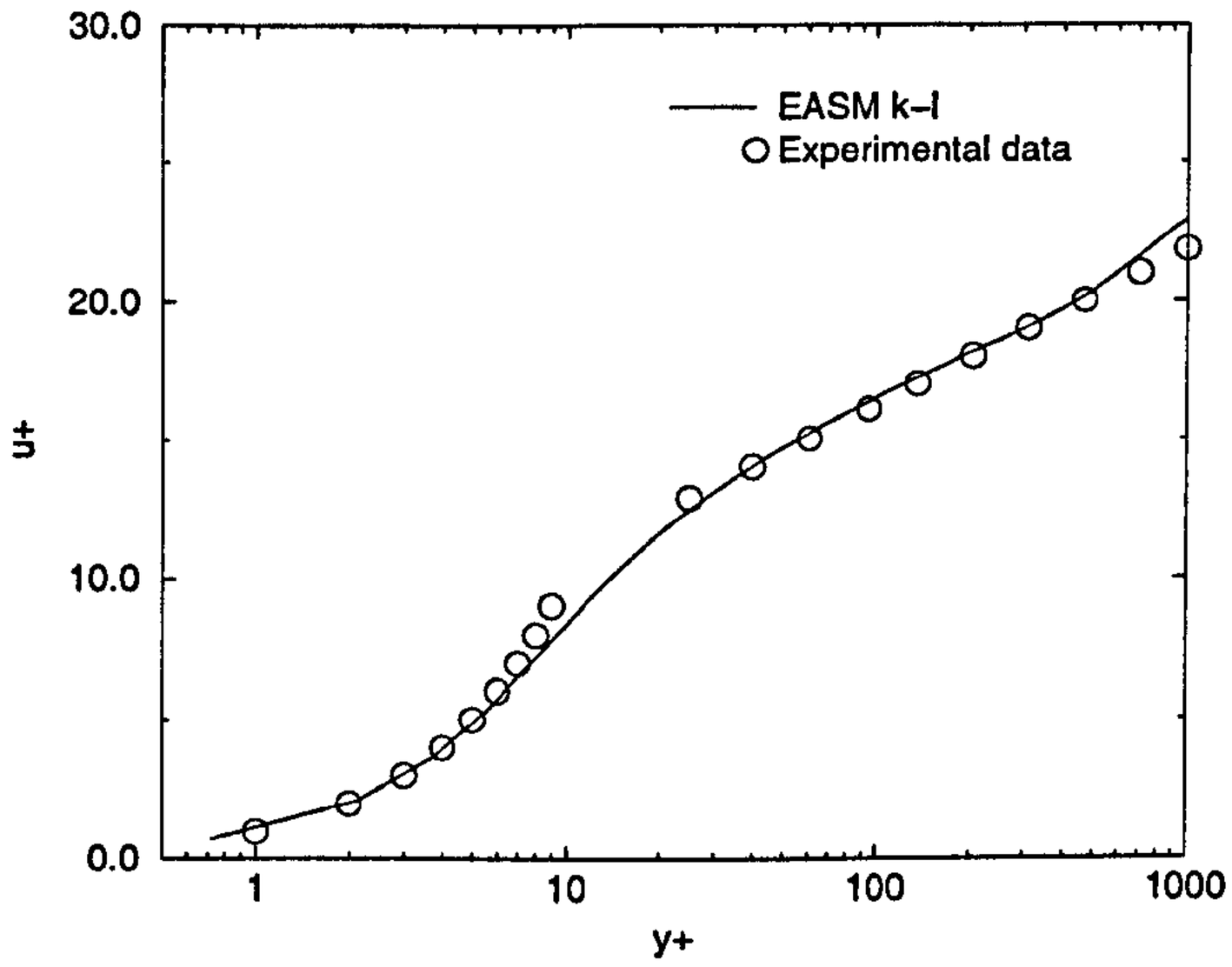

(a)

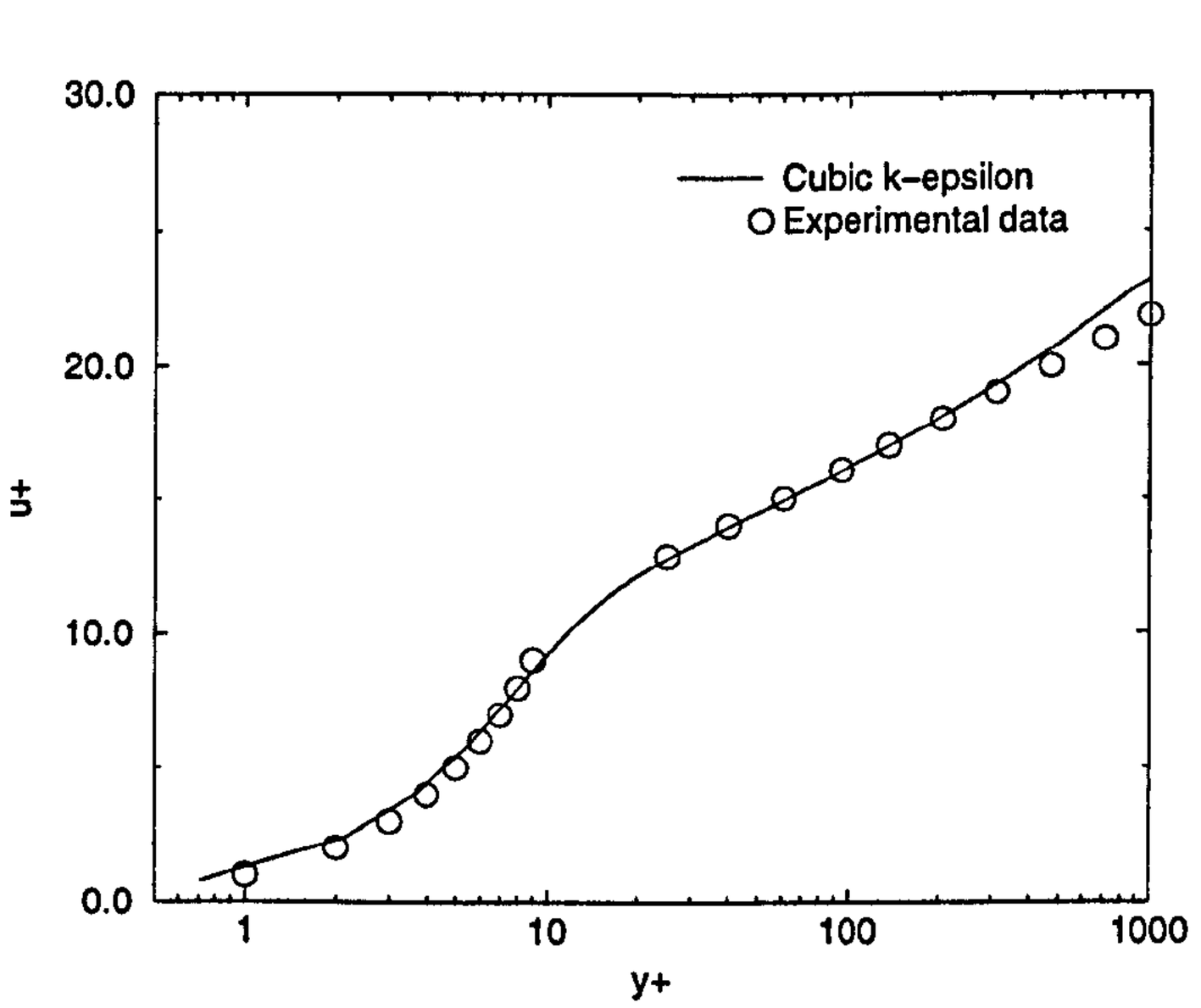

(b)

Figure 5.1: Near-wall velocity profile. (a) EASM $k-l$ model and (b) cubic $k-\epsilon$ model.

Measurements	Linear		EASM		cubic	
	$k-l$	$k-\epsilon$	$k-l$	$k-\epsilon$	$k-l$	$k-\epsilon$
18.64	18.57	19.49	18.20	18.24	17.65	19.37

Table 5.1: Non-dimensional wall shear stress $(\tau_w/(\rho U_0^2) \times 10^4)$.

Figure 5.1 (a) compares the EASM $k-l$ predictions with measurements of the near-wall streamwise velocity behaviour. In Figure 5.1 (b) the cubic eddy viscosity $k-\epsilon$ predictions are compared with the data of Laufer (1951). For the cubic model, the Launder and Sharma (1974) LRN model with Yap (1987) correction factor is used and, the turbulent viscosity is evaluated using Craft *et al.*'s (1996) formulation (see Section 3.2.2). A similar level of agreement between CFD and experimental data has been found when using the linear and EASM $k-\epsilon$ model with the various damping functions presented in Section 3.1.7. It has been found that the Lam-Bremhorst (1981) function is more unstable than the Launder and Sharma (1974) or Van Driest (1956) functions. Extremely small under-relaxation factor (typically below 0.1) are needed to stabilise the numerical simulation.

Table 5.1 presents a comparison of measured and predicted non-dimensional wall shear stress $\tau_w/(\rho U_0^2) \times 10^4$. The table shows good agreement between the CFD and measurements for all the models considered. The linear, EASM and cubic $k-\epsilon$ model use the Launder and Sharma (1974), AKN (1996) and Craft *et al.* (1996) damping functions respectively. The $k-l$ based models use the Wolfshtein (1969) damping function.

Figure 5.2 compares measured normal Reynolds stresses with the linear, EASM and cubic model predictions used in a $k-l$ framework. Relative to the linear $k-l$ model,

the EASM and cubic eddy viscosity model greatly improve the stress predictions. The figure shows for this case that the EASM is more accurate than the cubic model. This difference can partly be explained by the fact that the LRN version of the cubic model has been developed for a $k-\epsilon$ base model as discussed in Section 3.2.2.

Figure 5.3 compares Laufer's (1951) measurements with predicted stresses of the linear, EASM and cubic model in a LRN $k-\epsilon$ framework. The Lam-Bremhorst (1981) damping function has been used to obtain the EASM results. The Craft *et al.* (1996) cubic model is used with Yap (1987) correction factor. The figure suggests that, as might be expected, either non-linear model significantly improves the Reynolds stress predictions relative to the linear Lam-Bremhorst (1981) $k-\epsilon$ model.

Similar level of agreement has been found between the predicted and measured τ_{zz} for the EASM and cubic model in either a $k-\epsilon$ or $k-l$ framework. High Reynolds number variants of the $k-l$ and $k-\epsilon$ models have been tested and shown similar agreement levels to their LRN equivalents.

5.2.2 Variants of the EASM

The EASM results shown in Figure 5.2 and 5.3 have been obtained treating α_i as constants (*c.f.* Equation 3.66) and not as originally defined by Gatski and Speziale (1993) (*c.f.* Equation 3.64). As noted in Section 3.2.1, the use of either dynamic or fixed α_i coefficients has, in this case, only a minor effect on the solutions (Rokni (2000)). Figure 5.4 emphasises this point by showing the distribution of α_i across the channel. The linear part of Figure 5.4 (a) suggests α_i as:

$$\alpha_1 \simeq 0.1 \qquad \alpha_2 \simeq 0.165 \qquad \alpha_3 \simeq 0.077 \tag{5.1}$$

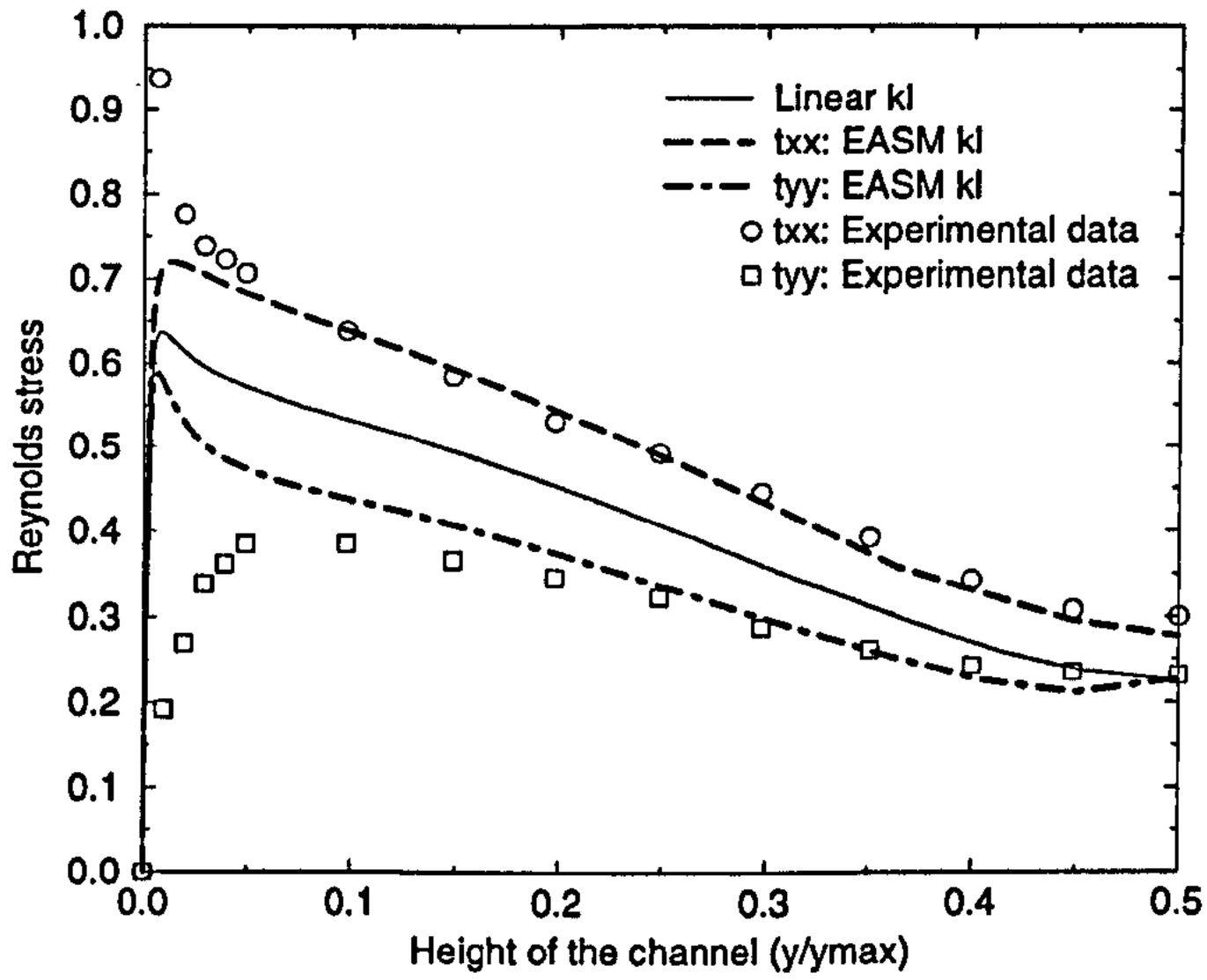

(a)

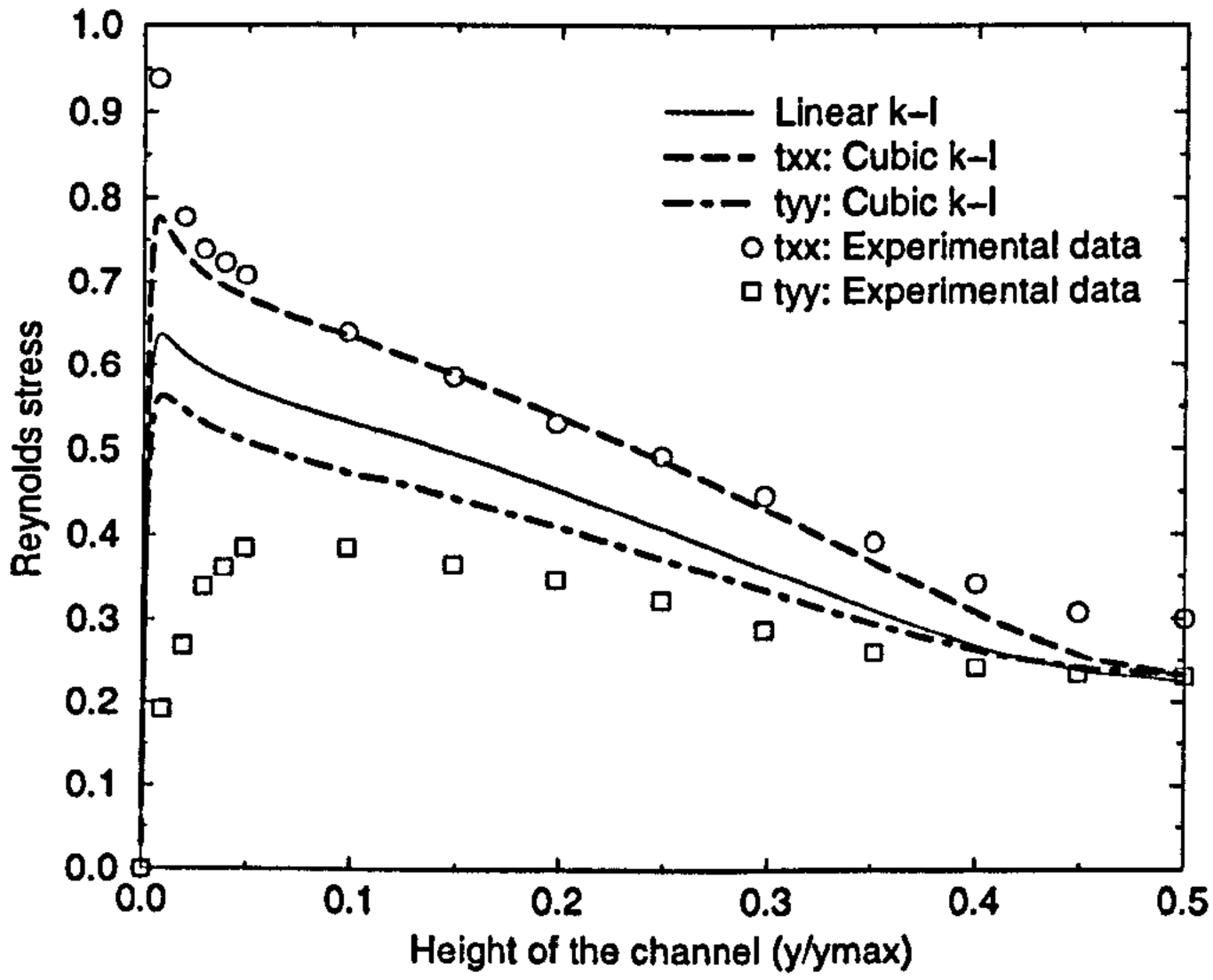

(b)

Figure 5.2: Comparison of non-linear Reynolds stresses in a $k-l$ framework with measurements: (a) EASM model and (b) cubic model.

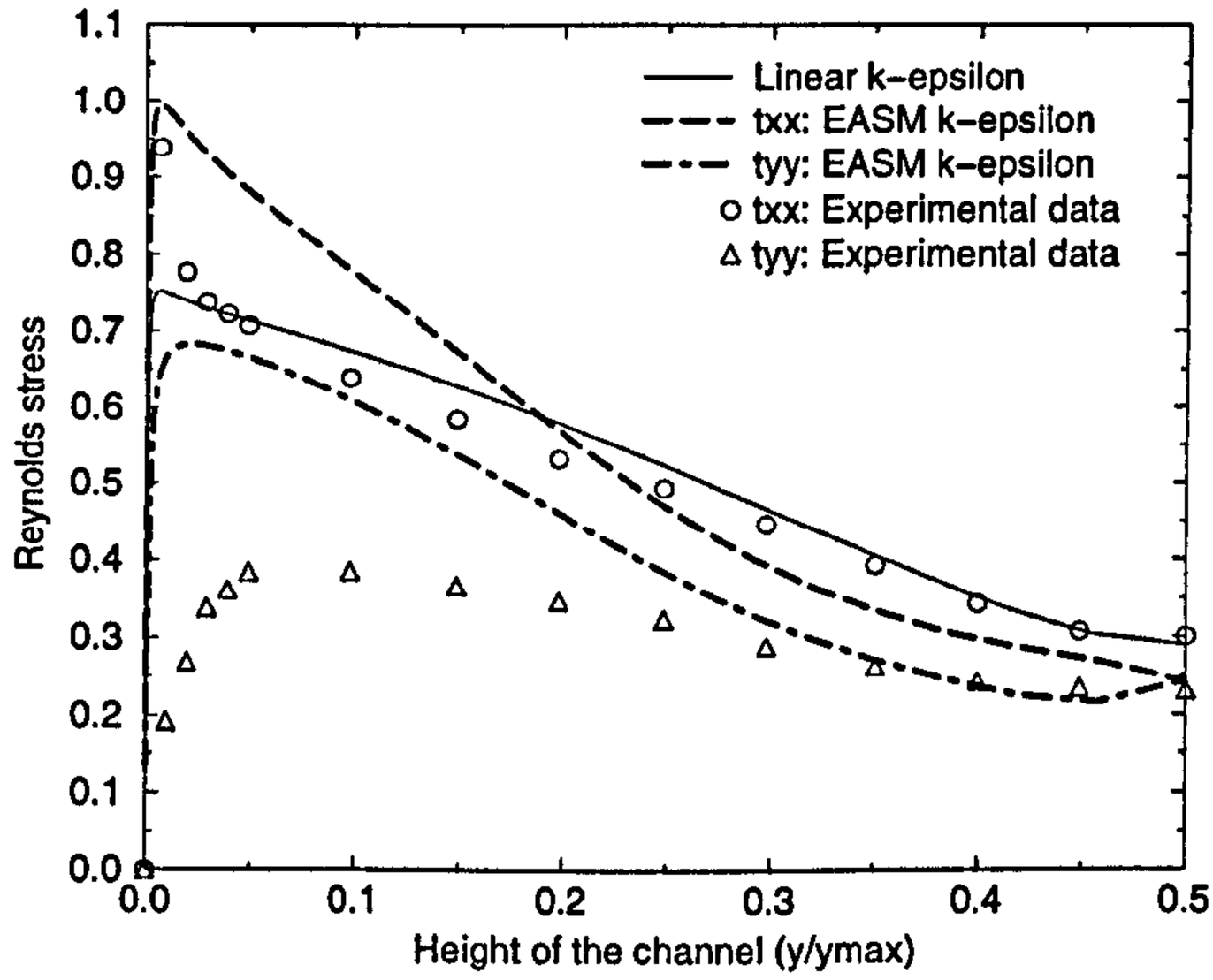

(a)

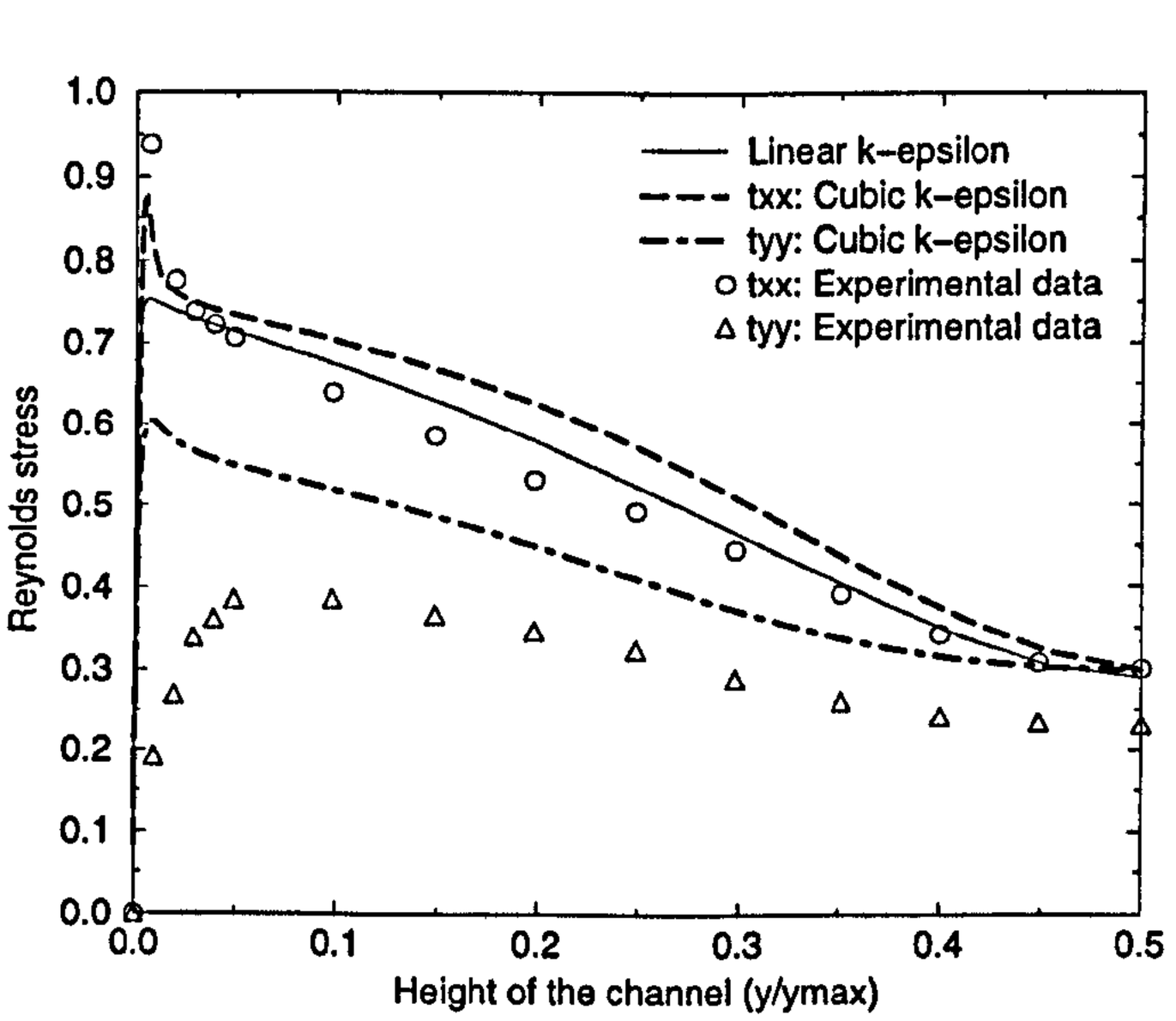

(b)

Figure 5.3: Comparison of non-linear Reynolds stresses in a $k-\epsilon$ framework with channel flow measurements: (a) EASM model and (b) Cubic model.

These values are found to be within 15% of Rokni's (2000) approximations shown in Equation 3.66. We also note from Figure 5.4 (a) that near the wall α_i is non-monotonic with the wall distance y. In the middle of the channel, α_i is found much greater than suggested by Equation 5.1 but, since the main velocity gradients are negligible in this area, using α_i as constants should not greatly influence the solution.

The original approximation of Gatski and Speziale (1993) (Equation 3.59 and Equation 3.60) have been used to generate Figures 5.1, 5.2 and 5.3 results. Figure 5.4 (b) compares the variations of the turbulent normal Reynolds stresses (τ_{xx} and τ_{yy}) between the original version of Gatski and Speziale (1993) with the approximation of Gatski (1996) for the evaluation of the $C_{\mu i}$ coefficients. It can be seen from Figure 5.4 (b) that the Gatski (1996) approximation gives much smoother Reynolds stress gradient in the middle of the channel. However, the predicted Reynolds stresses appear to be less accurate. In particular, the relative difference between the principal Reynolds stresses is reduced.

5.3 Side-injection channel flow

The next test case used for the validation of the turbulence models is a side-injection channel flow (see Figure 5.5) inspired by a Solid Rocket Motor (SRM). The case is chosen since, unlike the plane channel, the flow now exhibits extreme streamline curvature. As discussed in Section 3.2.2, it is expected to find that the cubic model will be highly sensitive to streamline curvature and should reveal significant improvement of the flow predictions when compared with linear models.

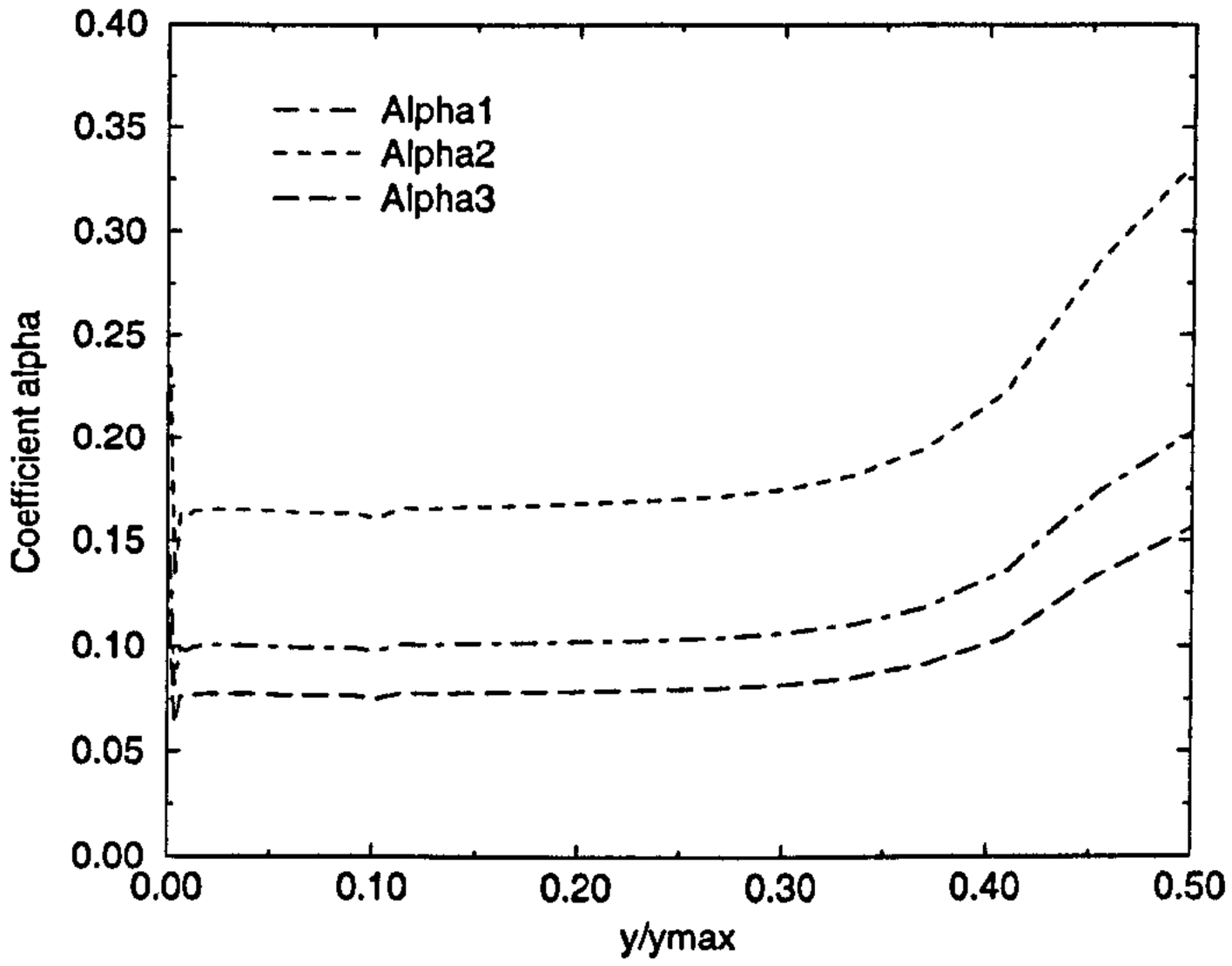

(a)

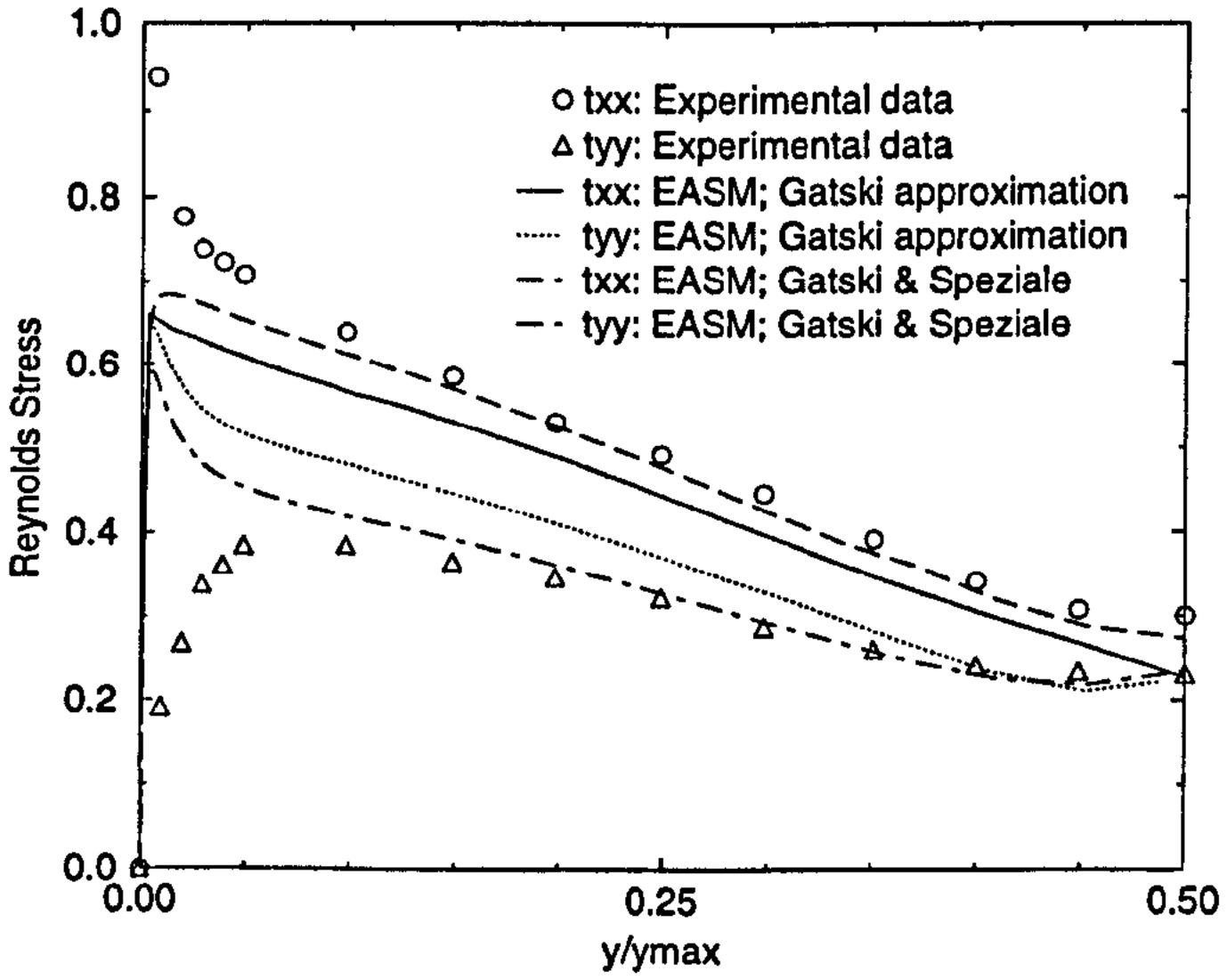

(b)

Figure 5.4: (a) Distribution of α_i across half of the channel and (b), influence of the $C_{\mu i}$ approximation on the Reynolds stresses.

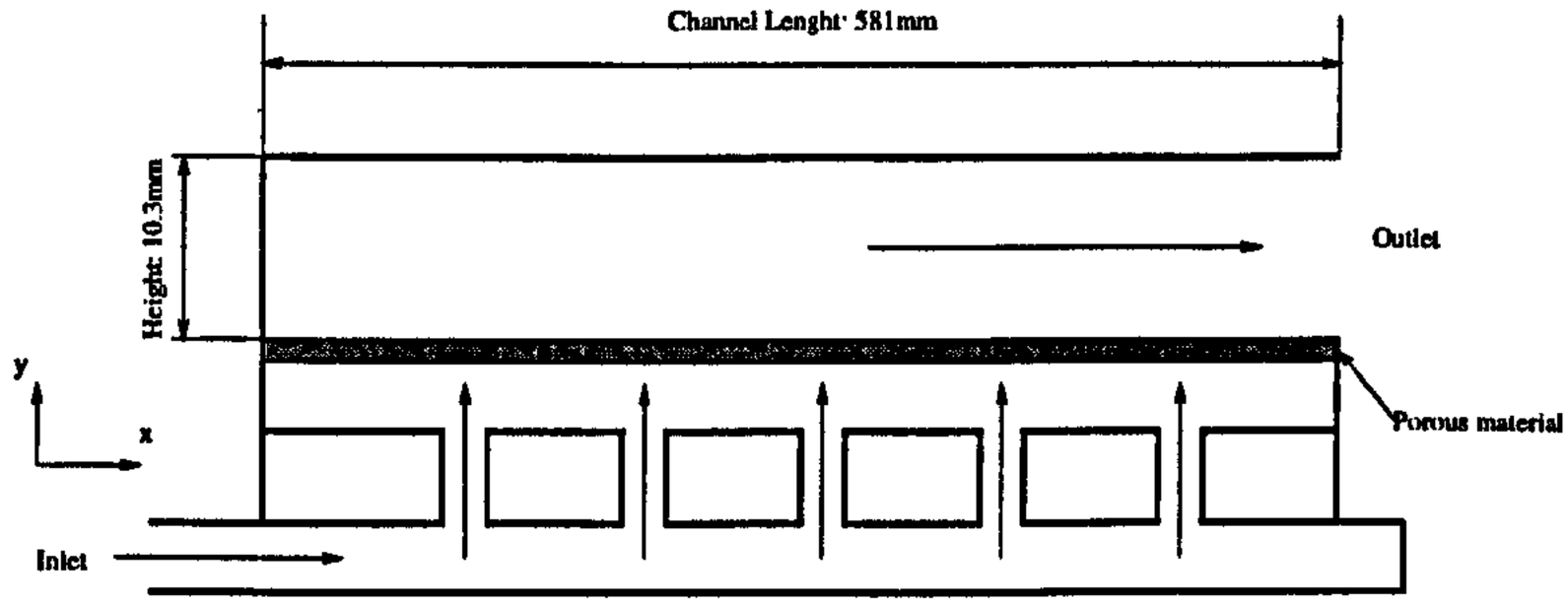

Figure 5.5: Schematic of the side-injection driven channel.

5.3.1 Numerical modelling

An inlet (or injection) velocity is used here as boundary condition. The injection velocity (u_s) used is a quadratic polynomial fit of the data of Chaouat (2000) as follows:

$$u_s = 0.5755x^2 - 0.0417x + 1.4829 \,, \tag{5.2}$$

where x is the distance along the inlet (see Figure 5.5). The outlet flow condition is set to conserve the mass flow rate.

The numerical simulations are carried out for the linear, EASM and cubic model in a $k-l$ and $k-\epsilon$ framework. The AKN model is used for the the linear and EASM $k-\epsilon$ model. The cubic $(k-\epsilon)$ model of Craft *et al.* (1996) is used with Launder and Sharma (1974) damping and Yap (1987) factor.

5.3.2 Results and discussion

Figure 5.6 shows a comparison of five velocity profiles in the channel between the linear, EASM, cubic model in a $k-l$ framework with measurements. The velocities shown in Figure 5.6 are non-dimensionalised by the injection velocity u_s and, the wall distances

are non-dimensionalised by the height of the channel ($y_{max} = 0.0103\ m$). The figure shows, as expected, that the cubic model gives higher predictive accuracy than the EASM or the linear model. The cubic model is found to predict well the peak velocity in the channel. However, the EASM and the linear model's predictions are more accurate near the inlet wall. Similar levels of agreement with measurements are obtained when using the linear, EASM and cubic model in a $k - \epsilon$ framework.

Figure 5.7 shows a comparison of the principal Reynolds stress τ_{xx} profile at a distance of 570 mm along x (see Figure 5.5) for the linear, EASM, cubic $k - l$ and $k - \epsilon$ model. In both figures, the cubic model is found to give better predictions than the EASM and linear models. The cubic $k - \epsilon$ model is found to perform better than the other model tested. Figure 5.8 (a) which plots the τ_{xx} profile at a distance of 450 mm also shows that the cubic $(k - \epsilon)$ predictions are more accurate than the EASM and linear predictions. Figure 5.8 (b) shows that the cubic $k - \epsilon$ is more accurate in predicting the τ_{yy} profile at a distance of 570 mm than the EASM and linear $k - \epsilon$ model. Figure 5.7 (a) and 5.8 (b) also reveal that only the cubic model is able to significantly predict the anisotropy of the Reynolds stress tensor.

This analysis clearly reveals the potential of the cubic model (in either a $k - l$ or $k - \epsilon$ form) in predicting flows that exhibit extreme streamline curvature. The cubic model is found to predict better the normal Reynolds stresses in the channel but does not excellent agreements with measured velocity profiles. Unlike the cubic model, the EASM has not shown here significant prediction improvements when compared to linear eddy viscosity models.

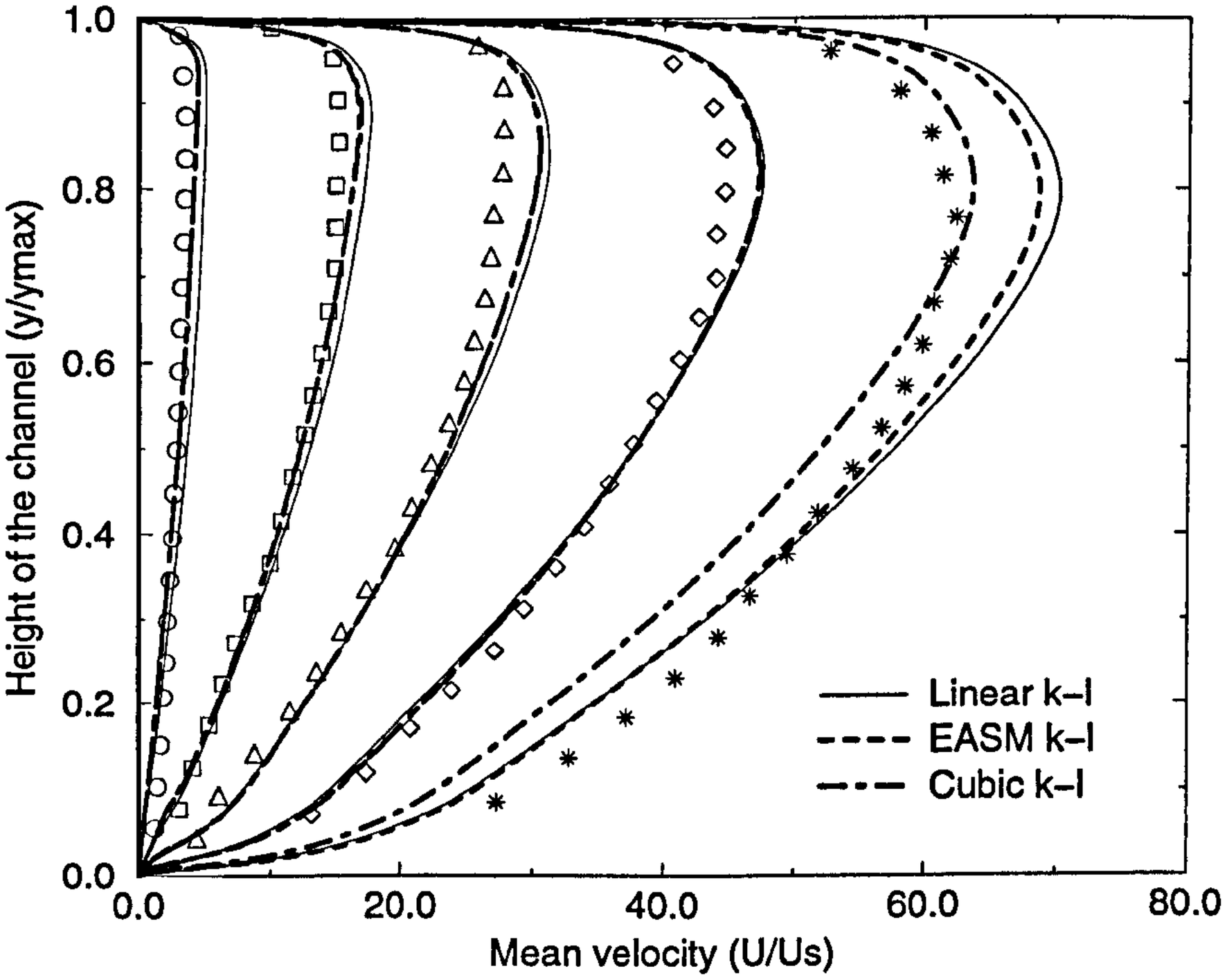

Figure 5.6: Comparison of linear, EASM and cubic $k-l$ models with measurements (symbols). Profiles located at $x = 0.031m$: $\circ$; $x = 0.031m$: $\triangle$; $x = 0.120m$: $\square$; $x = 0.220m$: $\diamond$; $x = 0.500m$: $*$.

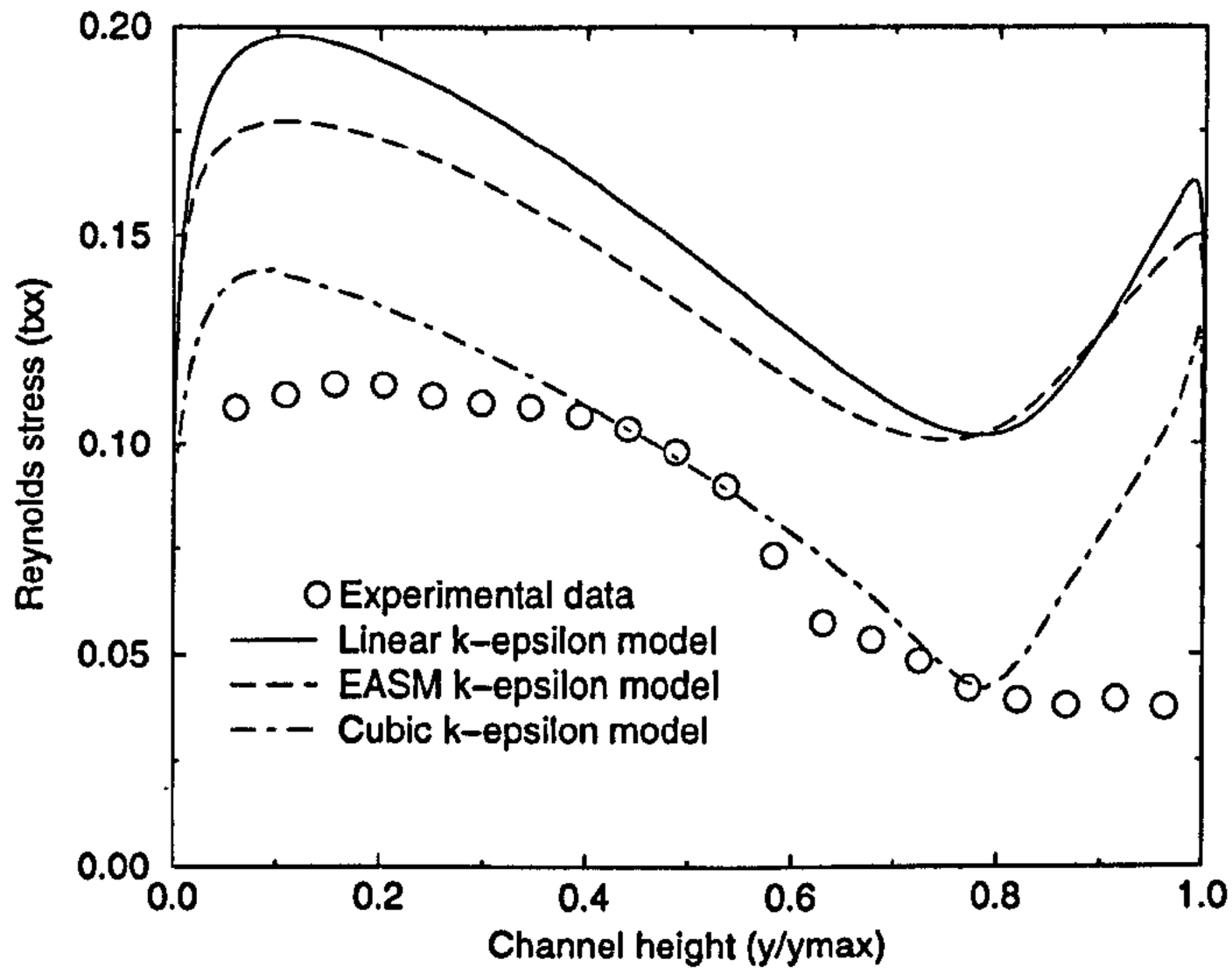

(a)

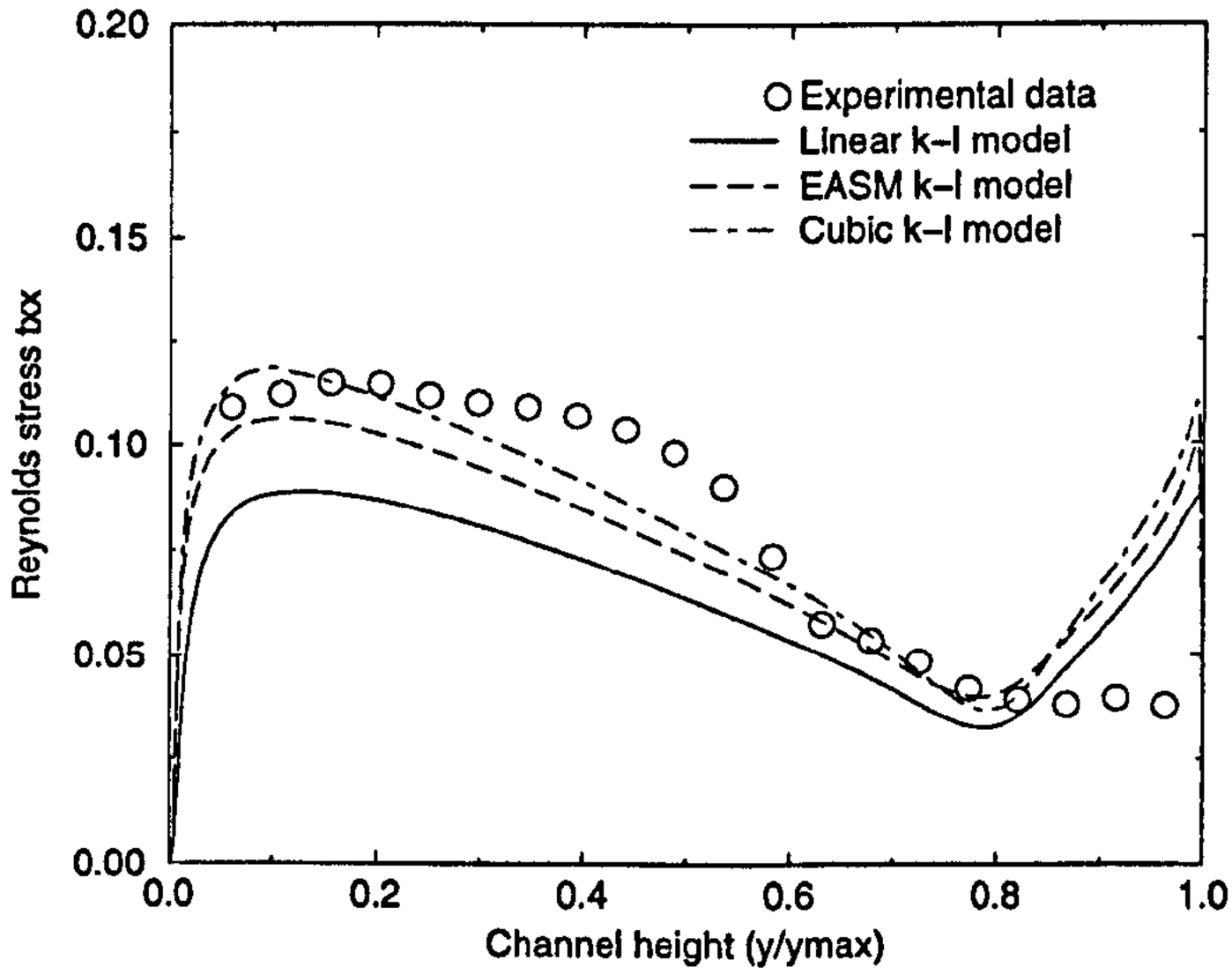

(b)

Figure 5.7: Comparison of normal Reynolds stress profiles: (a) and (b) τ_{xx} at a distance of 570 mm along x;

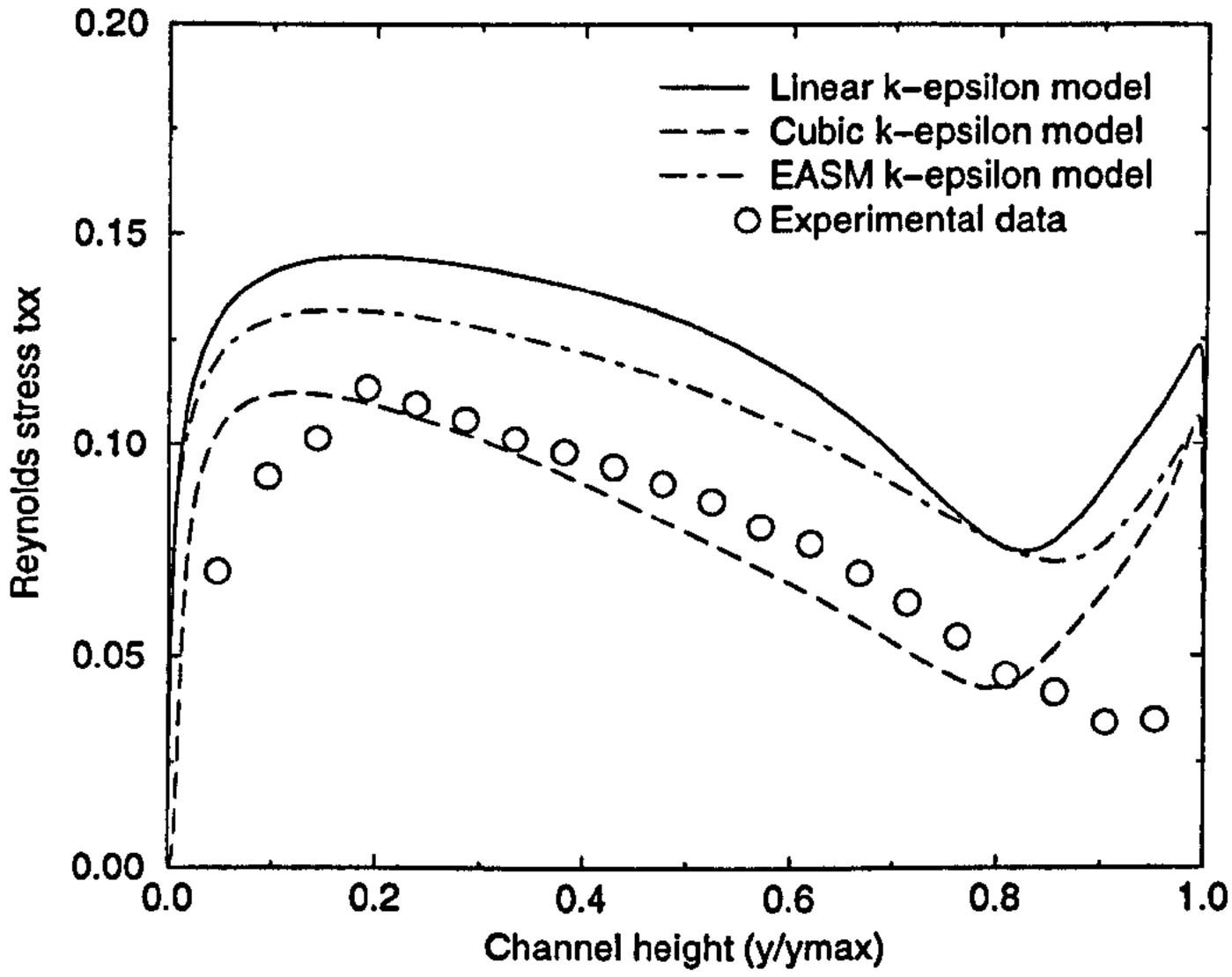

(a)

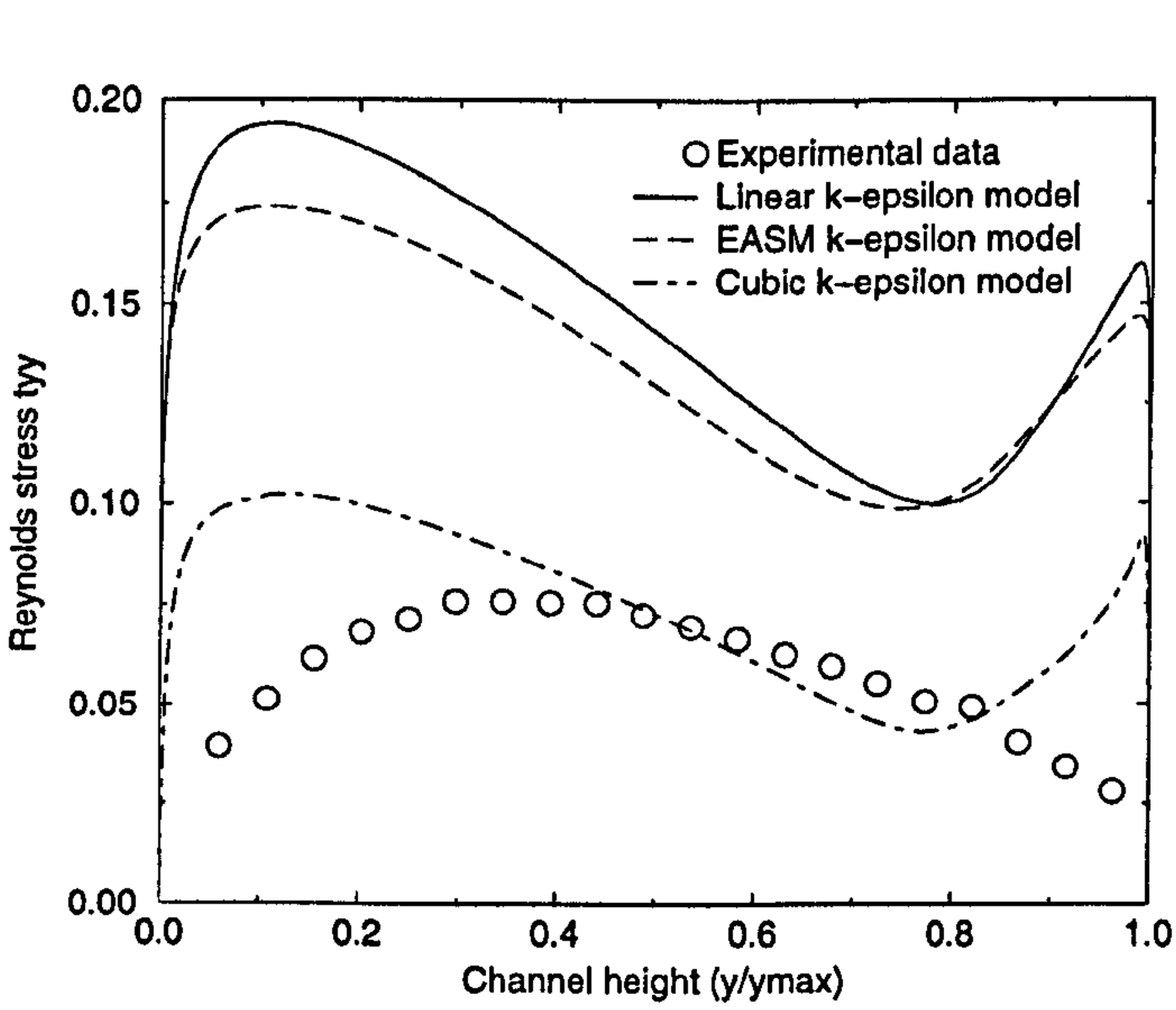

(b)

Figure 5.8: Comparison of normal Reynolds stress profiles: (a) τ_{xx} at a distance of 450 mm along x and (b) τ_{yy} at a distance of 570 mm along x.

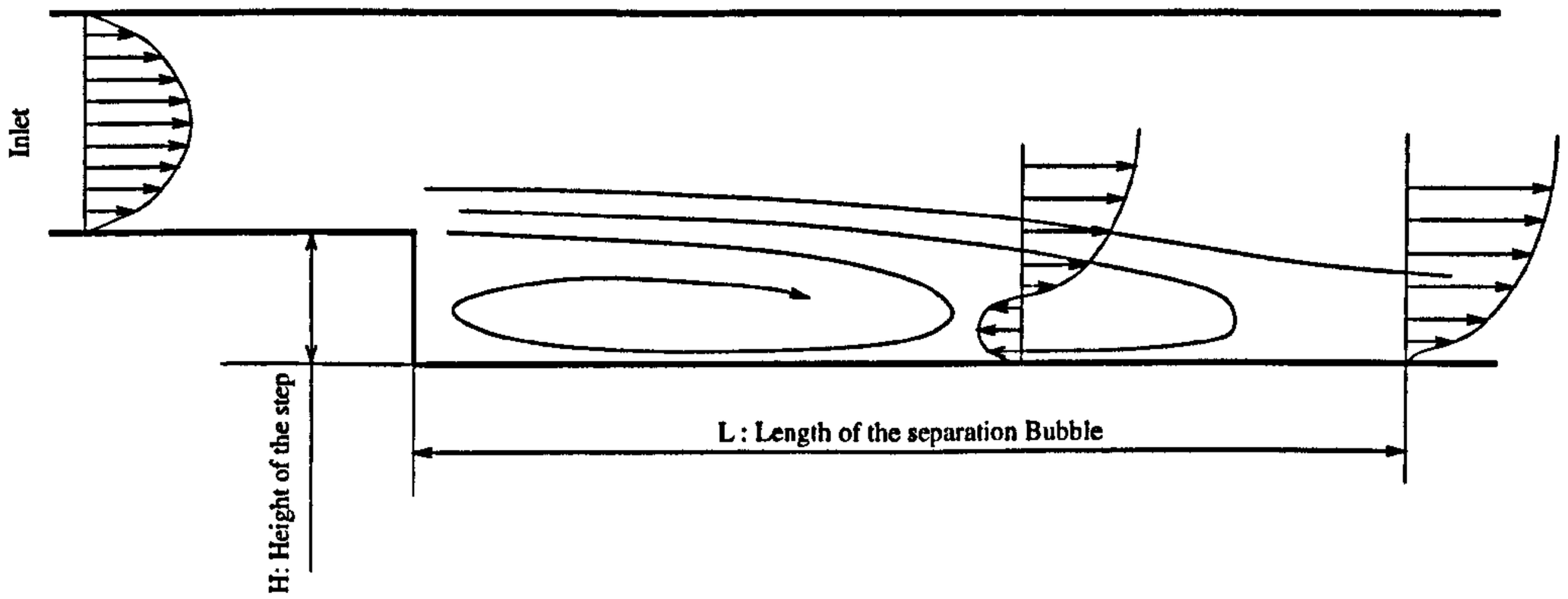

Figure 5.9: Backward-facing step: geometry and flow profile.

5.4 Backward-facing step flow configuration

The backward-facing step flow is a popular benchmark exhibiting not just streamline curvature but, separation and re-attachment. Hence, it is a challenging turbulence model test. Research in the early 80's concluded that predictions of backward-facing step flows can partly be validated by the length of the separation bubble that occurs downstream of the step itself as shown in Figure 5.9. As discussed at the 1980-1981 AFOSR-HTTM Stanford conference on turbulence, an accurate prediction of the backward-facing step flow should give the ratio $L/H \simeq 7$ (L being the length of the separation-bubble and H, the height of the step).

The configuration studied here is based on the work of Kim *et al.* (1980) and the main features of the setup corresponding to $Re = 1.32 \times 10^5$ (based on the inlet velocity and outlet channel height) are summarised in Table 5.2. The results presented here have all been obtained using $k - \epsilon$ based models.

Inlet velocity	18.18 $m.s^{-1}$	Channel Length	1.3025 m
Channel height	0.1143 m	Step height	0.0381 m
Step length	0.3 m	Computational grid	$69 \times 69 \times 15$
Turb. energy @ inlet	5 $m^2.s^{-2}$	Turb. dissipation @ inlet	690 $m^2.s^{-3}$
Reference temperature	296.3 K	Reference pressure	1.01 Bar

Table 5.2: Specifications of the backward-facing step flow.

The Launder and Sharma (1974) model with Yap (1987) correction is used for the EASM and cubic eddy-viscosity models. The ratio L/H is found to be equal to 4.98 for the linear model, 7.08 for the EASM and 6.75 for the cubic model. Two-equation models' predictions of backward-facing step flow is reviewed by Thangam and Speziale (1992). They find that the use of Speziale's (1987) non-linear eddy-viscosity model finds $L/H \simeq 6.9$ and the RNG model of Yakhot and Orzag (1986) finds $L/H \simeq 4$. These results enforce the encouraging predictions given here by the EASM and the cubic eddy-viscosity model.

The EASM and cubic model predictions are approximately within $\simeq 1\%$ and $\simeq 3\%$ of the established value whereas the linear model has a $\simeq 29\%$ error. The use of the advanced eddy-viscosity turbulence models tested here is hence found to significantly increase the predictive accuracy.

Inlet velocity	0.5670 m/s^1	Channel initial length	4 m
Channel height	0.0635 m	Channel width	0.0635 m
Reference pressure	1.01 Bar	Reference temperature	296.3 K
Turb. energy @ inlet	5 m^2/s^2	Turb. dissipation @ inlet	690 m^2/s^3

Table 5.3: Specifications of the square duct used to obtain secondary motion.

5.5 Secondary motion in a square duct

The final case used for the validation of the advanced turbulence models presented in Section 3.2 is the investigation of fully developed flows in a square duct. As demonstrated in Section 5.2, when considering fully developed flows, linear eddy-viscosity turbulence models predict $\tau_{xx} = \tau_{yy} = \tau_{zz}$. According to experimental data and the DNS work of Gavrilakis (1992), a secondary motion of a magnitude of approximately 6% of the mean flow occurs in straight square ducts (Prandtl's motion of the second kind). Speziale (1982) demonstrated that the numerical prediction of the secondary motions requires the term $\tau_{xx} - \tau_{yy}$ to be non-zero. Thus, linear turbulence models (predicting $\tau_{xx} = \tau_{yy} = \tau_{zz}$) will not predict secondary motions in straight square ducts. The secondary motions consists of two opposite vortices in each of the four corners of the duct. Table 5.3 presents the flow parameters as investigated by Gavrilakis (1992) corresponding to $Re \simeq 4410$.

To ensure that the flow is fully developed, a periodic boundary condition has been applied to the channel. The results shown by Figure 5.10 have been obtained using the EASM $k - l$ turbulence model. As shown by Gavrilakis (1992), the secondary motions occur mainly in the corners of the duct (where $\tau_{xx} - \tau_{yy}$ is largest) and thus an appropriate wall damping function is needed. The standard Van Driest (1956) or the

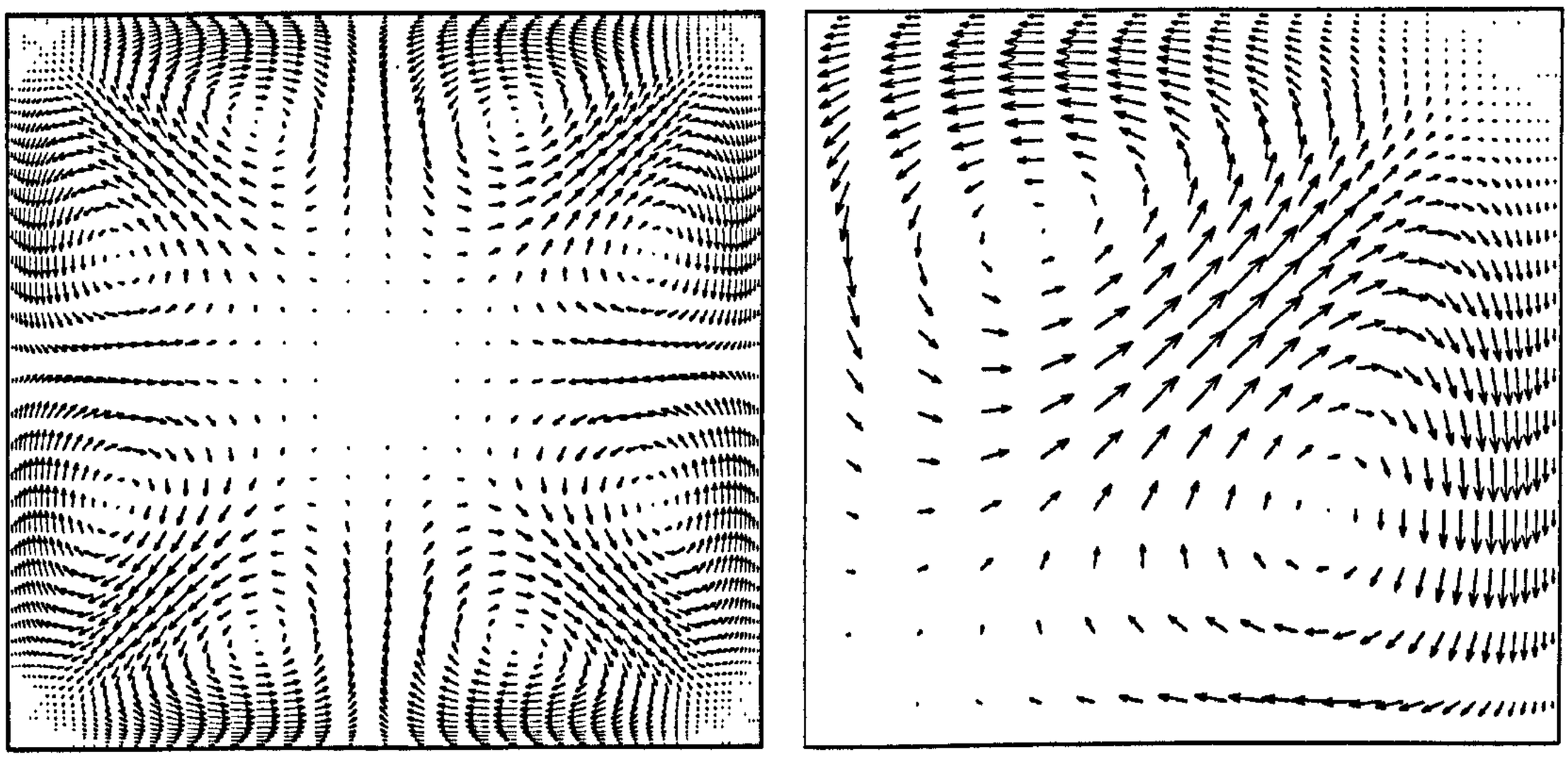

(a) (b)

Figure 5.10: Secondary motions in a square duct using the EASM $k-l$ model: (a) Full view and (b) zoom on the top right corner.

Wolfshtein (1969) damping functions described in Section 3.1.6 are not capable of detecting the presence of more than one wall and their use lead to a misprediction of the secondary motions. The results showed in Figure 5.10 for the EASM $k-l$ model, have been obtained using the Mompean (1998) damping function discussed in Section 3.1.6. It has the advantage of detecting the presence of more than one wall, hence giving better agreement with damping effects for corners implied by DNS data. The Mompean (1998) damping function has been applied to the turbulent viscosity (standard procedure) and to the invariance coefficients (η and ζ) of the EASM as suggested by Rokni (1997).

Figure 5.11 is obtained using a LRN version of the $k-\epsilon$ cubic eddy-viscosity model. The Launder and Sharma (1974) model with Yap (1987) correction factor has been used.

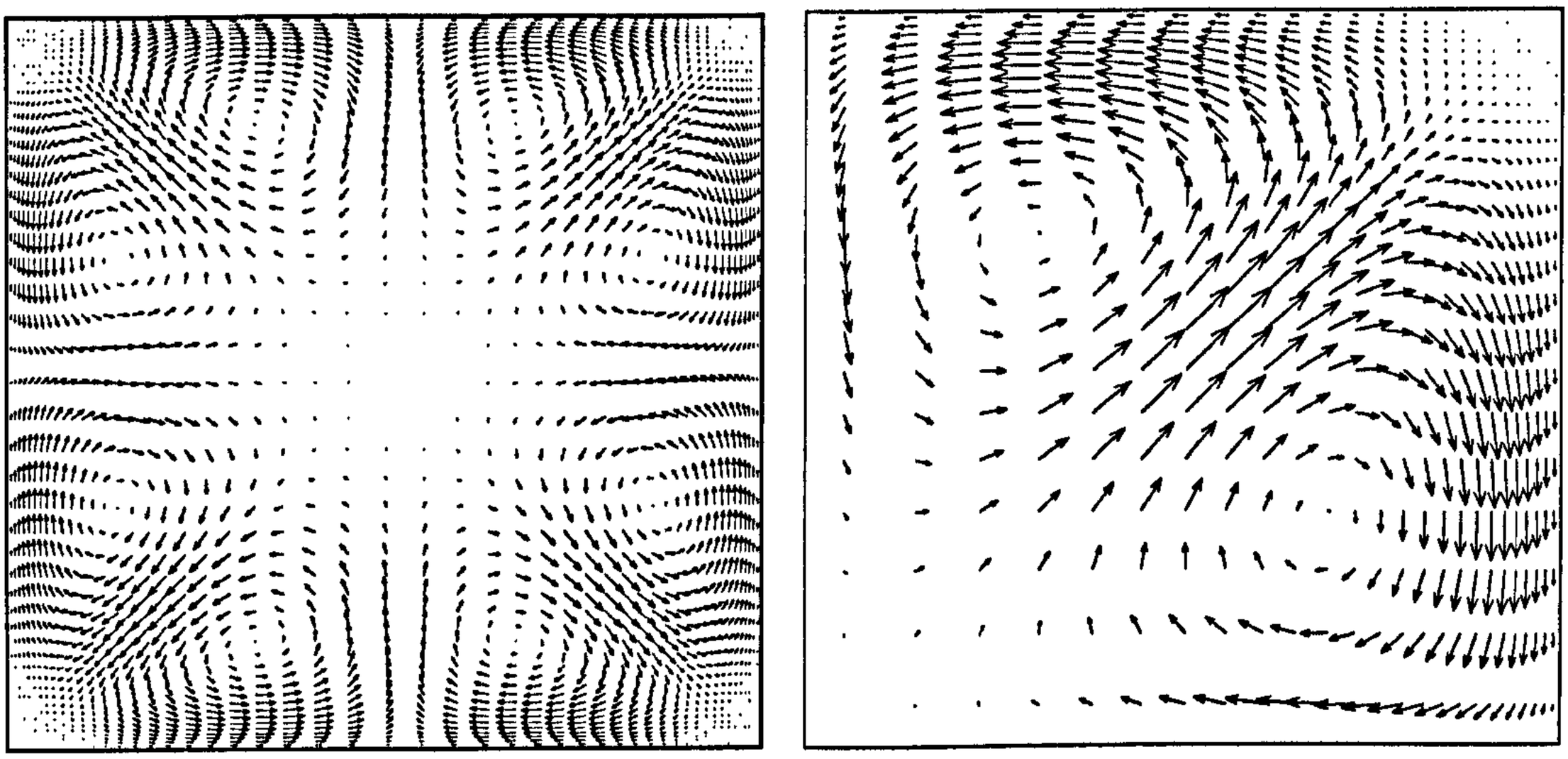

(a) (b)

Figure 5.11: Secondary motion in a square duct using the cubic eddy-viscosity model: (a) Full view and (b) zoom on the top right corner.

The turbulent viscosity has been evaluated using the standard equation:

$$\mu_t = C_\mu f_\mu \frac{k^2}{\epsilon} \,, \tag{5.3}$$

where C_μ is defined using the Craft *et al.* (1996) formulation. Unlike the standard model, the damping function f_μ is evaluated here according to Mompean's (1998) formulation.

Despite being of low magnitude ($\simeq$ 6% of the mean flow), the importance of the secondary motions is emphasised when considering particle trajectories, or streamlines, in the duct. Figure 5.12 shows the EASM $k-l$ predictions of eight streamlines in a 40 m long square duct and clearly highlights the effect of the secondary motions.

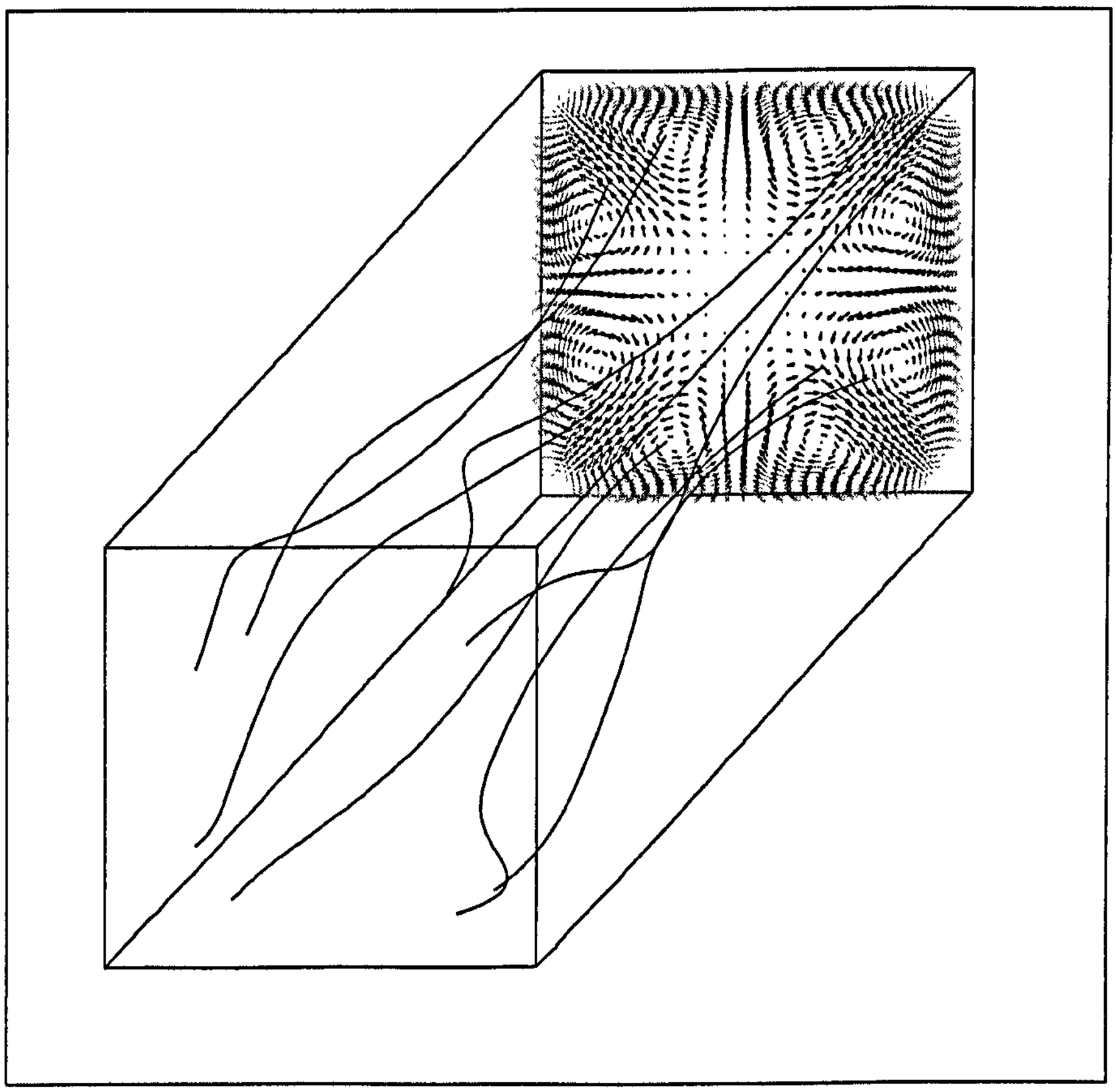

Figure 5.12: Scalar trajectory in a 40 m long square duct.

5.6 Conclusions

The two-dimensional channel flow shows that both the EASM and the cubic model are, unlike linear models, able to predict the anisotropy of the Reynolds stress tensor. Both EASM and cubic models are found to predict well the normal Reynolds stresses in the channel. In this case, the EASM predictions (in either a $k-l$ or $k-\epsilon$ framework) are found to be better than the cubic model's predictions.

The investigation of the side-injection channel flow clearly shows improved predictions (in terms of Reynolds stresses) of the cubic model (in either a $k-l$ or $k-\epsilon$ form) when compared to the EASM or linear eddy-viscosity models. The cubic model is also found to predict well the peak velocity in the channel but has lower accuracy nearer to the inlet wall. This case illustrates the potential of the cubic model in predicting flows that exhibits extreme streamline curvature. The EASM predictions only show in this case minor prediction improvements when compared with linear eddy-viscosity models.

For the backward-facing step excellent agreement of the separation-bubble length has been found for predictions of the EASM (less than 3% relative error) and cubic model (less than 1% relative error) in a $k-\epsilon$ framework.

Finally, unlike linear models, both EASM and cubic models have been able to predict (with the appropriate damping function) Prandtl's secondary motions in a straight square duct.

In the four cases tested, the EASM and the cubic eddy-viscosity models have shown increased accuracy when compared with their respective linear models ($k-l$ and $k-\epsilon$).

The four cases include some of the common flow features encountered in complex flow configurations. It thus might be expected to find similar predictive accuracy improvements when the EASM and cubic models are compared to their linear equivalent for room-ventilation problems.

Chapter 6

Experimental work: Layout and setup

6.1 Introduction

To test the turbulence models introduced in Section 3.2 for room-ventilation cases, a suitable experimental layout needs to be considered. The aim of this experimental work is to provide a set of accurate and realistic data in a ventilated office.

When considering the ventilation of a room, or an office, parameters such as the motion of the people in the room, their breathing patterns, or the influence of the sun on the windows affects the overall flow patterns. The CFD simulation of such a realistic room is possible but unless the problem is accurately defined, numerical results would depend on the whole CFD code rather than on the accuracy of a particular turbulence model. An accurate problem definition is key to assess the performances of a particular turbulence model.

The turbulence models introduced in Section 3.2 appear to be accurate when used on simple benchmark flows (for which they are calibrated *c.f.* Chapter 5). To further demonstrate their potential for the prediction of ventilation flows, some careful attention to the definition of the experimental model is required.

6.2 Experimental model

The experimental work was intended to provide velocity, temperature and pollutant concentration measurements in a typical ventilated office. The investigation has been carried out for the two main ventilation strategies introduced in Chapter 2: Displacement- and mixed-ventilation. Each ventilation strategy, or layout, has been tested for a range of inlet temperatures and ventilation rates. The overall layout and furnishing of the room, ventilation aspects and thermal aspects are key to the definition of the experimental model and are discussed below.

6.2.1 Overall layout and furnishing of the room

Since the test room aims to represent a typical working office, it has been decided that it would include two desks, a filing cabinet and a DIN man (idealised model of a working person). The definition of the DIN man is further discussed in Section 6.2.3. Figure 6.1 gives the overall dimensions of the room and its furniture. The furniture presented here have been idealised for cartesian grid CFD modelling and has smooth surfaces. No air exchange is observed between the inside and outside of each furniture block.

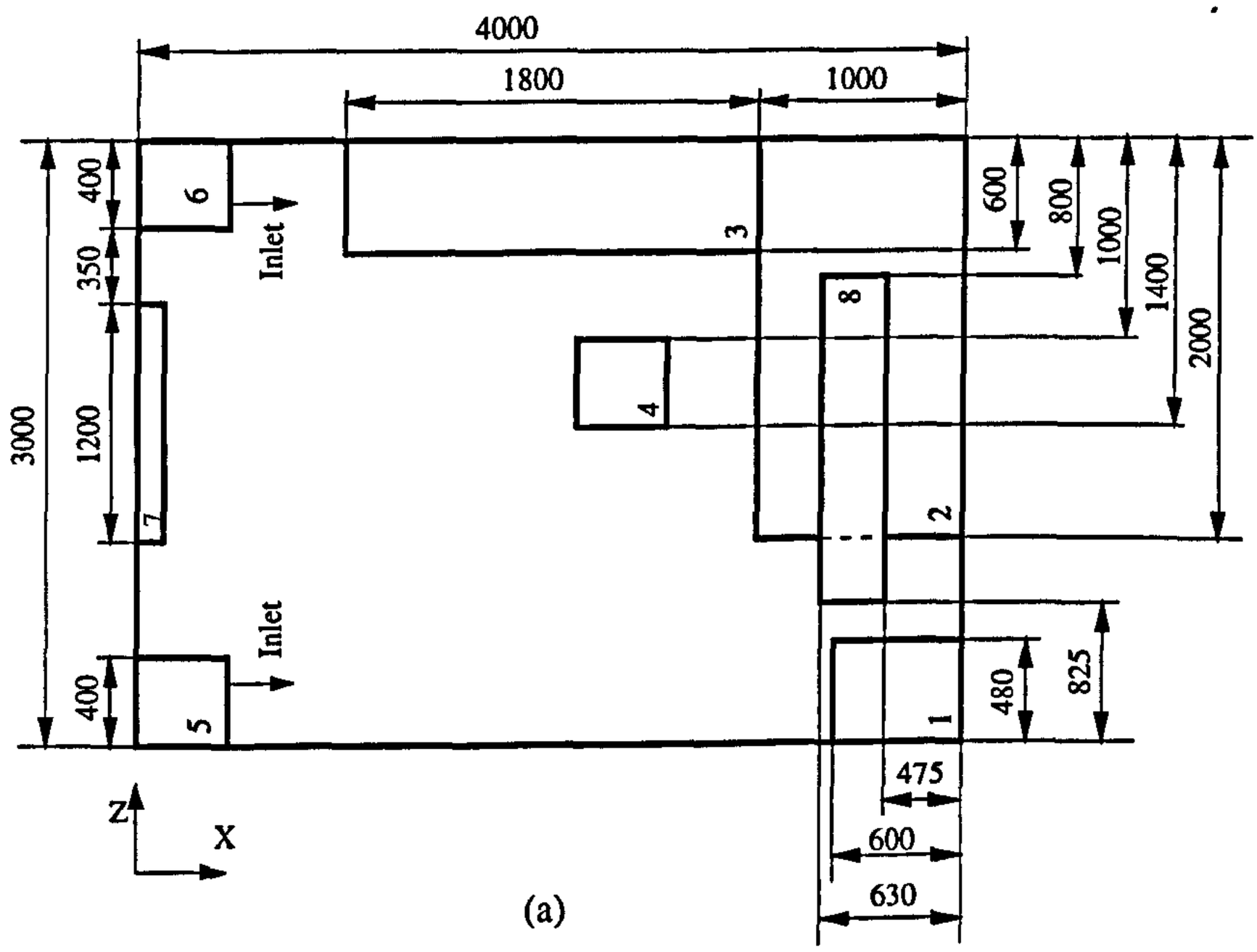

(a)

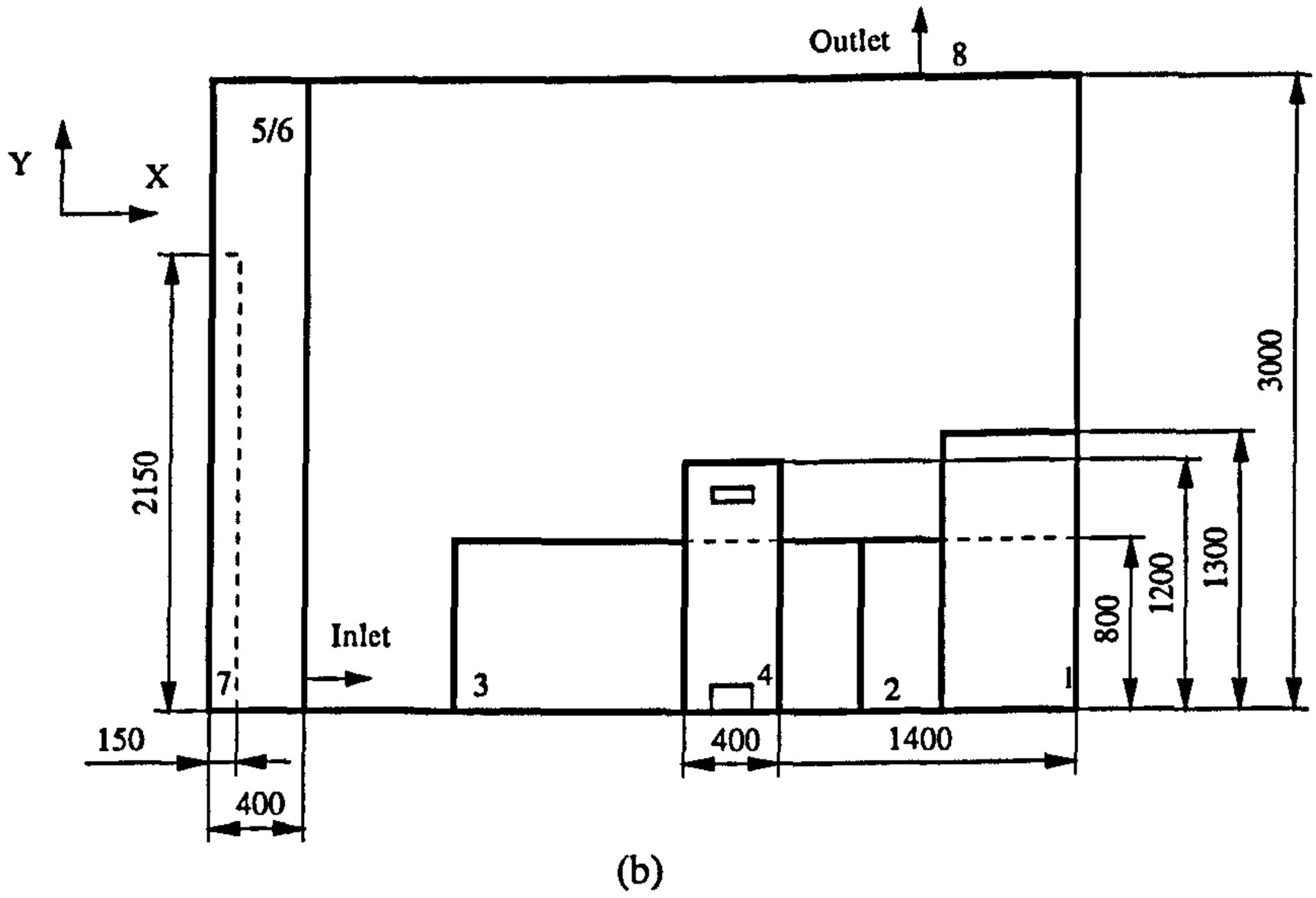

(b)

Figure 6.1: Overall view of the test room: (a) Top and (b) side view of the room layout. 1: Filing cabinet, 2 & 3: desks, 4: DIN man, 5 & 6: Inlet ducts, 7: Door and 8: Outlet. Dimensions in *mm*.

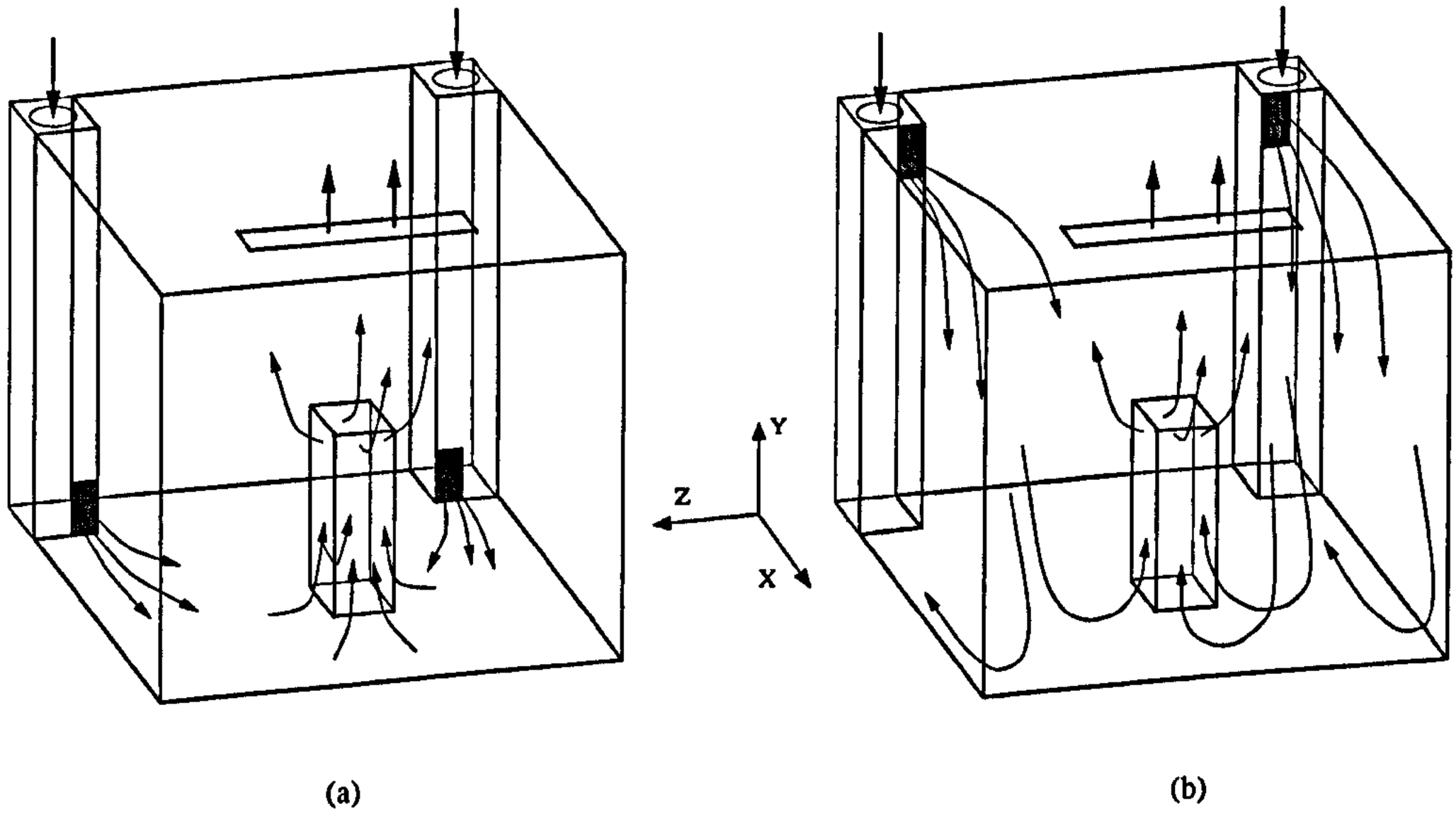

Figure 6.2: Ventilation layout and expected airflow pattern for the (a) displacement-ventilation and (b) mixed-ventilation layout.

6.2.2 Ventilation aspects

Ventilation involves a vast number of parameters and, it is intended to cover in this section the following three main points: The ventilation strategy, the inlets and the outlet.

To satisfy ventilation requirements, two separate inlets located in two corners of the test room are used. Figure 6.2 shows the position of the 150 by 400 mm inlets with their expected flow patterns for the displacement- and mixed-ventilation layouts.

Figure 6.3 illustrates the variety of diffusers commonly found in room ventilation. Each induces a different flow pattern. Diffuser-exit flows are non-uniform and so difficult

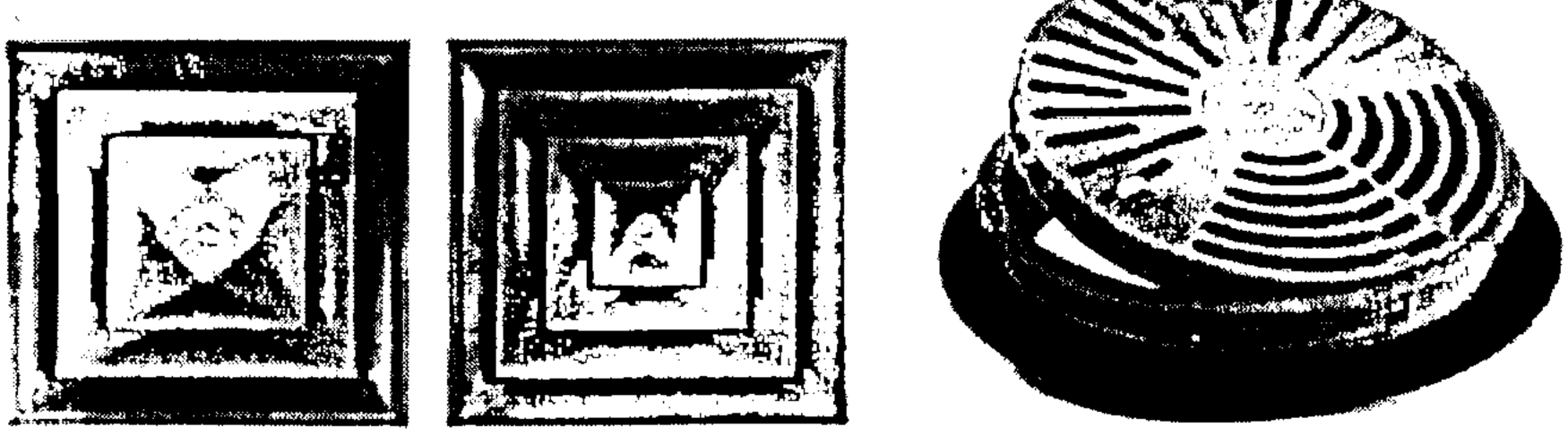

(a) Ceiling diffusers

(b) Floor diffuser

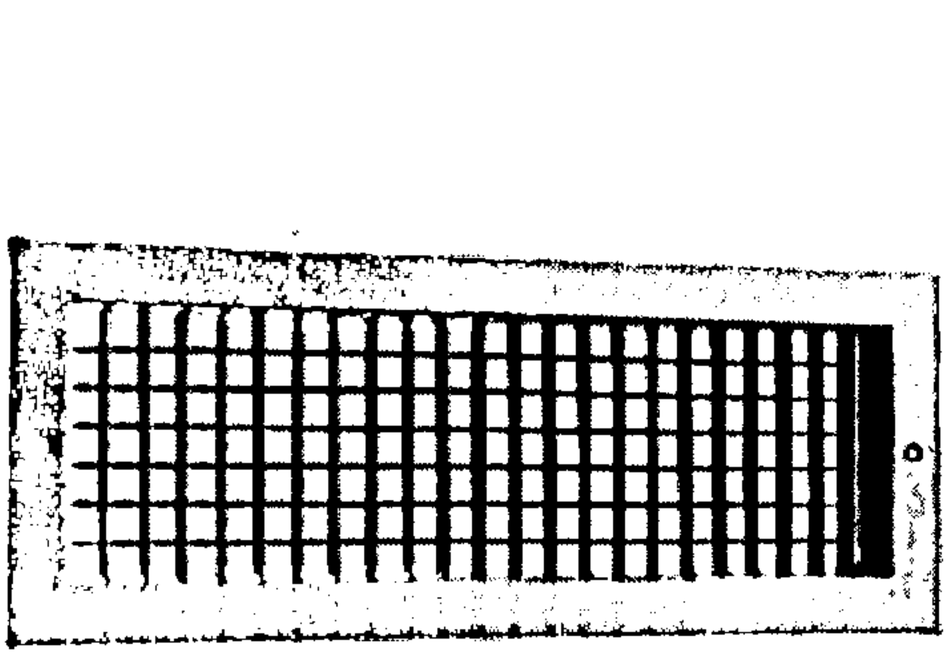

(c) Grille diffuser

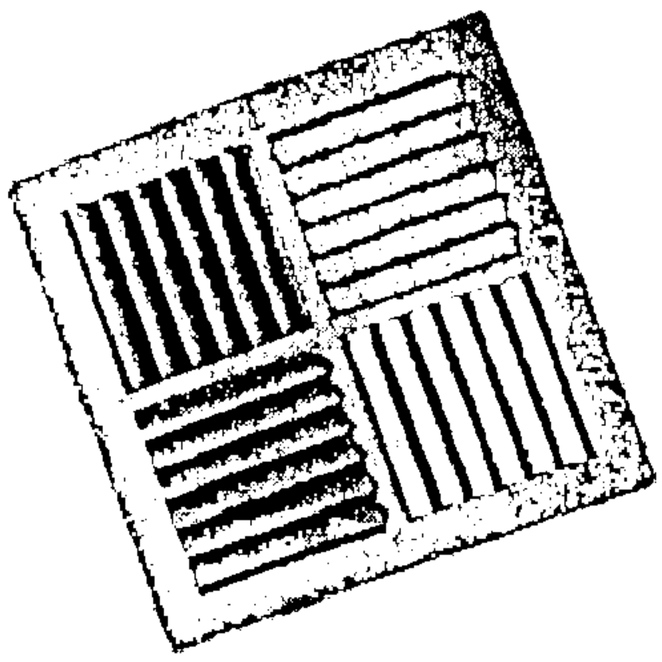

(d) Multidirectional diffuser

Figure 6.3: Various diffusers.(a,b):"www.price-hvac.com", (c):"www.airtechproducts.com" and (d): "www.poltech.com.au".

to numerically model (Srebric and Chen (2001)). Therefore, here, it has been decided to represent diffusers using a low-air-resistance fabric. The advantage of using a fabric diffuser is that it generates a uniform inlet velocity profile which can be accurately and easily modelled by a CFD code.

The inlet volume flow rate is measured using a 50 mm orifice flowmeter as shown by Figure 6.4 (b). Using the valve shown in figure 6.4 (a), it is possible to adjust the differential pressure ($\Delta_P = P1 - P2$) across the orifice plate and therefore, control the inlet volume flow rate. Assuming an air-tight system, this mode of regulation enables

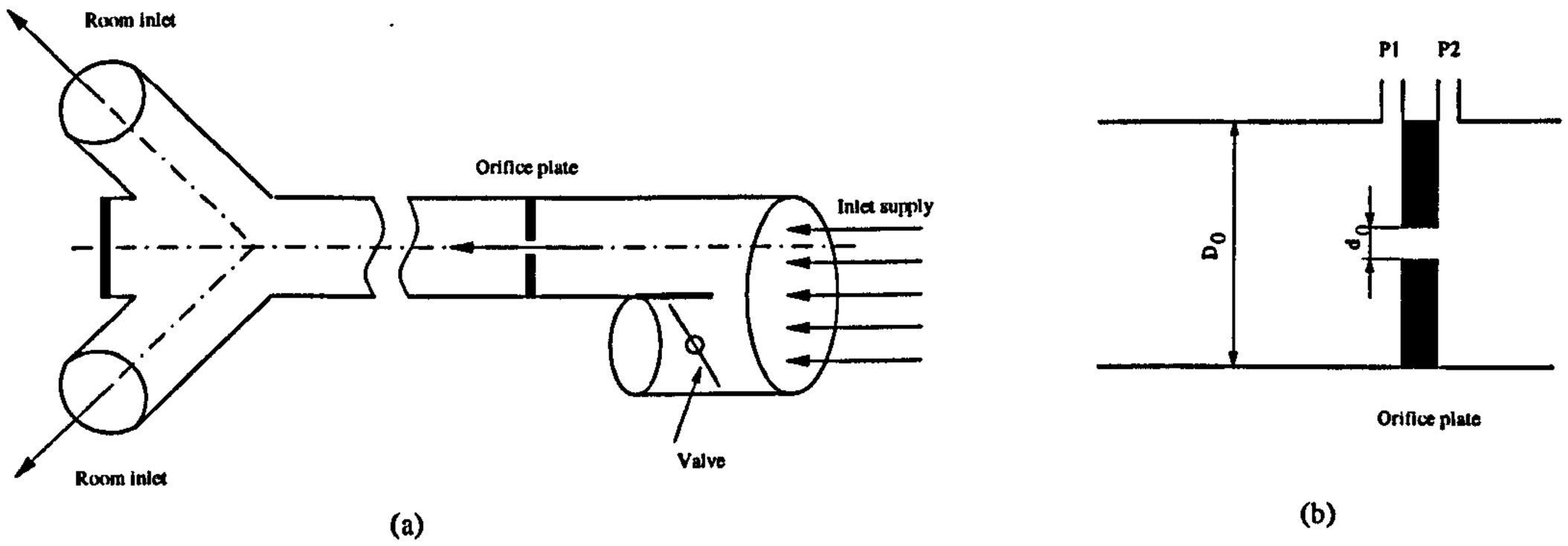

Figure 6.4: (a) Inlet duct system and (b) details of the orifice plate.

an accurate control of the volume flow through the orifice. To supply air to both inlets, a split in the main inlet duct downstream of the orifice plate is used. This split implies that the correct air flow rate is carried through the room inlets but does not ensure an equal air split flow between the two inlet ducts. Some differences have been recorded between the two room inlets and are discussed in Chapter 7.

Calculations of flows through orifice flowmeters are discussed in ASME (1971) and ISO 5167-1 (1991). In the present case, it is critical to determine the volume flow rate (V_0) that passes through the orifice at a given differential pressure (Δ_P). The more up-to-date ISO 5167-1/Amd.1 (1998) calculations on orifice flowmeters use:

$$V_0 = \frac{D_c\, a\, \sqrt{2\rho\Delta_p}}{\rho\sqrt{1-(d_0/D_0)^4}}, \tag{6.1}$$

where d_0 is the orifice diameter ($0.05\ m$), D_0 the pipe diameter ($0.2\ m$), V_0 the volume flow rate through the orifice (m^3/s), ρ the density of air ($\simeq 1.22\ kg/m^3$), Δ_p the differential pressure (Pa), U the velocity ($m.s^{-1}$) and a the cross section area of the orifice (m). The position of the pressure taps affects the discharge coefficient D_c. Here corner

taps (see Figure 6.4 (b)) are used. The discharge coefficient is given according to the ISO 5167-1/Amd.1 (1998) standard by:

$$D_c = 0.5961 + 0.0261\left(\frac{d_0}{D_0}\right)^2 - 0.216\left(\frac{d_0}{D_0}\right)^8 + 0.000521\left(\frac{10^6\, d_0/D_0}{Re_{D_0}}\right)^{0.7} + \frac{d_0}{D_0}^{3.5}\left(0.0188 + 0.0063\left(\frac{19000\, d_0/D_0}{Re_{D_0}}\right)^{0.8}\right)\left(\frac{10^6}{Re_{D_0}}\right)^{0.3} + \frac{0.043\frac{d_0}{D_0}^4}{1-\frac{d_0}{D_0}^4}\left(1 - 0.11\left(\frac{19000\, d_0/D_0}{Re_{D_0}}\right)^{0.8}\right), \quad (6.2)$$

where Re_{D_0} is the Reynolds number based on the pipe diameter D_0. The calculations of V_0 at the different differential pressure used in the experiments are found in Table 6.1.

Owing to fluctuations in the inlet supply, located outside of the building, some pressure fluctuations have been observed at the orifice plate and hence, at the room inlet. Those fluctuations have been found to be of minor importance and are further discussed in Chapter 7.

Since the magnitude of the inlet flow for the whole experimental program is small (below 0.5 m/s) no extraction mechanism has been used at the room outlet. To check that there is a negligible pressure difference between the test room and the outside environment, the room pressure has been monitored. No fluctuations of the room's pressure are observed during the experiments. The outlet itself is a grille similar to the one shown in Figure 6.3 (c). Its dimensions and location in the test room are shown in Figure 6.1.

Displacement-ventilation					
Case number	Air change rate/hour	Differential pressure Pa	Volume flow rate m^3/h	Mean inlet velocity m/s	Inlet temperature K
01	1.0	24	31.91	0.07386	297.65
02	2.0	94	63.82	0.14772	295.35
03	4.0	379	127.64	0.29544	293.35
Mixed-ventilation					
04	2.0	94	63.82	0.14772	295.95
05	4.0	379	127.64	0.29544	293.35
06	5.0	589	159.55	0.3693	294.55

Table 6.1: Inlet velocity and temperature used during the experiments.

6.2.3 Thermal aspects

In many practical room-ventilation papers thermal conditions are inadequately described. In order to perform a successful CFD simulation in ventilated areas where the magnitude of the mean flow is small (typically below 1 m/s) and therefore highly sensitive to heat fluxes, reasonable knowledge of the thermal behaviour is required. Four thermal aspects of significant importance can be identified: The definition of the thermal boundary condition at the walls, the thermal fluctuations of the inlet, the thermal boundary condition of the DIN man and the distribution between radiant and convective heat.

Figure 6.5 shows that the test room (inner chamber) is a room within a temperature-regulated enclosure (outer chamber). Temperature regulation in the outer chamber enables a more steady wall thermal boundary condition, although, an adiabatic wall

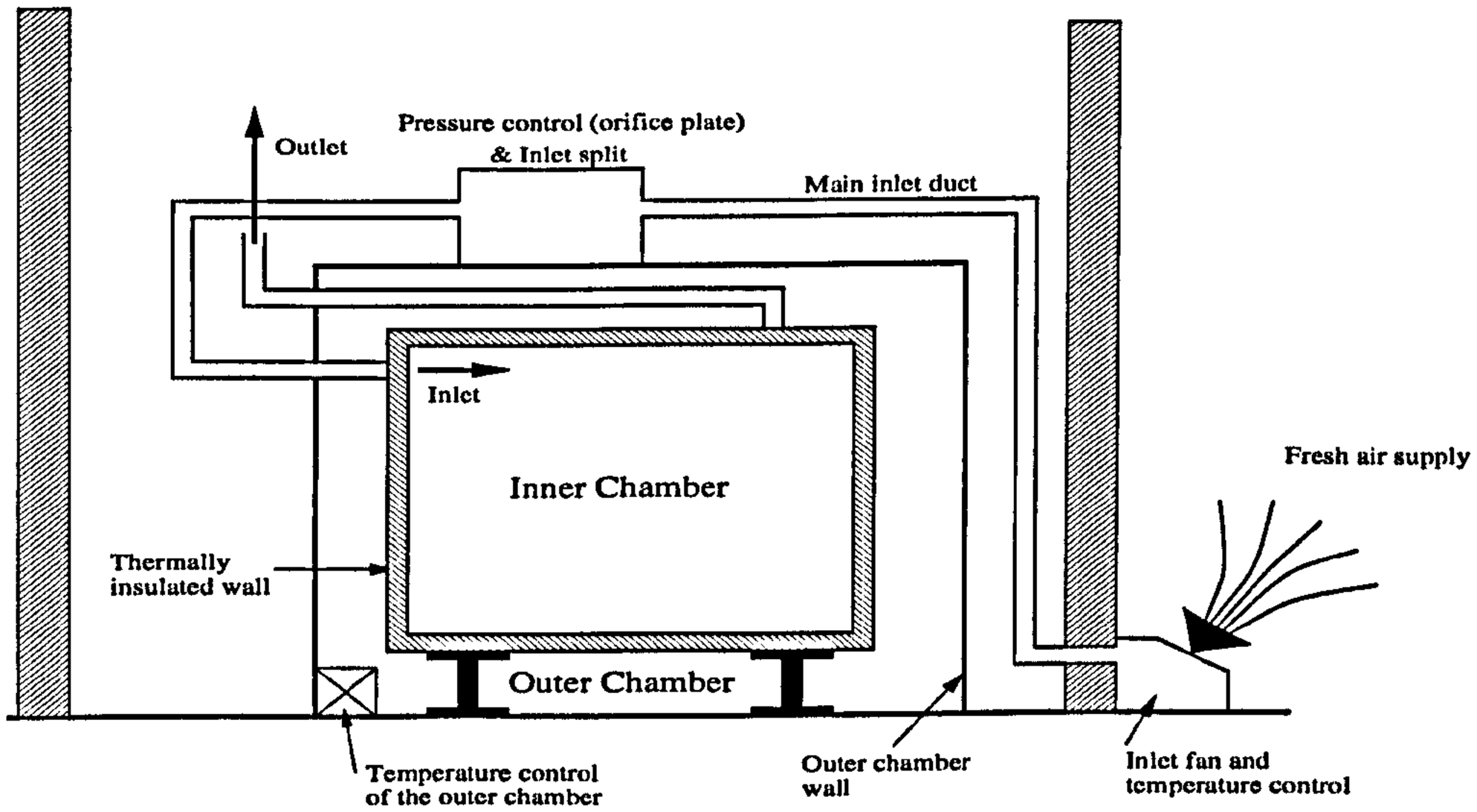

Figure 6.5: Schematic of the test facility.

boundary condition could not be reached. Owing to the high insulating properties of the inner chamber walls, a thermal inertia exists between the inner and the outer chamber. Any changes of inlet temperature for the inner chamber has been followed by a resting period of over twelve hours.

The inlet temperature is a key parameter in the definition of the room's thermal state. The use of a steady inlet temperature would greatly simplify the CFD modelling. Thus, to increase the steadiness of the inlet temperature, all inlet ducts have been thermally insulated. Temperature fluctuations at the fresh air supply located outside of the building (see Figure 6.5) influence the inlet room temperature. The fluctuations have been carefully recorded and are further discused in Chapter 7.

To allow displacement-ventilation studies, a heat source had to be introduced in the

test room. A DIN man is used to model the heat load produced by a human being. The standard DIN man design, as shown by Figure 6.6 (a), has the major drawback of being cylindrical and cannot be easily modelled using a Cartesian grid. The DIN man, however, has the advantage of being widely validated for room-ventilation purposes. To model a heat source that would satisfy both the CFD requirements of a cartesian grid and the need to be realistic, a square DIN man has been used (see Figure 6.6 (b)). The square DIN man is essentially a standard cylindrical DIN man covered with a square casing. In an attempt to mimic the airflow patterns for the standard DIN man, areas of openings at the top and bottom of the square DIN man are made similar to those for the cylindrical.

The heat load produced by a person depends on numerous factors (*i.e.* activity, metabolism, clothing, etc, ...). The average heat load of an individual ranges from 40 W/m^2 for a sleeping person to $\simeq$ 500 W/m^2 for highly demanding physical activities (ASHRAE (1997)). It is assumed here that a working person can be modelled by a heat load of 100 W. The DIN man used here contains three light bulbs. These generate exactly the 100 W required to model the heat load of a working person. The three light bulbs installed in the cylindrical DIN man are equally spaced along the vertical axis of the cylinder and hence do not match the typical heat distribution of a human body (60 W for the head and 40 W for the remainder of the body). No heat-load fluctuations have been observed during the experiments.

To simplify modelling, the effect of radiant heat has been minimised by avoiding test room lighting, and using a polished aluminium DIN-man casing. The white room walls (low emissivity) also contribute to low radiant heat. At 300 K, polished aluminium has

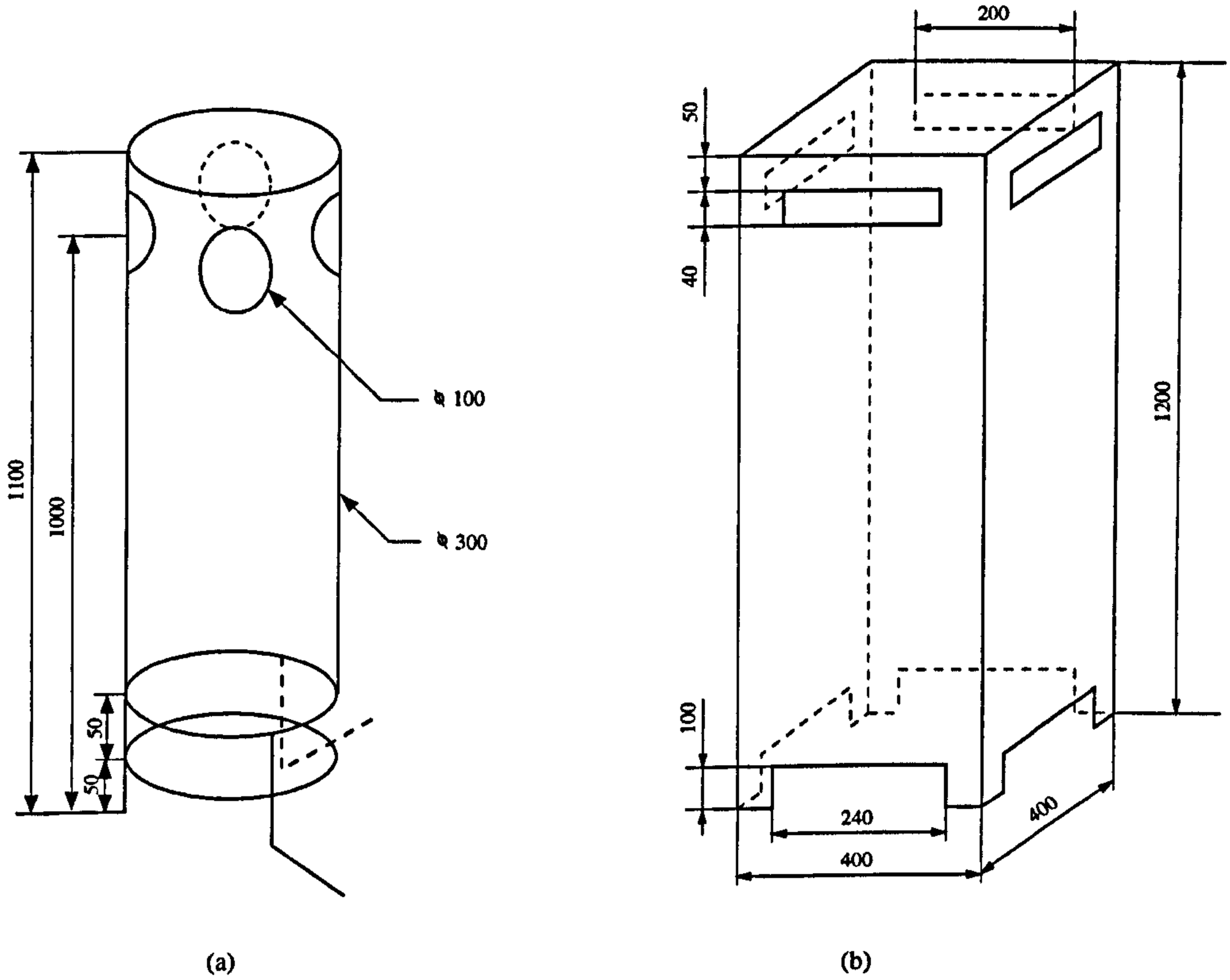

Figure 6.6: DIN man; (a) Standard cylindrical DIN man and (b) square cover.

an emissivity $\epsilon_s \simeq 0.04$. Using the Stefan-Boltzman law we have:

$$Q_{rad} = \epsilon_s \sigma (T^4 - T_{surr}^4) \tag{6.3}$$

where Q_{rad} the radiative heat flux (W/m^2), T the surface temperature (K) and σ the Stefan-Boltzman constant is equal to $5.67 \cdot 10^{-8}\ W/(K^4\ m^2)$. The average temperature of the square DIN man can be approximated from experimental data (see Section 7) to $\simeq$ 301 K. The lowest surrounding air temperature in the room is found to be above 293 K. The radiant heat flux from the square DIN man is thus lower than $Q_{rad} \simeq 1.9\ W/m^2$ or 3.71 W. Despite being non-negligible, this demonstrates the advantage of using this square DIN man to reduce radiant effects in the room.

6.3 Measurement Methods

The following sections introduce the various sensors used to monitor airflow temperature and velocity, wall temperature and pollutant concentration in the room. In particular the attention is drawn on the range of applicability, the limits, accuracy and overall layout of the sensors used.

6.3.1 Temperature and velocity measurements of air flows

To measure indoor flows, which are complex and vary both in magnitude and direction, the ASHRAE and ISO 7726 (1985) standards specify a minimum requirement for sensor range and accuracy. As shown by Table 6.2, the Dantec 54R10 omnidirectional transducers (see Figure 6.7) used for the measurement of airflow velocity and temperature, have been developed by Dantec to meet the ASHRAE and ISO 7726 (1985) standards.

The Dantec 54R10 is a Constant Temperature hot sphere Anemometer (CTA), having

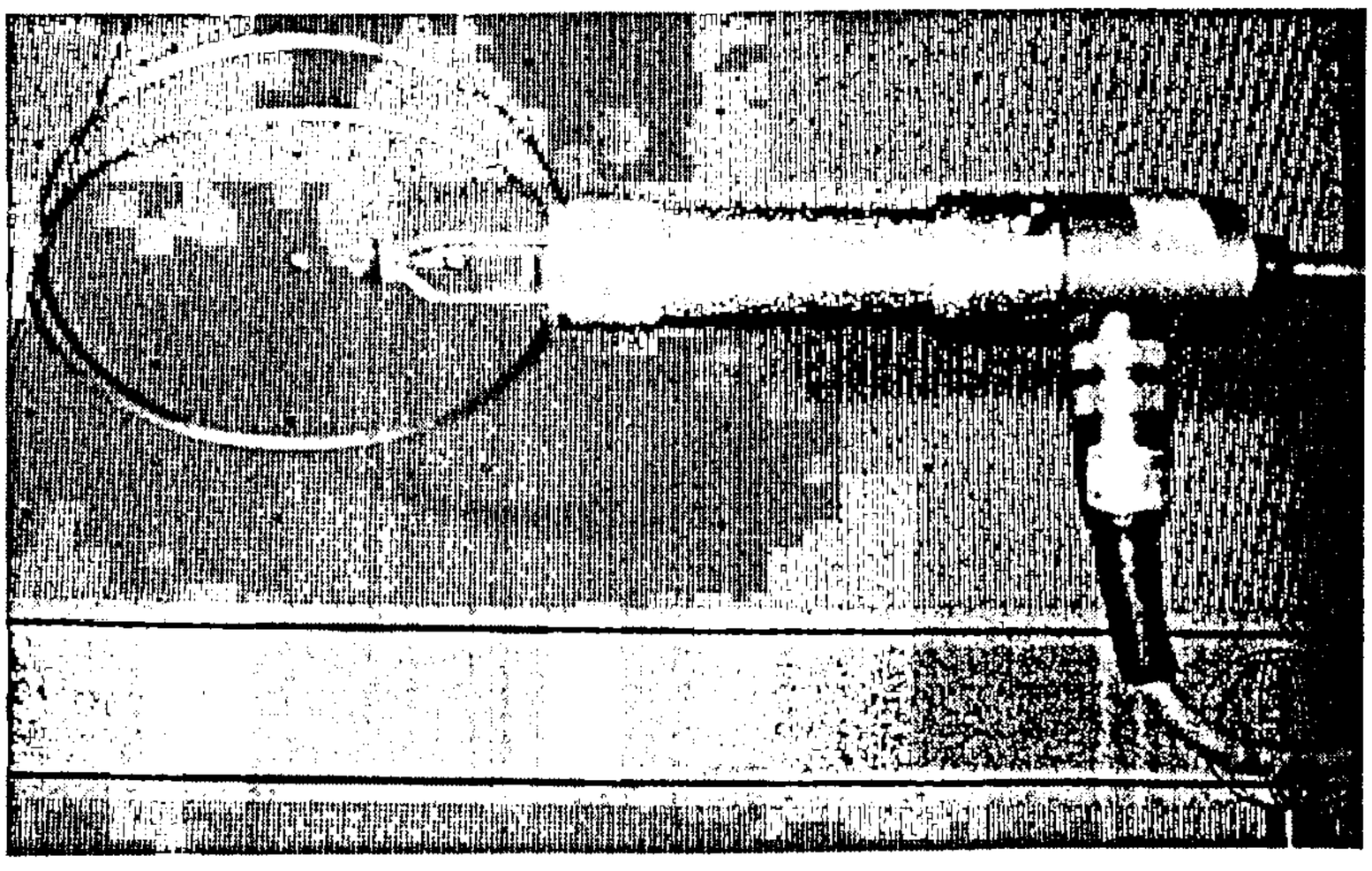

Figure 6.7: Dantec 54R10 transducer.

	Dantec 54R10	ASHRAE	ISO 7726	CAFS thermistors
Velocity range (m/s)	0. - 1.	0.05 - 0.5	0.05 - 1.	0.15-0.75
Accuracy (m/s)	$\pm$ 0.02	$\pm$ 0.05	$\pm$ 0.05	$\pm$ 0.025
Temperature Range $(°C)$	0. - 45.	-	-	0. - 100.
Accuracy $(°C)$	$\pm$ 0.2	-	-	$\pm$ 1.

Table 6.2: Specifications of the Dantec 54R10 anemometer and requirements of the ASHRAE and ISO 7726 (1985) standards.

similarities to a hot wire anemometer. In CTA, the wire, thin film or hot sphere is kept at a constant temperature and, the flow properties are related to the voltage required to maintain the wire (or sphere) at a constant temperature. Velocity is related to voltage through calibration curves. These are shown in Appendix B.

As showed by Figure 6.7, the Dantec 54R10 is physically large and quite intrusive. The Dantec 54R10 anemometer is used to measure velocities and temperatures at the locations specified by Figure 6.8. The flow in the vicinity of the DIN man is critical in this analysis. To minimise flow interference, smaller sensors have been used near the DIN man and at the DIN man's lower and upper openings (see Figure 6.9). These sensors manufactured by Cambridge Accusense Ltd. are thermistor based. They are less accurate than the Dantec 54R10 anemometers but are significantly smaller (typically $\simeq 10 \times 5 \times 1.5\ mm$). The low-profile CAFS sensors have been used with the ATM-24 interface board. More details on these sensors can be found at: "http://www.accusense.com/". Thermistors are based on the principle that the electrical resistance of a material is a function of its temperature. Thermistors use semiconductor materials which are known to have a large resistance variation over a small range of temperature. Details of the range of applicability and accuracy of the CAFS Accusense thermistors are found in Table 6.2.

6.3.2 Temperature measurements for walls

As discussed in Section 6.2.3, wall temperatures are key to the definition of the model. To gain information on wall temperatures, thermocouples have been used. Theoretical background on thermocouple applications can be found in Pollock (1991) or ASTM (1993). The thermocouples used here are known as T type. They use a combination of

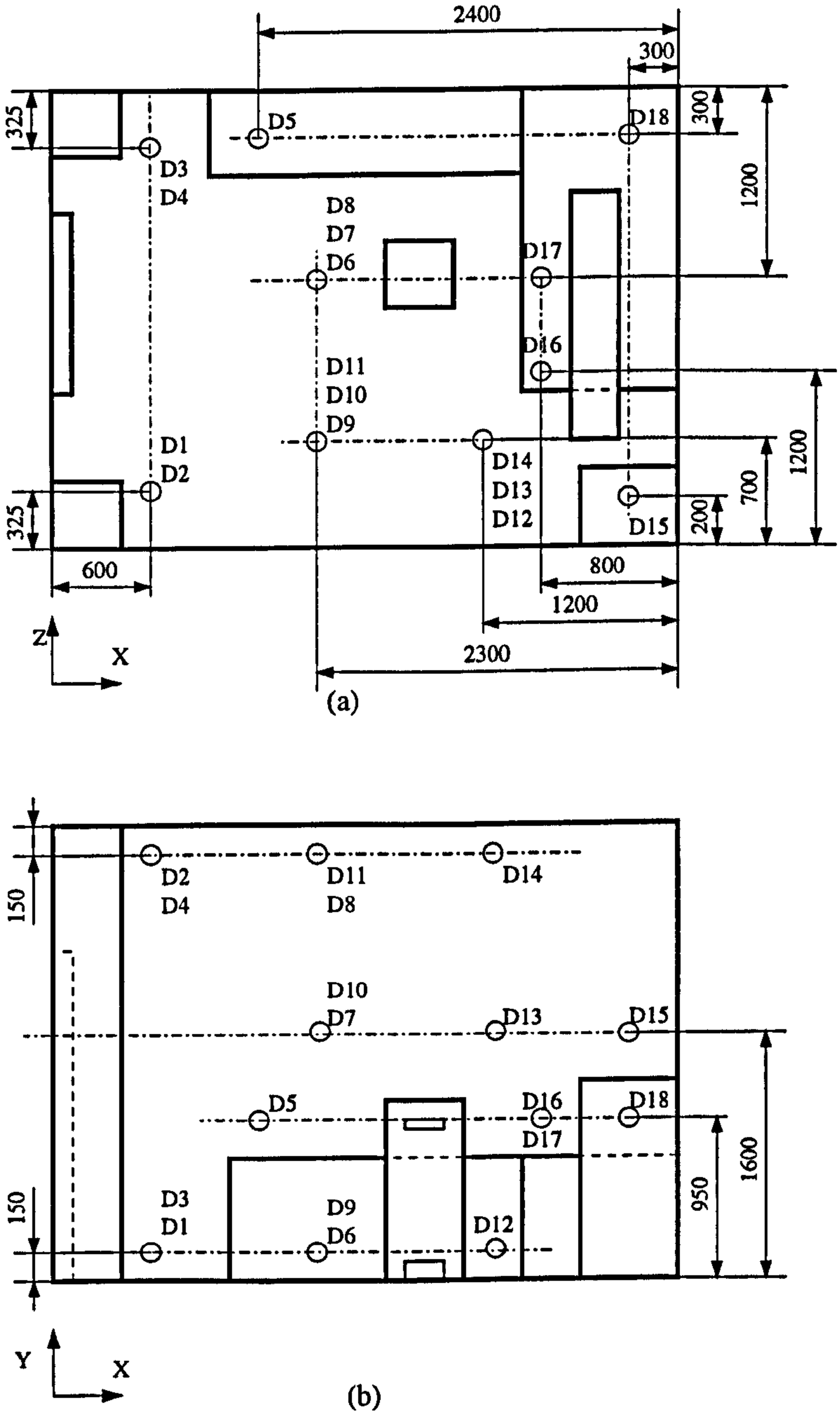

Figure 6.8: Location of the Dantec 54R10 transducers in the room. (a) Top view and (b) side view of the room. Dimensions in *mm*.

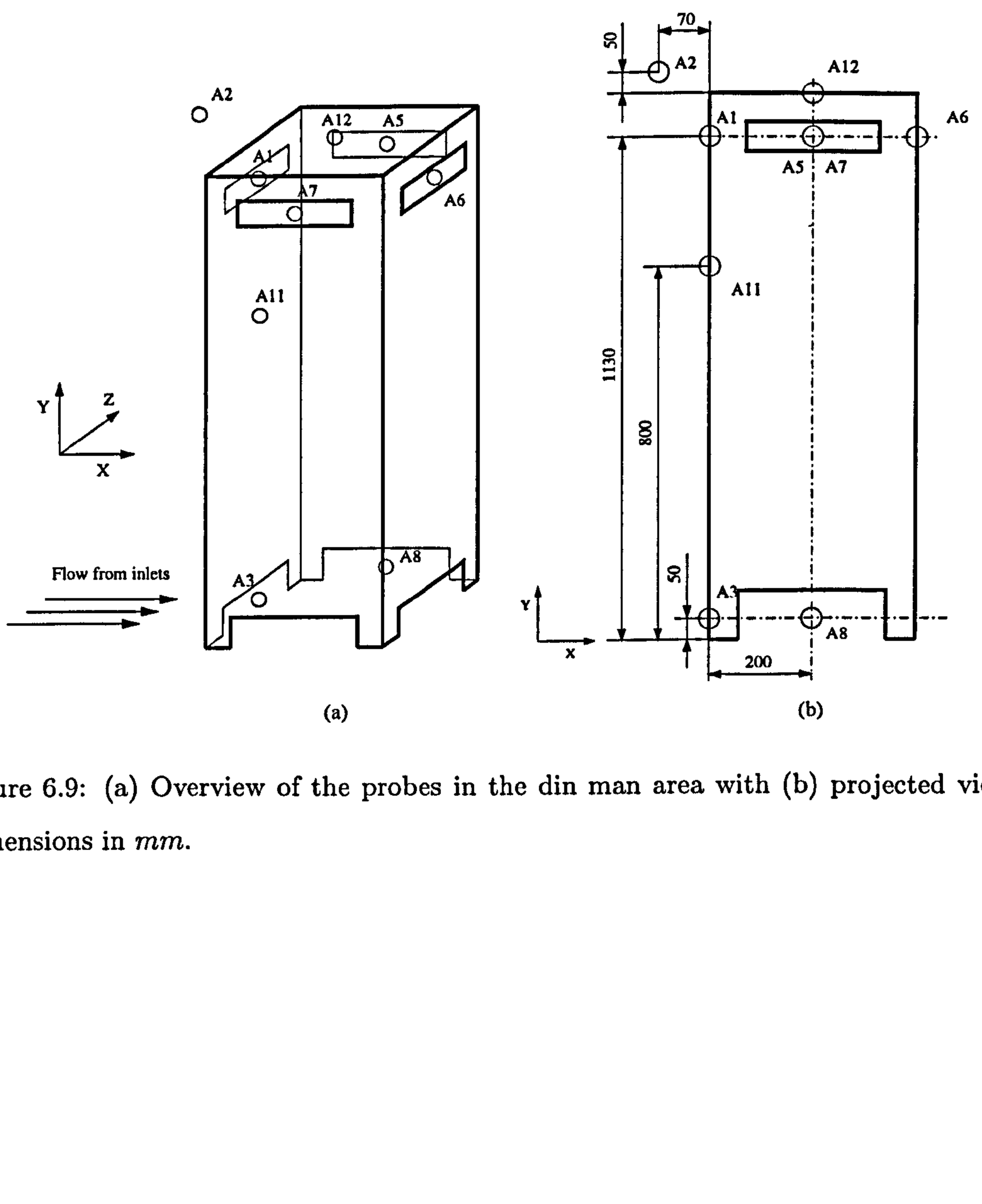

Figure 6.9: (a) Overview of the probes in the din man area with (b) projected view. Dimensions in *mm*.

copper and copper-nickel alloy. The T type thermocouple can operate between 3 and 640 K. At $\simeq 300$ K they are accurate to about ± 0.8 K.

As shown by Figure 6.10, a total of 27 thermocouples have been used to capture the thermal behaviour of the test-room's walls. To ensure that the temperature monitored by the thermocouple corresponds to the surface temperature and not the surrounding airflow temperature, some adhesive aluminium has been placed over the sensing part of the thermocouples. Another three thermocouples have been used to monitor the thermal stratification of the room air. The three thermocouples labelled $T28$, $T29$ and $T30$ are placed in the middle of the room (along the vertical $T21 - T25$ axis of Figure 6.10 (e) and 6.10 (f)) at a height of 0.75 m, 1.5 m and 1.8 m respectively.

6.3.3 Gas tracer device

The investigation of the diffusion of a pollutant source in the room is a key feature of the present work. The tracer gas, SF_6, chosen for the investigation is a non-toxic, chemically stable gas that can be detected to high sensitivity and is commonly used in room-ventilation measurements.

To mimic a breathing or even a smoking person, the pollutant source has been placed in the vicinity of the DIN man. To minimise flow disturbances at the upper opening of the DIN man, the pollutant source has been placed on top of the DIN man (see Figure 6.12) in a way that the pollutant itself would be entrained by the thermal plume.

The Innova multipoint sampler and doser type 1303 has been used in conjunction with the Innova multi-gas monitor type 1302 to supply and measure $SF6$ gas concen-

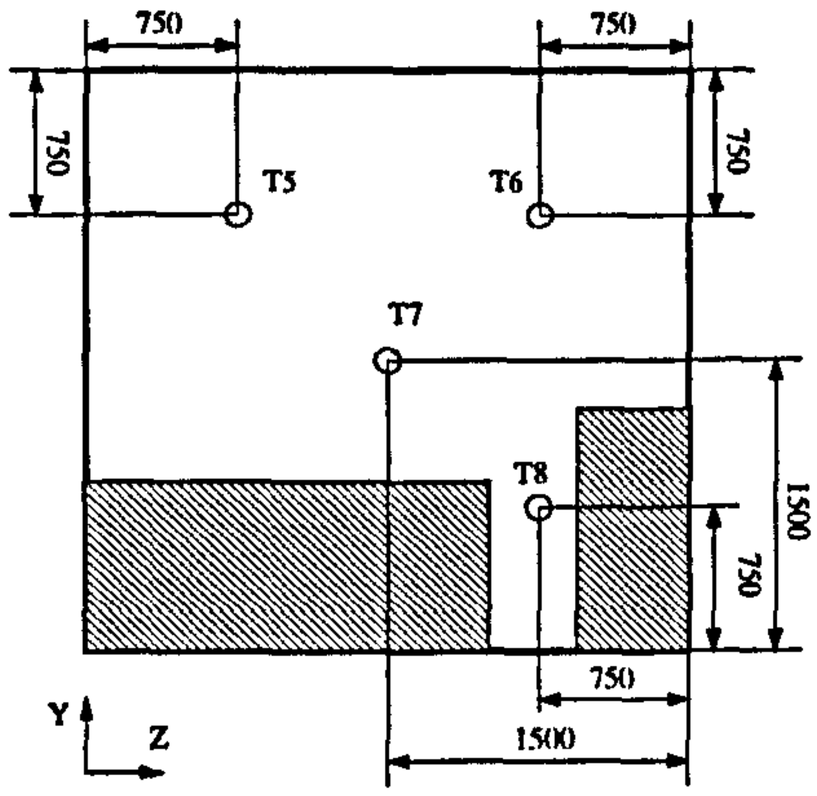

(a)

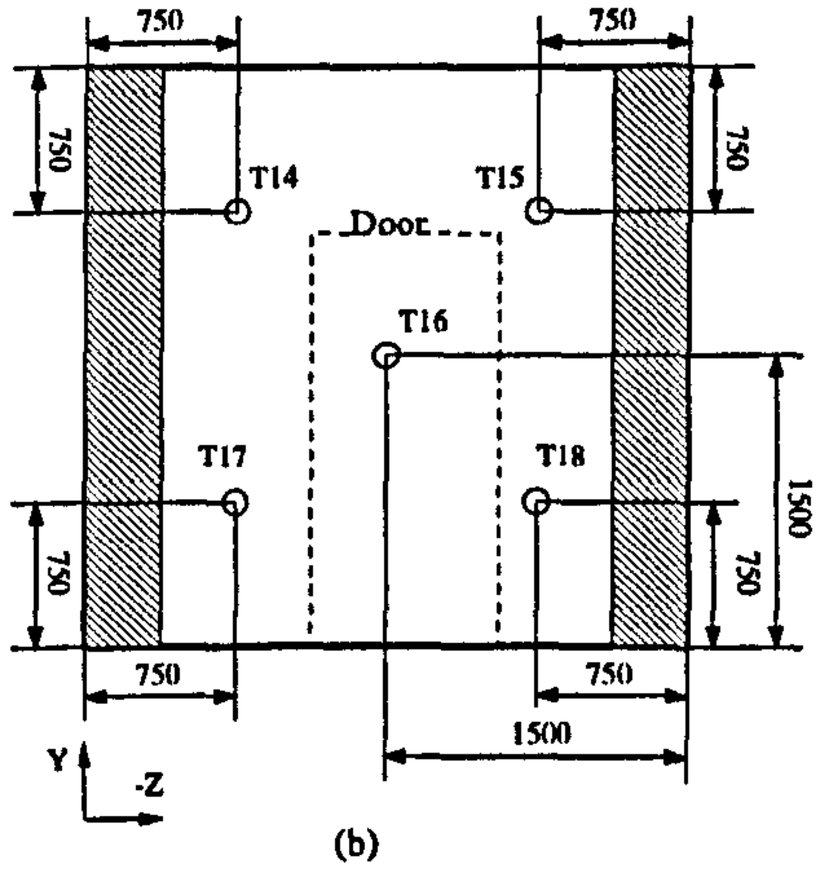

(b)

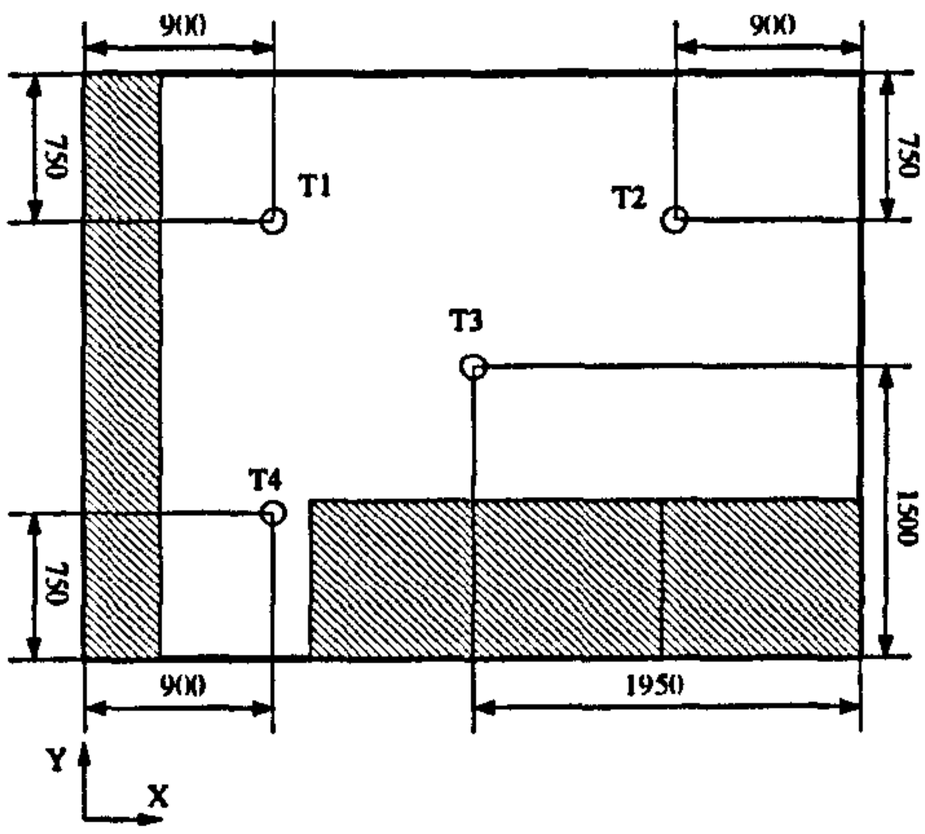

(c)

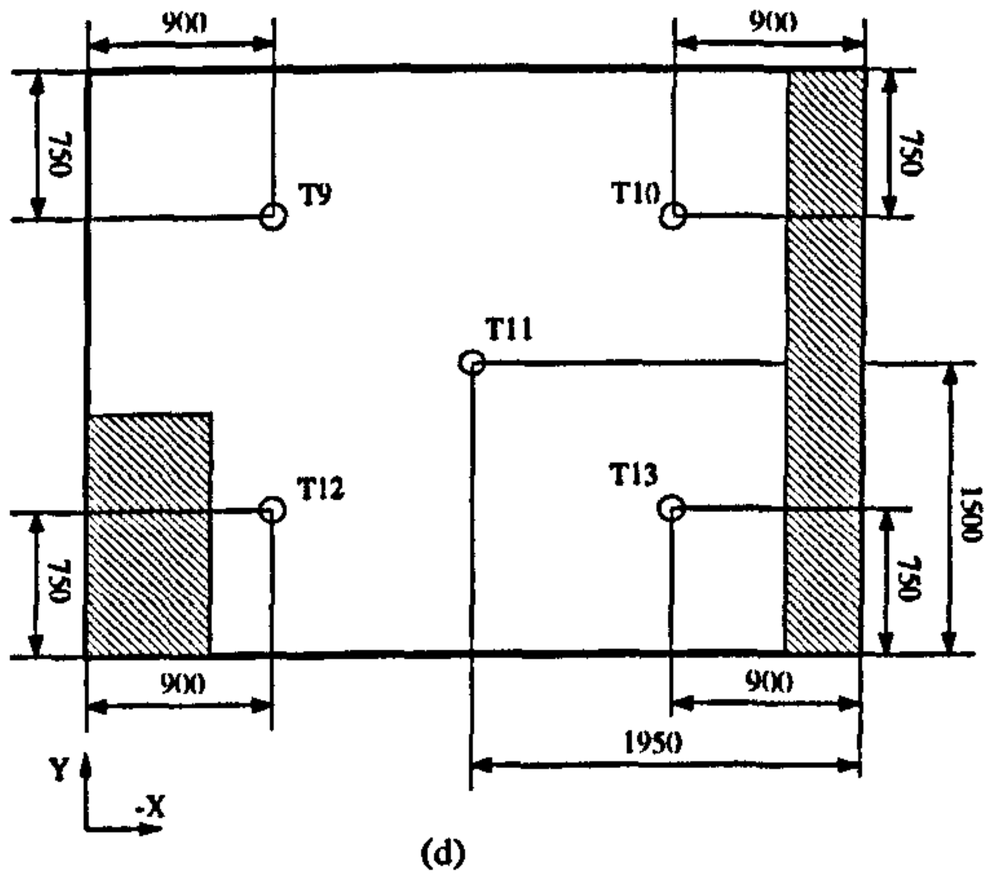

(d)

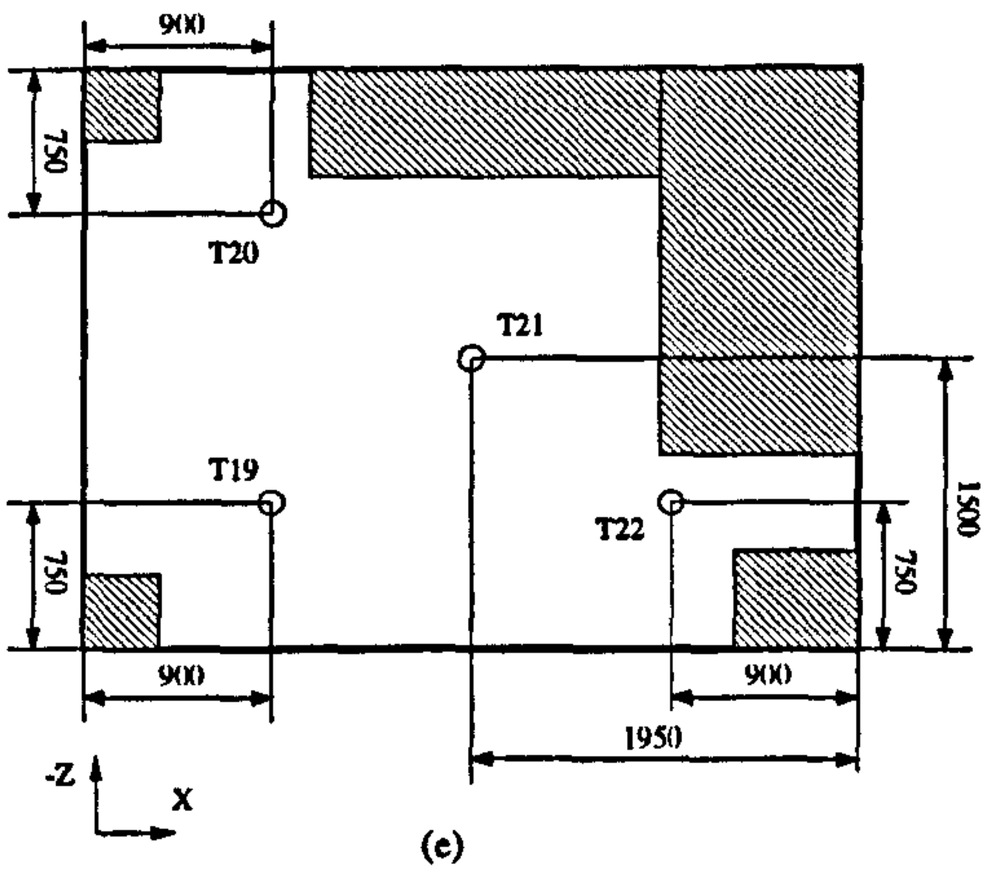

(e)

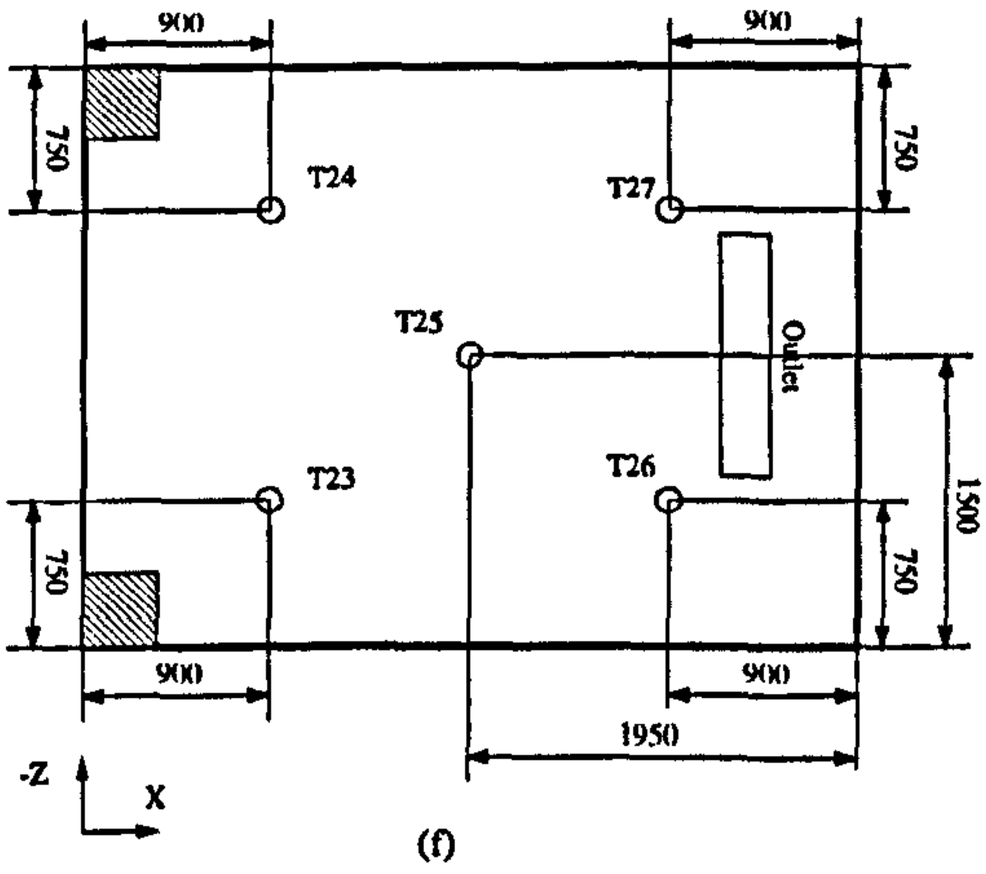

(f)

Figure 6.10: Layout of the thermocouple in the room (marked by o); (a) Back wall, (b) Front wall and door, (c) Left wall, (d) Right wall, (e) Floor and (f) Ceiling. The hatched areas represent the room's furniture. Dimensions in *mm*.

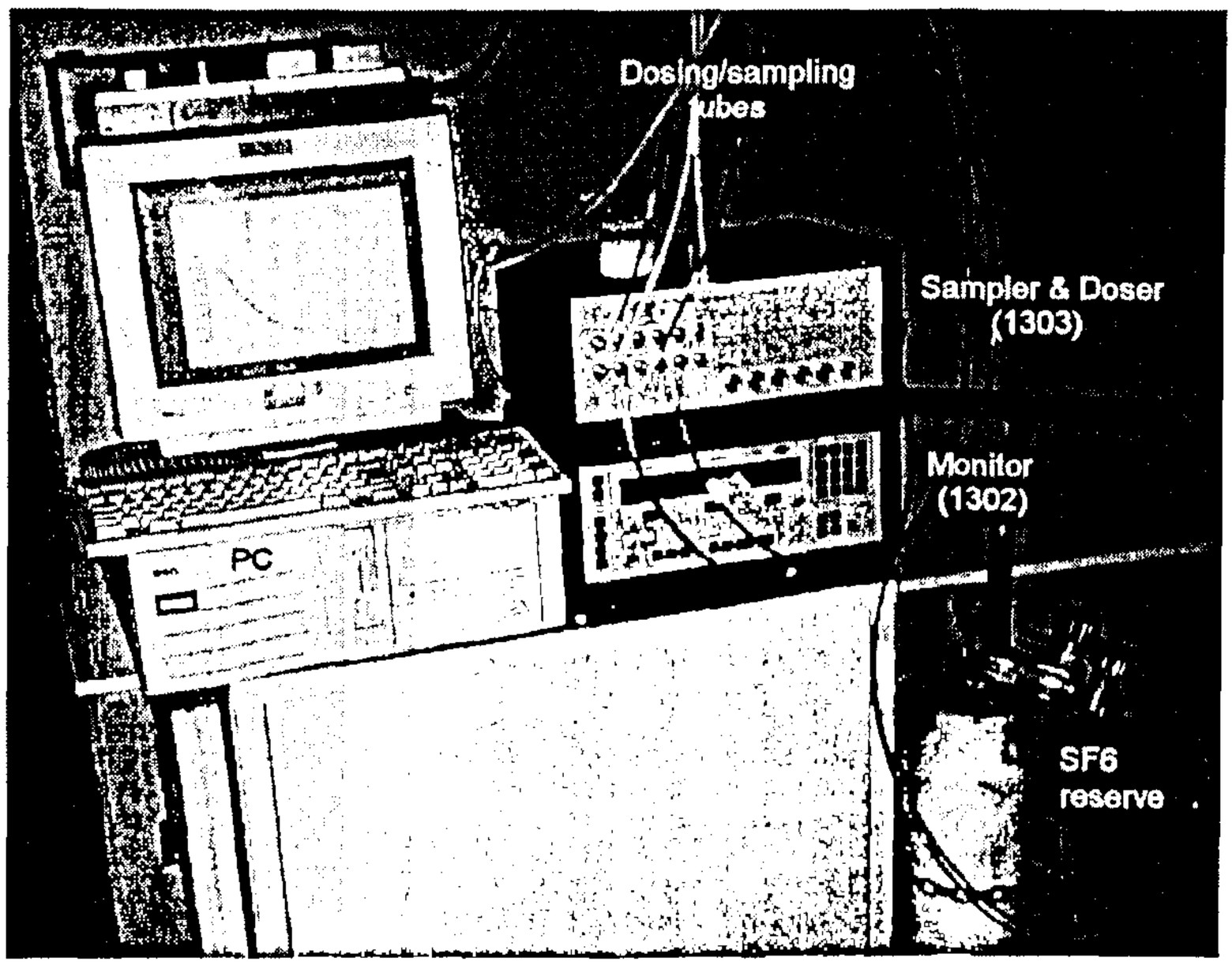

Figure 6.11: Gas tracer analyser.

tration in the room. Through a tubing system, the multipoint sampler and doser (1303) controls the dosing of SF_6 at one point in the room, and allows the measurement of SF_6 concentration in six locations. To enable the monitoring and processing of the data acquired the multi-gas monitor (1302) is used with a multiplexer and a PC. Figure 6.11 shows the multipoint sampler, doser and monitoring devices for which more details can be found at: http://www.innova.dk/products/1303/1303.html .

It has been decided to monitor the concentration of pollutant (SF_6) mainly in the breathing zone of a standing person (1.6 m from the floor). Figure 6.12 shows the position of the dosing and of the six measurement locations used during the experiment.

The system used was unable to supply a constant concentration of tracer gas in

the room. To build up a steady-state concentration a cyclic release of SF_6 has been used. The the amount of SF_6 released during each cycle has been calibrated on SF_6 measurements done at a particular sampling point in the room. Here, the concentration readings at the outlet of the room (GR in Figure 6.12) have been used as a reference to quantify the amount of SF_6 to be realease during the following cycle. The mutliplexer used does not enable the simultaneous sampling of the six locations. Each of the six channels are sampled sequentially at a rate of $\simeq 44\ s$ per channel. This sampling cycle implies that the sampling of the room outlet (the reference point used to evaluate the amount of SF_6 to be released) is only done once every $\simeq 264\ s$ (nearly 5 min). For the cases studied, 5 min corresponds to the air renewal of a minimum of 7% of the room. Owing to convection effects in the vicinity of the DIN-man and hence, of the SF_6 supply, the non-supply of SF_6 for over 5 min has been found to lead to the removal of a large proportion of SF_6 in the room. As a result a steady-state concentration of SF_6 is difficult to obtain (see Chapter 7 for further details).

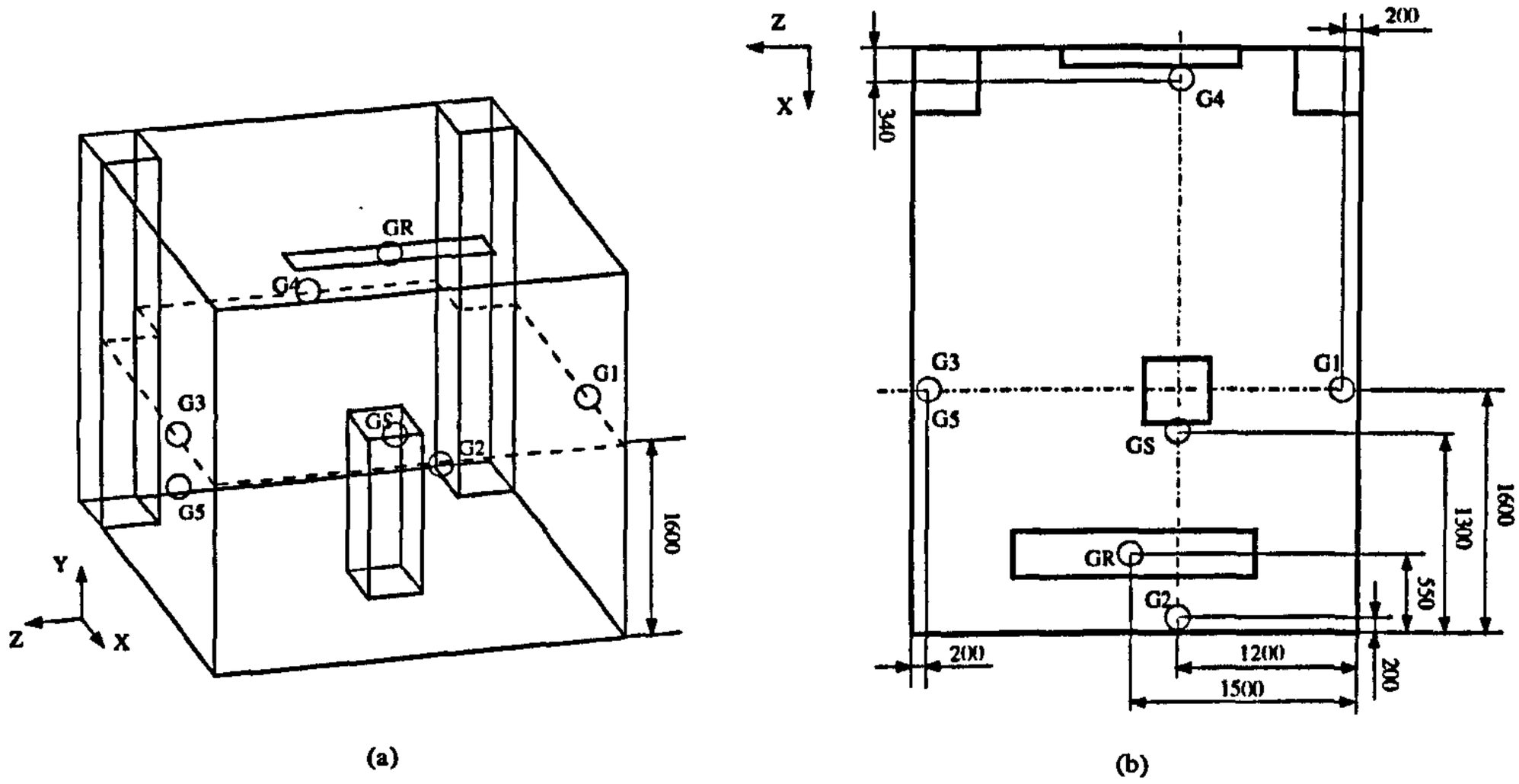

Figure 6.12: Probe layout for the gas tracer analysis marked by o: (a) Overview and (b) top view of the room. Dimensions in *mm*.

Chapter 7

Experimental results

7.1 Introduction

This Chapter presents the key measurements made on the test room introduced in Chapter 6. The experimental program was intended to give velocity, temperature and pollutant concentration data. Owing to the large amount of data generated, only Case 01 is presented in detail. Overall results for Case 02 to 06 are also presented here and in Appendices C and D.

The cases studied for the displacement-ventilation layout (Case 01, 02 and 03) correspond to ventilation rates of one, two and four air changes per hour. The cases (Case 04, 05 and 06) for the mixed-ventilation layout correspond to ventilation rates of two, four and five air changes per hour respectively (see Table 6.1 for details). Case 06 corresponds to the maximum ventilation rate that can be provided by the system using this configuration. The gas tracer analysis, a key feature in this work, is presented first.

7.2 Gas tracer analysis

The monitoring of temperatures and velocities can be achieved quickly (a few minutes) but, to analyse the dispersion of a contaminant source (SF_6) in the room, each test had to be carried out for periods of time exceeding four hours. Figure 7.1 illustrates the time required to conduct the experiments by plotting the time trace of SF_6 at the outlet of the room (GR) and at the sampling location G1 (see Figure 6.12) for Case 01. Similar time requirements are found when using the mixed-ventilation layout.

The concentration (C) given in Figure 7.1 is expressed in in mg/m^3 and not in ppm as discussed in Chapter 6. The conversion between ppm and mg/m^3 can be achieved using the following equation $C_{mg/m^3} = P\ MW\ C_{ppm}/R\ T$, where P is the air pressure ($mmHg$), MW the molecular weight (g), R the ideal gas constant and T the temperature (K). In cases 01, 02 and 03 the target concentration setting of 4 ppm corresponds to a concentration of $\simeq 23.89\ mg/m^3$. In cases 04, 05 and 06, the target concentration of 10 ppm corresponds to $\simeq 59.73\ mg/m^3$.

Figure 7.1 clearly reveals the two distinct phases of a gas tracer study. In the first phase, the SF_6 is supplied until a target concentration is reached. The SF_6 is dosed once every $\simeq 264\ s$ (see Chapter 6), the time required for the monitoring device to analyse each of the six sampling locations and evaluate the amount of SF_6 needed to be released to reach a steady concentration in the room. When considering Case 01, the time for one dosing sequence represents the air renewal of $\simeq 7.33\%$ of the room. This time is sufficient for the tracer gas to be entrained by the thermal plume of the DIN man towards the outlet of the room. Thus, a steady-state concentration is difficult to reach. In the second phase, the supply of SF_6 is cut off and the rate of decay of SF_6

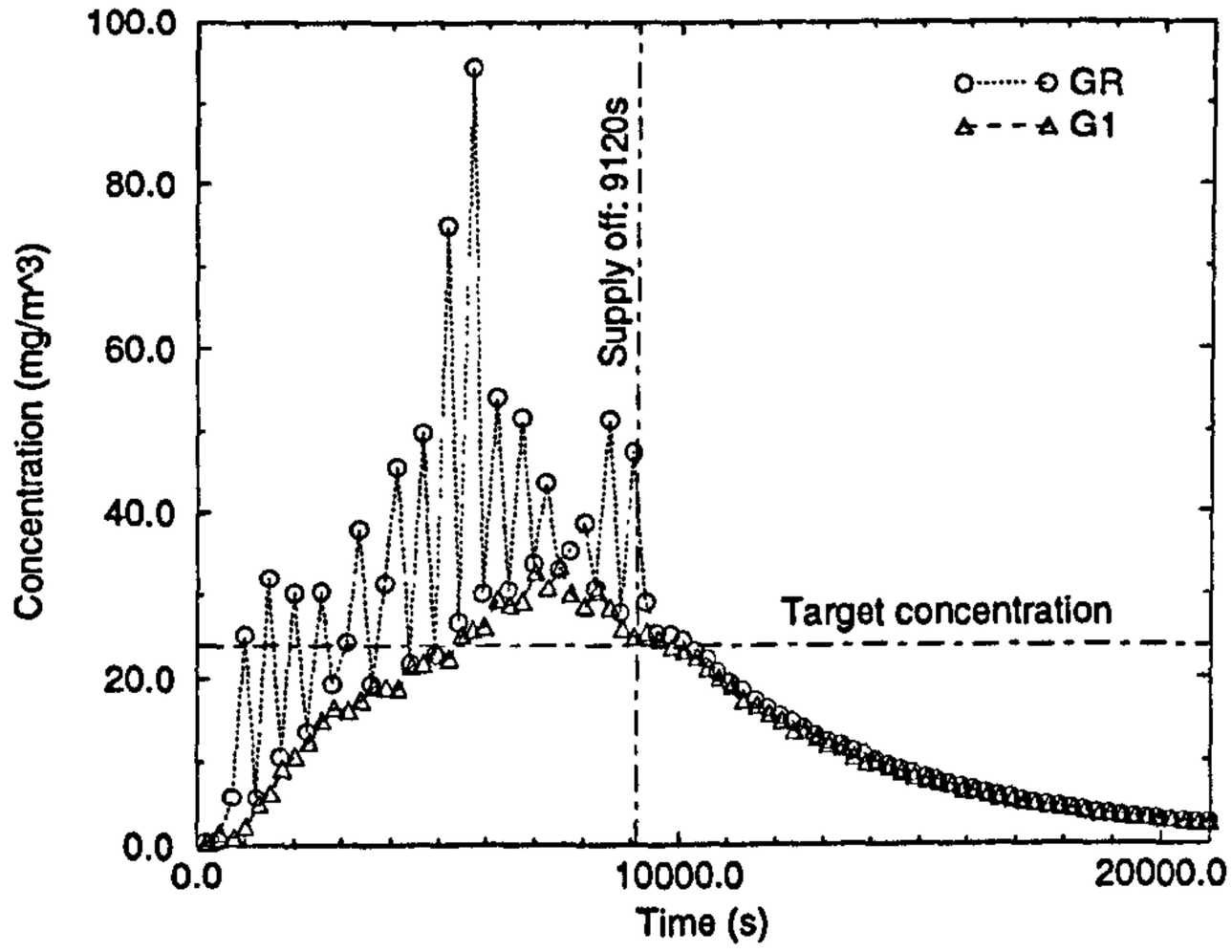

Figure 7.1: Gas concentration in the room for Case 01.

is monitored. The time-decay of SF_6 has been conducted when a quasi-steady-state is reached. For higher ventilation rates (cases 04, 05 and 06) a higher SF_6 target concentration (10 *ppm*) was required.

Figure 7.2 and 7.3 plot the time-decay of SF_6 at the various sampling locations for the displacement-ventilation and mixed-ventilation cases respectively. The results shown in Figure 7.2 and 7.3 are non-dimensionalised by the time required to renew the air in the room and by the target concentration. The time $t = 0$ is used in Figure 7.2 and 7.3 to indicate the start of the SF_6 decay. Those times are taken at $t_{g-01} = 9120\ s$, $t_{g-02} = 9800\ s$, $t_{g-03} = 7300\ s$, $t_{g-04} = 6300\ s$, $t_{g-05} = 6600\ s$ and $t_{g-06} = 9000\ s$ from the beginning of each test run for cases 01 to 06 respectively.

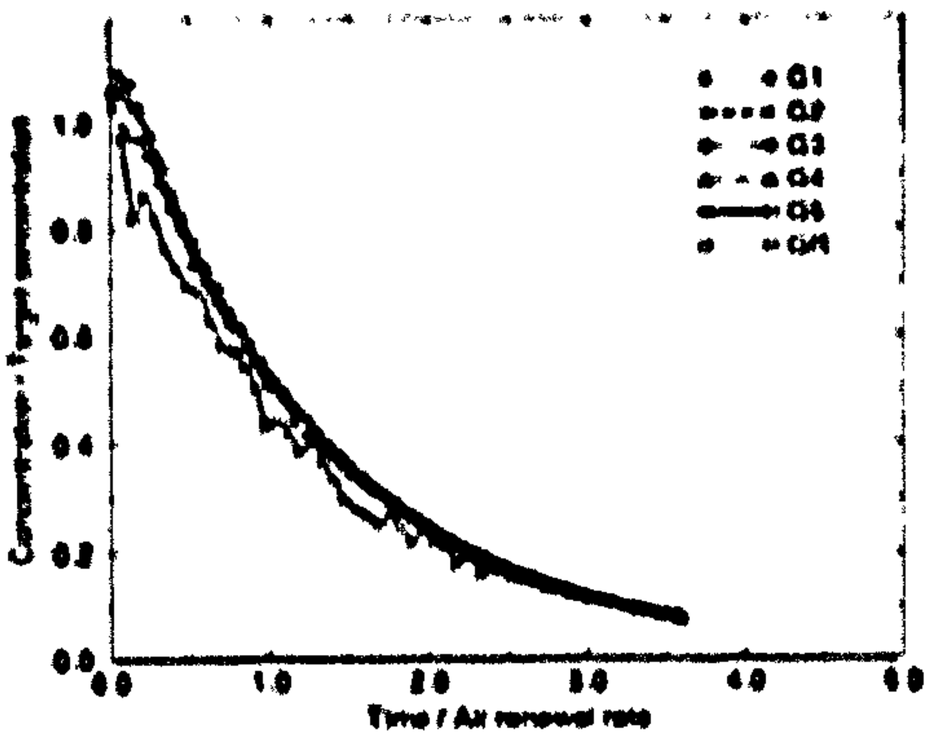

(a)

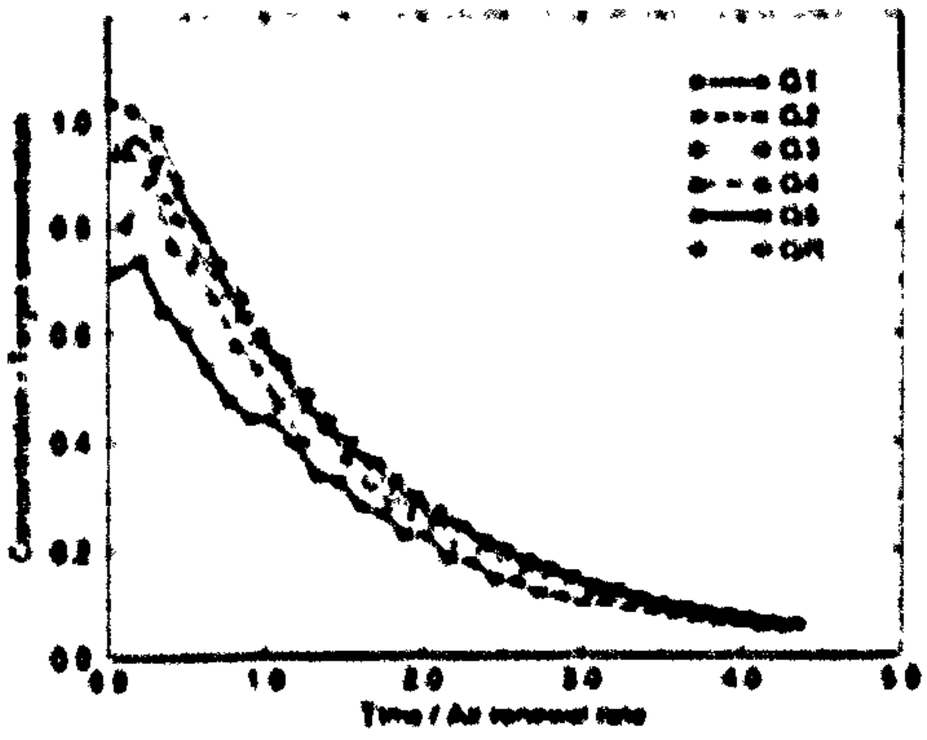

(b)

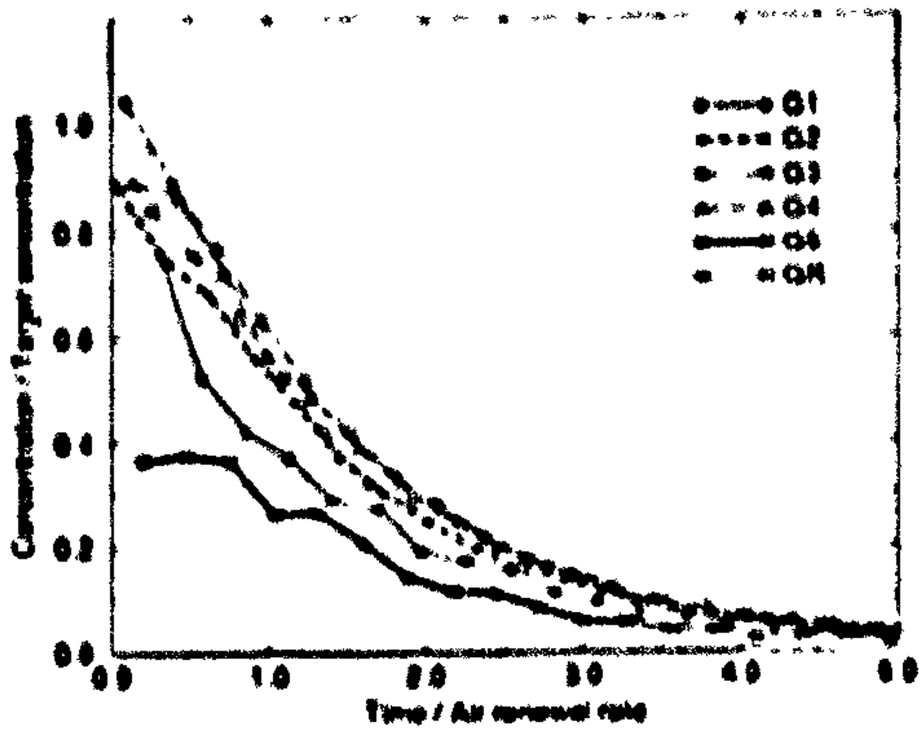

(c)

Figure 7.2: Time-decay of gas concentration in the room for (a) Case 01, (b) Case 02 and (c) Case 03.

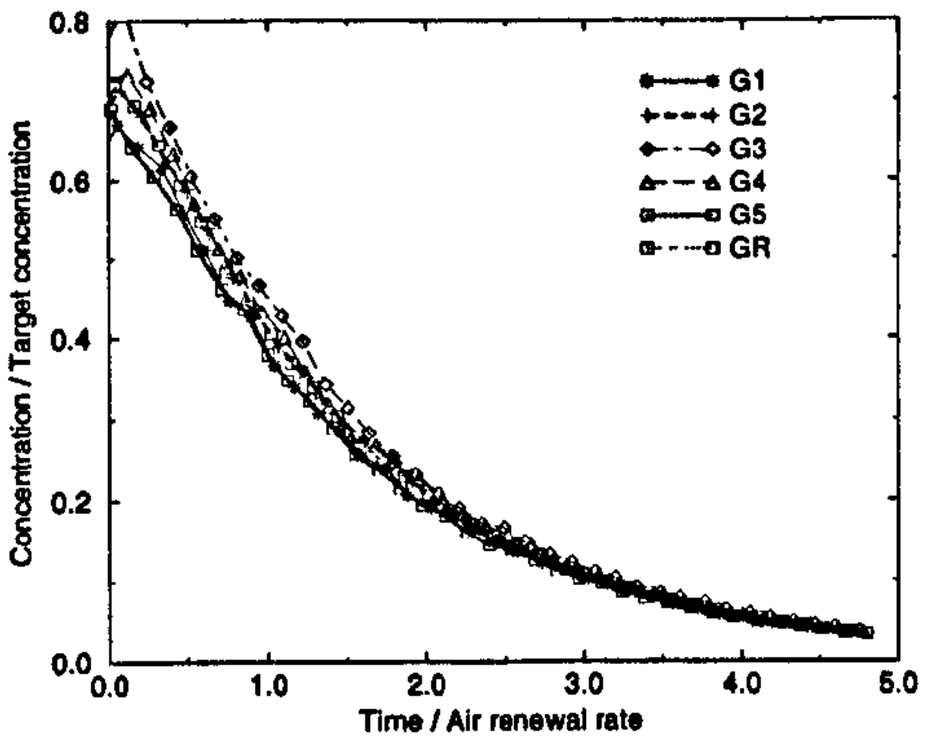

(a)

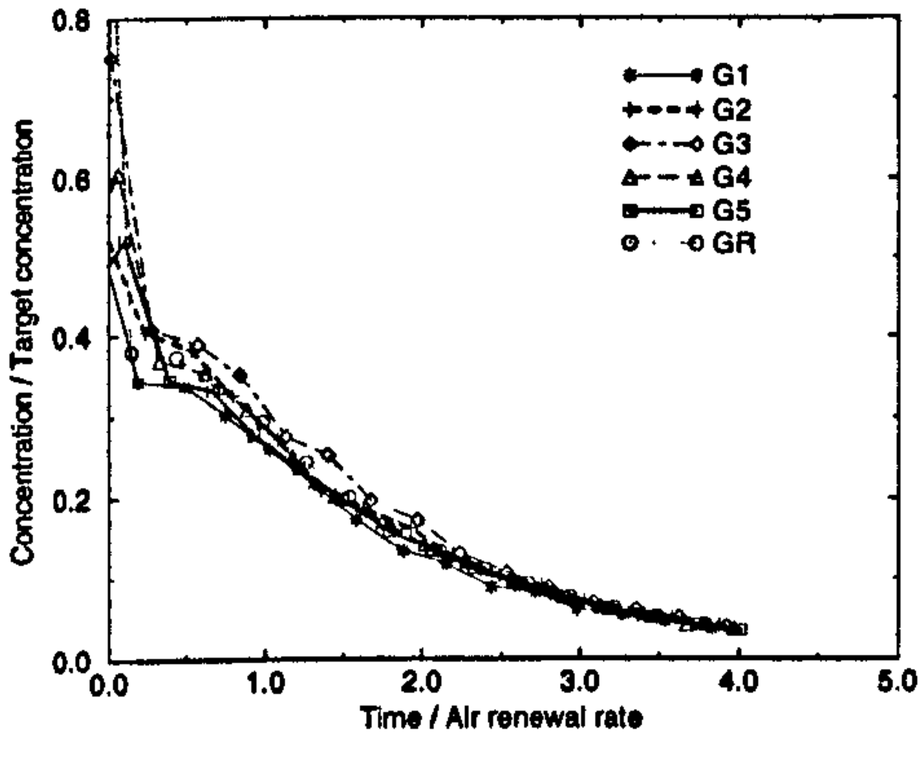

(b)

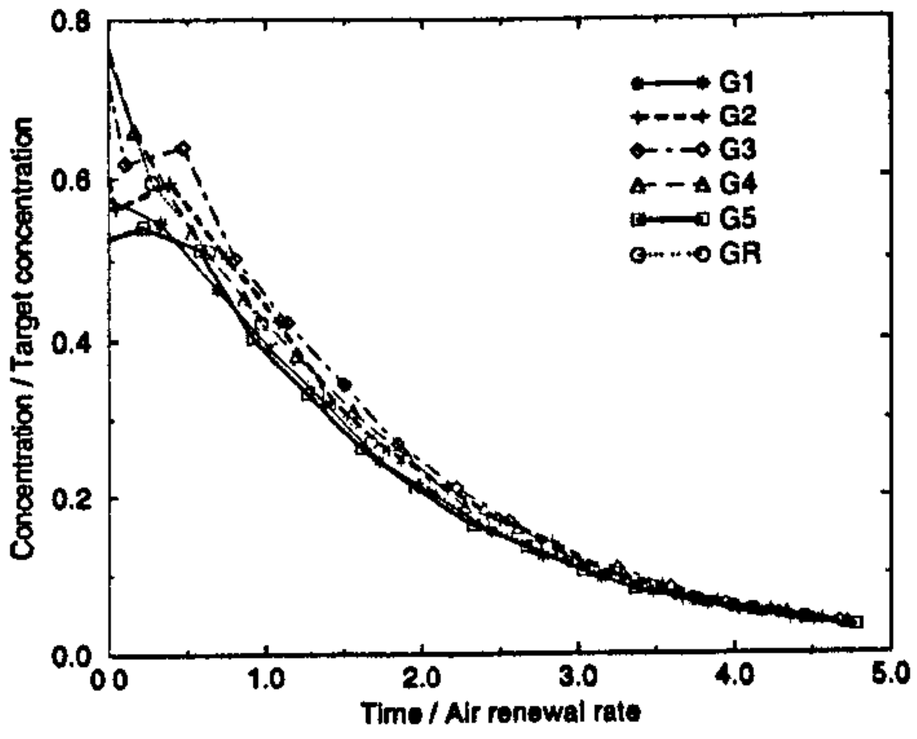

(c)

Figure 7.3: Time-decay of gas concentration in the room for (a) Case 04, (b) Case 05 and (c) Case 06.

Figure 7.2 shows that the average decay rate of SF_6 is virtually identical for cases 01, 02 and 03. Thus, for the displacement-ventilation configuration, the average decay rate of SF_6 is independent of the ventilation rate. This suggests a relashionship between the decay rate of SF_6 and the ventilation rate in the room. Figure 7.3 shows that the average rate of SF_6 decay is identical for cases 04, 05 and 06. This indicates that the decay rate of SF_6 is also relatively independent of the ventilation rate for a mixed-ventilation layout. Figures 7.2 and 7.3 show that the average decay rate of SF_6 is $\simeq$ 20% higher for the displacement-ventilation layout when compared to the mixed-ventilation layout.

Figure 7.2 shows that the relative concentration difference between the various sampling points increases with displacement ventilation rate. Figure 7.2, Case 01, indicates a maximum relative difference of less than 26% between the sampling points whereas Case 02 and Case 03 show relative variations of $\simeq$ 32% and $\simeq$ 59%, respectively. A common feature of Figure 7.2 is that the lower sampling point, $G5$, is found to give consistently lower concentration readings relative to the average concentration of the other sampling points. This could indicate a form of stratification of SF_6 in the room. For the mixed-ventilation mode (Figure 7.3), no relative concentration differences are found between the sampling stations. This indicates, as expected, a more uniformly mixed air throughout the room. Figure 7.3 shows that the target concentration is not reached by any of the sampling points for the mixed-ventilation layout.

7.3 Time considerations

As illustrated by Figure 7.1, the amount of data generated during these experiments is large. For CFD purposes data averaged over a two-hour snapshot is used. The snapshot is made when wall temperatures are quasi-steady. The snapshot are taken

at 14600 s < t_{01} < 21000 s, 9000 s < t_{02} < 16200 s, 7200 s < t_{03} < 11700 s, 7500 s < t_{04} < 13000 s, 1000 s < t_{05} < 7000 s and 6000 s < t_{06} < 11000 s for cases 01 to 06 respectively. The reference $t = 0$ s corresponds to the beginning of the experiments. A time compensation has been applied to the results to account for the local variations marking the start of the recording for the different measurement devices (*i.e* Thermocouples, SF_6 tracer gas, air velocities and temperatures).

7.4 Surface temperature

Figure 7.4 plots the time trace of the surface temperatures for Case 01. Figure 7.4 shows sudden changes in temperature. These unexpected changes, of magnitude $\simeq 0.3$ C, are found to be recorded by all thermocouples at the same time. This is highly improbable. The changes like the ones seen at the times $t \simeq 15700$ s and $t \simeq 20000$ s are assumed to be noise induced by the recording device. The other temperature fluctuations seen in Figure 7.4 are found to be of lesser magnitude than the accuracy of the thermocouple used (± 0.8 K). Thus, the readings seen in Figure 7.4 are approximated by their respective time average. Plots of the surface temperatures for all the other cases show similar fluctuations. Thus, all surface temperatures are approximated by their respective time averages.

Figure 7.4 shows that the surface temperatures are not uniform throughout the room for case 01. As expected, a thermal stratification occurs. This is emphasied by Figures 7.5 and 7.6. These show the average thermocouple temperature as a function of vertical position the thermocouples in the room for the displacement-ventilation cases (Figure 7.5) and mixed-ventilation cases (Figure 7.6). The results shown in figures 7.5

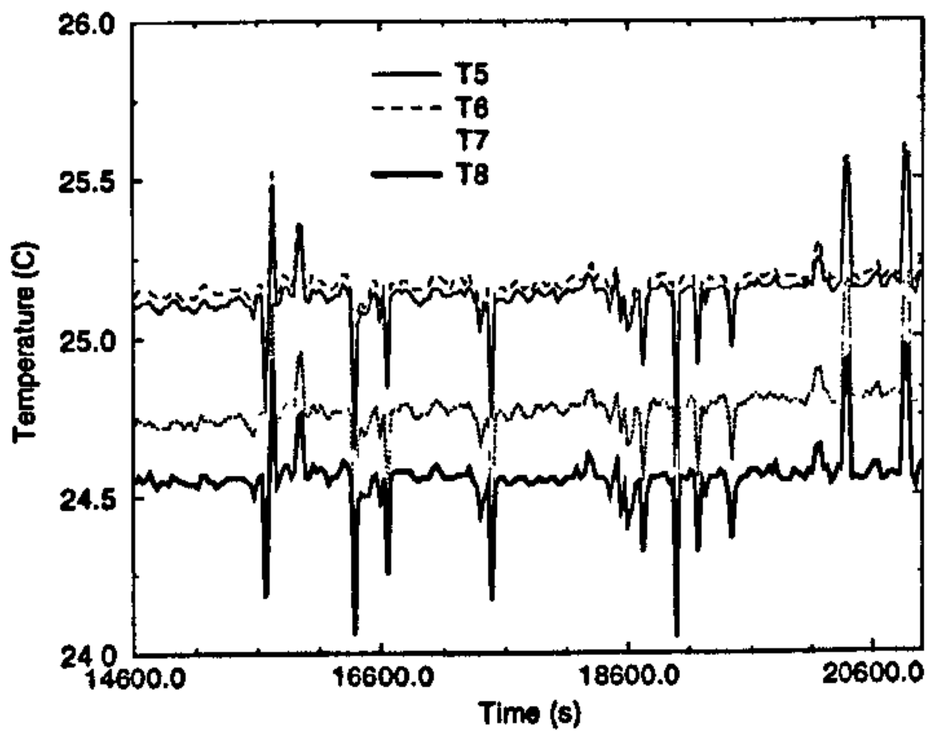

(a)

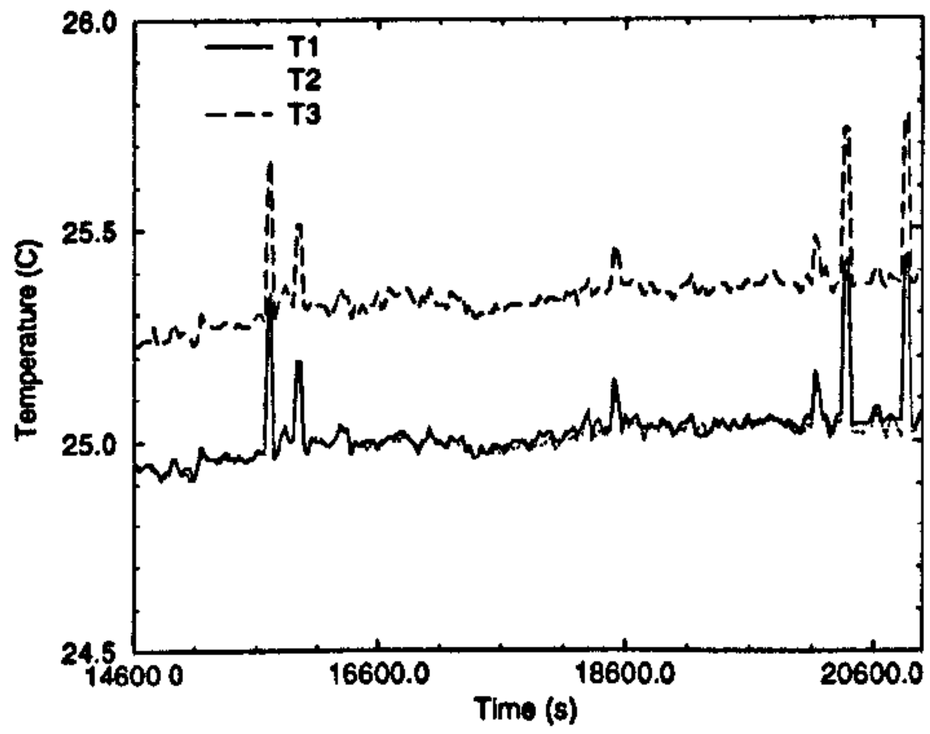

(b)

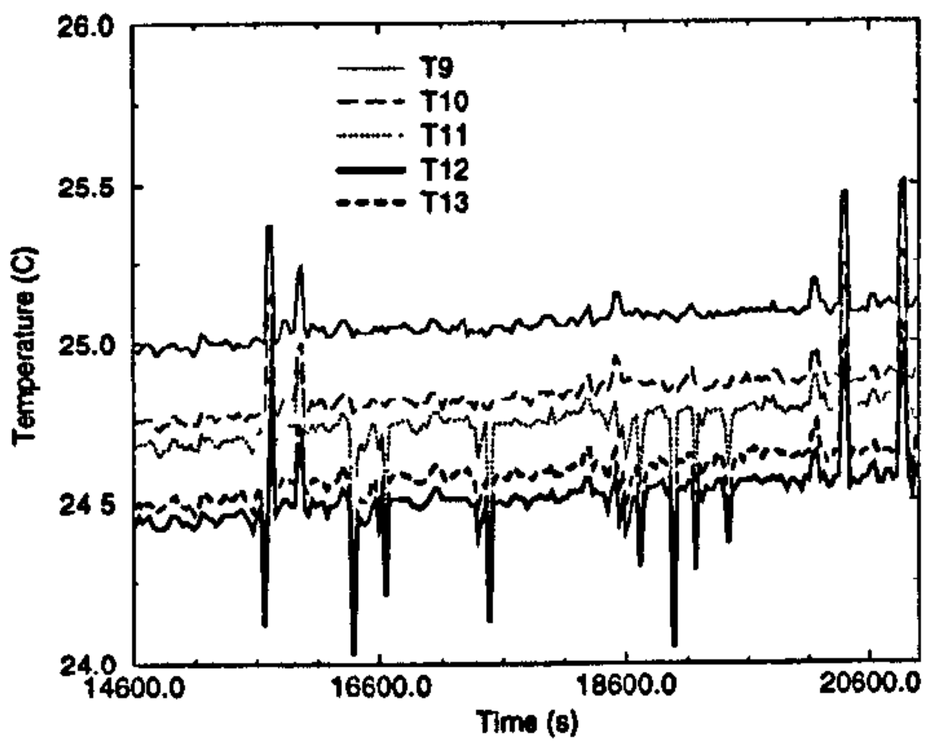

(c)

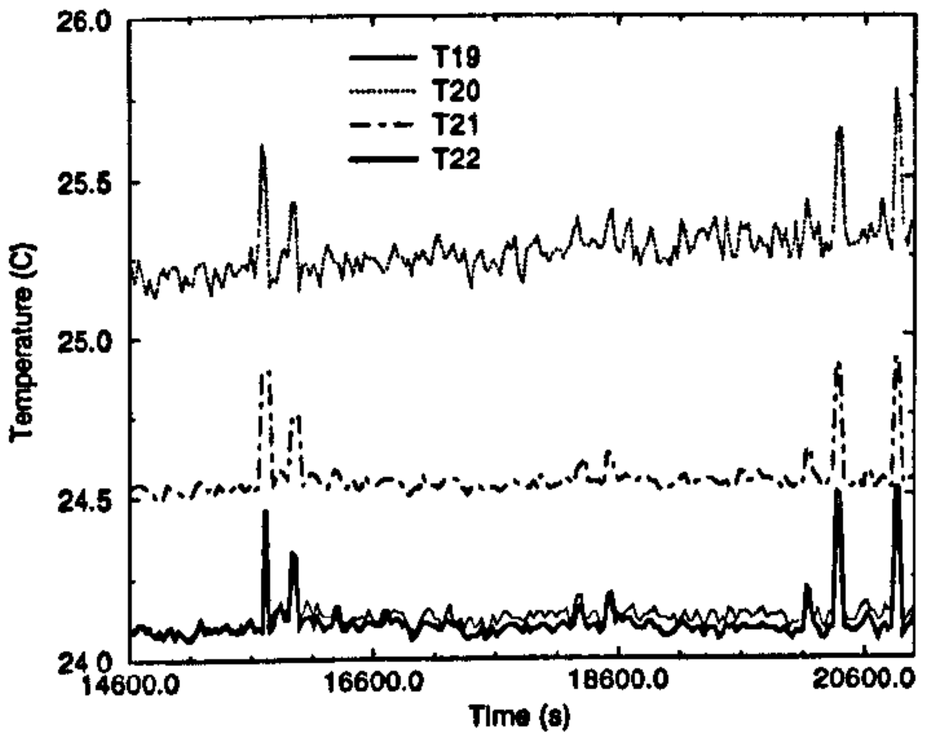

(d)

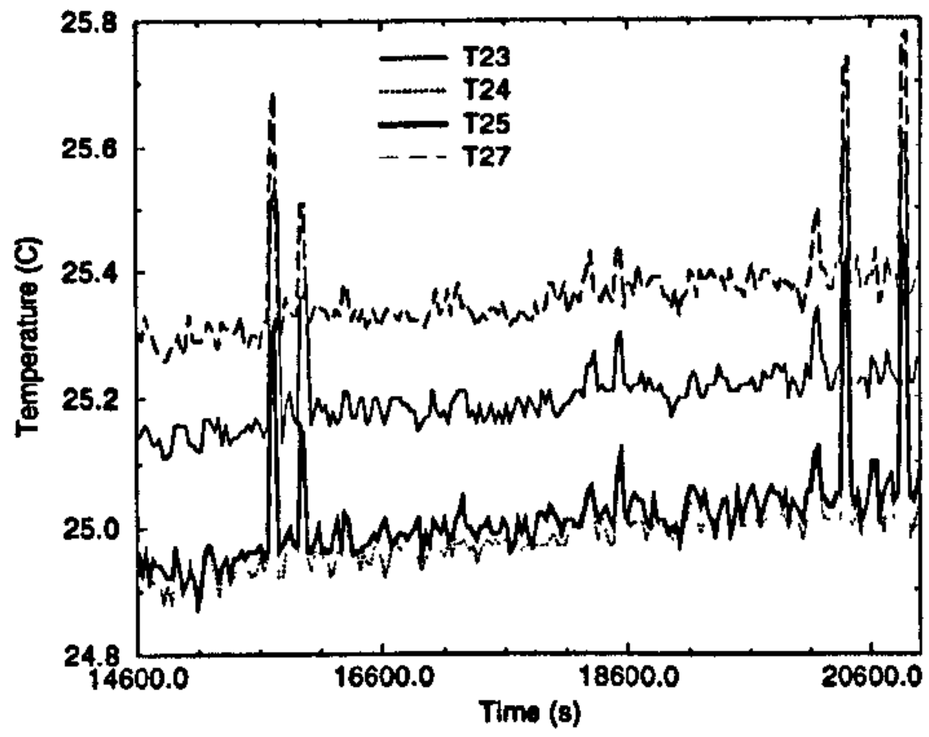

(e)

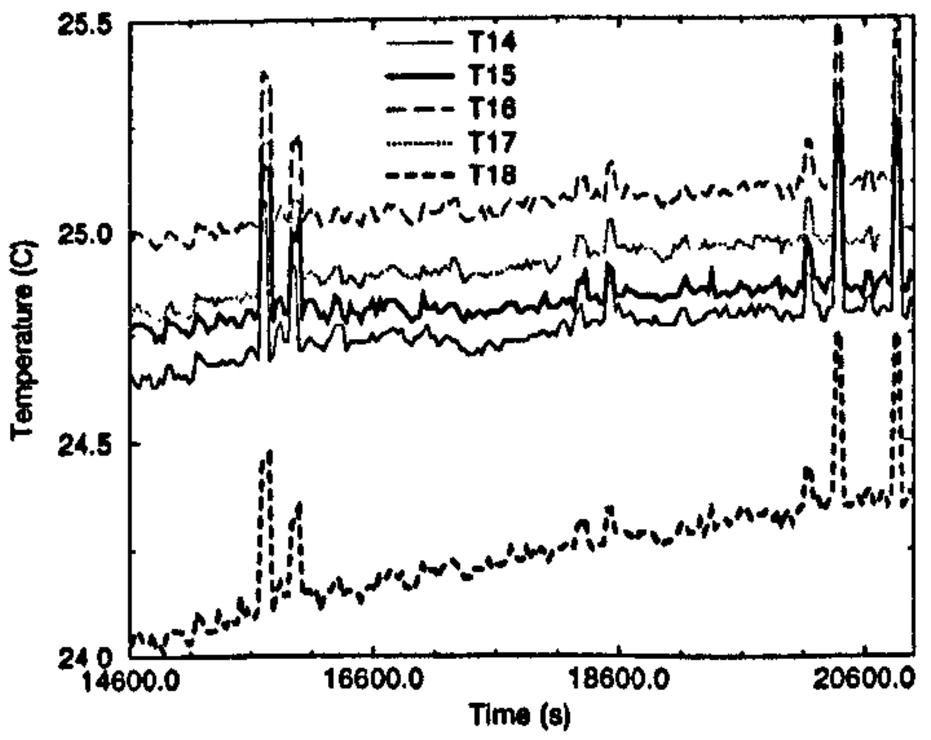

(f)

Figure 7.4: Wall temperatures for Case 01: (a) back wall, (b) left wall, (c) right wall, (d) floor, (e) ceiling and (f) door.

and 7.6 are non-dimensionalised. The temperatures are non-dimensionalised as follows: $(T - T_{in})/(T_{din} - T_{in})$ where T_{in} is the inlet temperature and T_{din} is the averaged air temperature measured at the top openings of the DIN man. The x-axis of Figure 7.5 and 7.6 are non-dimensionalised by the room height. Figure 7.5 indicates a similar level of thermal stratification for cases 01, 02 and 03. The figure also indicates that the average surface temperature increases with the increase of ventilation rate. This result appears as an important finding. It indicates, contrary to intuition, that for the displacement-ventilation, the use of higher ventilation rates leads to hotter surface temperatures. Figure 7.6 shows that unlike with displacement-ventilation, the thermal stratification for mixed-ventilation is not so well defined. Figure 7.6 indicates that the intensity of the thermal stratification reduces with increasing ventilation rate. The figure also indicates that, for mixed-ventilation, the use of higher ventilation rate leads to cooler surface temperatures.

Tables of the time-averaged surface temperature for cases 01 to 06 are available in Appendix C. These values are used as boundary conditions for the numerical modelling of this room discussed in Chapter 11

7.5 Velocity and air temperature analysis

As discussed by Yuan *et al.* (1999), the measurement of low velocities, such as those encountered in room ventilation, using hot-sphere anemometers is difficult. The key problem is that at low velocities, the thermal plume of the anemometer induces a flow of similar magnitude as the local room flow. Figure 7.7 shows a typical Case 01 time trace of the velocity measurements in the room using the Dantec hot-sphere anemome-

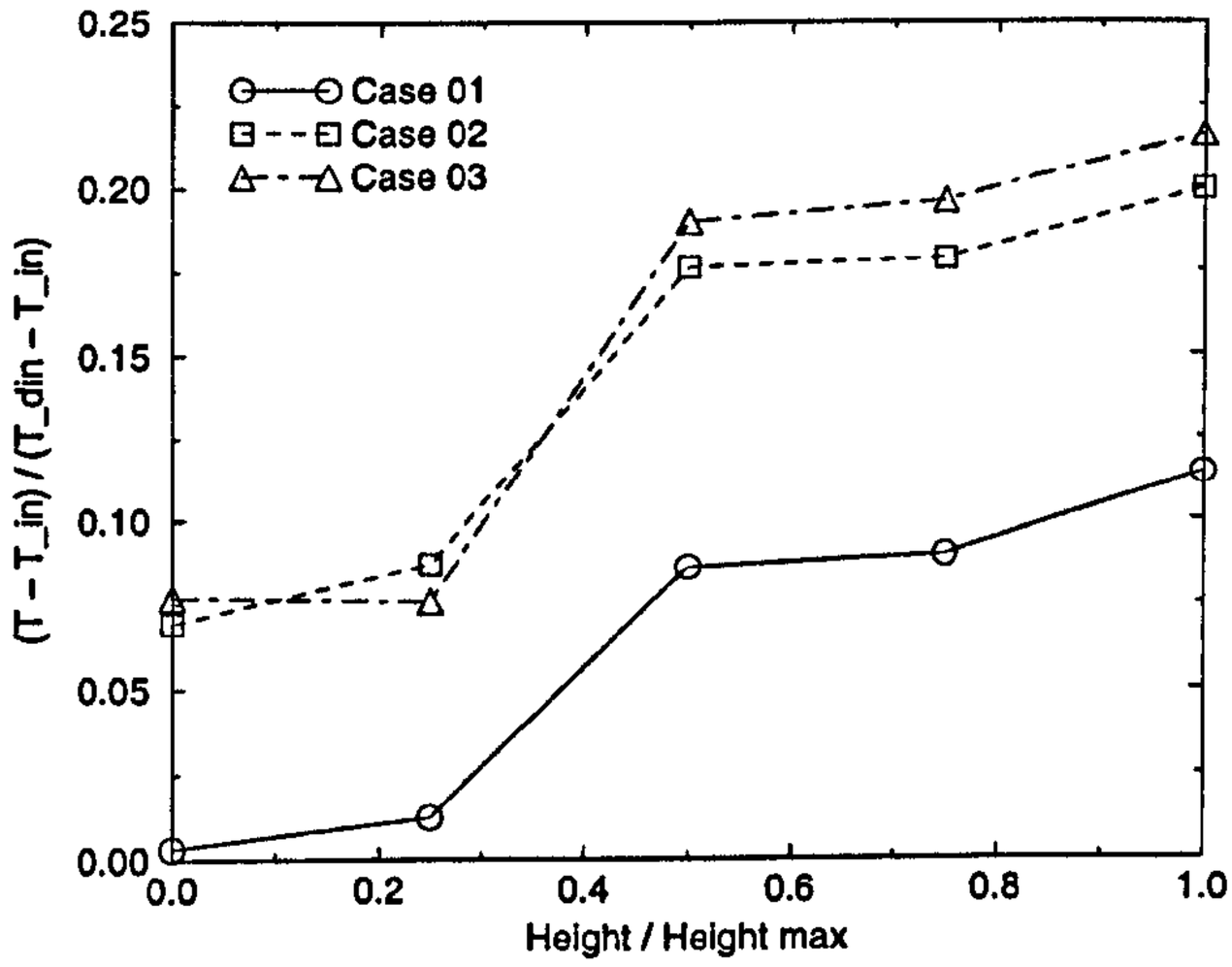

Figure 7.5: Thermal stratification in the room for Cases 01, 02 and 03.

Figure 7.6: Thermal stratification in the room for Cases 04, 05 and 06.

ters. The results shown in Figure 7.7 corresponds to the left (D3) and right (D1) inlet sensors. The velocity fluctuations of Figure 7.7 are of lesser magnitude than the error induced by the equipment ($\pm 0.020\ m/s$). Thus, the Dantec measurements are approximated by their respective time averages. Since $D1$ and $D3$ are located 200 mm from the actual inlets, lower velocity readings from the anemometers than the initial set inlet velocity are expected. The time-averaged velocity reading of $D3$ ($0.0668\ m/s$) and $D1$ ($0.0565\ m/s$) are consistent with the initial ventilation settings of Case 01 ($0.7386\ m/s$). The combined averaged inlet velocity (see Figure 7.7) has lower fluctuation amplitudes than each separate inlet. This emphasises the expected steadiness of the overall mass flow rate coming into the room (see Chapter 6).

Table 7.1 shows the time-averaged velocities and temperatures of the anemometers for Case 01. The data presented in Table 7.1 are used for comparison with numerical models in Chapter 11. Similar velocity and temperature table for Case 02 to 06 are available in Appendix D.

7.6 DIN man area

This last section focuses on the flow around the DIN man. The highest velocities and temperatures are observed in this area. The thermal plume emitted by the DIN man is key to the airflow pattern in the room. This is especially so for displacement-ventilation. The physically small Accusense thermistors have been used to characterise the flow in this area. The plots of velocity fluctuations against time for the Accusense sensors shows that their error ($\pm 0.025\ m/s$ or $\pm 1\ C$) is of greater magnitude than the observed fluctuations. Thus both velocities and temperatures of the Accusense thermistors are time

Designation	x	y	z	Velocity (m/s)	Temperature (C)
D1	600	150	325	0.0565	25.286
D2	600	2850	325	0.0518	26.161
D3	600	150	2675	0.0668	24.236
D4	600	2850	2675	0.0757	26.142
D7	1600	1600	1800	0.1696	25.758
D8	1600	2850	1800	0.0722	25.374
D10	1600	1600	700	0.0676	25.121
D13	2700	1600	700	0.0607	25.047
D14	2700	2850	700	0.0773	25.739
D15	3600	1600	200	0.0556	26.051
D17	3100	950	1800	0.0391	25.884
D18	3600	950	2700	0.0726	26.707

Table 7.1: Location, mean temperature and velocity of the Dantec anemometers for Case 01 (dimensions in mm).

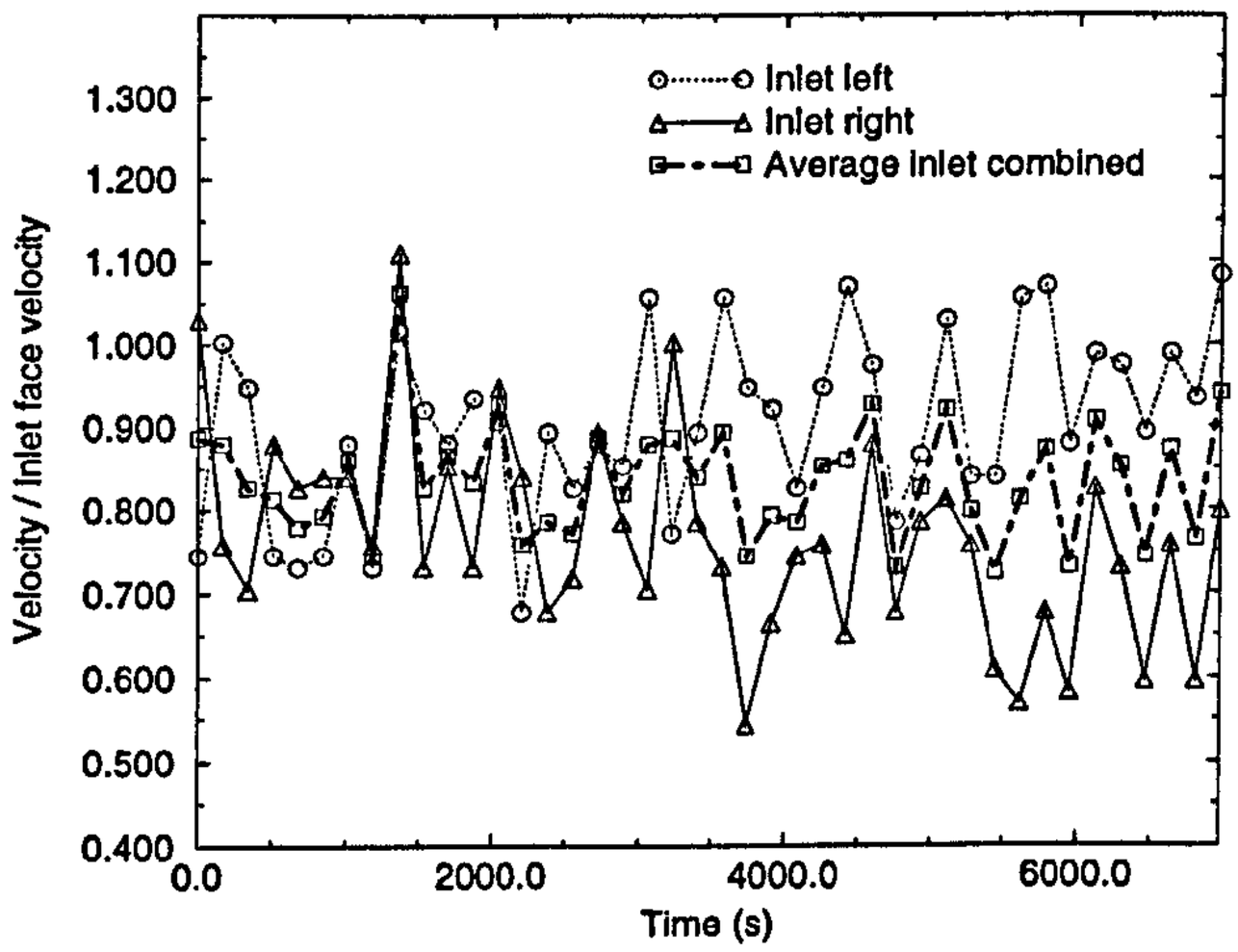

Figure 7.7: Inlet velocity measurements from the Dantec anemometers for Case 01.

averaged. Table 7.2 and 7.3 shows the averaged velocity and temperature readings of the Accusense thermistors.

As might be expected probes $A3$ and $A8$ (which correspond to the lower opening of the DIN man) give similar results (velocity and temperature). For all cases, the increase of ventilation rate increases the average velocity of sensors $A3$ and $A8$. These velocities are found to be independent on the ventilation layout. Table 7.4 shows that for mixed-ventilation the temperature of $A3$ and $A8$ decreases with increased ventilation rate. This is not the case for displacement-ventilation.

The sensors $A1$, $A5$, $A6$ and $A7$ correspond to the top opening of the DIN man. It is found that the velocities of all these sensors are mostly independent of the ventilation

	Case 01		Case 02		Case 03	
Designation	V (m/s)	T (C)	V (m/s)	T (C)	V (m/s)	T (C)
A1	0.2833	30.06	0.2833	28.38	0.2768	25.88
A2	0.0409	28.46	0.0415	26.77	0.0374	24.92
A3	0.0799	27.77	0.0822	25.82	0.1071	22.82
A5	0.2954	30.30	0.3026	28.68	0.2894	26.38
A6	0.2909	30.10	0.2967	28.38	0.2903	25.99
A7	0.2991	30.25	0.2941	28.53	0.2897	26.15
A8	0.0792	27.82	0.0708	26.51	0.1086	22.97
A11	N/A	29.73	N/A	27.19	N/A	24.98
A12	N/A	30.41	N/A	28.15	N/A	25.86

Table 7.2: Mean temperature and velocity of the Accusense thermistors for cases 01, 02 and 03.

layout and increase with ventilation rate. This increase with ventilation rate is similar to the one at the lower opening of the DIN man. The averaged temperature (taken as $T - T_{inlet}$) of sensors $A1$, $A5$, $A6$ and $A7$ (see Table 7.4) shows similar variations to those seen in the lower part of the DIN man area ($A3$ and $A8$). The velocities and temperatures from the Accusense thermistors are used as boundary conditions in the CFD analysis (see Chapter 11).

7.7 Conclusions

The gas tracer analysis shows that the rate of decay of SF_6 is independent of the ventilation rate for both the mixed- and displacement-ventilation layouts. The decay rate

	Case 04		Case 05		Case 06	
Designation	V (m/s)	T (C)	V (m/s)	T (C)	V (m/s)	T (C)
A1	0.2865	28.80	0.2988	26.16	0.3058	27.13
A2	0.0449	26.84	0.0503	24.04	0.0584	24.79
A3	0.0854	26.87	0.0975	23.94	0.0990	24.91
A5	0.3178	29.10	0.3083	26.57	0.3191	27.43
A6	0.3029	28.94	0.3077	26.31	0.3106	27.12
A7	0.3082	29.01	0.3074	26.49	0.3209	27.34
A8	0.0824	26.97	0.0911	24.02	0.1028	24.78
A11	N/A	28.49	N/A	25.25	N/A	26.91
A12	N/A	29.13	N/A	25.91	N/A	27.46

Table 7.3: Mean temperature and velocity of the Accusense thermistors for cases 04, 05 and 06.

Designation	Case 01	Case 02	Case 03	Case 04	Case 05	Case 06
A3	3.27	3.62	2.62	4.27	3.74	3.51
A8	3.32	4.31	2.77	4.37	3.82	3.38
A1	5.56	6.18	5.68	6.20	5.96	5.73
A5	5.80	6.48	6.18	6.50	6.37	6.03
A6	5.60	6.18	5.79	6.34	6.11	5.72
A7	5.75	6.33	5.95	6.41	6.29	5.94

Table 7.4: Temperature of the Accusense thermistors taken as: $T - T_{inlet}$.

of SF_6 for displacement-ventilation is found to be $\simeq$ 20% higher than for the mixed-ventilation layout. Analysis of the surface temperatures show that the displacement-ventilation mode induces a well-defined thermal stratification in the room. For displacement-ventilation, the averaged surface temperature is found to increase with ventilation rate. In the mixed-ventilation mode, the thermal stratification is not so well defined as expected, and seems to reduce with increasing ventilation rate. For mixed-ventilation, the averaged surface temperature decreases with increased ventilation rate. The flow properties at the four DIN man faces are similar. This is helpful when specifying CFD boundary conditions. The velocities at the top and bottom of the DIN man are found to be mostly independent ventilation layout and increase with ventilation rate. The data presented in this chapter are used for CFD validation purposes in Chapter 11.

Chapter 8

Modelling of a jet-ventilated room

In this analysis the experiment of He *et al.* (1999) for an empty, jet-ventilated room is considered. The room is empty and hence does not present any great problem-definition issues. Therefore, it is intended to compare the flow predictions for a wide range of turbulence models. A total of ten models have been tested. They are the: mixing length ($ml1$ and $ml2$), $k-l$, $k-\epsilon$, EASM ($k-l$ and $k-\epsilon$), cubic $k-\epsilon$, LES (Smagorinsky (1963) and Yoshizawa (1993)) and LNS models. The inlet Reynolds number is around 49000. The data of He *et al.* (1999) include velocity samples at the various locations defined in Figure 8.1. Velocities are measured using a three dimensional ultrasonic anemometer at sixteen heights along a series of nine vertical axes labeled A_i in Figure 8.1. One-thousand measurements are recorded for each of the 144 sampling points at a frequency of 9 Hz.

8.1 Numerical modelling

Ventilation settings in the room are as follows: The air is supplied at a rate of $\simeq$ 578.11 m^3/h which corresponds to an inlet velocity of $\simeq$ 4.956 m/s and, to an outlet ve-

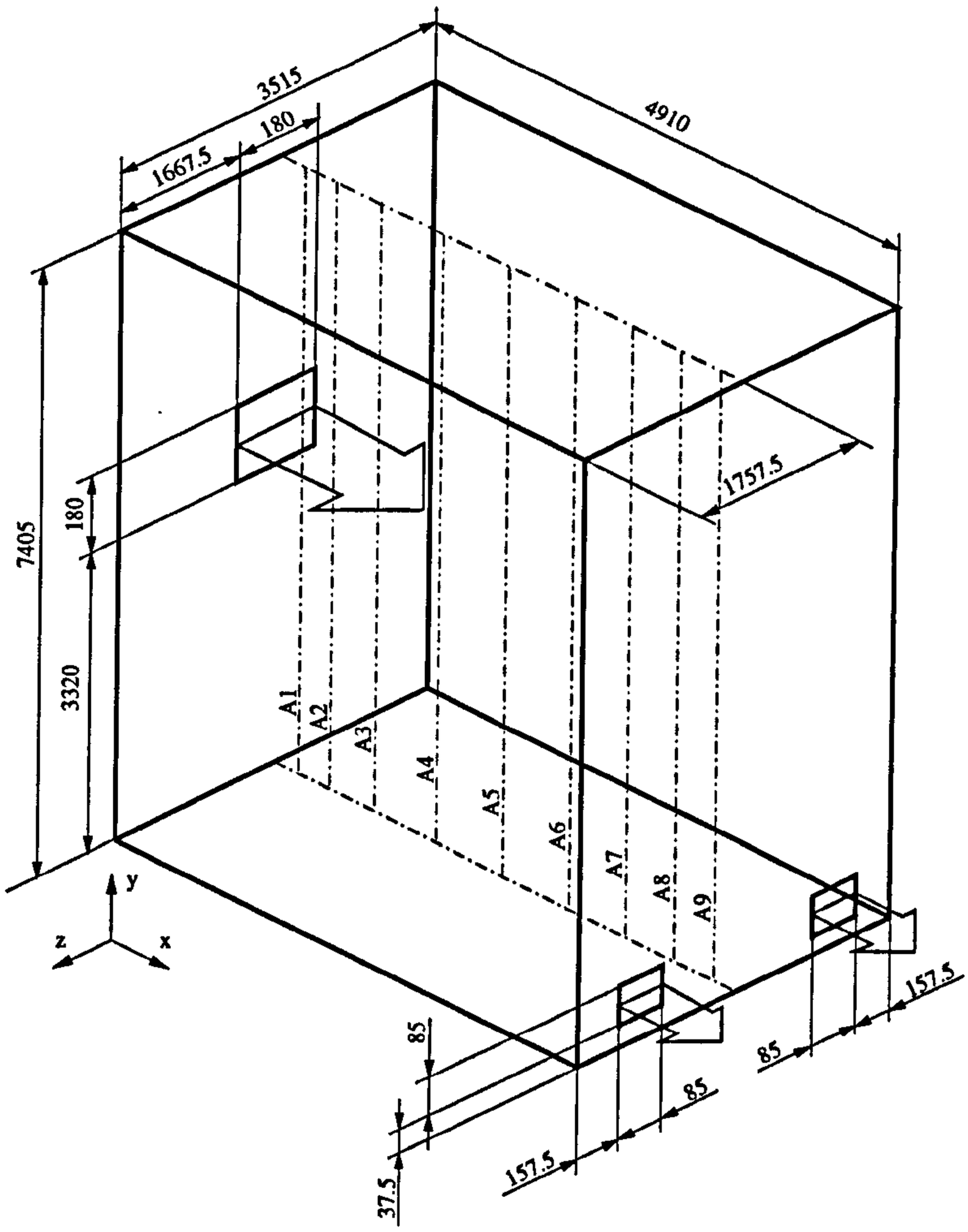

Figure 8.1: Room geometry and position of vertical measurement axes (Dimensions in mm).

Distance from inlet along x: $A1 = 190\ mm$; $A2 = 515mm$; $A3 = 965\ mm$; $A4 = 1555\ mm$; $A5 = 2355\ mm$; $A6 = 3155\ mm$; $A7 = 3945\ mm$; $A8 = 4395\ mm$; $A9 = 4720\ mm$.

locity of $\simeq 11.113\ m/s$. The inlet flow is assumed to be unidirectional ($v_{inlet} \simeq w_{inlet} \simeq 0$). The inlet turbulent kinetic energy is approximated to be $\simeq 3\%$ of the mean flow kinetic energy (or $\simeq 1.83\ m^2/s^2$). ϵ at the inlet is set as $\epsilon \simeq 0.096\ m^2/s^3$. The flow is assumed isothermal. A grid of $49 \times 71 \times 85$ (x, y, z) nodes giving an average first off-wall $y^+ \simeq 0.7$ on key surfaces is used. This grid gives an average $\Delta z^+ \simeq 17$ and has also been used for LES.

8.2 Results and discussion

Figure 8.2 plots predicted against measured velocities at all the room data points for a selection of models. The figure shows that overall, the turbulence models perform better at higher velocities ($> 0.1\ m/s$). This can be partly explained by the measurement error which could be significant at low velocities. However, He *et al.* (1999) provide no accuracy information and thus, no firm conclusions can be made on this aspect. To assess the performances of the models, more specific flow features are next analysed.

8.2.1 Jet centerline decay analysis

The overall flow in the room is governed by the jet. Thus, comparison of measurements and predictions at the centerline of the inlet jet are made.

Figure 8.3 compares predictions with measurements for the mixing length ($ml1$ and $ml2$), $k-l$ (Wolfshtein (1969)) and $k-\epsilon$ (Launder and Sharma (1974) with Yap (1987) correction) models. The standard mixing-length model discussed in Section 3.1.1 uses $l_m = \kappa y f_\mu$. Here, to predict more accurately the inlet jet, a modified mixing length is

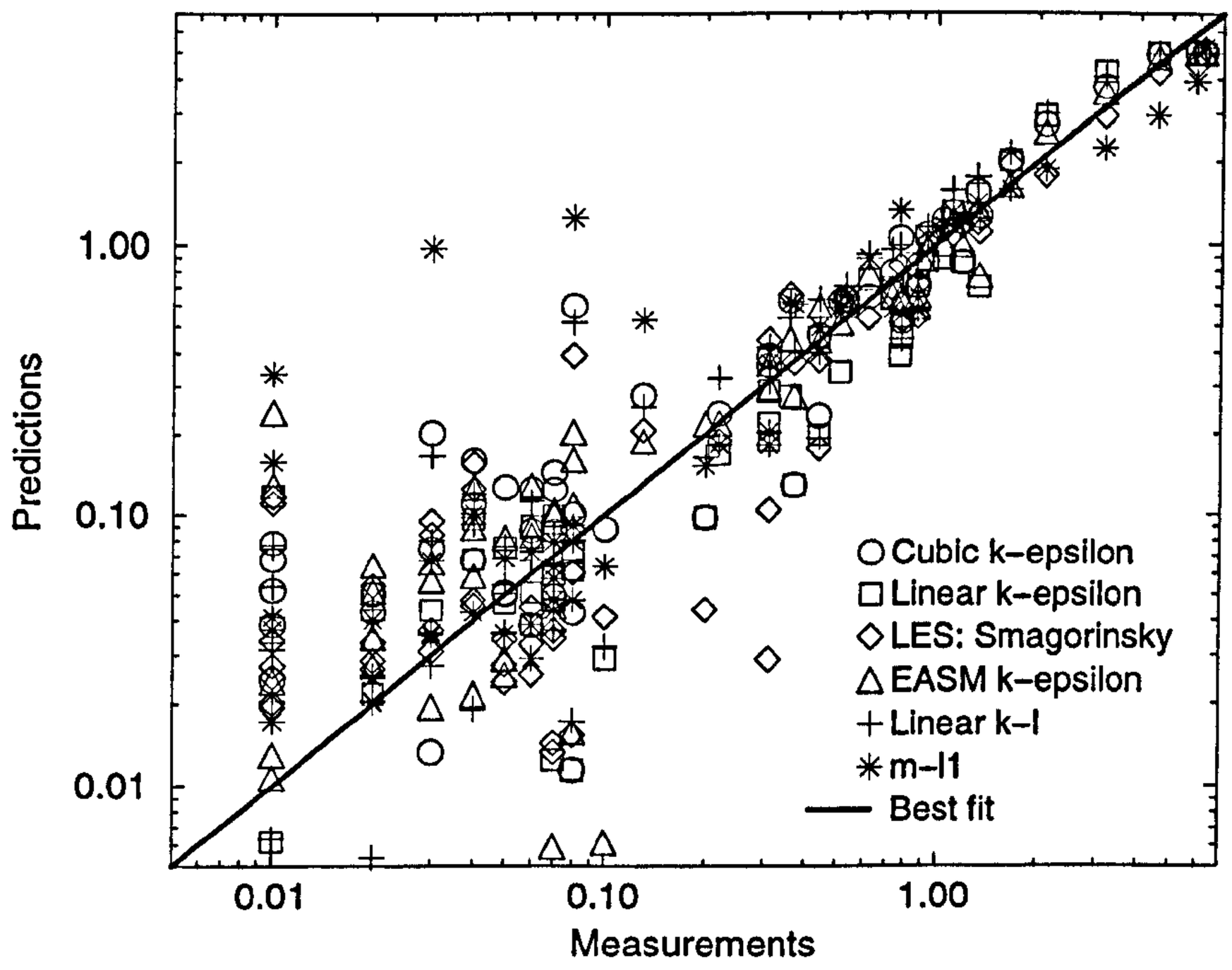

Figure 8.2: Comparison of predicted velocities with measurements (m/s).

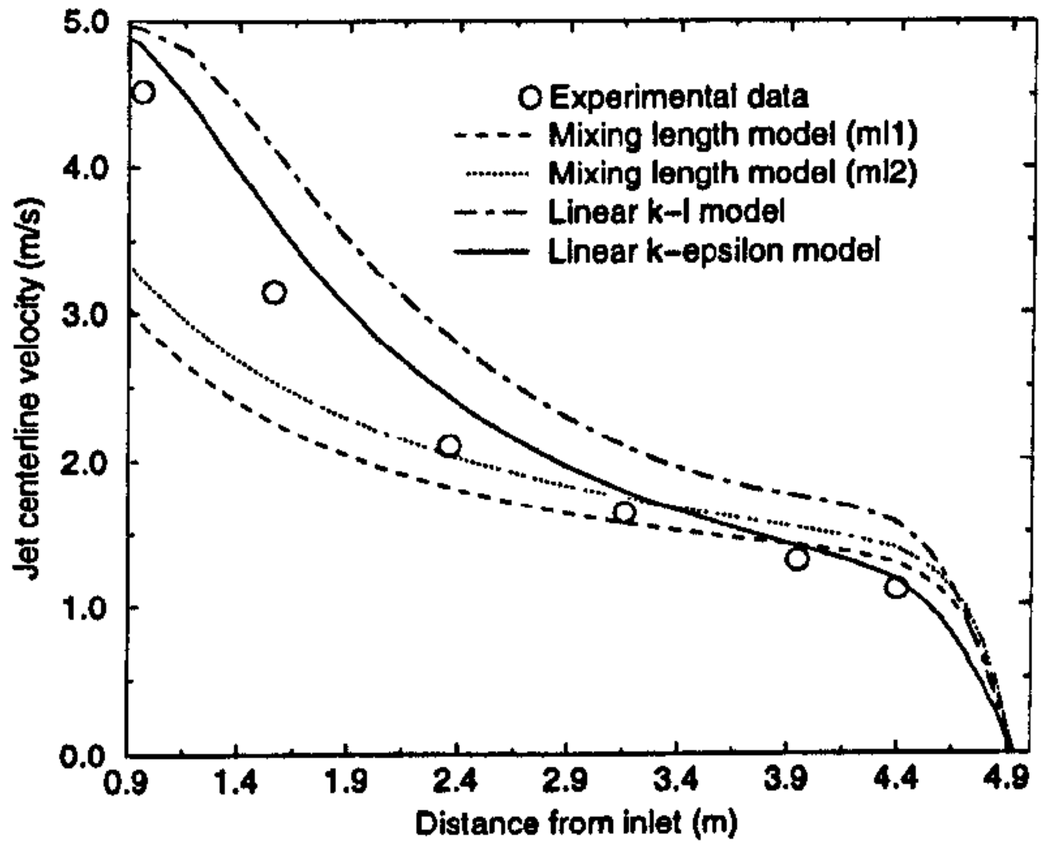

Figure 8.3: Centerline velocity decay of the inlet jet: Comparison of measurements with linear eddy-viscosity models.

used within the jet. In the simulations, the jet itself is detected (using local velocity gradients and geometrical positioning) and, a mixing length of $l_m = C_m L$ is used in the jet (L is the jet half width and $0.075 < C_m < 0.09$). The sensitivity of the mixing length model to C_m is tested. The mixing length model $ml1$ uses $C_m = 0.09$ and the $ml2$ uses $C_m = 0.075$ (Launder *et al.* (1972)). As shown by Figure 8.3 both $ml1$ and $ml2$ have a low predictive accuracy especially in the vicinity of the inlet. The accuracy of both mixing-length models is found to increase as the jet develops. Because both mixing-length models are unable to predict the decay rate of the jet, they are not further considered. The linear $k - \epsilon$ model performs better than the $k - l$ and both mixing-length models. The $k - \epsilon$ is thus chosen as framework for the EASM and cubic models.

Figure 8.4 compares the jet centerline velocity predictions of the linear, EASM

	$ml1$	$ml2$	$k-\epsilon$	$k-l$	EASM	Cubic	LES_1	LES_2	LNS
Error (%)	13.21	17.73	11.19	27.35	8.65	7.36	8.53	5.89	4.34

Table 8.1: Averaged prediction error at the jet centerline.

(AKN) and cubic models (Craft *et al.* (1996) with Yap (1987) correction factor) with measurements. The figure shows that the EASM and the cubic models only give minor accuracy improvements ($< 10\%$) when compared to the linear $k-\epsilon$ model. Figure 8.4 indicates that the cubic's predictions are best in the vicinity of the inlet jet ($x < 2.5\ m$) and the EASM's predictions are best further away form the inlet ($x > 2.5\ m$). Overall, the cubic model has better accuracy than the EASM and linear models.

Figure 8.5 compares the predictions of the LES (Smagorinsky (1963)), Yoshizawa (1993)) and LNS models with measurements. The Smagorinsky (1963) and LNS models show excellent agreement with measurements (less than 6% relative error). The figure shows that the LNS predicts more accurately the centerline velocity decay of the jet than both LES models. The figure also shows that the Smagorinsky (1963) model has better predictive accuracy than the Yoshizawa model (1993) which underpredicts the centerline velocity.

Using Equation 4.3, the relative predictive accuracy of the different models over the jet centerline is given in Table 8.1. In Table 8.1, LES_1 and LES_2 are the Yoshizawa (1993) and Smagorinsky (1963) models respectively. Like Figures 8.3, 8.4 and 8.5, the table shows that the LNS model agrees best with measurements ($< 5\%$ error). The Smagorinsky model also shows excellent agreements with measurements ($< 6\%$ error). The $k-l$ model has the lowest average accuracy. However, unlike both mixing-length

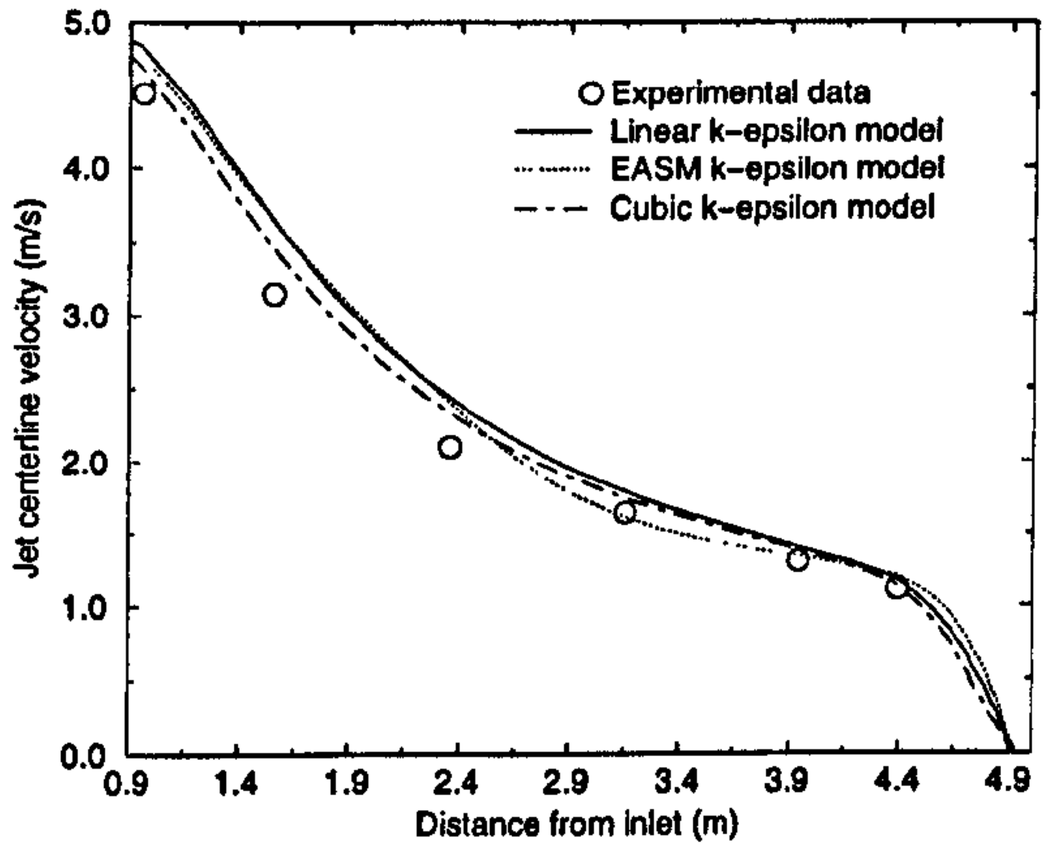

Figure 8.4: Centerline velocity decay of the inlet jet: Comparison of measurements with non-linear eddy-viscosity models.

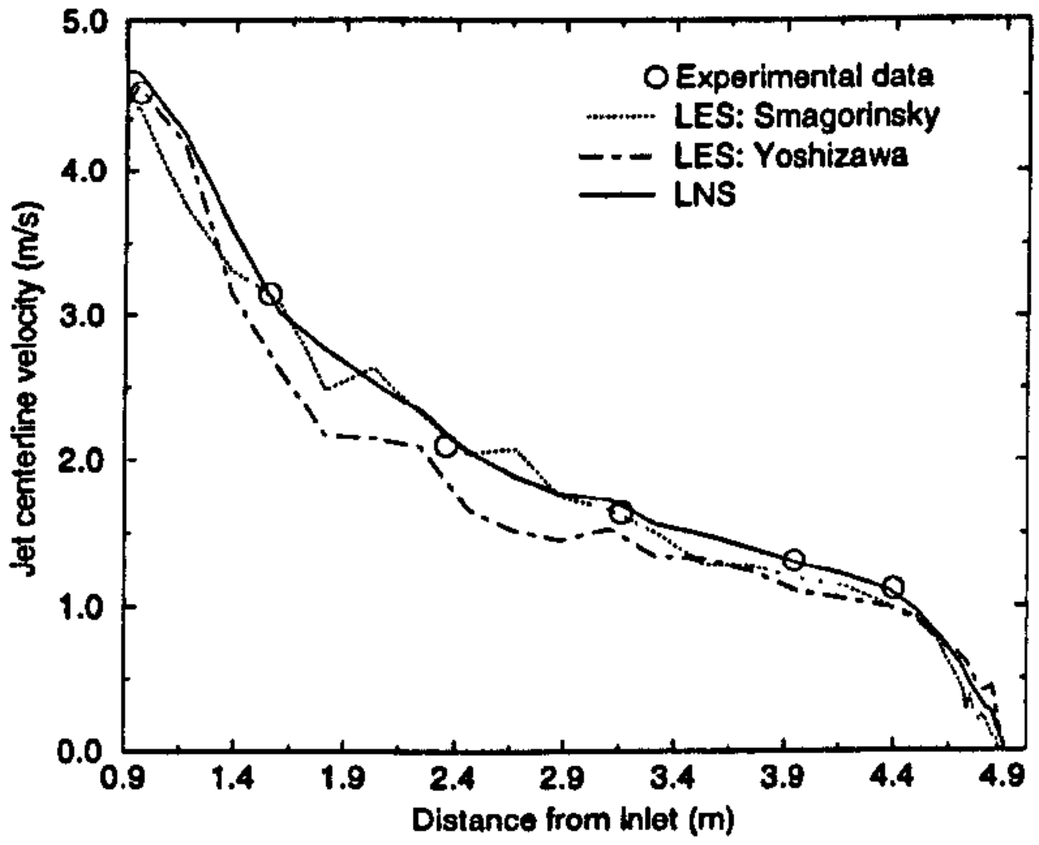

Figure 8.5: Centerline velocity decay of the inlet jet: Comparison of measurements with LES and LNS models.

models (of better average accuracy), the $k-l$ model predicts the correct decay profile of the inlet jet.

To further emphasise the respective differences between the models tested, measured and predicted normal Reynolds stresses are compared. Figure 8.6, 8.7 and 8.8 plots the normal Reynolds stresses τ_{xx}/ρ, τ_{yy}/ρ and τ_{zz}/ρ along the jet centerline for the linear, EASM, cubic, Smagorinsky and LNS models.

The figures show, as expected, that the linear $k-\epsilon$ model is not able to predict the anisotropy of the Reynolds stress tensor. The $k-\epsilon$ model predicts well τ_{xx} but greatly overestimates τ_{yy} and τ_{zz}. The other models tested show the ability to predict the anisotropy of the Reynolds stress tensor hence giving an overall higher accuracy than the linear model. The cubic and EASM are found to have similar levels of agreement with measurements. A maximum relative prediction difference of $\simeq 20\%$ is observed between these two models. Like Figure 8.4, Reynolds stress predictions of the cubic model are best in the vicinity of the inlet ($x < 2.5\ m$) and, as the jet diffuses ($x > 2.5\ m$), the EASM becomes more accurate.

Excellent agreement is found between the Smagorinsky LES and measurements. The Yoshizawa (1993) LES shows similar Reynolds stress accuracy to the cubic model. The LNS model is also found to perform well. In particular, excellent agreement with measured τ_{yy} is found. For LNS, the Reynolds stresses are plotted as the sum of the contribution from the LES and RANS (cubic) models as:

$$\tau_{ij}^{LNS} = \alpha\tau_{ij}^{RANS} + (1-\alpha)\tau_{ij}^{LES} \tag{8.1}$$

where α is the scaling coefficient applied to the RANS model (see Chapter 3). Figure

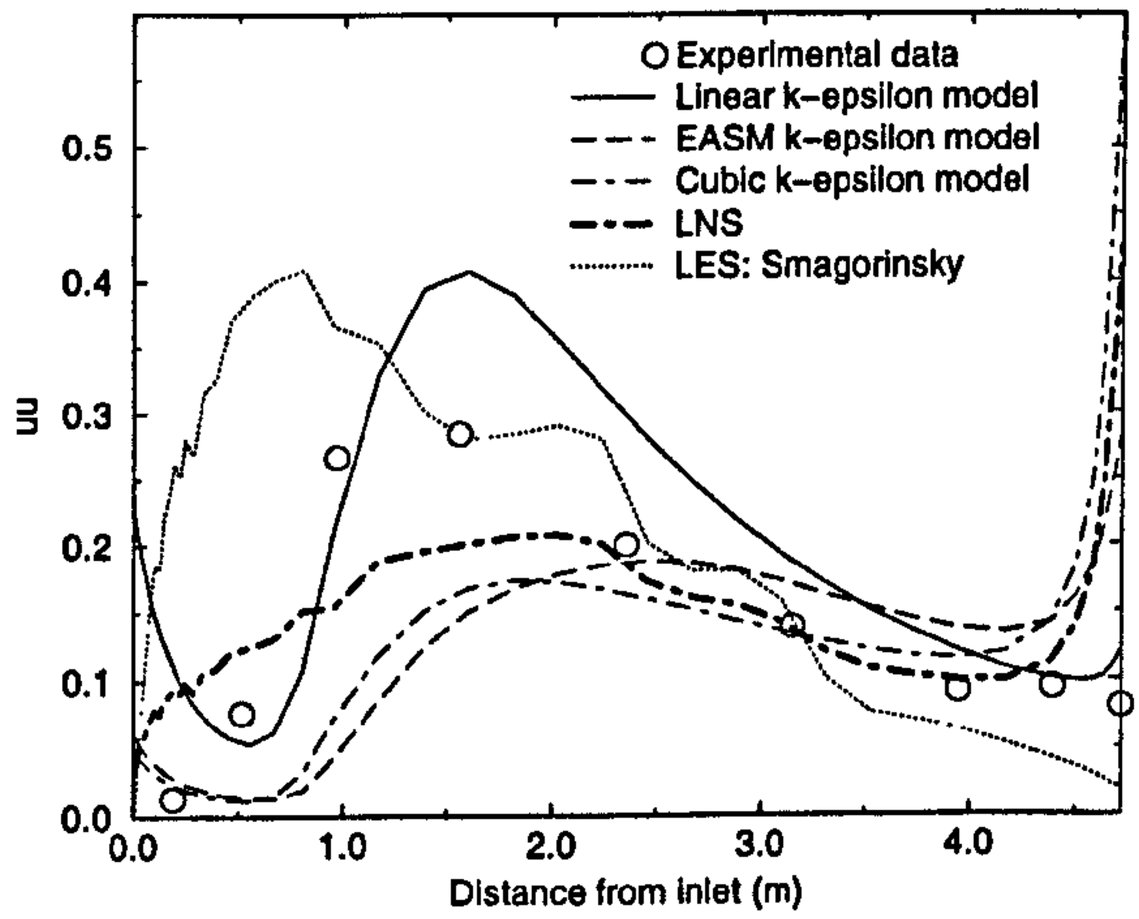

Figure 8.6: Normal Reynolds stresses τ_{xx}/ρ along the jet centerline.

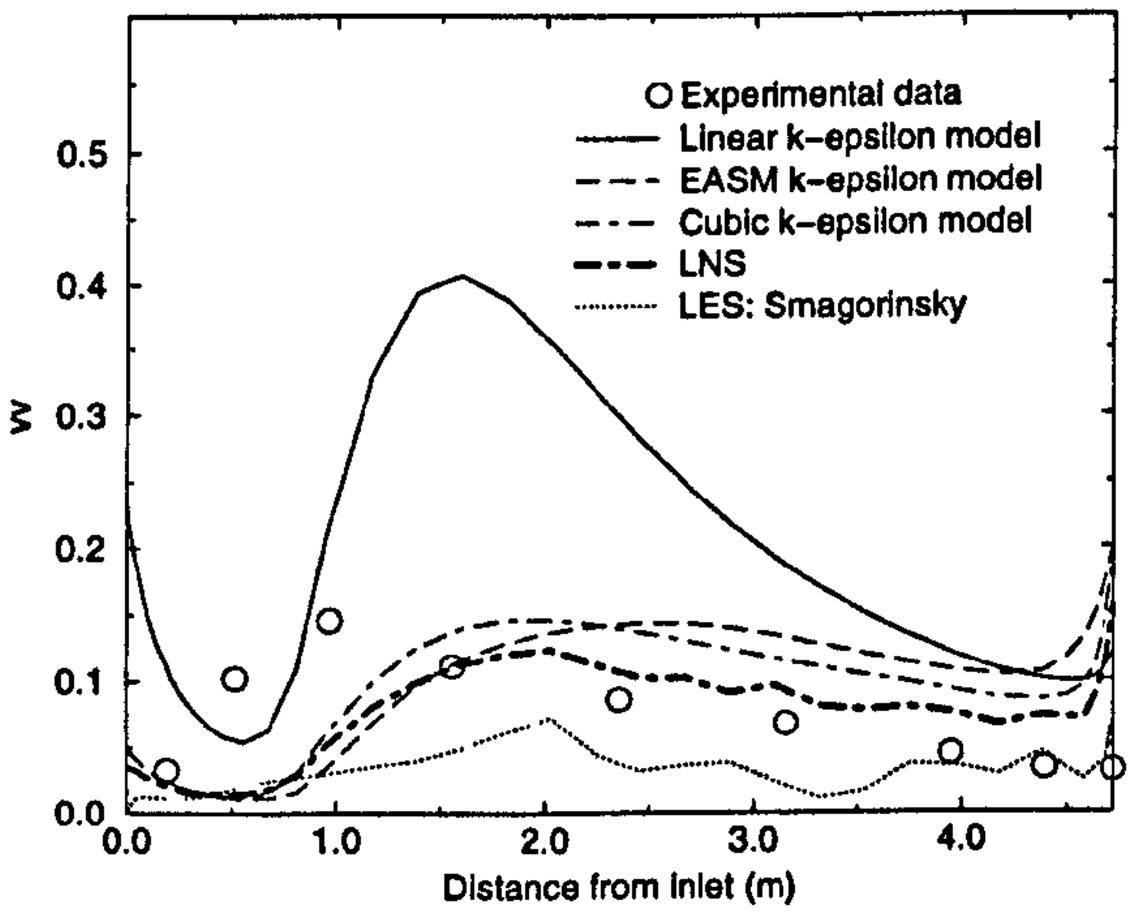

Figure 8.7: Normal Reynolds stresses τ_{yy}/ρ along the jet centerline.

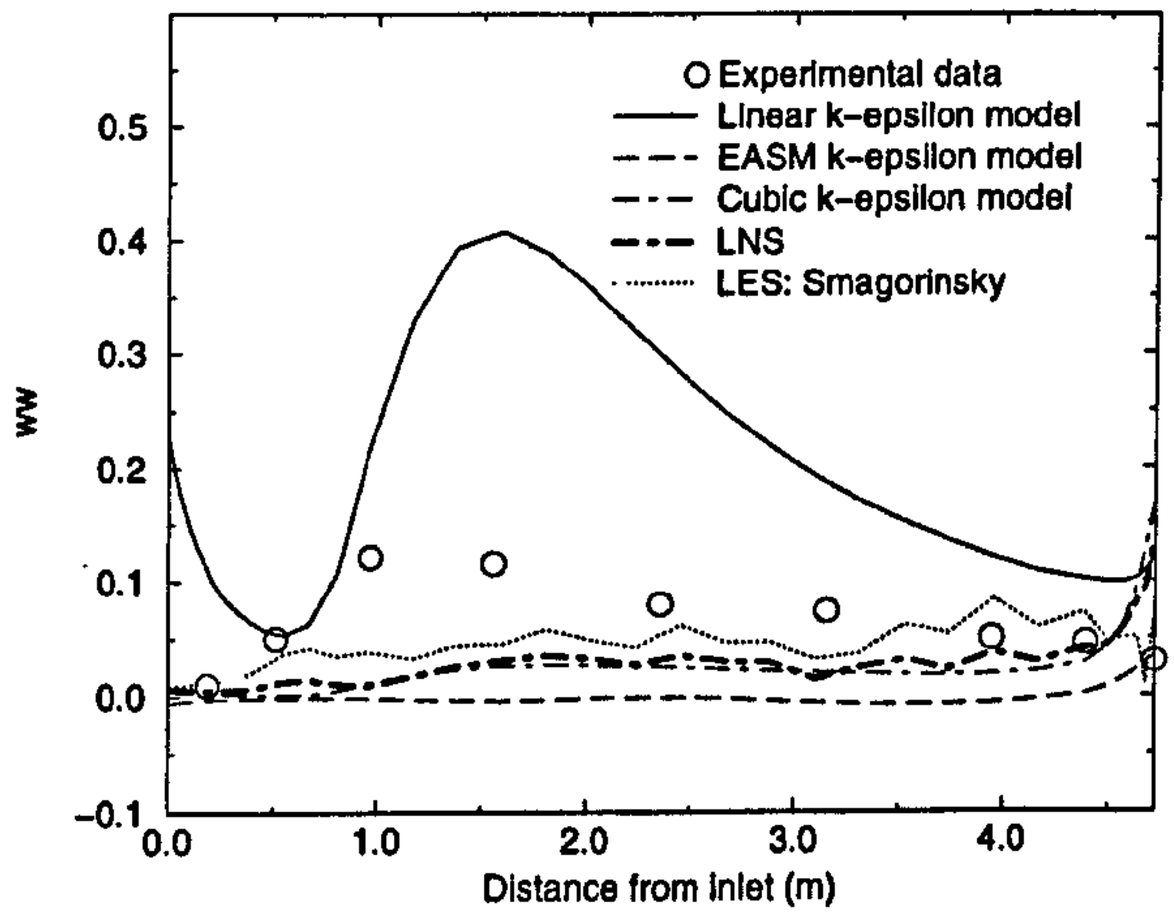

Figure 8.8: Normal Reynolds stresses τ_{zz}/ρ along the jet centerline.

8.9 shows the distribution of α for the LNS model along the jet centerline. Interestingly, the Figure shows, as perhaps might be expected, that most of the flow along the jet centerline is computed using RANS.

The difference between the LNS and the other models is also illustrated in Figure 8.10. This figure shows predicted streaklines for the linear $k-\epsilon$, cubic, Smagorinsky and LNS models. The LNS streaklines are a compromise between the smooth RANS predictions and more chaotic LES. Asymmetries in the RANS streaklines are due to asymmetries in the weightless particles seeding used to generate the streaklines.

8.2.2 Near-wall behaviour

As discussed in previous chapters, near-wall effects in ventilated rooms are important since average y^+ values tends to be of smaller magnitude than in most engineering flows.

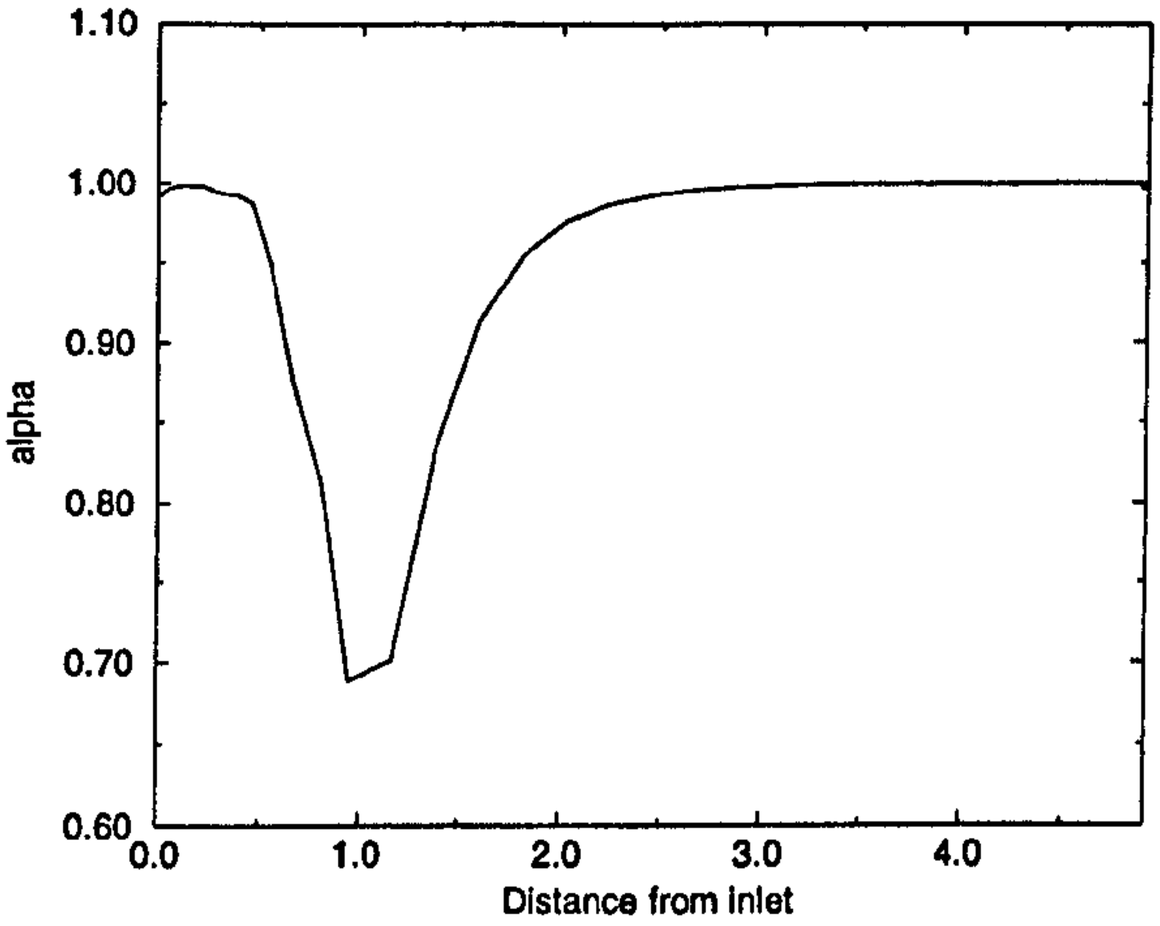

Figure 8.9: Centerline distribution of α for the LNS model.

Figure 8.11 plots measured and predicted velocity profiles $A2$, $A4$, $A6$ and $A8$ (see Figure 8.1) in the lower part of the room ($0 < y < 2.5\ m$). The figure shows that the cubic model gives excellent agreement with measurements. As for the jet centerline, the cubic model has higher predictive accuracy for $x < 2.5\ m$ and the EASM has better accuracy for $x > 2.5\ m$. The cubic model's prediction for $x > 2.5\ m$ can probably be improved by adopting the c_μ formulation of Craft *et al.* (1999). The latter shows improved accuracy for impinging jets.

Figure 8.11 shows that in the near-wall region ($y < 0.25\ m$) the turbulence models predict different flow structures. This is emphasied by Figure 8.12 which shows a top view ($x - z$ plane) of the velocity contour plot in the lower part of the room (at $y^+ \simeq 30$) for the EASM and cubic $k - \epsilon$ models. Owing to symmetrical property of the flow using RANS modelling, results are only presented for half of the room. Figure 8.12

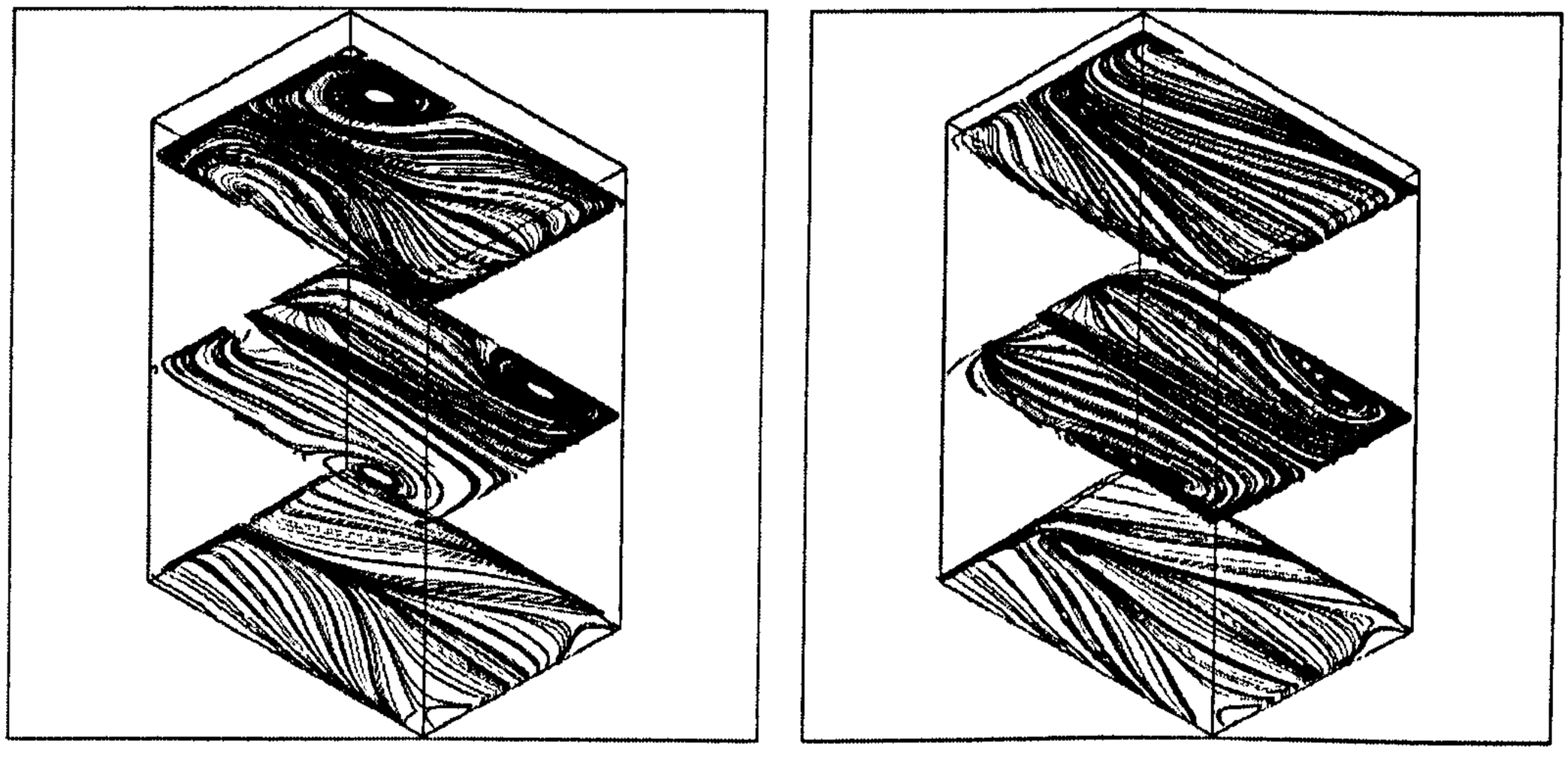

(a) (b)

(c) (d)

Figure 8.10: Streaklines in the room. (a) Linear $k-\epsilon$, (b) cubic, (c) LES (Smagorinsky) and (d) LNS models.

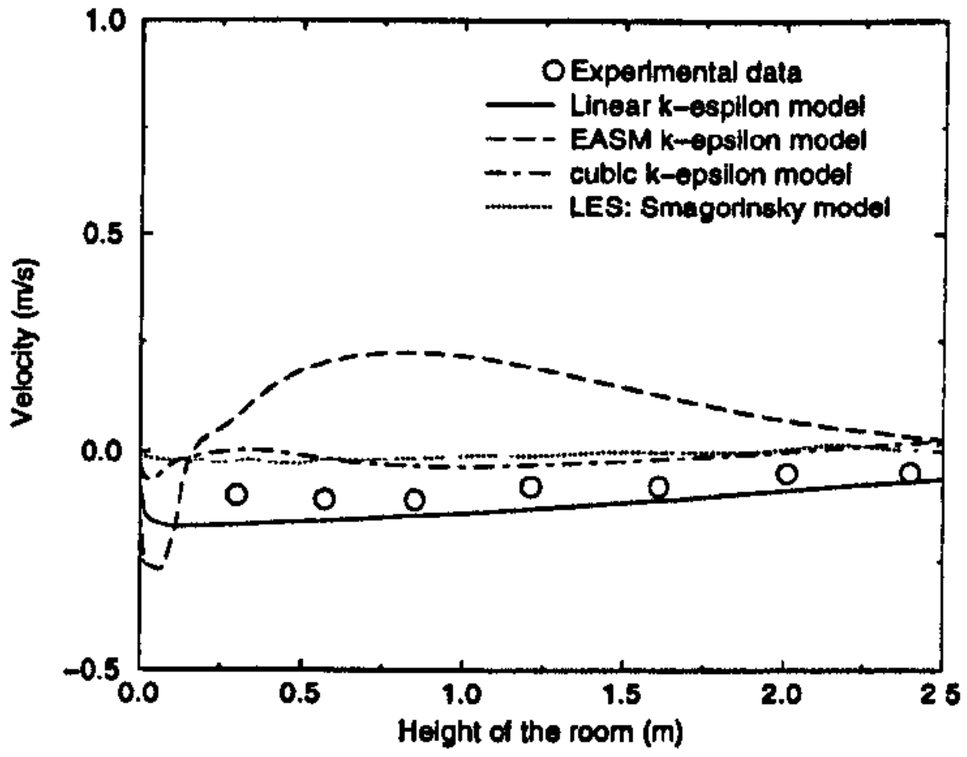

(a)

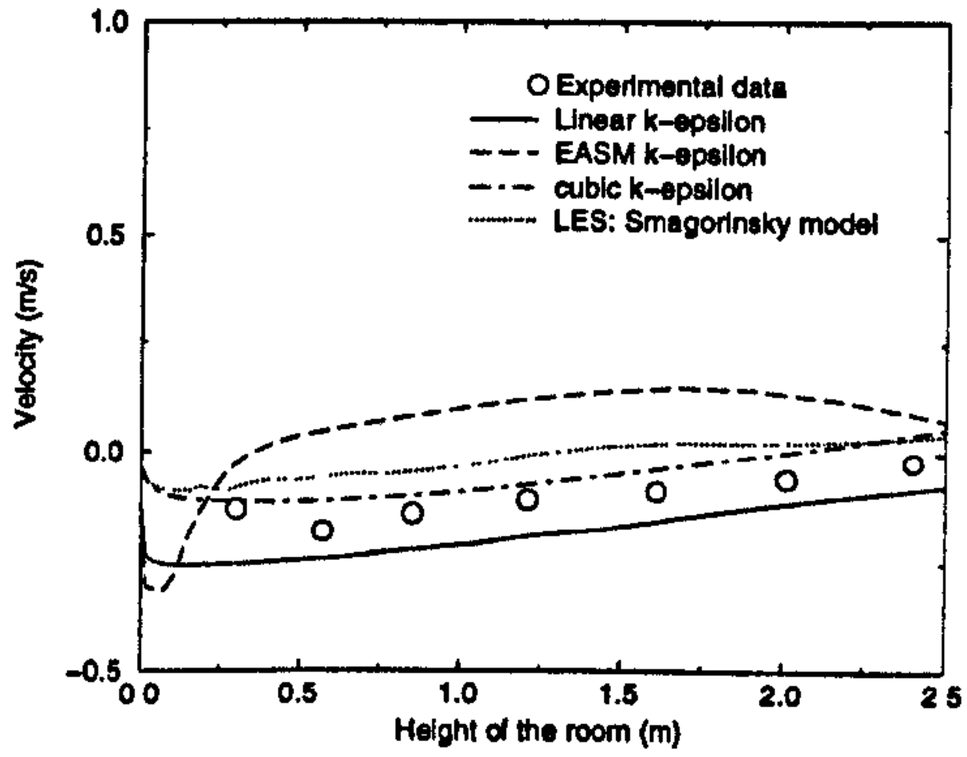

(b)

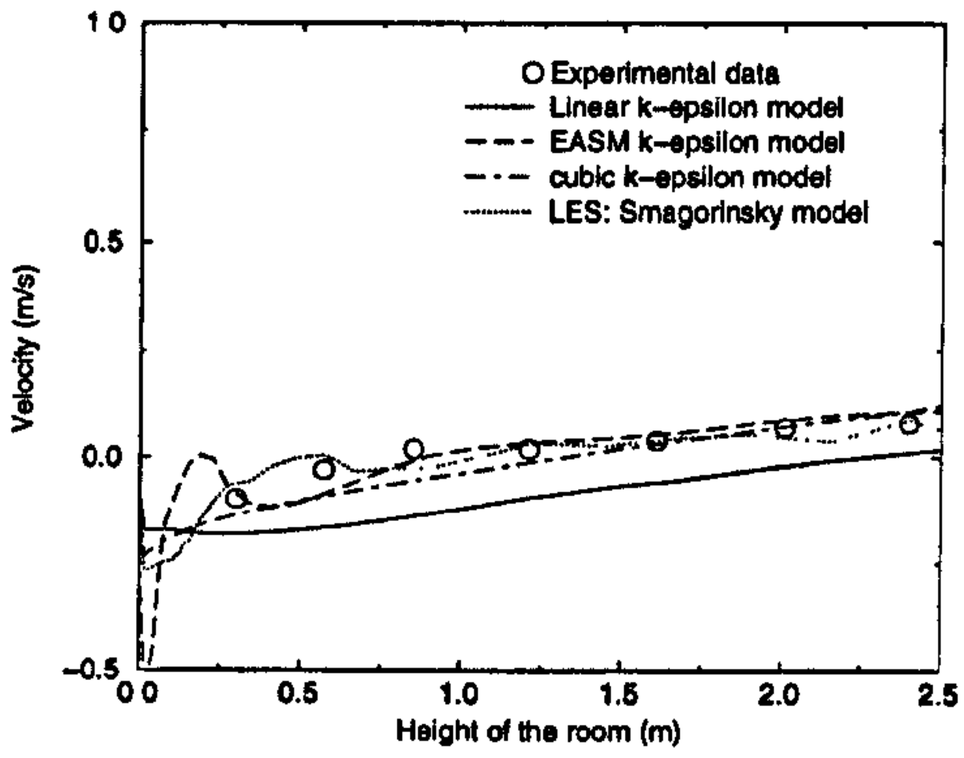

(c)

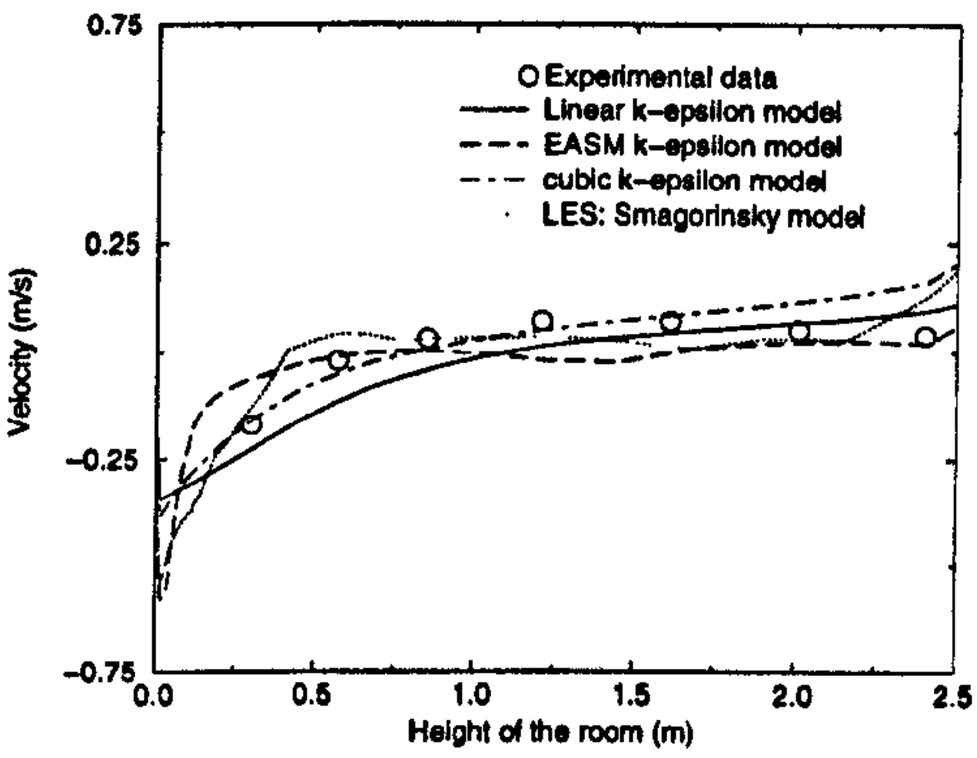

(d)

Figure 8.11: Velocity profile in the lower part of the room. (a) Profile A2, (b) profile A4, (c) profile A6 and (d) profile A8.

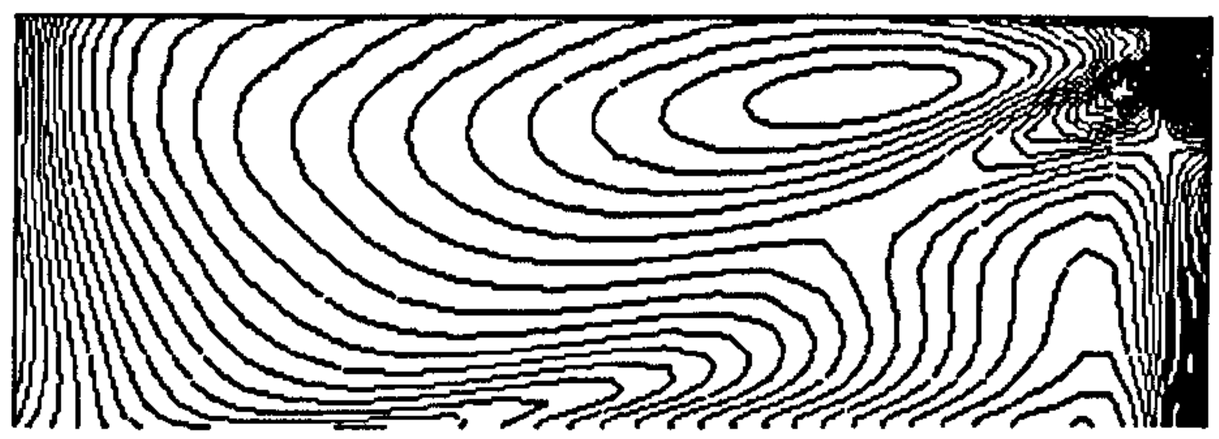

(a)

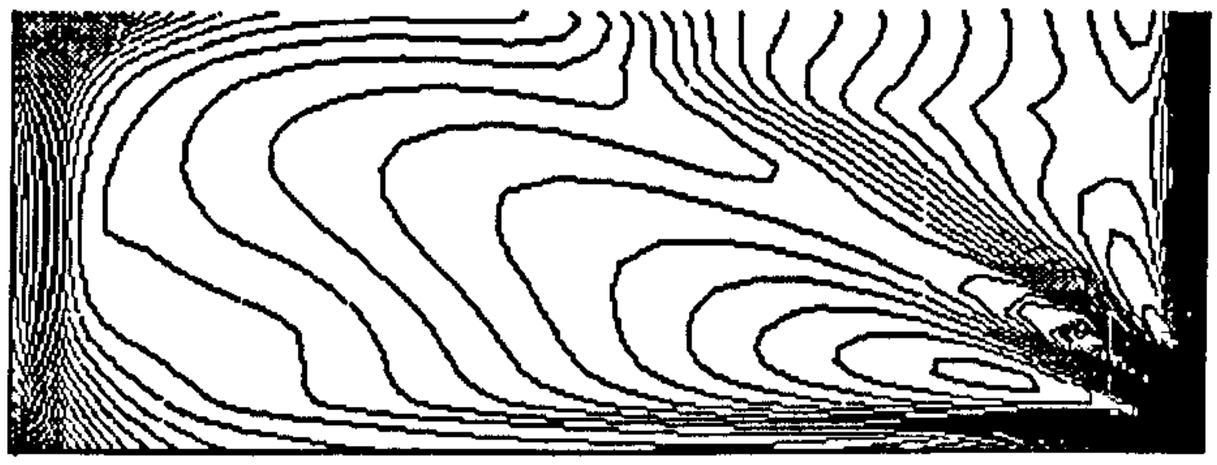

(b)

Figure 8.12: Contour plot of velocity at $y^+ \simeq 30$ in the lower part of the room. (a) Cubic model and (b) EASM $k-\epsilon$ model.

(a) shows the cubic's velocity contour plot for $0 < x < x_{max}/2$. Figure 8.12 (b) shows the other side of the room's velocity contour plots ($x_{max}/2 < x < x_{max}$) as predicted by the EASM. The figure highlights different flow structures in the near-wall area for different turbulence models and is consistent with the results of Figure 8.11. Owing to a lack of experimental data in that area, no firm conclusions can be made on the accuracy of the numerical simulations.

8.3 Conclusions

A CFD analysis of the flow inside a simply ventilated room has been conducted. Mixing-length models are found to greatly under-estimate the initial jet development. Because of this, they are not further considered here for the numerical modelling of ventilated rooms. It could, however, be expected to find that in more conventional ventilated

rooms, without high-velocity inlet jets, the mixing-length models will perform better than presented in this chapter. The EASM and cubic model are found to increase the accuracy predictions of velocities by $\simeq 6\%$ when compared to their linear equivalents. Also they are found to give significant improvements when considering normal Reynolds stresses along the centerline of the inlet jet. Generally, excellent agreement is found between measurements (both velocities ($< 6\%$) and Reynolds stresses) and the LES (Smagorinsky model (1963)). The Yoshizawa (1993) LES model underpredicts the velocity of the jet centerline and has similar Reynolds stress predictions to the cubic model. The LNS appears as a promising model and shows here best velocity agreements with measurements ($< 5\%$). Excellent agreement with measured Reynolds stresses is also found especially for τ_{yy}.

Chapter 9

Modelling of gas tracer decay in an office

It is often found that studies of ventilated rooms are focused on air quality rather than airflow patterns. In Shaw's (2000) investigation, the decay analysis of a contaminant source (SF_6 gas tracer) aims to evaluate the effects of a range of parameters on ventilation efficiency. The parameters tested include the design and layout of the diffusers (inlet and outlets) and the layout of the ventilated space. A total of fifteen configurations are analysed by Shaw *et al.* (1993-a) and Shaw *et al.* (1993-b) and are summarised in Shaw (2000). Case 1 of Shaw (2000) illustrated by Figure 9.1 is used in this investigation. The layout includes two desks, a filing cabinet, a bookcase and a partition surrounding the working area. Dimensions details are given in Table 9.1. The case is chosen to demonstrate the predictive accuracy of CFD for gas tracer decay in a ventilated space.

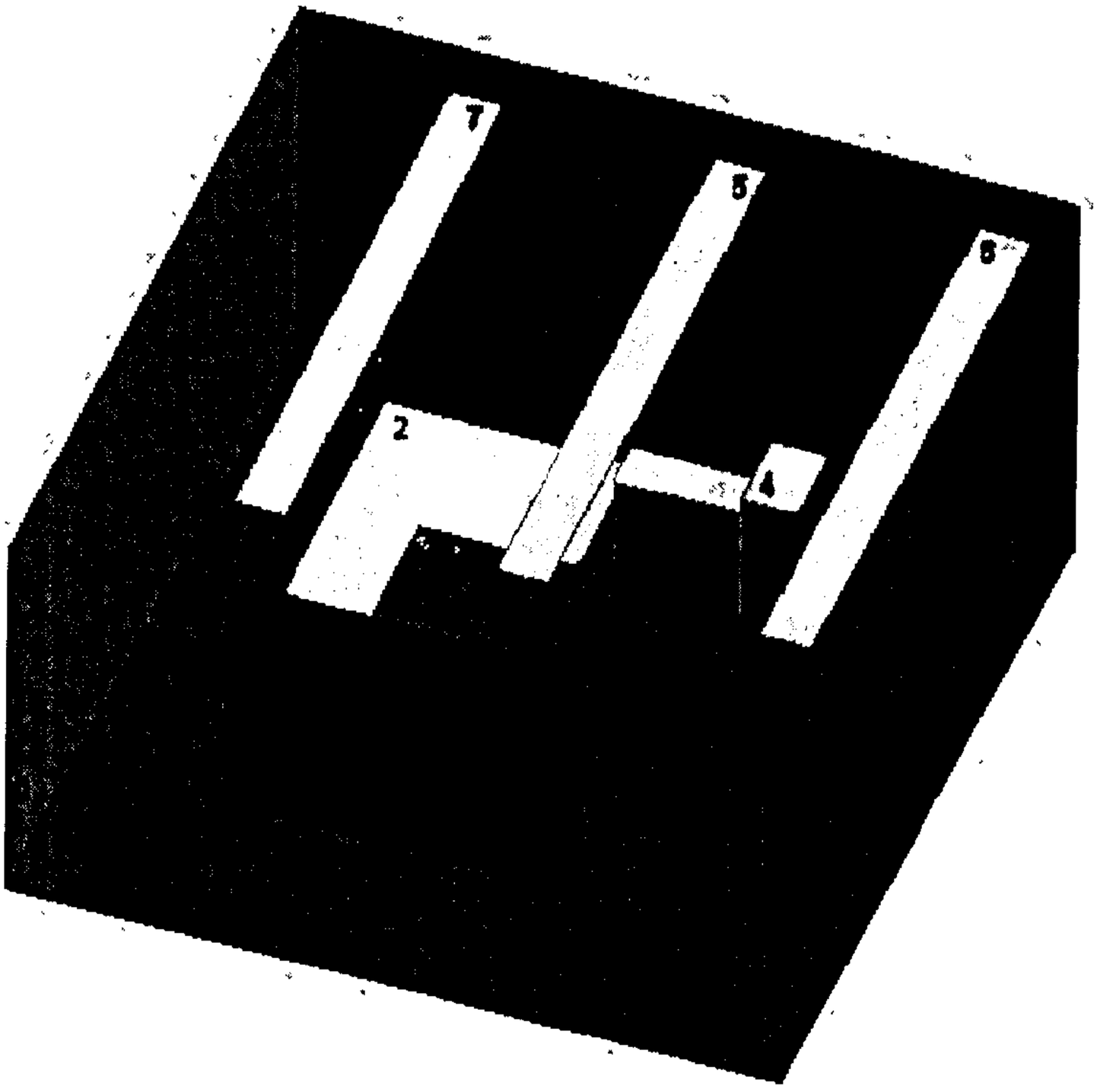

Figure 9.1: Shaw's room layout: 1: Partition; 2: Two desks; 3: Bookcase; 4: Filing cabinet; 5: Inlet; 6 & 7: Outlets.

Label	x_{min}	x_{max}	y_{min}	y_{max}	z_{min}	z_{max}
0	0.0	4.877	0.0	2.9	0.0	4.877
1-a	0.915	0.965	0.0	1.9	1.077	3.800
1-b	0.965	3.175	0.0	1.9	3.750	3.800
1-c	0.965	3.961	0.0	1.9	1.077	1.127
1-d	3.911	3.961	0.0	1.9	1.127	3.094
2-a	0.965	2.514	0.550	0.600	1.127	2.042
2-b	0.965	1.513	0.550	0.600	2.042	3.750
3	2.514	3.393	0.0	1.100	1.127	1.432
4	3.393	3.911	0.0	1.440	1.127	1.645
5	2.425	2.750	2.9	2.9	0.638	4.239
6	0.900	1.225	2.9	2.9	0.638	4.239
7	3.950	4.275	2.9	2.9	0.638	4.239

Table 9.1: Room dimensions (m). Label 1-a to 1-d corresponds to the four sides of the partition. Label 2-a ands 2-b are the two desks.

9.1 Numerical modelling

In Shaw's (2000) investigation, the ventilation efficiency in a real office is studied. To model this office, four main assumptions are made. These concern the definition of the inlet and outlets of the ventilation system, the definition of the room's furniture, the distribution of heat in the room and assumptions on the SF_6 gas tracer.

As discussed in Chapter 6, the numerical modelling of diffusers is critical in CFD modelling of ventilated rooms. Case 1 of Shaw (2000) uses a light troffer diffuser for the inlet and grilles for the outlets. Light troffer diffusers exists under many forms (see http://www.metalaire.com/dfltrof.htm) and can be compared to slot diffusers. The inlet diffuser is here assumed as a plain opening with a flow direction normal to the ceiling. The outlet diffusers are assumed to have a minor influence on the airflow pattern. Thus, they are also modelled as a plain opening with a flow direction normal to the wall. The outlets are set to conserve mass flow. The inlet and outlets velocities are as follows: $6.0756 \cdot 10^{-2}\ m/s$ and $3.0378 \cdot 10^{-2}\ m/s$ respectively.

The room contains heat sources (a PC, lightings and the equivalent heat load of a person) but, very little is known about the location and intensity of these sources. Moreover, no data are available on outlet and surface temperatures and on the distribution between convective and radiant heat. In displacement-ventilated rooms, thermal effects are crucial but here the room is mixed-ventilated. Owing to a lack of information on thermal boundary conditions an isothermal analysis is made first.

The furniture is assumed to be solid blocks. To enable the prediction of the near-floor airflow, the two desks are modelled as thin plates.

The SF_6 tracer gas is assumed to be a weightless particle and is modelled as a passive scalar (see Section 3.1.5). The transport equation for a passive scalar uses the standard gradient approach in which the turbulent contributions to the scalar transport are modelled by a linear relation. In this study, the contribution of the non-linear part of the Reynolds stresses to the scalar transport is not included. Thus, it is perhaps expected to find only minor changes in concentration predictions between linear and non-linear eddy-viscosity models. A scalar transport equation that accounts for the non-linear part of the Reynolds stress tensor is left as future work and is expected to further improve prediction accuracy.

For the SF_6 decay simulations, an initial steady-state velocity field is used. From this steady state, a concentration of 210 *ppb* (corresponding to the release of 14 *ml* of SF_6) is set at the inlet of the ventilation system. Unsteady RANS (URANS) is then used (with a fully implicit time scheme) to predict the time-decay of SF_6. The results presented in this chapter have been obtained using a CONDIF scheme (see Chapter 4).

For this analysis, a grid containing $111 \times 59 \times 111$ (x, y, z) nodes is used. This gives an averaged first off-wall node $y^+ \simeq 1.0$ inside the partitioned area and $y^+ \simeq 0.7$ in the room. The linear and EASM $k - \epsilon$ models use the Lam-Bremhorst (1981) damping function. The cubic $k - \epsilon$ model of Craft *et al.* (1996) is used with the Yap (1987) correction.

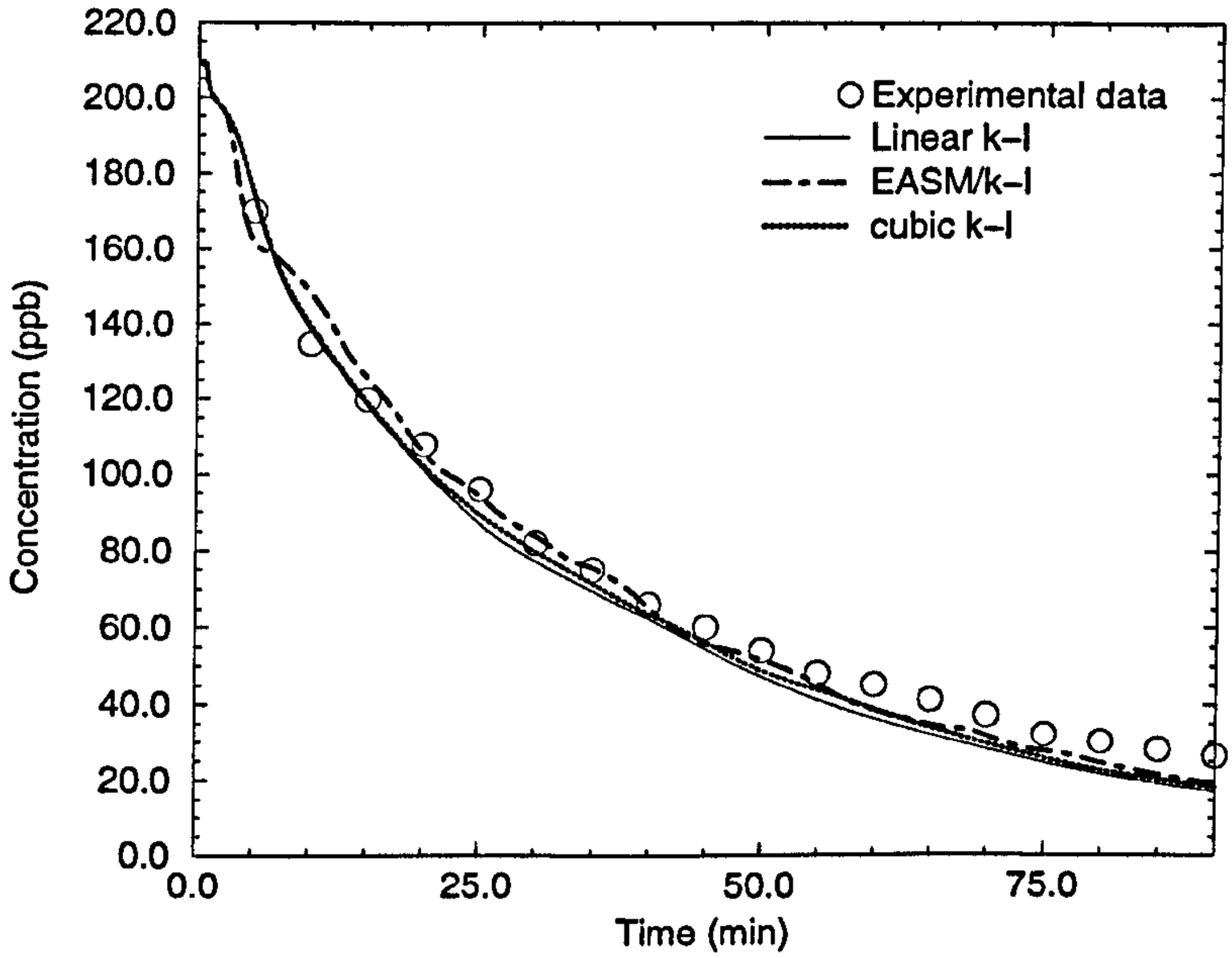

Figure 9.2: Time-decay of SF_6 in the room. Measurements and predictions of eddy-viscosity models in a $k-l$ framework.

9.2 Results and discussion

Figure 9.2 compares SF_6 time-decay measurements with predictions of the linear, EASM and cubic $k-l$ models. The concentrations shown in Figure 9.2 are average of SF_6 at the breathing height ($y = 1.6\ m$) inside the partitioned area. The figure shows that both EASM and cubic models have better predictive accuracy than the linear model. The improvements are, however, found to be of minor importance. This result is expected since the scalar transport equation is identical for all three models. Changes in concentration observed in Figure 9.2 are thus due to prediction changes in airflow patterns.

The decay predictions found using a $k-\epsilon$ base model show similar agreements to the results shown in Figure 9.2. The difference between the models is emphasised by Table 9.2 which compares relative prediction errors of concentrations. The relative errors seen in Table 9.2 is obtained using Equation 4.3.

The table shows that the linear $k-\epsilon$ model has better accuracy ($\simeq 4\%$) than the linear $k-l$ model (worse averaged prediction error $\simeq 14.5\%$). The EASM $k-l$ gives best overall agreement with measurements (9.7% error). The EASM in a $k-\epsilon$ framework is found however to have be less accurate by +0.6% than its linear equivalent. The table also indicates that the relative error of the $k-l$ based models increases with time. This is not so for the $k-\epsilon$ based models. This can partly be explained by Figure 9.3 which shows a snapshot of velocity contour plots at the breathing height ($y = 1.6\ m$) at $t = 20\ mins$. The figure shows that the flow features of the two $k-l$ models are similar but differ from the flow features predicted by the $k-\epsilon$ models. As in Chapter 8 different flow features are predicted by different models. Also, the linear $k-l$ model again has lowest predictive accuracy.

The work of Shaw (2000) aims to assess ventilation performances in the room. Following Shaw's (2000) procedure, a comparison of the ventilation efficiency in the room is made. The ventilation efficiency (E_f) index of Shaw (2000) is defined as follows:

$$E_f = \frac{C_{ra} - C_S}{C_{ws} - C_S} \tag{9.1}$$

where C_{ra} is the concentration at the room exhaust, C_S, the concentration at the room supply and, C_{ws}, the concentration in the breathing zone inside the partitioned area. In the simulations, the SF_6 tracer gas is supplied at the time $t = 0$ only. Thus, unlike measurements, no concentration is observed at the inlet itself for $t > 0\ s$. To compare

Time (min)	Linear		EASM		cubic	
	$k-l$	$k-\epsilon$	$k-l$	$k-\epsilon$	$k-l$	$k-\epsilon$
5	1.8	9.0	-4.5	11.7	3.3	10.3
10	2.15	14.8	9.5	14.6	3.3	14.7
15	-1.6	7.7	4.3	11.7	-0.9	9.5
20	-5.9	1.9	-2.3	8.3	-5.5	4.5
25	-9.3	-3.1	-2.2	7.3	-7.1	1.9
30	-6.1	-2.4	2.2	13.4	-2.9	-2.1
35	-7.6	-2.7	0.7	13.3	-4.9	-2.4
40	-5.8	-7.6	-1.1	15.1	-3.8	-5.6
45	-9.8	-11.7	-7.3	11.7	-6.7	-9.2
50	-12.5	-7.1	-4.5	15.2	-9.1	-9.7
55	-9.4	-12.5	-5.6	12.5	-14.6	-11.7
60	-20.0	-15.6	-14.7	12.2	-14.2	-14.5
65	-22.9	-15.8	-15.9	10.7	-18.1	-15.1
70	-24.9	-16.0	-14.9	11.1	-20.3	-15.5
75	-24.3	-12.5	-14.7	10.9	-19.7	-12.3
80	-28.7	-15.0	-19.3	10.0	-25.0	-14.1
85	-32.5	-14.3	-23.6	3.6	-27.9	-13.0
90	-36.2	-15.1	-28.3	3.8	-31.3	-12.2
Average	**14.5**	**10.3**	**9.7**	**10.9**	**12.1**	**9.9**

Table 9.2: Relative prediction error (%) of concentration decay for the models tested.

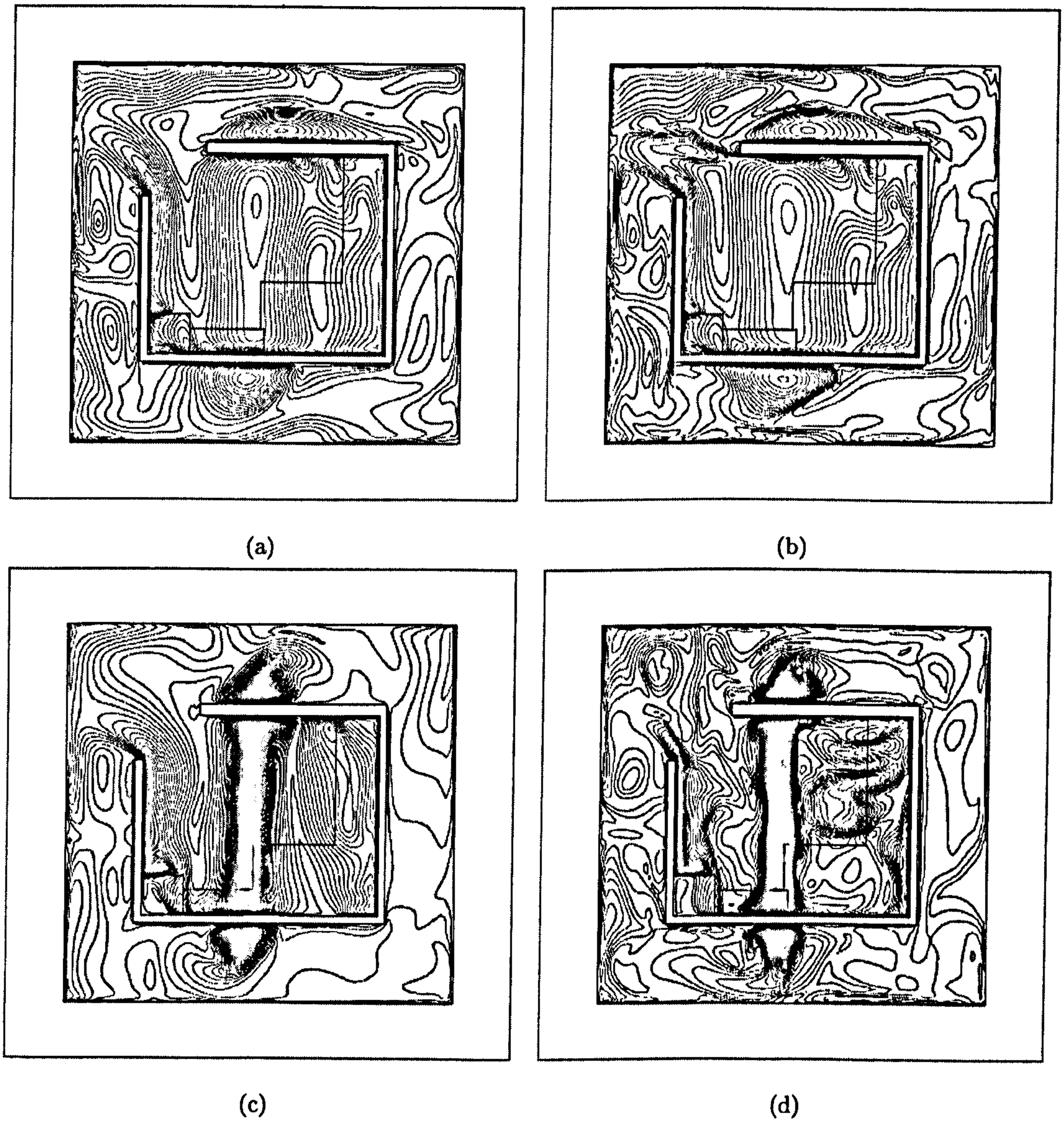

Figure 9.3: Velocity contour plots in the breathing zone ($y = 1.6\ m$) for (a) $k - l$, (b) cubic $k - l$, (c) $k - \epsilon$ and (d) EASM $k - \epsilon$ models.

Measurements	Linear		EASM		cubic	
	$k-l$	$k-\epsilon$	$k-l$	$k-\epsilon$	$k-l$	$k-\epsilon$
0.90	0.960	0.938	0.913	0.926	1.199	1.095
Error (%)	6.67	4.22	1.44	2.89	33.22	21.67

Table 9.3: Ventilation efficiency index E_f at the time $t = 20$ *mins*.

measurements with predictions, the ventilation efficiency index E_f is re-written in a simpler form as:

$$E_f = \frac{C_{ra}}{C_{ws}} \tag{9.2}$$

This index is identical to the contaminant-removal index of Collignan and Riberon (2000). A ventilation efficiency index $E_f < 1$ is preferred and indicates higher concentration at the exhaust than in the breathing zone of the room. $E_f > 1$ indicates a low ventilation efficiency. Predicted concentrations at the room exhaust are taken as averaged concentration over the surface area of the exhaust. Table 9.3 compares measured and predicted ventilation efficiency index E_f at the time $t = 20$ *mins*. The table shows that the EASM (in either a $k-l$ or $k-\epsilon$ form) gives excellent agreement with measurements ($< 3\%$ error). Like in Table 9.2, the linear $k-\epsilon$ has better prediction accuracy than the $k-l$ model. Both EASM and linear models predict $E_f < 1$ and indicate satisfactory ventilation efficiency. However, the cubic model (in either a $k-l$ or $k-\epsilon$ form) predicts low concentration at the exhaust of the room. Hence, for the cubic model, $E_f > 1$. This does not agree well with measurements since it indicates low ventilation efficiency.

Despite having made significant assumptions on the thermal behaviour in the room, the decay predictions are found to agree well with measurements. Owing to problem-

definition issues, it is expected to find that a non-isothermal analysis would not reveal any significant changes. Thus, the non-isothermal analysis is not carried out. However, it can be expected that the presence of heat flux in the room would increase the vertical motion of particle from the partitioned area towards the room exhaust. This would further increase predicted ventilation efficiency.

9.3 Conclusions

This analysis demonstrates the potential of non-linear eddy-viscosity models in predicting time decay of pollutants in ventilated spaces. The linear $k-\epsilon$ model is found to have better predictive accuracy than the linear $k-l$ model. The EASM $k-l$ also perform well. It has excellent concentration agreement with measurements in the breathing zone (9.7% error) and at the room exhaust. The EASM $k-\epsilon$ model has lower predictive accuracy than its linear equivalent (for concentrations in the breathing zone only). The cubic model in either a $k-l$ or $k-\epsilon$ form shows good agreement with measured concentration in the breathing zone. However, the cubic model under-predicts concentrations at the room exhaust hence predicting low ventilation efficiency. Despite considering isothermal analysis the predictions show excellent agreement with measurements. Owing to problem definition issues and because isothermal predictions are found to agree well with measurements, non-isothermal analysis is not carried out. Also results presented here assume a standard gradient approach for the modelling of the scalar quantity. The use of a scalar transport equation that includes non-linear effects of the Reynolds stress tensor is left as future work and is expected to further improve prediction accuracy.

Chapter 10

Modelling of a displacement-ventilated office

As previously discussed, problem definition is key to an accurate CFD modelling of complex flows. The measurements of Yuan *et al.* (1999), like the measurements presented in Chapter 6 and 7, are aimed towards the validation of CFD codes. Hence a detailed description of the various boundary conditions is given. The case is chosen to demonstrate prediction accuracy in a non-isothermal displacement-ventilated room. However, as illustrated by Figure 10.1, the room is complex, possess numerous heat sources and, with regards to problem definition, is a more challenging case than the one of Chapter 6 and 7. The data of Yuan *et al.* (1999) comprises velocity and temperature measurements along nine vertical axis of the room (labelled M1 to M9 in Figure 10.1 (b)). The velocities are measured using hot-sphere anemometers and have an error of $\simeq 0.01\ m/s$. The temperature errors are known to be about $0.3°C$.

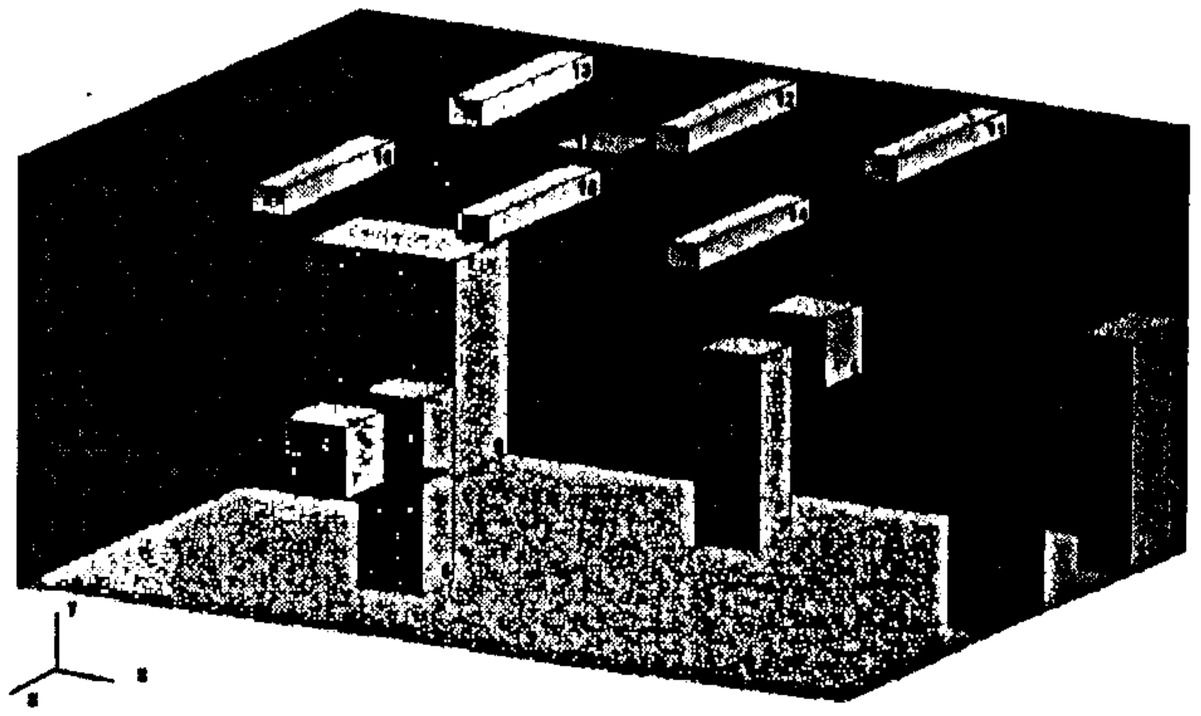

(a)

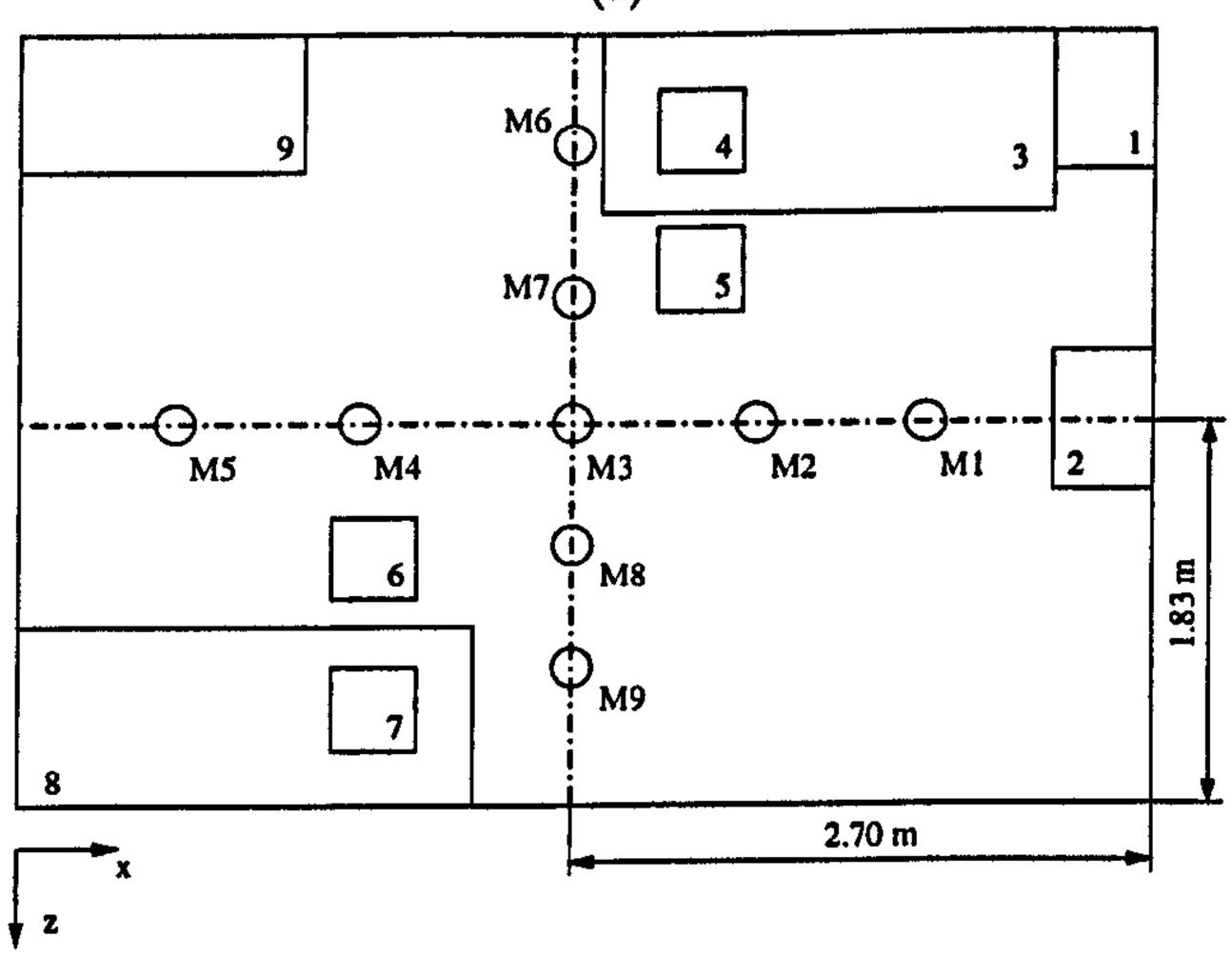

(b)

Figure 10.1: Room layout. (a) Three-dimensional view and (b) top view with location of measurement points.

10.1 Numerical modelling

Table 10.1 summarises the dimensions, location and heat load of each of the room's components. The displacement-ventilation unit (labelled 2 in Figure 10.1) is defined as a three-dimensional block. The room inlet, however, is only one side of the ventilation unit, the side facing the window. Like most displacement-ventilated units, a grille is present at the inlet's surface. This grille implies that only 10% of the inlet area is effective. Since the grille is not modelled here, the inlet velocity is evaluated according to the effective area of the diffuser. The ventilation settings of four air changes per hour correspond to an inlet velocity of $\simeq 0.834\ m/s$. The outlet, modelled by a plain opening in the ceiling, is set to conserve mass flow having a velocity of $\simeq 0.265\ m/s$. The inlet and outlet flow temperatures are set to $17.2°C$ and $24.1°C$ respectively. A grid of $117 \times 69 \times 83$ $(x,\ y,\ z)$ nodes is used for the simulations. This grid gives an average first off-wall $y^+ \simeq 0.9$.

10.1.1 Thermal aspects

In this displacement-ventilated room, buoyancy and thermal effects are expected to be of significant importance. Thus only non-isothermal analyses are made. To model buoyancy effects, the appropriate source terms are added to the momentum (in the vertical direction), k and ϵ equations (see Section 3.1.5). A summary of heat loads for each of the room components is given in Table 10.1. The heat load given in the table includes both convective and radiant effects. The distribution between radiant and convective heat is not given here and, radiant effects are not modelled in this study. Only convective heat loads are used and, they are given as follows:

Label	Description	x_{min}	x_{max}	y_{min}	y_{max}	z_{min}	z_{max}	Q (W)
0	Room	0.0	5.16	0.0	2.43	0.0	3.65	-
1	Cupboard 1	4.83	5.16	0.0	1.32	0.0	0.58	-
2	Inlet	4.88	5.16	0.0	1.14	1.51	2.04	-
3	Table 1	2.50	4.81	0.74	0.75	0.0	0.75	-
4	PC 1	2.78	3.18	0.75	1.14	0.1	0.5	108.5
5	DIN 1	2.78	3.18	0.0	1.1	0.85	1.20	75
6	DIN 2	1.63	2.03	0.0	1.1	2.45	2.8	75
7	PC 2	1.63	2.03	0.75	1.14	3.15	3.55	173.4
8	Table 1	0.0	2.23	0.74	0.75	2.90	3.65	-
9	Cupboard 2	0.0	0.95	0.0	1.24	0.0	0.58	-
10	Window	0.0	0.02	0.94	2.1	0.16	3.50	-
11	Light 1	3.93	4.13	2.18	2.33	0.16	1.36	34
12	Light 2	2.63	2.83	2.18	2.33	0.16	1.36	34
13	Light 3	1.35	1.55	2.18	2.33	0.16	1.36	34
14	Light 4	3.93	4.13	2.18	2.33	2.29	3.50	34
15	Light 5	2.63	2.83	2.18	2.33	2.29	3.50	34
16	Light 6	1.35	1.55	2.18	2.33	2.29	3.50	34
17	Outlet	2.35	2.78	2.43	2.43	1.51	2.04	

Table 10.1: Dimensions of the room configuration (dimensions in m).

The shape and size of the lighting seen in Figure 10.1 seems to indicate that fluorescent neon lights are used. Each type of lighting has a different distribution of radiant to convective heat. For fluorescent neon lights, $\simeq$ 30% of the heat is assumed to be radiant (CIBSE (1999)). Here, this corresponds to a convective heat load of 23.8 W per light.

The room also contains two PCs. Again little is known about the distribution between radiant and convective heat for such equipment. For a desktop computer 85% of the heat can be assumed convective (CIBSE (1999)). For its monitor, the convective heat reduces to 65% of the total heat load. Here 85% of convective heat is assumed for both PCs. This corresponds to a convective heat load of $\simeq$ 92.2 W and $\simeq$ 147.4 W for PC 1 and PC 2 respectively.

Finally, two occupants are present in the room. As shown by Figure 10.1, the two occupants show strong similarities (in terms of shape and size) to the square DIN man discussed in Chapter 6 and 7. The radiant heat emitted by the square DIN man of Chapter 6 and 7 is evaluated to be $\simeq$ 35% of the total heat. Similar heat distribution is assumed for the two room occupants of Figure 10.1. The convective heat load is then $\simeq$ 65% of the total heat load or, 48.75 W for each occupant.

Measured surface temperatures are also used as boundary conditions. The data provided do not allow to specify a thermal stratification along each wall. Thus averaged wall temperature are used. These are as follows. Front wall: 22.65 $°C$, Back wall: 22.90 $°C$, East wall: 22.57 $°C$, West wall: 21.69 $°C$, Floor: $\simeq$ 21.87 $°C$ and Ceiling: 22.87 $°C$.

As seen in Figure 10.1, a large window is present in the room. In real rooms and offices, windows have an important role on airflow patterns (*i.e.* draught) and thermal regulation (*i.e.* solar heat gains). Calculations of heat loss/gain from windows depend on a wide range of parameters (*i.e.* window orientation, solar exposure, etc...) not available here. The window is treated as isothermal based on measurements.

10.2 Results and discussion

Figure 10.2 shows a selection of four velocity profiles for the linear (Lam-Bremhorst (1981)), EASM (AKN (1996)) and cubic (Craft *et al.* (1996)) $k-\epsilon$ models. The figure indicates that the $k-\epsilon$ models predict the correct behaviour of the velocity profile. It also shows that, for the four profiles, only minor differences are observed between the linear, EASM and cubic models. Figure 10.3 compares the same measured velocity profiles as seen in Figure 10.2 for the linear, EASM and cubic $k-l$ models. The figure shows that the velocity profiles of the linear, EASM and cubic $k-l$ models are not as monotonic as the ones predicted by the $k-\epsilon$ based models. It also shows that the differences between the linear, EASM and cubic models are greater when used in a $k-l$ framework.

The differences observed between the models is also illustrated by Figure 10.4 which shows the velocity contour plots in the room for the linear and EASM $k-\epsilon$ models. The velocity contours are taken in the plane containing the M1 to M5 measurements profiles. The $k-l$ based models show similar features as seen in Figure 10.4.

The accuracy of the models tested is emphasised by Table 10.2 which shows the relative error at each of the nine profiles. The errors given in Table 10.2 are obtained using equation 4.3. The table shows overall that the $k-\epsilon$ based models are more accurate

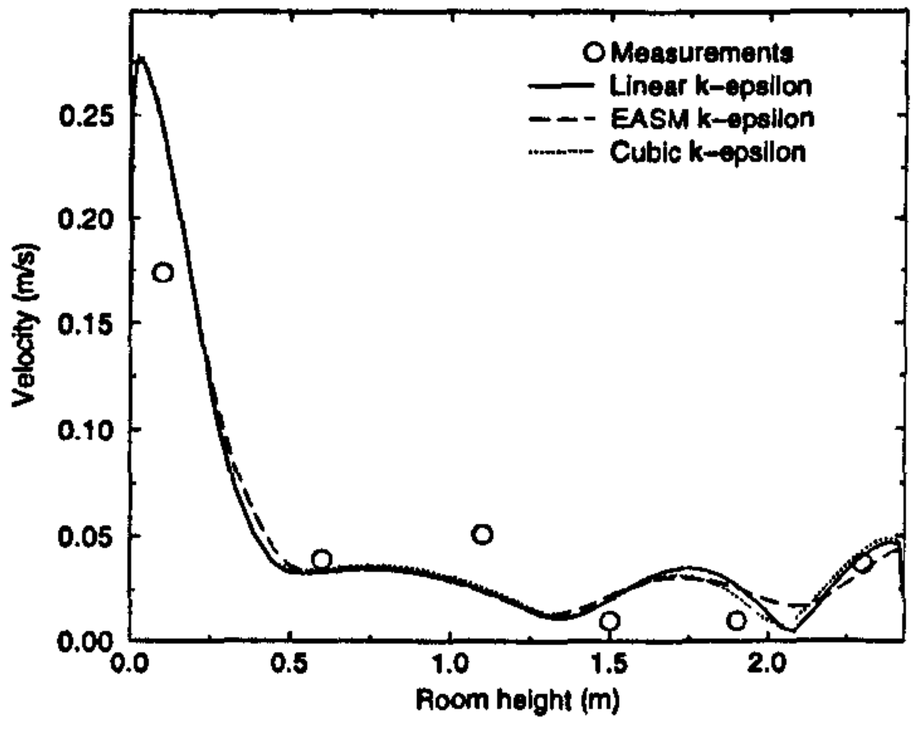

(a)

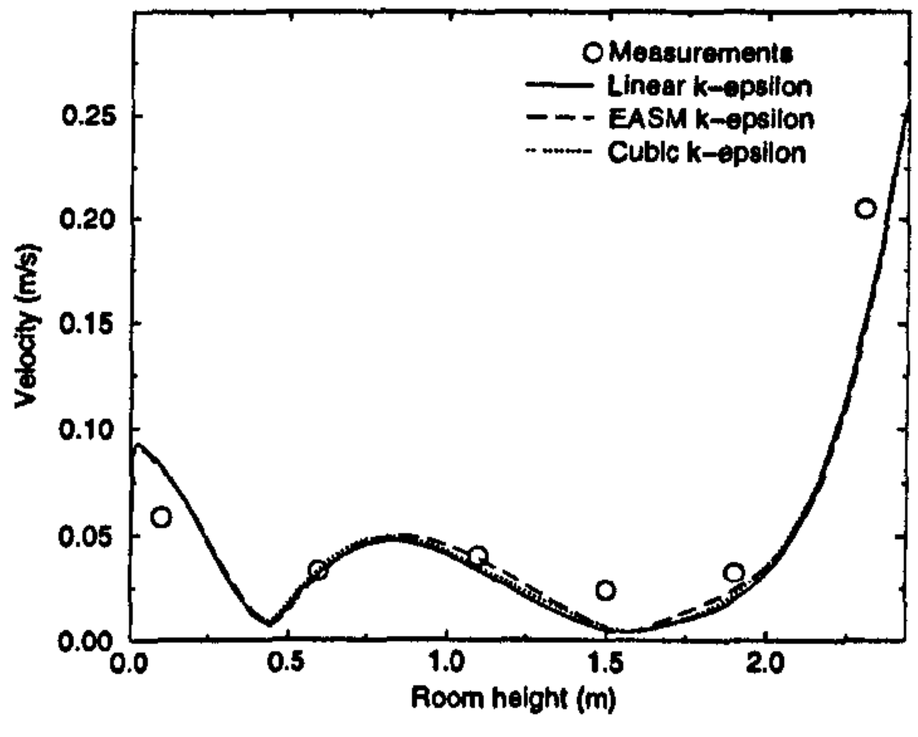

(b)

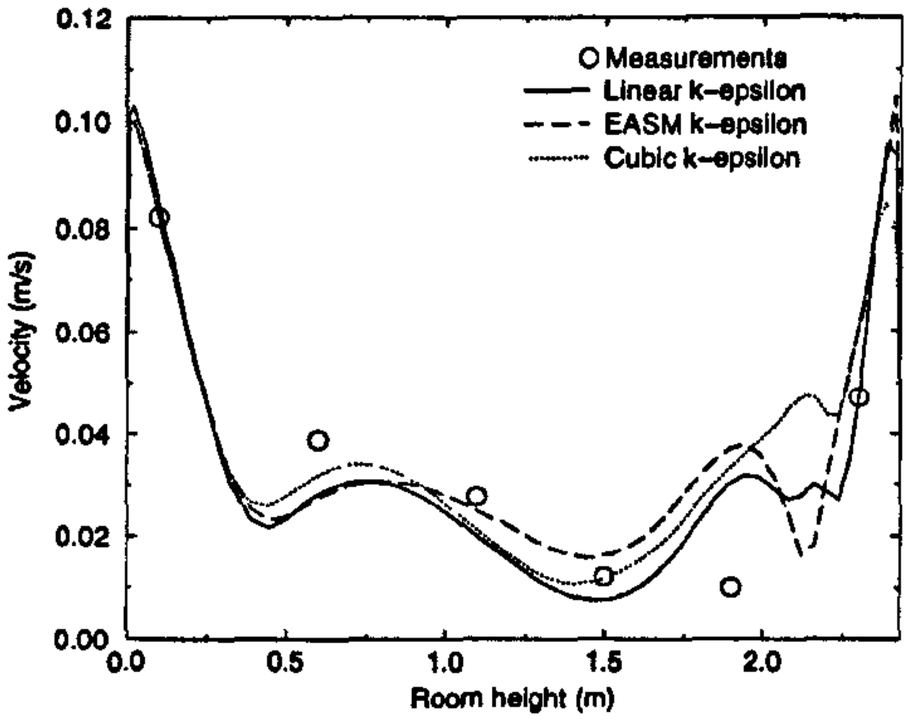

(c)

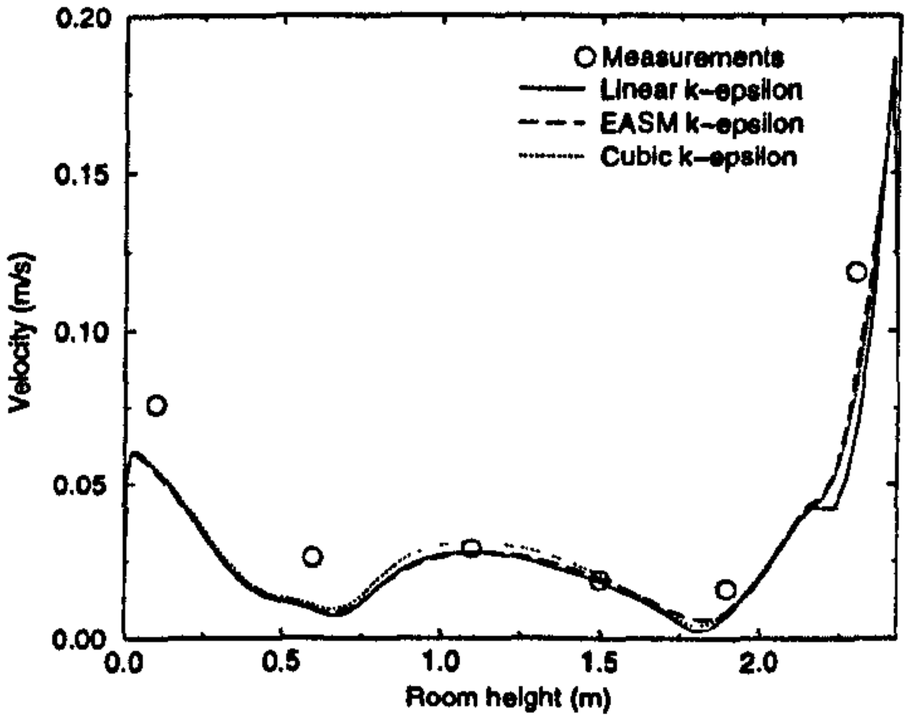

(d)

Figure 10.2: Comparison of measured velocity profiles (a) M1, (b) M3, (c) M7 and (d) M9 with predictions of the linear, EASM and cubic $k - \epsilon$ models.

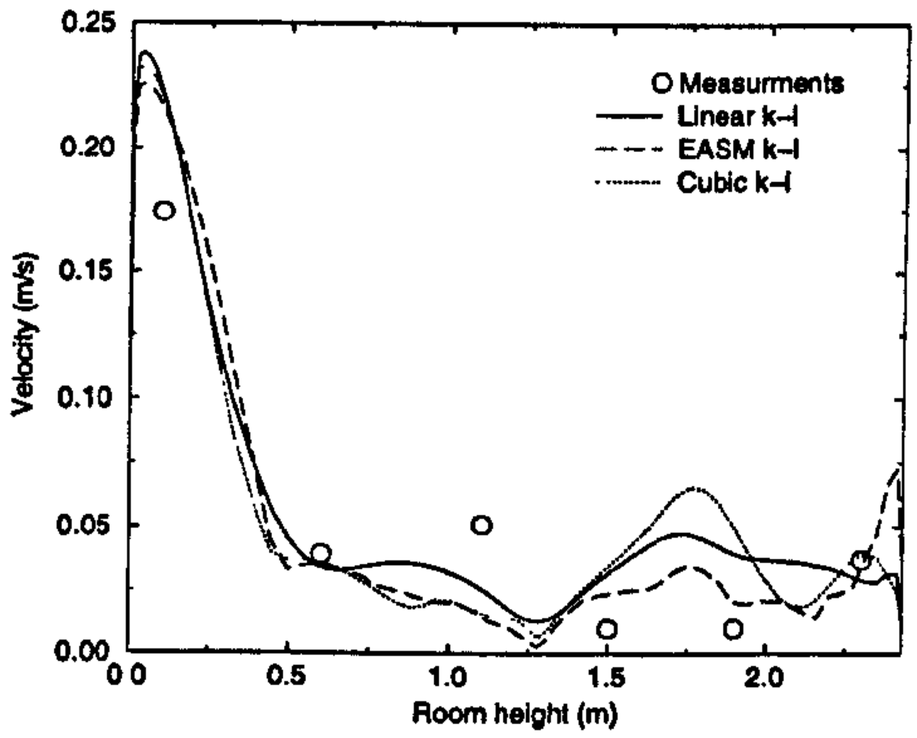

(a)

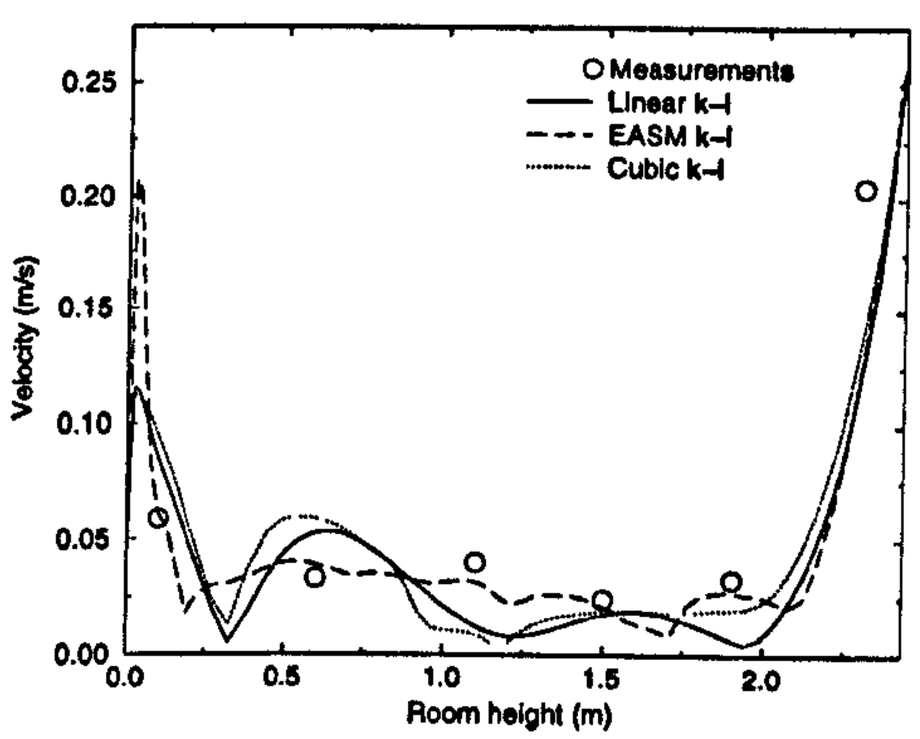

(b)

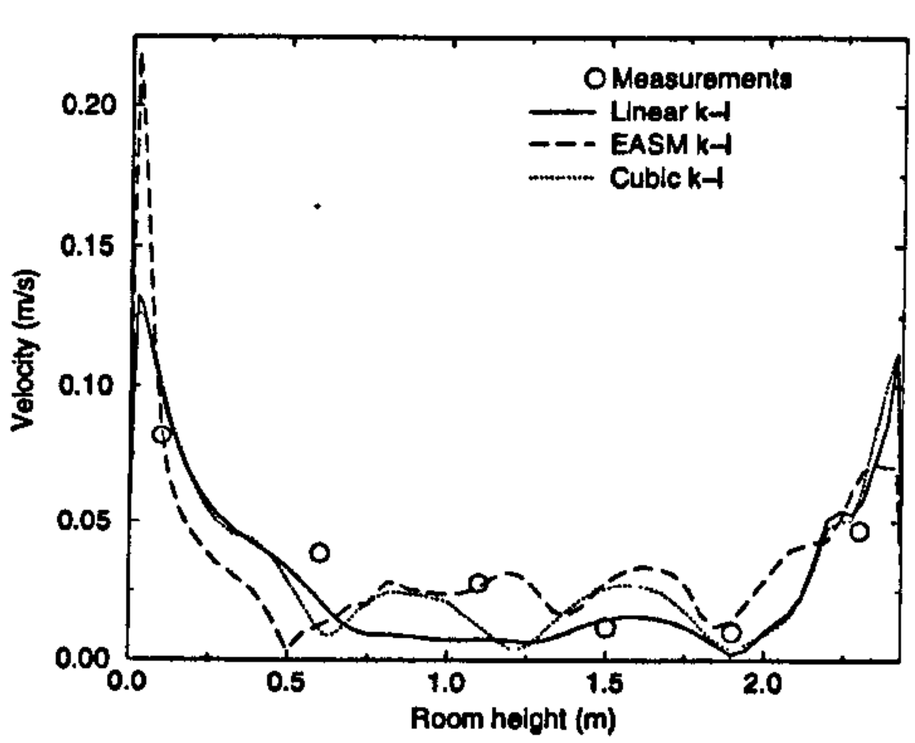

(c)

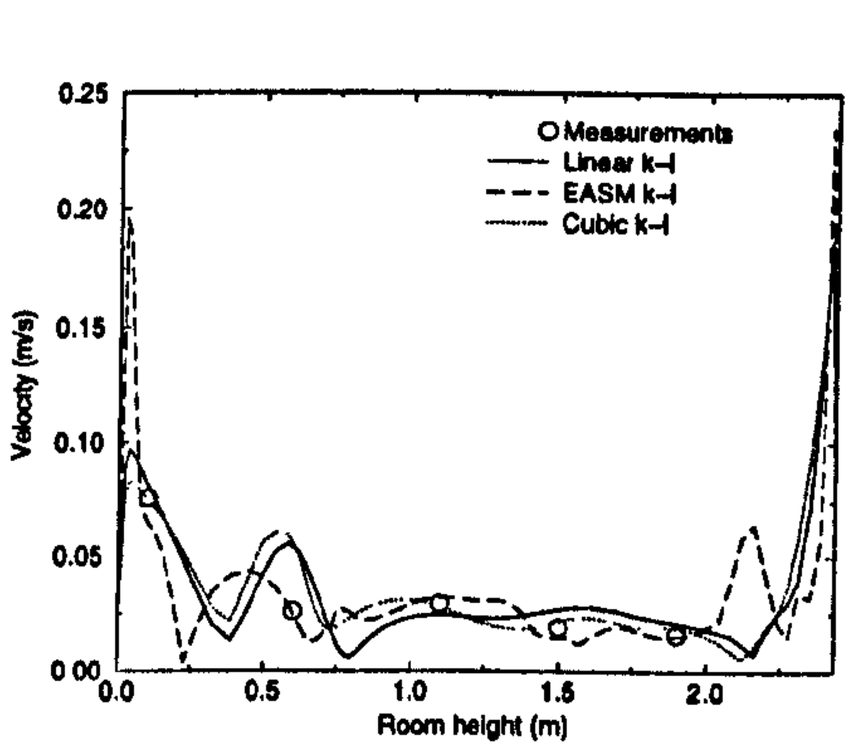

(d)

Figure 10.3: Comparison of measured velocity profiles (a) M1, (b) M3, (c) M7 and (d) M9 with predictions of the linear, EASM and cubic $k - l$ models.

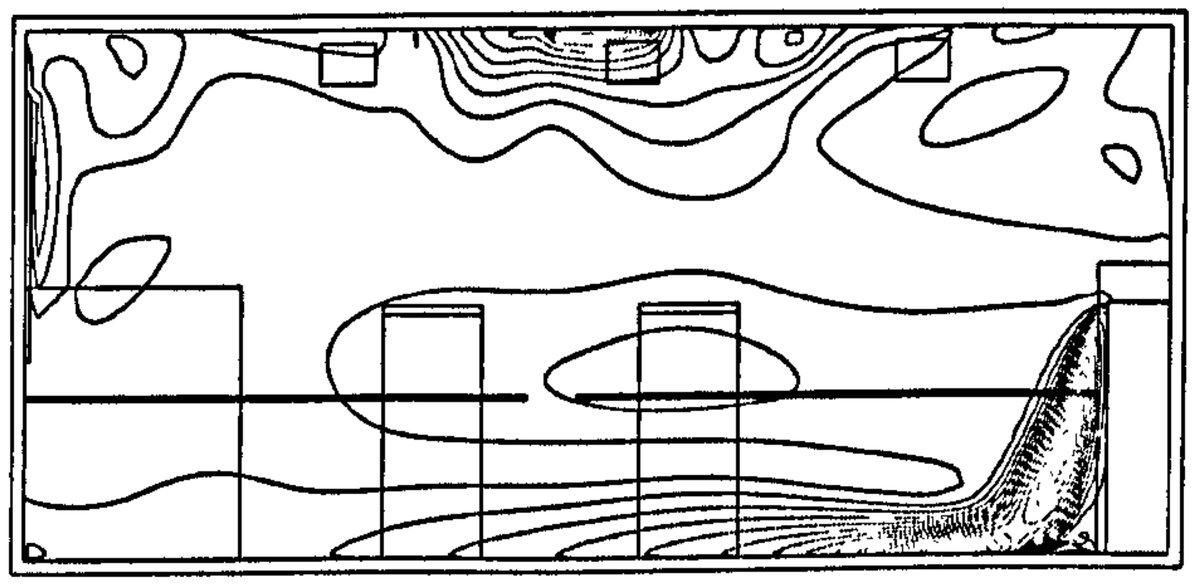

(a)

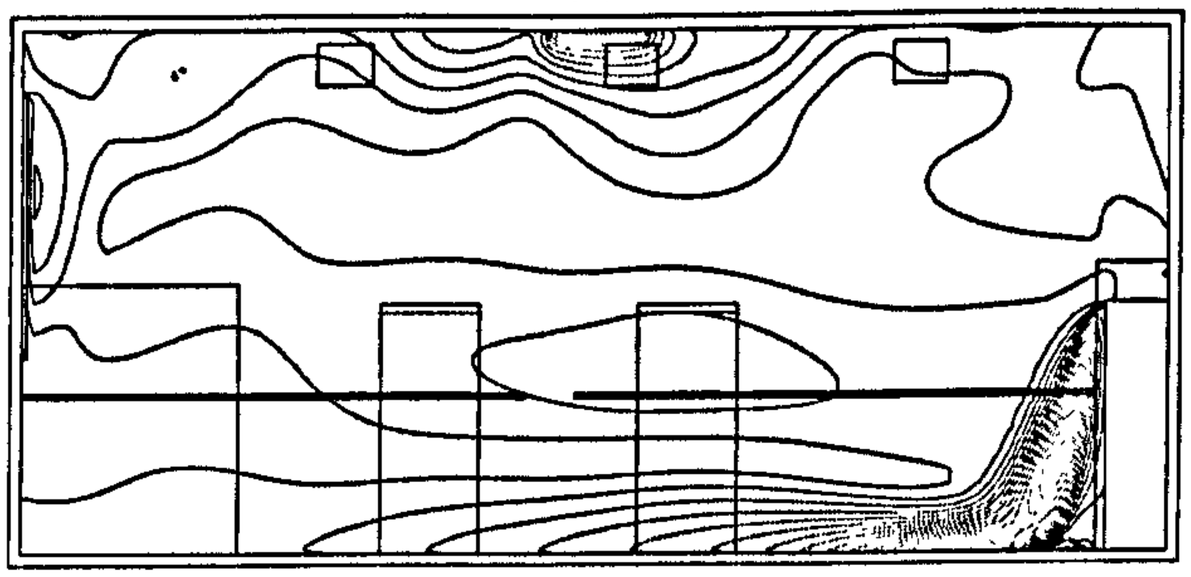

(b)

Figure 10.4: Velocity contour plots in the room for (a) the linear and (b) EASM $k-\epsilon$ models.

	$k-l$			$k-\epsilon$		
Profile	Linear	EASM	Cubic	Linear	EASM	Cubic
1	90.3	49.5	98.5	51.5	53.3	42.9
2	67.0	57.9	98.1	59.1	48.0	59.6
3	43.7	16.8	41.4	26.8	22.3	25.0
4	41.2	47.2	38.6	32.9	25.4	30.7
5	34.2	55.3	52.5	59.1	53.5	61.9
6	25.4	37.6	18.5	25.1	23.4	25.9
7	35.3	54.8	50.5	46.7	56.7	50.1
8	23.4	65.6	31.4	26.1	36.9	32.2
9	36.2	12.6	23.7	23.1	21.7	21.2
Average	44.1	44.1	50.4	38.9	37.9	38.8

Table 10.2: Relative velocity error for each of the nine measured profiles.

than the $k-l$ models by about 5%. The relatively high errors reported in Table 10.2 can partly be explained by measurement errors. The hot-sphere anemometers errors are of significant importance at low velocities ($\simeq 0.1\ m/s$). The table shows that the EASM $k-\epsilon$ has better accuracy than the other models tested. The accuracy improvements found using the EASM and cubic model over the linear $k-\epsilon$ model are, however, much less ($< 1\%$) than seen in previous chapters. In a $k-l$ framework, the EASM has similar overall accuracy as the linear model and, the cubic model is the worse.

Figure 10.5 compares temperature measurements of four profiles with the linear, EASM and cubic $k-\epsilon$ model predictions. Figure 10.6 is a repeat of Figure 10.5 using this time $k-l$ based models. Figure 10.6 shows that, unlike the $k-\epsilon$, all $k-l$ based mod-

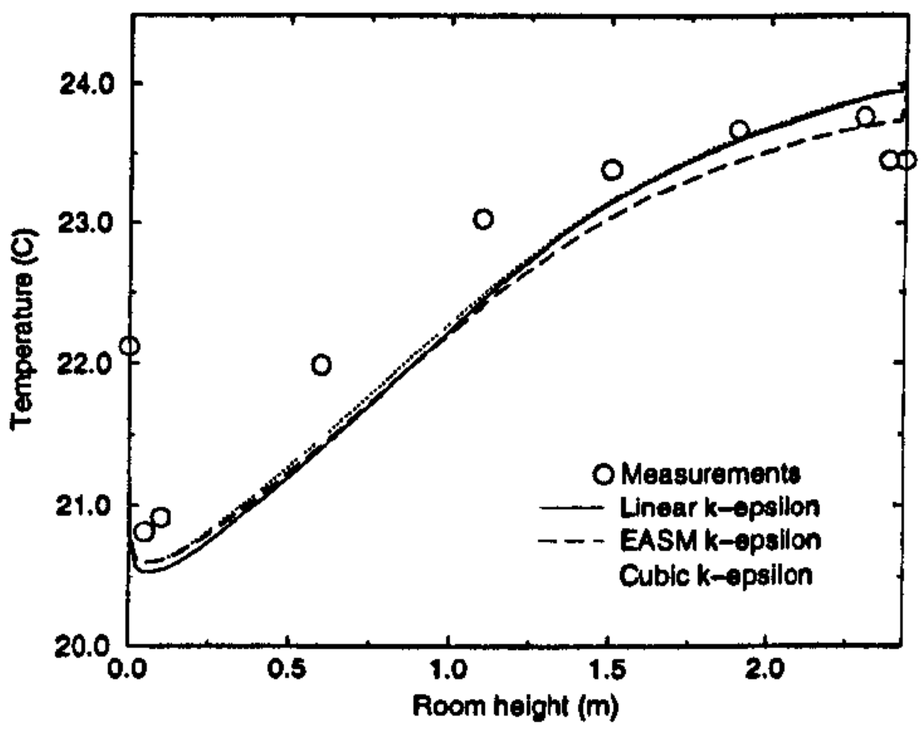

(a)

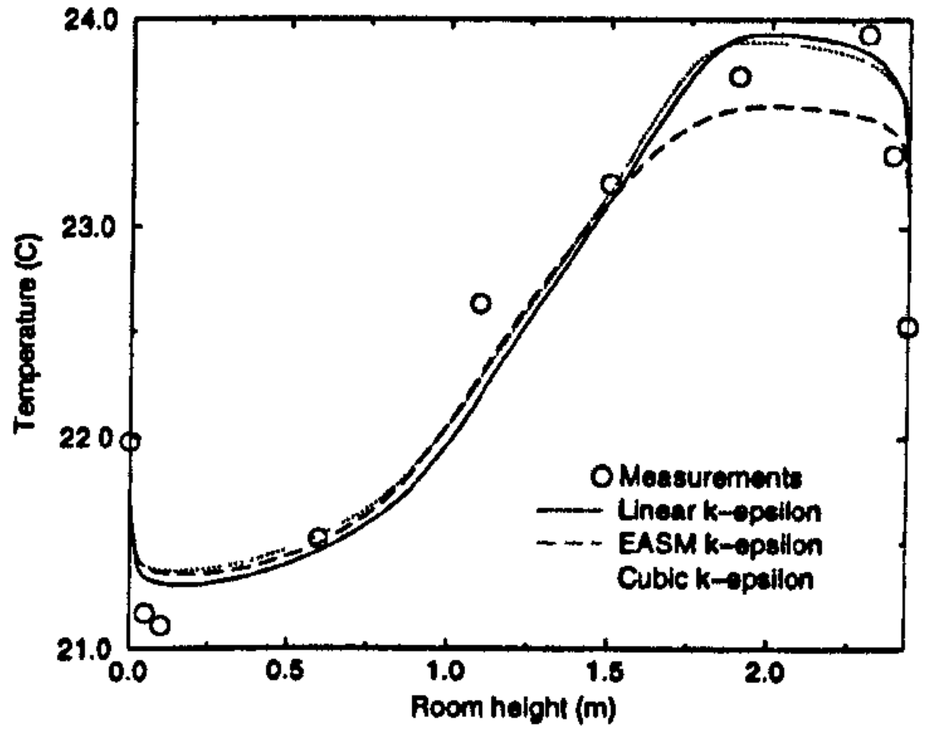

(b)

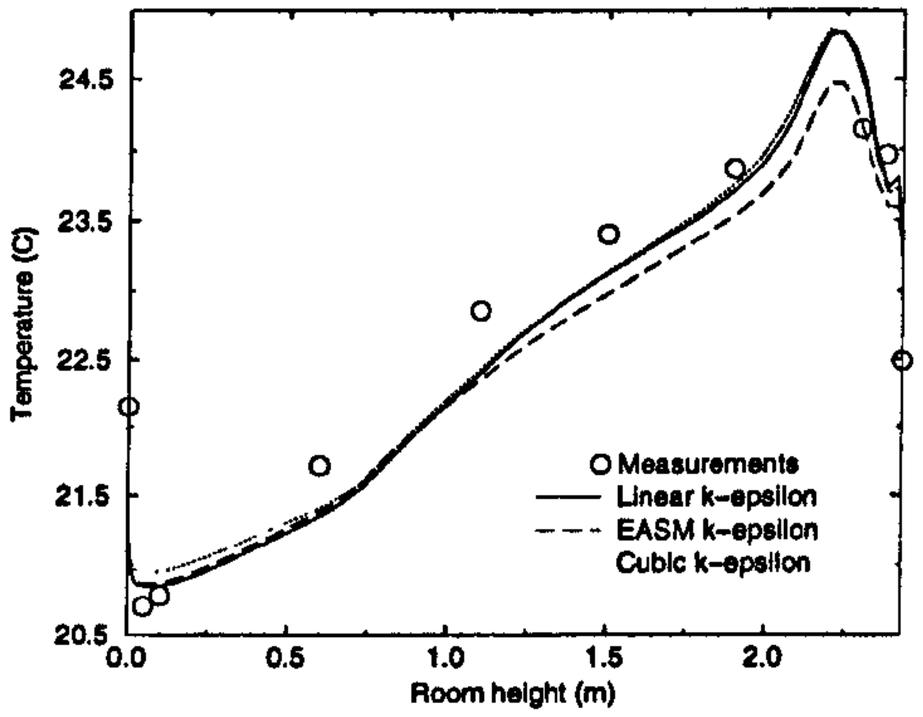

(c)

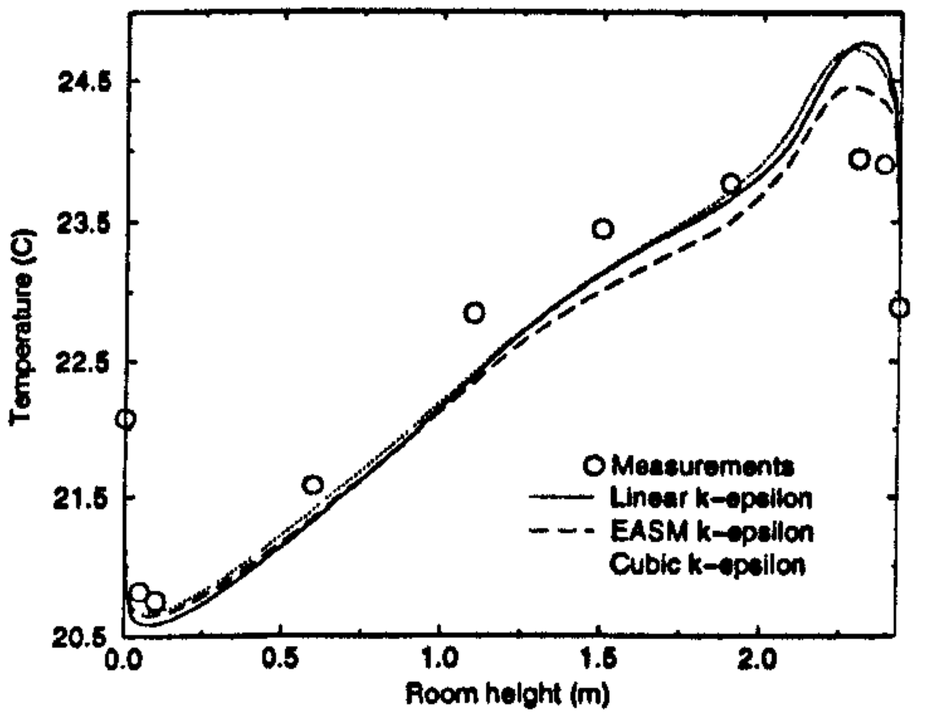

(d)

Figure 10.5: Comparison of measured temperature profiles (a) M3, (b) M5, (c) M6 and (d) M8 with predictions of the linear, EASM and cubic $k-\epsilon$ models.

els are unable to predict the correct thermal stratification in the lower part of the room ($y < 1\ m$). As for the velocities, Figures 10.5 and 10.6 indicates only minor prediction differences between the linear, EASM and cubic models, especially in a $k-\epsilon$ framework.

A summary of temperature prediction errors for all profiles and models is shown in Table 10.3. The errors are again obtained using Equation 4.3. The table shows that, as for the velocities, the $k-l$ based models give greater errors than the $k-\epsilon$ based models ($\simeq 2\%$). Moreover, the EASM and cubic $k-l$ models have a higher error than the linear $k-l$ model. The EASM $k-l$ model giving the biggest overall errors. In a $k-\epsilon$ framework, the EASM and cubic models are found to improve accuracy when compared to the linear model. The cubic model is found to have the best accuracy. However, improvements are, as might be expected, small ($< 0.1\%$).

10.3 Conclusions

The numerical investigation of this displacement-ventilated office reveals once more that the $k-l$ based models have lower accuracies than the $k-\epsilon$ based models. For the first time in this study, the EASM and the cubic model (in a $k-l$ framework) have worse accuracy than the linear $k-l$ model. The relatively high velocity errors found in this study could partly be explained by measurement errors. These become significant when considering low-velocity flows. Also, despite the efforts of Yuan *et al.* (1999), boundary conditions uncertainties could have a significant importance in the comparison presented here. Overall, the EASM and cubic $k-\epsilon$ models offer minor velocity and temperature-prediction improvements when compared with the linear model. The use of more physically consistent models for heat transfer modelling and, accounting for radiant heat is left for future work and would further increase accuracies.

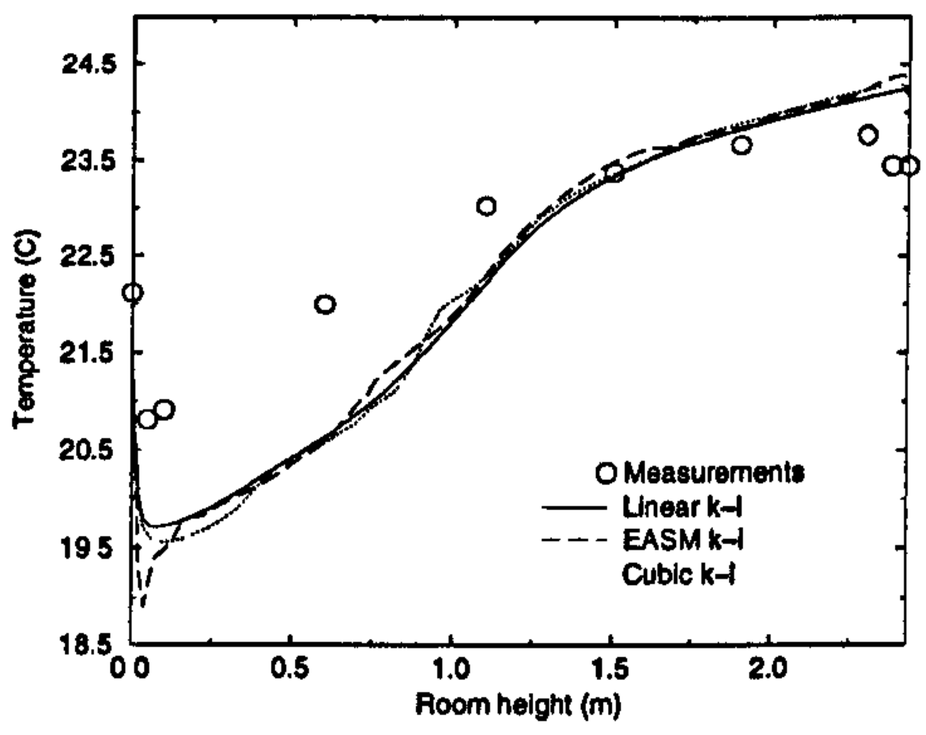

(a)

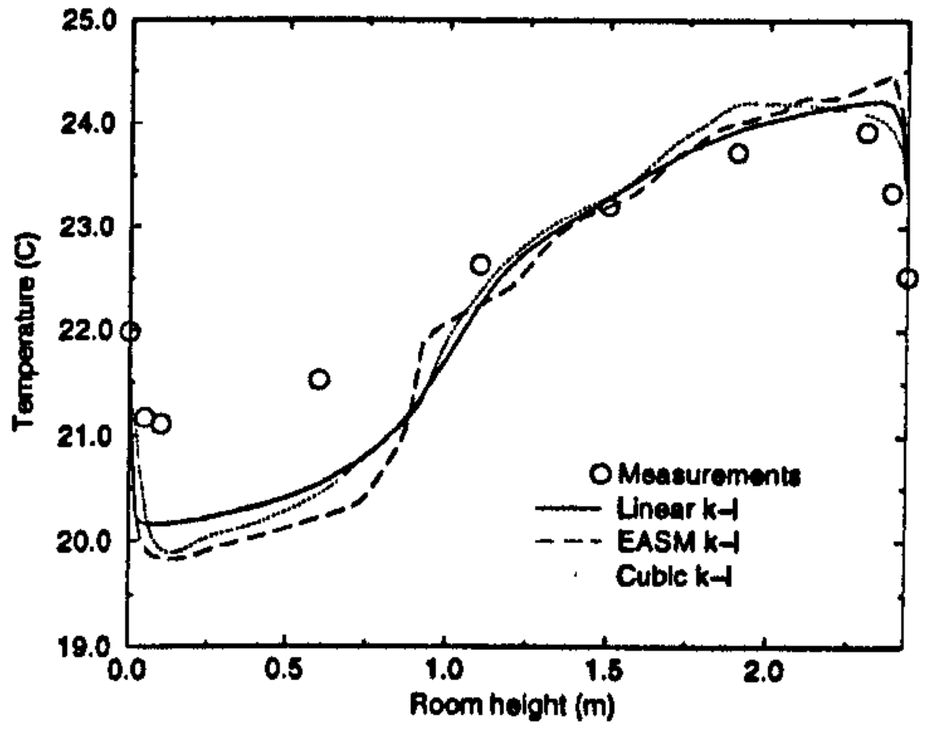

(b)

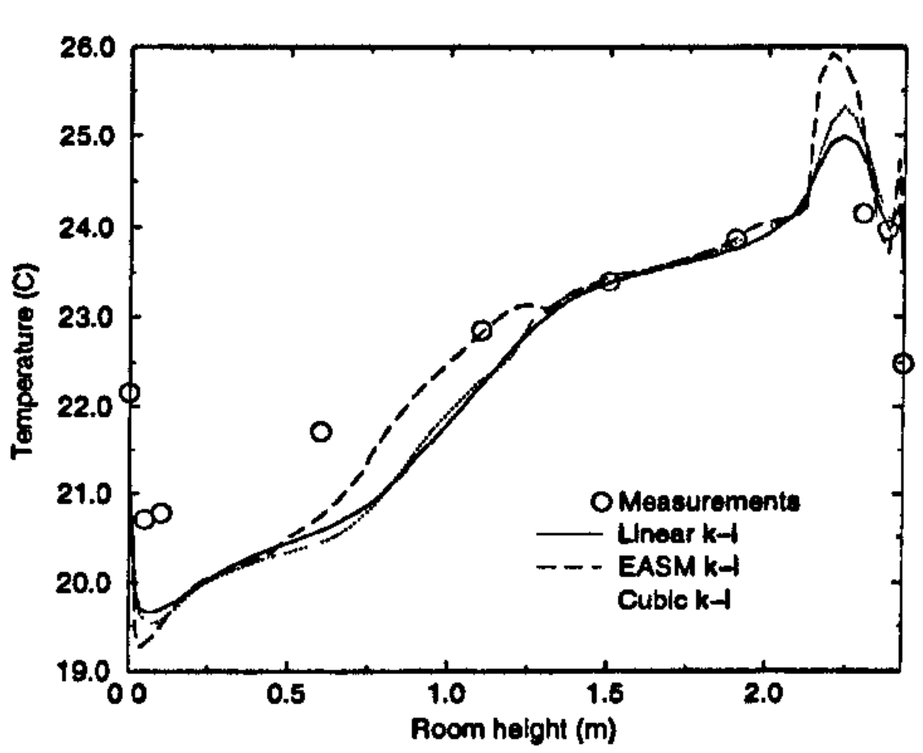

(c)

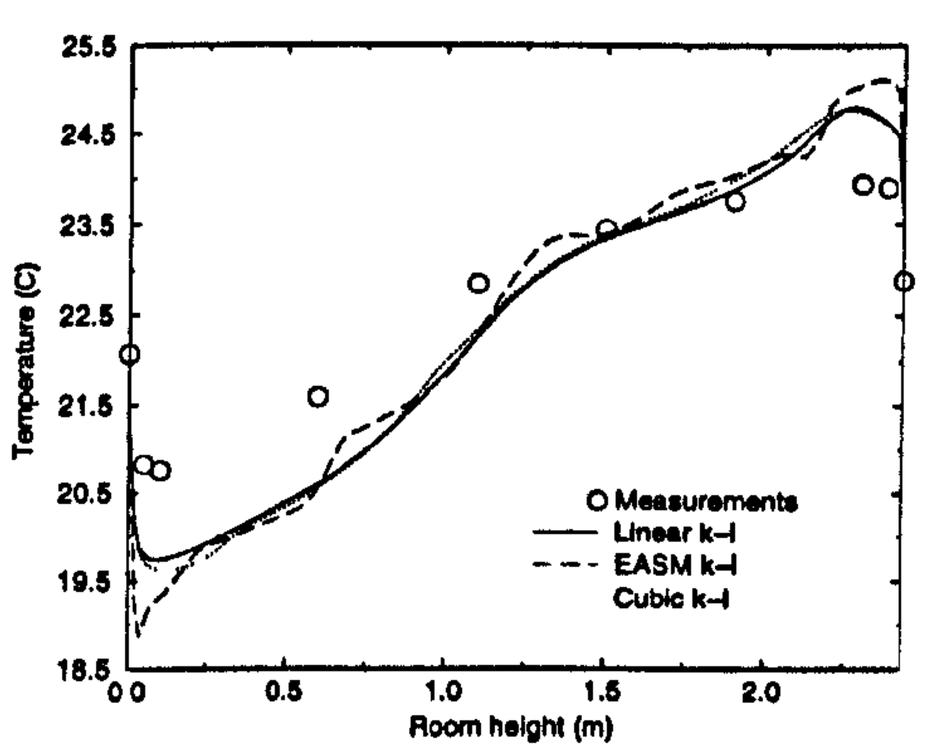

(d)

Figure 10.6: Comparison of measured temperature profiles (a) M3, (b) M5, (c) M6 and (d) M8 with predictions of the linear, EASM and cubic $k-l$ models.

	$k-l$			$k-\epsilon$		
Profile	Linear	EASM	Cubic	Linear	EASM	Cubic
1	4.16	4.76	3.98	3.22	2.94	3.25
2	2.95	3.60	3.10	1.70	1.50	1.61
3	3.10	3.45	3.38	1.88	1.80	1.76
4	2.20	3.32	2.37	0.97	1.11	0.89
5	2.48	3.02	2.40	0.90	0.89	0.91
6	2.51	2.62	2.79	1.37	1.46	1.36
7	2.62	3.63	2.97	1.58	1.82	1.50
8	2.61	3.39	2.74	1.67	1.47	1.47
9	2.74	3.57	2.74	1.43	1.51	1.32
Average	2.82	3.48	2.94	1.64	1.61	1.56

Table 10.3: Relative temperature error for each of the nine measured profiles.

Chapter 11

Modelling of the CFD idealised office

The final investigation presented in this thesis is based on the ventilated office, idealised for CFD modelling, discussed in Chapter 6 and 7 (see Figure 11.1). To reduce problem definition and increase solution accuracy, the room boundary conditions given were carefully considered. Six sets of measurements corresponding to different ventilation settings and layouts are presented in Chapter 7. Here, the numerical investigations of Case 01 (displacement-ventilation at one air change per hour) and of Case 06 (mixed-ventilation layout at five air change per hour) are presented.

11.1 Numerical modelling

The inlet velocities are set according to the ventilation rates set for the measurements. These are 0.07386 m/s and 0.3693 m/s per inlet for cases 01 and 06 respectively. The inlet airflow temperatures of 297.65 K and 294.55 K for Case 01 and Case 06 are also specified. The outlet, modelled as a plain opening in the ceiling of the room, is set

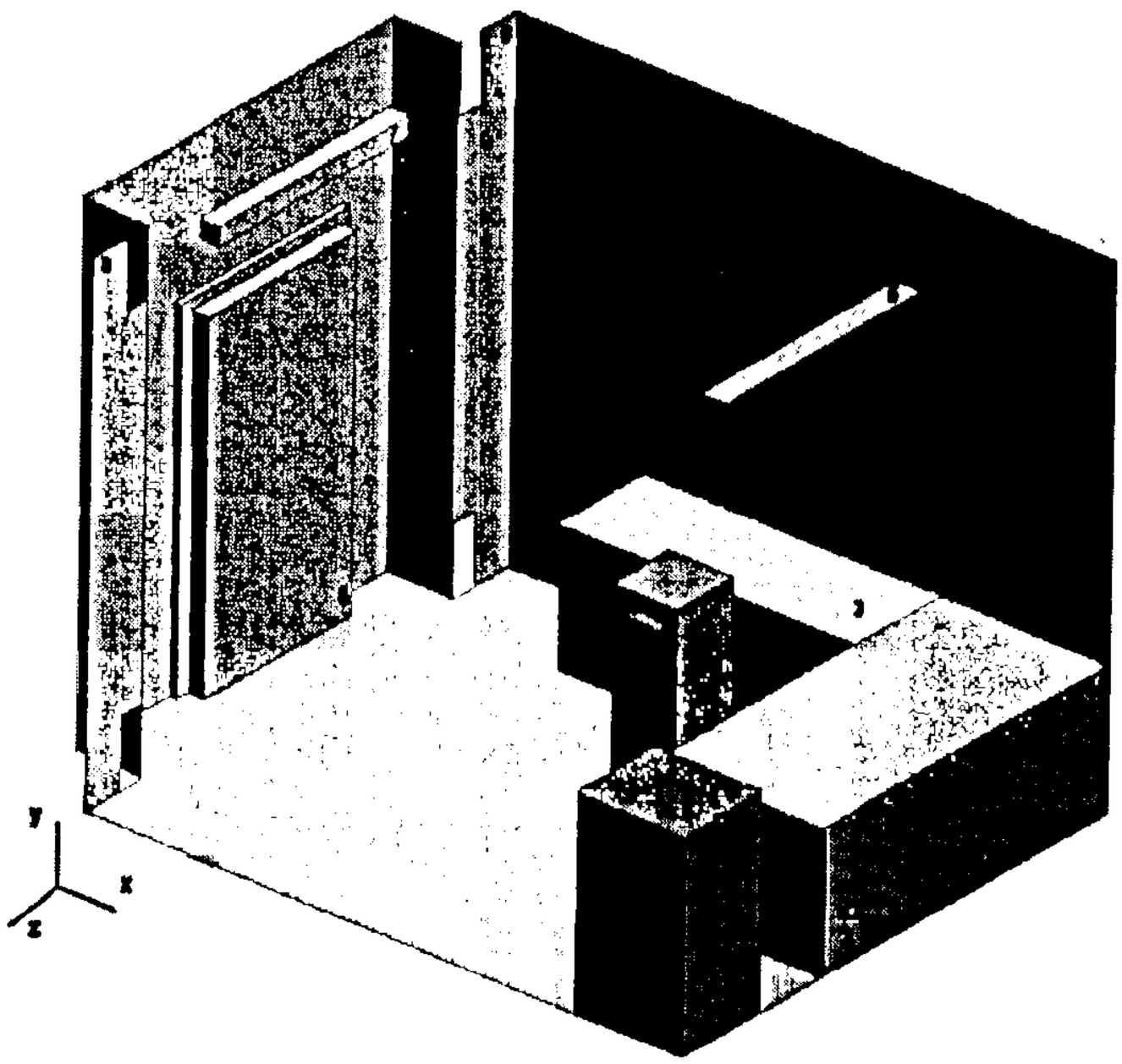

Figure 11.1: Room layout: 1: Filing cabinet; 2: Large desk; 3: Desk; 4: DIN man; 5: Outlet; 6: Door; 7: Light; 8: Mixed-ventilation inlet; 9: Displacement-ventilation inlet.

to conserve mass flow. For both cases, a grid of $75 \times 83 \times 63$ (x, y, z) nodes is used. This gives an average first off-wall y^+ value of 0.45 for Case 01 and 0.62 for Case 06. The linear, EASM and cubic $k-\epsilon$ models use the Lam-Bremhorst (1981), AKN (1996) and Craft *et al.* (1996) damping functions respectively (see Section 3.1.6). LES is also used to model the Case 01. The grid used for LES has been locally modified to ensure cross-streamwise non-dimensional grid spacing (Δx^+, Δy^+ or Δz^+) below twenty five at the walls.

It is expected to find that the flow in the room is greatly affected by thermal effects (especially for Case 01). Therefore, buoyancy effects are modelled as described in Section 3.1.5.

11.1.1 Surface temperature

Specified wall-temperature data is used as boundary conditions. For Case 01, two types of wall-temperature specification are tested. They are:

- Averaged wall temperature and,
- Specification of an averaged vertical thermal stratification.

For Case 06, only averaged wall temperatures are used. The averaged wall temperatures of Case 01 and Case 06 are summarised in Table 11.1.

For the specification of the vertical temperature stratification a quadratic polynomial of the form:

$$T_s\ (K) = \alpha_t\ y^2 + \beta_t\ y + \gamma_t \tag{11.1}$$

Temperature (K)	Door	Back wall	Left wall	Right wall	Floor	Ceiling
Case 01	297.99	298.09	298.78	297.97	297.37	298.34
Case 06	294.61	295.06	294.91	294.74	294.94	295.11

Table 11.1: Averaged wall temperatures for Case 01 and Case 06.

	Left wall	Right wall	Door	Back wall	DIN man 01	DIN man 06
α_t	-0.222	0.008	-0.669	0.142	-0.032	-1.067
β_t	0.950	0.250	2.150	-0.028	1.956	3.539
γ_t	297.40	297.51	296.51	297.65	300.98	297.84

Table 11.2: Coefficients of the polynomial fit for wall temperature of Case 01.

is used where, T_s is the surface temperature and, y is the local height in the room. The coefficients α_t, β_t and γ_t are calculated from a polynomial fit of the measurements and are given, for each walls of Case 01, in Table 11.2. For the floor and ceiling, only averaged surface temperatures are used.

11.1.2 DIN-man modelling

The specification of the DIN-man room heat source is crucial in this study. Especially for Case 01. A quadratic polynomial fit to the measurements is used to specify, as boundary conditions, the vertical variation of the DIN-man's surface temperature for both cases. Equation 11.1 coefficients describing the DIN-man's temperature can be found in Table 11.2.

Airflow velocities and temperatures at the top and bottom opening of the DIN man are also specified as boundary conditions. These are as follows: $T_{top-01} = 303.05\ K$,

$V_{top-01} = 0.291\ m/s$, $T_{bottom-01} = 301.77\ K$, $V_{bottom-01} = 0.079\ m/s$, $T_{top-06} = 300.41\ K$, $V_{top-06} = 0.314\ m/s$, $T_{bottom-06} = 297.99\ K$ and $V_{bottom-06} = 0.101\ m/s$. The flow orientation at the top and bottom opening of the DIN-man are assumed normal to the DIN-man's surface.

11.1.3 Gas tracer decay

The modelling of the decay of SF_6 (treated as a passive scalar) in the room is carried out in this study. Like in Chapter 9, Equation 3.22 is used to model the time decay of an arbitrary concentration. Again, it is expected to find only minor concentration prediction differences between the different models tested. For both cases, the averaged measured concentration of the sampling points located in the breathing zone of the room ($y = 1.6\ m$) are used as initial condition. For the decay simulation, the averaged concentrations of 25.56 *ppm* for Case 01 and of 51.50 *ppm* for Case 06 are initially uniformly set in the room. Unsteady RANS models (with a fully implicit time scheme) are used for the decay analysis.

11.2 Results and discussion

11.2.1 Thermal stratification

Figure 11.2 compares the averaged measured and predicted thermal stratification in the room for Case 01. The EASM $k-\epsilon$ is chosen for the comparison since it has best overall accuracy. The figure is non-dimensionalised in a similar was as in Chapter 7. The EASM $k-\epsilon$ (a) uses averaged-wall-temperature boundary conditions. The EASM $k-\epsilon$ (b) model uses the polynomial T_s fit. As shown in the figure, only minor differ-

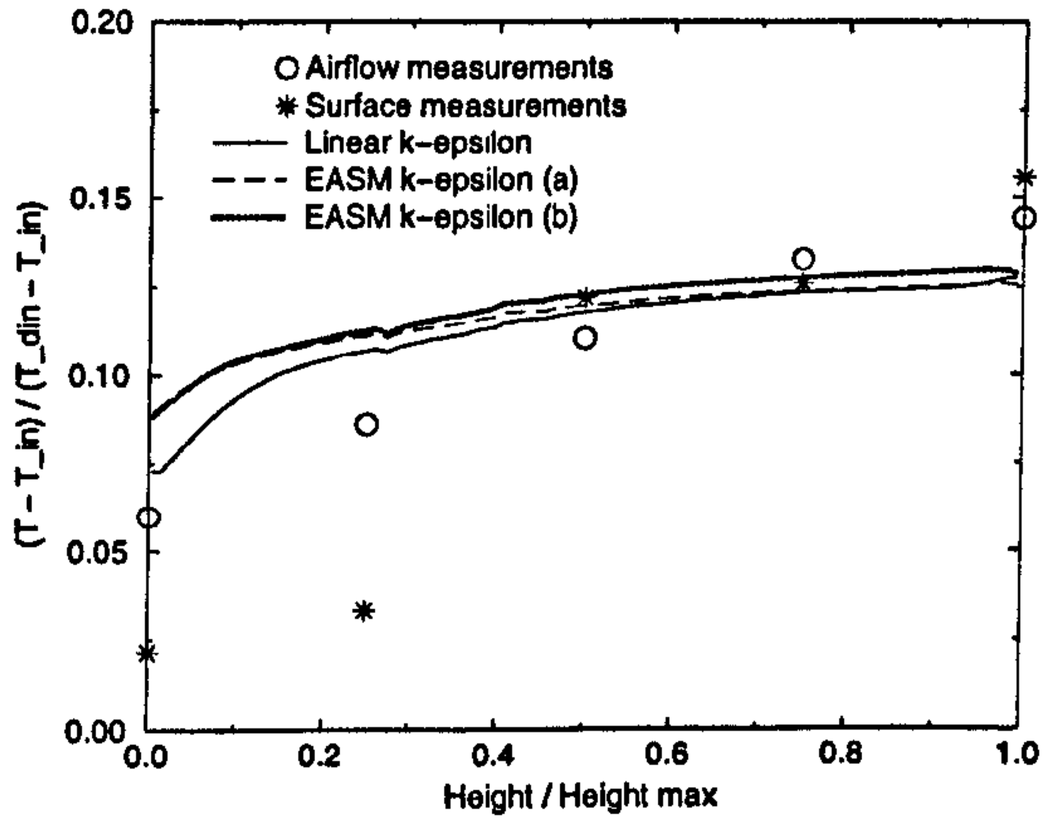

Figure 11.2: Averaged temperature stratification in the room for Case 01.

ences are observed between the two boundary conditions. The other flow variables are also found to be insensitive to the changes in boundary conditions. Hence, for simplicity, the results presented thereafter use average-wall-temperature boundary conditions. Figure 11.2 shows that the magnitude of the thermal stratification is not well-predicted especially in the vicinity of the floor and ceiling. The figure shows that the surface temperature is of lower magnitude than the airflow temperature. Reasonable temperature agreement is found away from the floor and ceiling. The relatively poor agreement in the near-wall region can perhaps be partly explained by the use of simple models for heat transfer and buoyancy effects. The use of more advanced models is left as future work.

Figure 11.3 compares the averaged measured and predicted thermal stratification for Case 06. The EASM $k-\epsilon$ model predictions are compared with the averaged measurements of wall temperatures and the averaged measurements of air temperature. Unlike

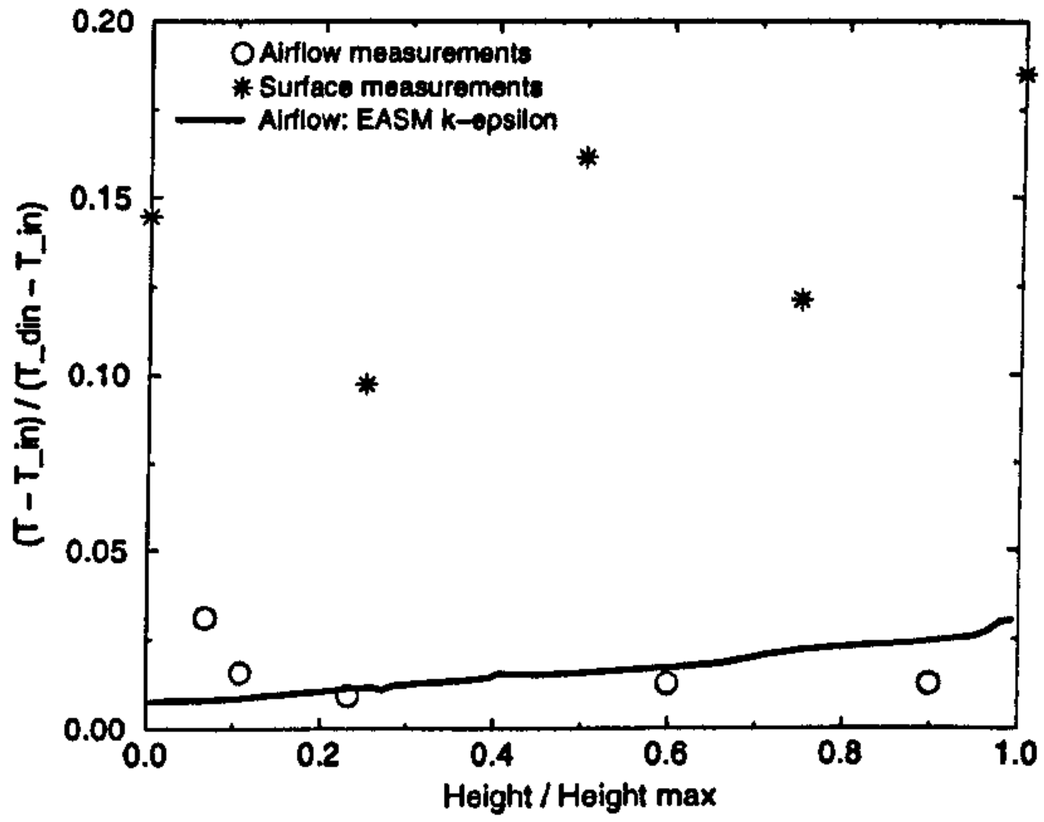

Figure 11.3: Averaged airflow temperature stratification in the room for Case 06.

for Case 01, Figure 11.3 shows, as might be expected, that a clear thermal stratification is not present in the room. The predictions of the EASM $k-\epsilon$ model are found to agree well with air temperature measurements. The figure also indicates that the averaged surface temperature (used as boundary conditions) are, as for Case 01, higher than the air temperatures.

The temperature prediction accuracy of the RANS models for Case 01 and Case 06 are summarised in Table 11.3. The errors of Table 11.3 are obtained by applying Equation 4.3. The table shows that, for Case 01, the use of the EASM and cubic models significantly improve linear model accuracy. For Case 06, the improvements found using the EASM or cubic models are minor. The EASM, in either a $k-l$ or $k-\epsilon$ framework has best accuracy.

	Linear		EASM		cubic	
	$k-l$	$k-\epsilon$	$k-l$	$k-\epsilon$	$k-l$	$k-\epsilon$
Case 01	8.5	8.4	3.9	3.7	3.8	3.4
Case 06	7.1	6.8	6.8	6.3	7.0	6.6

Table 11.3: Averaged temperature error (%) of the models for Case 01 and 06.

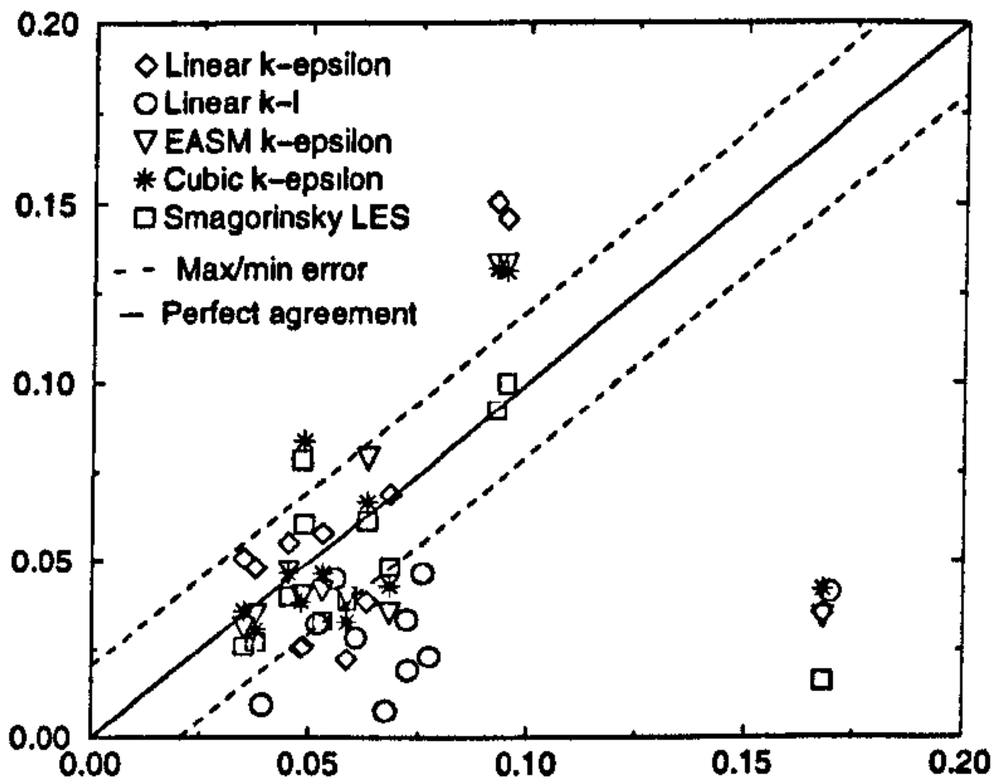

Figure 11.4: Comparison of measured and predicted airflow velocities for Case 01.

11.2.2 Air velocities

Figure 11.4 and 11.5 compare measured and predicted room velocities for Case 01 and Case 06, respectively. It is clear from both figures that the highest velocities in the room (in the vicinity of the DIN man) are not well predicted for any of the models. The highest velocity recorded in the room (probe labelled *D7* in Figure 6.8) is induced experimentally by the top opening of the DIN man. The models tested all predict that the probe *D7* is located outside of the convective area of the DIN man whereas the mea-

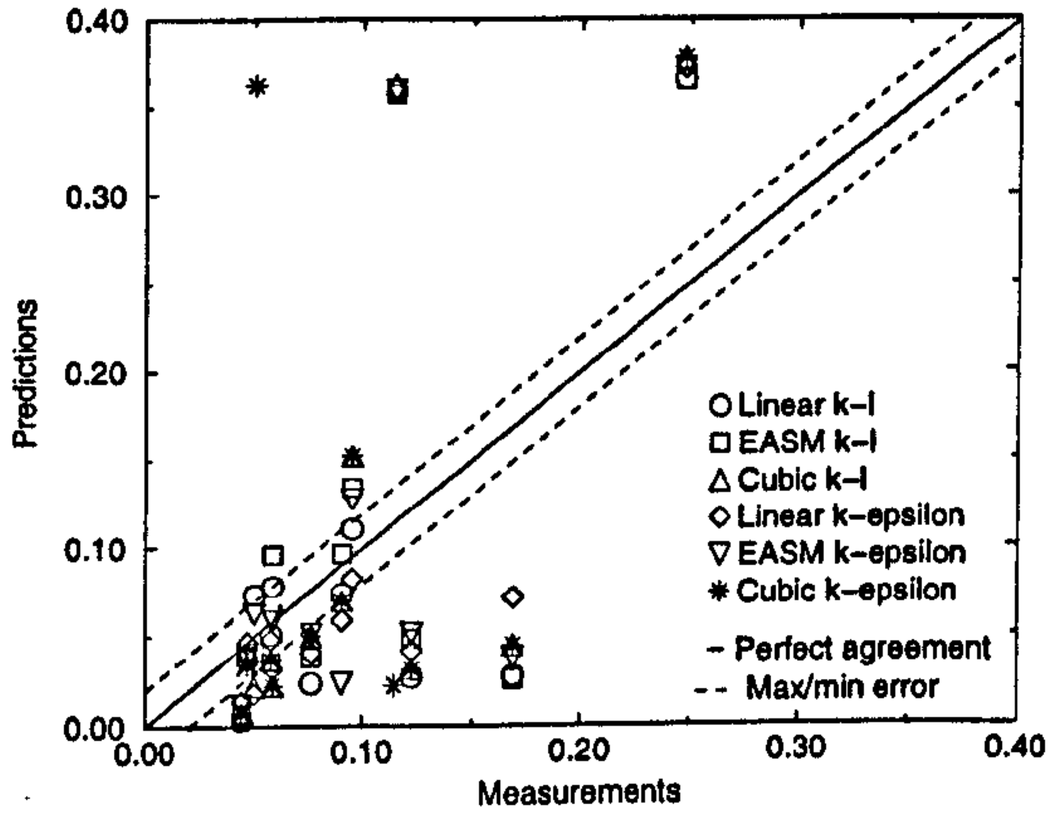

Figure 11.5: Comparison of measured and predicted airflow velocities for Case 06.

surements indicate otherwise. Further investigation on the boundary conditions applied to the top area of the DIN man is required to make any significant conclusions. This is left as future work. The convective area of the DIN man as well as the overall airflow patterns in the room are illustrated by the velocity contour plots for Case 01 and Case 06 seen in Figures 11.6 and 11.7 respectively.

To emphasise the differences between the models tested, the averaged velocity errors for Case 01 and Case 06 are presented in Table 11.4. The percentage errors given in Table 11.4 are obtained using equation 4.3. The table shows once more that the $k-l$ based models have significantly lower accuracy than the $k-\epsilon$ based models especially for Case 01. The relatively low velocity predictive accuracy seen in Table 11.4 is partly explained by the low measurement accuracy for velocities ($\pm 0.02 m/s$). It can, however, be noted that these prediction errors are of lower magnitude than previously seen in Chapter 10. This may indicate that a more accurate definition of the boundary condi-

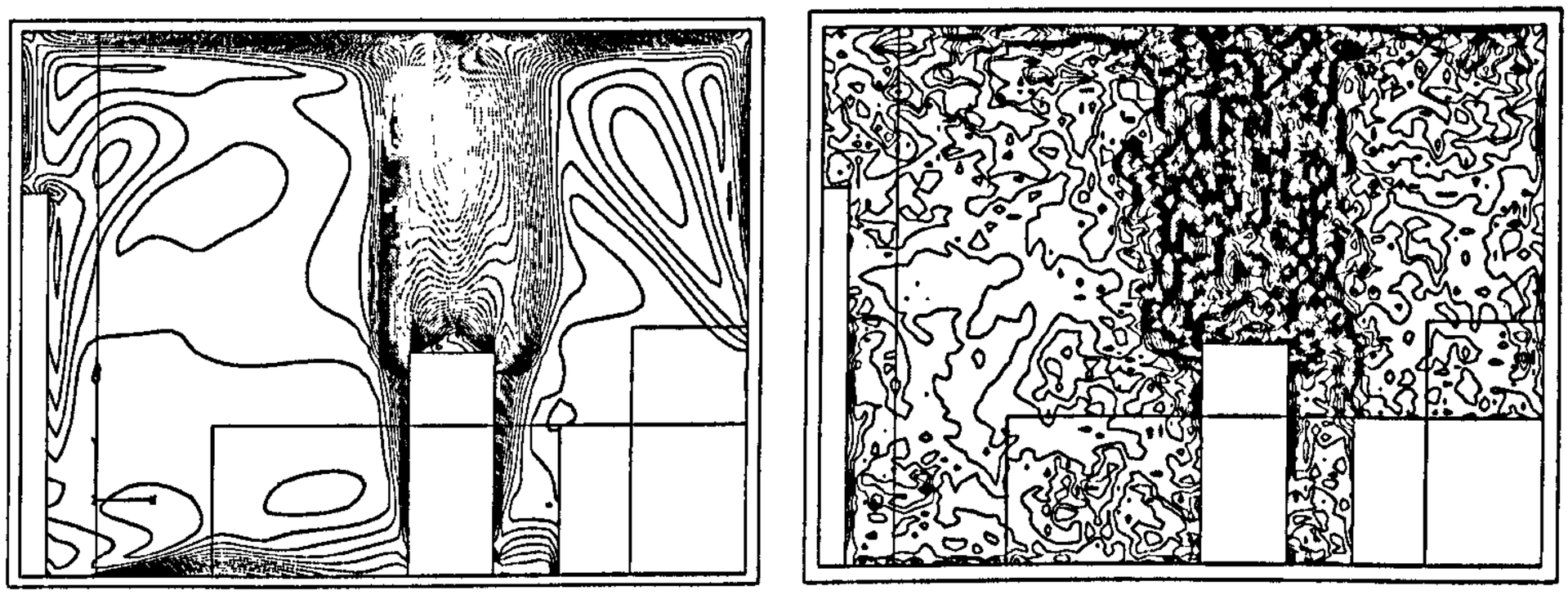

(a) (b)

Figure 11.6: Velocity contour plots in the DIN man's mid-plane for Case 01. (a) $k-\epsilon$ model and (b), instantaneous Smagorinsky LES.

(a) (b)

Figure 11.7: Velocity contour plots in the DIN man's mid-plane for Case 06. (a) linear and (b) EASM $k-\epsilon$ model.

	Linear		EASM		cubic		LES	LNS
	$k-l$	$k-\epsilon$	$k-l$	$k-\epsilon$	$k-l$	$k-\epsilon$		
Case 01	58.5	34.7	47.3	22.2	50.0	24.6	21.7	23
Case 06	26.9	25.9	26.3	24.3	30.1	28.1	N/A	N/A

Table 11.4: Averaged velocity errors (%).

tions is used. This would further emphasise the importance of the experimental work presented in this thesis.

Relative to its linear equivalent, the EASM is found to improve accuracy. For Case 01, the EASM $k-\epsilon$ model is only 0.5% less accurate than the Smagorinsky LES. The latter, besides having best agreement with measurements, is extremely computationally expensive compared to the EASM. The cubic model is not always found to improve accuracy. The partial results shown by the LNS model are extremely encouraging. The LNS model applied to Case 01 is still running to reach maturity and shows accuracy improvements with simulation time.

11.2.3 Gas tracer decay

Figure 11.8 and 11.9 compare measured and predicted SF_6 concentration decay in the breathing zone of the room ($y = 1.6\ m$) for Case 01 and Case 06. Both figures are non dimensionalised as in Chapter 7 and use the EASM model. For both cases, reasonable agreement is found between measurements and predictions. The relative prediction errors for the models used are summarised in Table 11.5. The table shows that the $k-l$ based models have lower accuracy than those of the $k-\epsilon$ based models. The overall

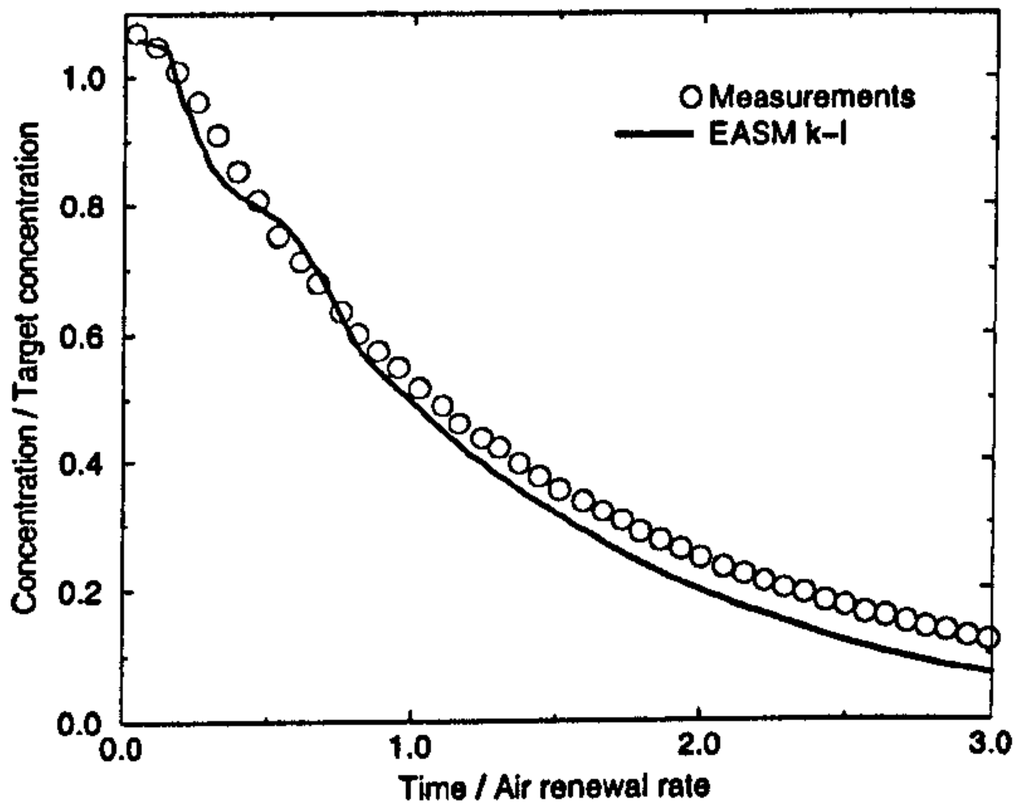

Figure 11.8: Averaged concentration decay for Case 01.

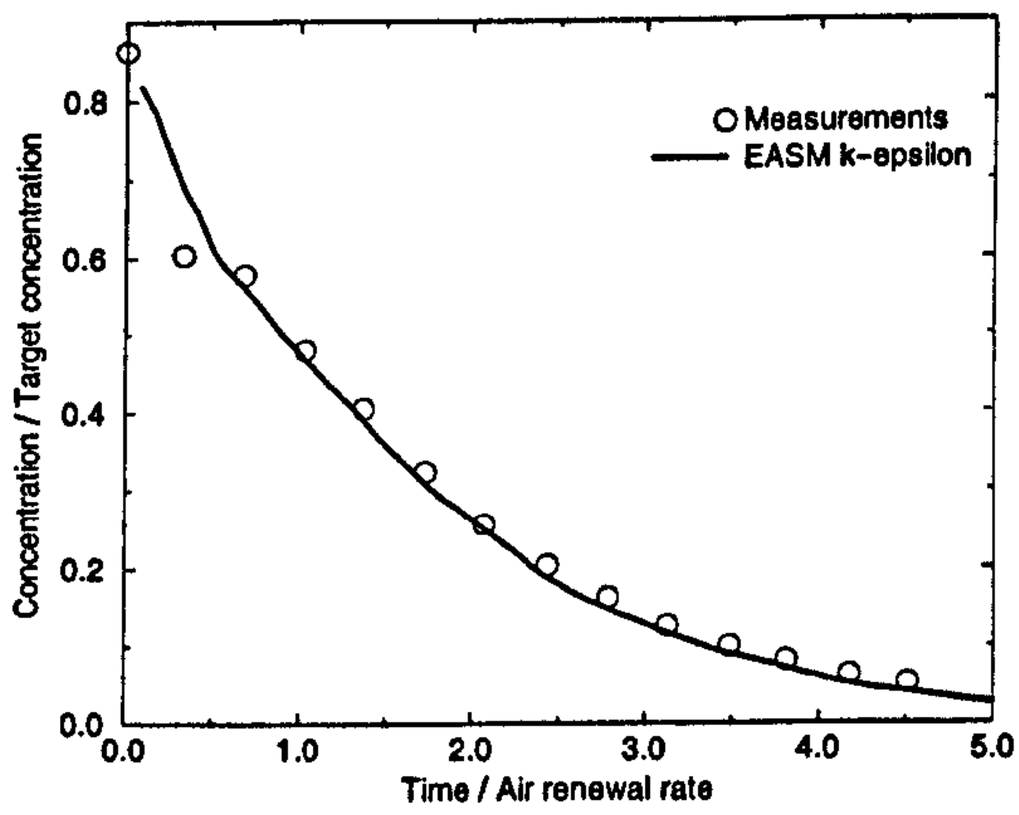

Figure 11.9: Averaged concentration decay for Case 06.

	Linear		EASM		cubic	
	$k-l$	$k-\epsilon$	$k-l$	$k-\epsilon$	$k-l$	$k-\epsilon$
Case 01	22.4	19.2	17.7	17.2	21.4	18.5
Case 06	13.4	10.9	9.7	9.1	11.5	10.5

Table 11.5: Relative averaged error (%) of the models compared with measurements.

accuracy of Case 06 is better than for Case 01. This could partly be explained by thermal effects occurring only for the displacement-ventilated case. The EASM, in either a $k-l$ or a $k-\epsilon$ framework, is found to give the best decay predictions. In particular, excellent agreement is found using the EASM for Case 06 ($< 6\%$ relative error). The accuracy improvements found using the cubic model are lower than those of the EASM.

In a similar way to Chapter 9, ventilation efficiency in this room is assessed using the contaminant-removal index E_f (see Equation 9.2). This index, shown in Table 11.6 for the various models tested, is the ratio between averaged concentrations in the breathing zone and concentrations at the room exhaust. The concentration at the exhaust are taken as averaged concentrations over the surface area of the room outlet. The table shows that the $k-\epsilon$ based models have higher accuracy than the $k-l$ based models. The table also shows that for cases 01 and 06, the cubic model in a $k-l$ framework has worse accuracy than its linear equivalent. Again the EASM models are found to be most accurate.

	Measurements	Linear		EASM		cubic	
		$k-l$	$k-\epsilon$	$k-l$	$k-\epsilon$	$k-l$	$k-\epsilon$
Case 01	1.0	1.05	0.97	1.02	0.98	1.09	1.05
Case 06	1.09	1.14	1.11	1.11	1.10	1.17	1.07

Table 11.6: Contaminant-removal index.

11.3 Conclusions

The investigation shows in all cases that the predictions of the $k-l$ based models are of lower accuracy those of the $k-\epsilon$ based models. The EASM $k-\epsilon$ is found to give excellent agreement with measurements, in terms of velocities, temperatures and passive scalar decay. For Case 01, the EASM $k-\epsilon$ is found to predict velocities within 0.5% of the Smagorinsky LES predictions. The latter being substantially more computationally demanding than any of the RANS models. The semi-matured LNS simulation gives encouraging Case 01 velocity predictions. The cubic model is again found to give mixed results. It improves temperature and passive scalar decay predictions but gives worse Case 06 velocities than its linear equivalent. For displacement-ventilated configurations, the study shows poor thermal-stratification predictions for the RANS models. This can perhaps partly be explained by the simplicity of the heat transfer and buoyancy models used.

Chapter 12

Conclusions and recommendation for future work

In this thesis, a range of RANS, LES and hybrid RANS/LES models have been applied to the modelling of flows in ventilated rooms. The potential of RANS modelling, and in particular of the EASM and of the cubic eddy viscosity model, was first studied on four relatively simple benchmark flow configurations. These were a turbulent plane channel flow, a channel flow with a side inflow boundary giving rise to extreme streamline curvature, the flow past a backward facing step and the flow in straight square ducts inducing Prandtl's motion of the second kind.

The two-dimensional turbulent-channel-flow analysis showed that both the EASM and the cubic models in either a $k-\epsilon$ or $k-l$ framework are, unlike linear models, able to predict the anisotropy of the Reynolds stress tensor. Both EASM and cubic model predicted well the principal Reynolds stresses in the channel. The EASM's Reynolds stress predictions were found to be better than those of the cubic model.

The investigation for the side-inflow channel showed, as might be expected, improved predictions of Reynolds stresses for the cubic model, in either a $k-l$ or $k-\epsilon$ framework, when compared with other RANS models. The cubic model was also found to predict well the peak flow velocity in the channel but had lower prediction accuracy near the the inflow wall. This case showed the potential of the cubic model in predicting flows that exhibits extreme streamline curvature. For this side inflow-case, the EASM only gave minor improvements when compared to its linear equivalents.

For the flow past a backward-facing step excellent predictions of the separation bubble length occurring behind the step for both the EASM (less than 3% relative error) and cubic model (less than 1% relative error) in a $k-\epsilon$ framework were gained.

As a final test, the EASM and the cubic model in either a $k-\epsilon$ or $k-l$ framework were found to successfully predict (with the appropriate damping function) Prandtl's secondary motions in a straight square duct. This is not achievable using linear RANS models.

The four benchmark flows described above clearly showed the range of improvements offered by the EASM and cubic models when compared with their linear equivalents. In terms of computing expenses, the EASM and cubic models were found to be 20 to 30% more expensive than their linear equivalents. The cubic model was also found to be more numerically unstable than the EASM. In high Reynolds number forms both non-linear models were found to be much more stable.

An investigation of four ventilated rooms was carried out. These were a jet-ventilated

empty room, a mixed-ventilated room with a workstation, a complex displacement-ventilated office and a displacement, or mixed, ventilated small office idealised for CFD modelling. Flows in ventilated rooms are complex and, to ensure accurate CFD modelling, accurate definition of the various boundary conditions in the room is required (referred to here as problem-definition issues). It is often found in the literature that measurements of ventilated rooms or offices lack a clear description of these boundary conditions especially thermal boundary conditions. The latter are particularly important for displacement ventilation.

For the empty jet-ventilated room and the mixed ventilated room with a workstation, no information is given on thermal aspects. Thus only isothermal analysis were made. The investigation of the jet-ventilated empty room did not present any major problem definition-issues. Hence, a wide range of turbulence models were tested. The study showed that zero-equation mixing-length models greatly underestimated the initial jet diffusion. As the jet develops, the accuracy of the mixing-length models improved. However, it still remained lower than that of the two-equation $k-\epsilon$ model. Also, in the jet area, the linear one-equation $k-l$ model had a significantly lower predictive accuracy than the linear two-equation $k-\epsilon$ model. The EASM and cubic models in a $k-\epsilon$ framework were found to increase predictive accuracy for jet centerline velocities by $\simeq 6\%$ when compared to the linear model. The EASM and cubic models also significantly improved the predicted normal Reynolds stresses along the centerline of the jet. Also, the Smagorinsky LES had excellent agreement with measurements for both velocities ($< 6\%$ relative error) and Reynolds stresses. The Yoshizawa LES had a similar Reynolds stress accuracy to the cubic model. However, it underpredicted jet centerline velocity. The LNS model appeared promising. It showed best agreements with velocity

measurements (< 5% relative error) and also gave excellent agreement with measured normal Reynolds stresses, especially τ_{yy}. In terms of computational expense, the LES simulations needed over ten weeks of cpu time. The unsteady LNS model was also computationally demanding (about eight weeks of cpu time) but had less demanding grid requirements than the LES. This makes the LNS more suited for practical engineering applications. The steady RANS solutions were obtained in less than one week. The trade off between computing time and predictive accuracy is crucial in industry. This justifies the need for considering non-linear eddy-viscosity models.

The analysis of the mixed-ventilated room with a workstation was aimed at demonstrating the potential of non-linear RANS models when predicting the time decay of a pollutant source (SF_6 gas tracer) modelled as a passive scalar. For this case, problem-definition is an issue since the thermal boundary conditions and initial conditions of the tracer gas initial release were not accurately described. The investigation revealed that the linear one-equation $k-l$ model had lower accuracy than the linear two-equation $k-\epsilon$ model. The EASM $k-l$ model was found, however, to have better accuracy than the other models tested (less than 10% relative concentration error in the breathing zone of the room). It improved accuracy by 4.8% and 0.6% when compared with the linear $k-l$ and $k-\epsilon$ models, respectively. The cubic model in either a $k-l$ or $k-\epsilon$ framework gave mixed results. It improved predicted concentration in the breathing zone but gave worse results at the exhaust of the room than those for the linear models. Since a standard gradient approach was used for the modelling of turbulence effects on the passive scalar, the results presented for this case do not reveal any significant differences between the different models. The use of a scalar transport equation that includes non-linear effects of the Reynolds stress tensor is left as future work and is expected to further improve

accuracy.

The numerical investigation of a complex displacement-ventilated office is made to emphasise the importance of thermal boundary conditions in displacement ventilation modelling. The investigation revealed once more that the $k-l$ based models (linear, EASM and cubic) have lower accuracy than the $k-\epsilon$ based models. Here again, the EASM and cubic models give mixed results. In a $k-l$ framework, both models have worse accuracy than their linear equivalent. Overall, the EASM and cubic models in a $k-\epsilon$ framework offer minor velocity and temperature improvements when compared with the linear model. The use of more physically consistent heat transfer models that includes radiant effects and a more accurate model accounting for buoyancy effects is left as future work. In this complex room, the low accuracy found, especially for velocities, can partly be explained by measurement errors which become significant when considering low velocity flows. The prediction errors can also be partly explained by the complexity of the room itself leading to problem-definition issues.

The last room studied is based on measurements, done as part of this work, in a ventilated room idealised for CFD modelling. For this room, a careful description of the boundary conditions is given and measurements of airflow velocities, temperatures as well as studies of the decay of a pollutant source (SF_6 gas tracer) are available for six ventilation configurations (either mixed- or displacement-ventilation). This room is thus seen as an ideal test case for the validation of CFD models for room ventilation. The numerical investigation of the room, in a displacement- or mixed-ventilation layout, revealed that the predictions (temperature, velocities and gas tracer decay) of the one-equation $k-l$ based models (linear, EASM and cubic) were less accurate than the

predictions of the two-equation $k-\epsilon$ based models. In a $k-\epsilon$ framework, the EASM and cubic models were found to significantly improve accuracy (up to 14.7% for the cubic model). The overall flow predictions in the room were found to agree well with measurements. This seemed to emphasise the need to have well-defined boundary condition for the numerical modelling of flows in ventilated rooms. The more computationally demanding Smagorinsky LES had the best accuracy when compared with measurements. Preliminary results using the LNS model shows that it had similar agreement levels to the Smagorinsky LES model.

Analysis of the four ventilated rooms clearly revealed that zero- or one-equation-based models (linear, EASM and cubic $k-l$) have lower accuracy than the two-equation-based $k-\epsilon$ models. This is an important finding since zero- and one-equation models remains popular for the computation of flows in ventilated rooms. The EASM in either a $k-l$ or $k-\epsilon$ framework was found to improve accuracy for the majority of the flows presented in this work. The EASM improvements found for room-ventilation configurations were however of lesser importance than previously observed for the four benchmark flow configurations. The cubic model, besides being more numerically unstable than the EASM or the linear models, was not always found to increase accuracy when compared with its linear equivalent. Moreover, as for the EASM, the improvements for the cubic model applied to flows in ventilated rooms were less than for the benchmark flow configurations. The use of LES, as might be expected, gave the most satisfactory predictions but, remains too computationally expensive for practical engineering applications. The novel LNS model, which is not as computationally demanding as the LES, appeared promising and should be considered in future research.

Chapter 13

References

Abe K., Kondoh T. and Nagano Y. (1996), " A new turbulence model for predicting fluid flow and heat transfer in separating and reattaching flows, thermal field calculations", *Int. J. of Heat and Mass Transfer*, Vol. 38, No. 8, pp. 1467-1481.

Akabayashi S-I., Kuwahara R., Mizutani K., Sakaguchi J. and Sato H., (2000), "An experimental and numerical study of the relationship between ventilation efficiency and air supply/exhaust system of an office room", *Proc. Roomvent 2000*, Vol. II, pp 867-874, Ed. Awbi H.B., Elsevier Science Ltd.

Apsley D.D. and Leschziner M.A. (1998), "A low Reynolds number non linear two equation model for complex flow", *Int. J. of Heat and Mass Transfer*, Vol. 19, pp. 209-222.

ASHRAE Standard 55-1992 (1993), "Thermal environment conditions for human occupancy.", American Society of Heating, Refigerating and Air-conditioning Engineers (ASHRAE), Atlanta, USA, 1993.

ASHRAE (1997), "ASHRAE handbook of fundamentals", American Society of Heating,

Refigerating and Air-conditioning Engineers (ASHRAE), Atlanta, USA.

ASME (1971), "Fluid meters: Their theory and application", *Report of ASME Research Committee on Fluid Meters*, Edited by Bean H.S. 6^{th} ed.

ASTM (1993), "Standard guide for statistical evaluation of indoor air quality models", ASTM Designation D 5157.

Awbi H.B. (1991), "Ventilation of buildings", Spon, London.

Awbi H.B. (1996), "Air movement in naturally-ventilated buildings", *Renewable Energy*, Vol. 8, pp. 241-246.

Awbi H.B. (1998), "Chapter 7 - Ventilation", *Renewable and Sustainable Energy Reviews*, Vol. 2, pp. 157-188.

Baines W.D., Turner J.S., (1968), "Turbulent buoyant convection from a source in a confined region", *J. Fluid Mech.*, Vol. 37, pp. 51-80.

Batten P., Goldberg U. and Chakravarthy S. (2000), "Sub-grid turbulence modelling for unsteady flow with acoustic resonance", 38^{th} *AIAA Aerospace science meeting*, AIAA-00-0473.

Batten P., Goldberg U. and Chakravarthy S. (2002), "LNS - An approach towards embedded LES", *AIAA paper*, AIAA-2002-0427.

Boussinesq J. (1877),"Théorie de l'écoulement tourbillant", *Mémoires presentées par divers savants a l'Académie des Sciences de Paris.*

Brandt A. (1977),"Multi-level adaptive solution to boundary-value problems", *Math. Comp.*, Vol. 31 (138), pp. 333-390.

Brohus H. (1997), "Personal exposure to contaminant sources in ventilated rooms", *PhD Thesis*, Aalborg University, Denmark.

Building Amendment Regulation (2001), (www.hmso.gov.uk/si/si2001/20013335.htm) , refering to building regulation part L2 and BB87: Building bulletin 87, "Guidelines for environmental design in schools", *Architects and building branch*, DfEE.

Chaouat B. (2000), "Numerical simulations of channel flows with fluid injection using Reynolds stress model", *AIAA paper*, AIAA-2000-0992.

Chapman D.R. (1979),"Computational aerodynamics development and outlook", *AIAA Journal* , Vol. 17, pp. 1293.

Chen H.C. and Patel V.C. (1988),"Near wall turbulence models for complex flows including separation", *AIAA journal*, Vol. 26, No. 6, pp. 641-648.

Chen Q. (1996), "Comparison of different $k-\epsilon$ models for indoor airflow computations", *Numerical heat transfer, Part B: Fundamentals*, Vol. 28, pp. 353-359.

Chen Q. (1997), "Computational fluid dynamics for HVAC: Successes and failures", *ASHRAE Trans.*, Vol. 103, Part 1, pp. 178-187.

Chen Q. and Xu W. (1998), "A zero-equation turbulence model for indoor airflow simulation", *Energy and Buildings*, Vol. 28, pp. 137-144.

Chen Y.S. and Kim S.W. (1987), "Computation of turbulent flows using an extended $k-\epsilon$ turbulence closure model", NASA CR-179204.

Chikamoto T., Murakami S. and Kato S. (1992), "Numerical simulation of velocity and temperature fields within atrium based on modified $k-\epsilon$ model incorporating damping

effect due to thermal stratification", *Proc. of ISRACVE*, Tokyo, 1992.

CIBSE (1999), "Guide A, Chapter 1: Environmental criteria for design".

Collignan C. and Riberon J. (2000), "A numerical study on polutant removal effectiveness of a room",*Proc. Roomvent 2000*, Vol. II, pp. 931-936, Ed. Awbi H.B., Elsevier Science Ltd.

Cradle Co. ltd. (1990): "Computational fluid dynamics program STREAM", Version 2.7, 1990.

Craft T.J. (1998), "Developments in a low Reynolds number second-moment closure and its application to separating and reataching flows", *Int. J. of heat and fluid flows*, Vol. 19, No. 5, pp. 541-548.

Craft T.J. and Launder B.E. (1996), "A Reynolds stress closure designed for complex geometries", *Int. J. of Heat Fluid Flow*, Vol. 17, pp. 245-254.

Craft T.J., Launder B.E. and Suga K. (1996), " Development and application of a cubic eddy viscosity model of turbulence", *Int. J. of Heat and Fluid Flow*, Vol. 17, pp. 108-115.

Craft T.J., Iacovides H. and Yoon J.H. (1999), "Progress in the use of non-linear two-equation models in the computation of convective heat-transfer in impinging and separated flows", *Flow turbulence and combustion*, Vol. 63, pp. 59-80.

Croome D.J. and Roberts B.M. (1981), "Air conditioning and ventilation of buildings", Pergamon Press, Second Ed.

Cumo F., De Santoli L. and Lo Giudice G.M. (2000), "Experimental evaluation of smok-

ing lounges: A case study", *Proc. Roomvent 2000*, Vol. I, pp. 161-166, Ed. Awbi H.B., Elsevier Science Ltd.

Davidson L. (1997), "Large eddy simulation: A dynamic one-equation subgrid model for three dimensional recirculating flow, 11^{th} *Int. Symp. on Turbulent Shear Flow*, Vol. 3, pp. 26.1-26.6, Grenoble, France.

Davidson L. (2001), "Hybrid LES/RANS: A combination of a one equation SGS model and a $k-\omega$ model for predicting recirculating flows", *Proc. ECCOMAS CFD conference*, September 2001, Swansea, U.K.

Davidson L. (2001-b), "A hybrid LES-RANS model based on a one-equation SGS model and a two-equation $k-\omega$ model", *The second international Symp. on turbulence and shear flow phenomena*, Vol. 2, pp. 175-180, Stockholm, 2001.

Davidson L. and Nielsen P.V. (1996), "Large eddy simulations of the flow in a three-dimensional ventilated room", *Proc. Roomvent 1996*, Vol. 2, pp. 161-168.

Davidson L., Nielsen P.V. and Topp C. (2000), "Low-Reynolds number effect in ventilated rooms: A numerical study", *Proc. Roomvent 2000*, Vol. I, pp. 307-312, Ed. Awbi H.B., Elsevier Science Ltd.

Deardorff J.W. (1974), "Three-dimensional study of the height and mean structure of a heated planetary boundary layer", *Boundary Layer Meteorology*, Vol. 18, pp. 495-527.

Emmerich S.J. and McGrattan K.B. (1998), "Application of a large eddy simulation model to study room airflow", *ASHRAE Trans.*, Vol. 104, Part 1-B, pp. 1128-1140.

Fanger P.O., K. Melikov A.K., Hanzawa H. and Ring J. (1988), " Air turbulence and sensation of draught", *Energy and Buildings*, Vol. 12, pp. 21-39.

Ferziger J.H. and Peric M. (1999), "Computational method for fluid dynamics", Second edition, Springer 1996, 1999.

Fureby C. (1999)," Large eddy simulation of rearward-facing step flow", *AIAA journal*, Vol 37, No. 11, pp. 1401-1411.

Galperin B. and Orzag S.A. (1993), "Large eddy simulation of complex engineering and geophysical flows", Cambridge University Press, 1993.

Gatski T.B. (1996), "Prediction of aerofoil characteristics with higher order turbulence models", NASA *Tech. Memo.* 110246.

Gatski T.B. and Speziale C.G. (1993), "On explicit algebraic stress model for complex turbulent flows", *J. Fluid Mech.*, Vol. 254, pp. 59-78.

Gavrilakis S. (1992), "Numerical simulation of low Reynolds number turbulent flow through a straight square duct", *J. Fluid Mech.* Vol. 244, pp. 101-129.

Gebhart B. (1959), "A new method for calculating radiant exchanges", *ASHRAE Trans.*, Vol. 65, pp. 321-332.

Germano M., Piomelli U., Moin P. and Cabot W.H. (1991), "A dynamic subgrid scale eddy viscosity model", *Physics of Fluids, A. 3*, 1760-1765.

Hart R.H. (1970), "The concept of APS: Air Pollution Syndrome(s)", *J. South Carolina Medical Association*, Vol. 66, pp. 71-73.

Hayashi T., Ishizu Y., Kato S. and Murakami S. (2002), "CFD analysis on characteristics of contamined indoor air ventilation and its application in the evaluation of the effects of contaminant inhalation by a human occupant", *Building and Environment*,

Vol. 37, pp. 219-230.

He P., Kuwahara R. and Mizutani K. (1999), "Numerical study on air conditioned indoor airflow by dynamic large eddy simulation", *Proc. Indoor Air 1999*, Vol. 1, pp. 714-719.

Hedge A. (1992), "Indoor air quality and "sick" building syndrome in offices", *Hum. Ecological Forum*, Vol. 20, pp. 2-6.

Hinze J.O. (1975), "Turbulence", McGraw-Hill, New York.

Hirt C.W. (1968),"Heuristic stability theory for finite difference equations", *Phys. Fluids*, Suppl. II, pp. 219-227.

Hodgson M. (2000), "Sick building syndrome", *Occupational medecine*, Vol. 15, No. 3, pp. 571-585.

Holmes S. H., Jouvray A. and Tucker P. G. (2000), "An assessment of a range of turbulence models when predicting room ventilation", *Proc. Healthy Buildings 2000*, Vol. 2, pp. 401-406, ISBN 952-5236-09-9.

Hu S.-C., Barber J.M. and Chuah Y.K. (1999), "A CFD study for cold air distribution systems", *ASHRAE transactions*, Vol. 105, Part 1, pp. 614-630.

Hunt G.R., Cooper P., Linden P.F. (2000), "Thermal stratification produced by plumes and jets in enclosed spaces", *Proc. Roomvent 2000*, Vol. I, pp. 191-198, Ed. Awbi H.B., Elsevier Science Ltd.

Hyun S. and Kleinstreuer C. (2000), "Computational exposure and dose assessment analyses for transient turbulent flow and gaseous pollutant transport", *Proc. Roomvent*

2000, Vol. I, pp. 119-124, Ed. Awbi H.B., Elsevier Science Ltd.

Iacovides H. and Raisee M. (1997), "Computation of flow and heat transfer in 2D rib roughened passages", *Proc. of the 2nd Int. Symp. on turbulence, heat and mass transfer*, Delft University press, Addendum pp. 21-30.

ISO 7726 (1985), "Thermal environments - Instruments and methods for measuring physical quantities", Reference number: ISO 7726:1985.

ISO 5167-1 (1991), "Measurement of fluid flow by means of pressure differential devices, Part I: Orifice plates, nozzles, and venturi tubes inserted in circular cross-section conduits running full", Reference number: ISO 5167-1:1991(E).

ISO 7730 (1994), "Moderate thermal environments- Determination of the PMV and PPD indices and specification of the conditions for thermal comfort."

ISO 5167-1/Amd.1 (1998), "Amendment 1: Measurement of fluid flow by means of pressure differential devices, Part I: Orifice plates, nozzles, and venturi tubes inserted in circular cross-section conduits running full", Reference number: ISO 5167-1:1991/Amd.1:1998(E).

Jacobsen T.V. and Nielsen P.V. (1993), "Numerical modelling of thermal environment in a displacement-ventilated room", *Proc. Indoor Air' 93*, Vol. 5, pp. 301-306.

Jones W.P. and Launder B.E. (1972), "The prediction of laminarization with a two equation model of turbulence", *Int. J. of Heat and Mass Transfer*, Vol. 15, pp. 301-314.

Jones W.P. (1997), "Air conditioning applications and design", Second Ed., Arnold, 1997.

Joubert P., Sergent A., Le Quere P. and Allard F. (2000), "Large eddy simulation approach for non-isothermal airflows in partitioned rooms", *Proc. Roomvent 2000*, Vol. 1, pp. 461-466., Ed. Awbi H.B., Elsevier Science Ltd.

Jouvray A. and Tucker P. G. (2003), "On non linear RANS, hybrid and LES models applied to complex flows", *Proceedings of the 4th International Symposium on Turbulence, Heat and Mass Transfer*, pp. 665-670, Ed. Hanjalic K., Nagano Y. and Tummers M., Begell House Inc., New-York, Swansea (UK).

Karimipanah T., Sandberg M. and Awbi H.B. (2000), "A comparative study of different air distribution systems in a classroom", *Proc. Roomvent 2000*, Vol. II, pp. 1013-1018, Ed. Awbi H.B., Elsevier Science Ltd.

Kato S. and Murakami S. (1986), "New scale for ventilation efficiency and calculation method by means of 3-dimensional numerical simulation for turbulent flow", *Trans. of the Society of Heating, Air Conditioning and Sanitary Engineers of Japan*, Vol. 32, pp. 91-102.

Kim J.J. (1978), "Investigation of separation and reattachment of turbulence shear layer: Flow over a backward facing step", *PhD. Thesis*, University of Stanford, .

Kim J.J., Kline S.J. and Johnston J.P. (1980), "Investigation of a reataching turbulent shear layer: Flow over a backward-facing Sstep", *ASME Trans, J. of Fluids Engineering*, Vol. 102, pp. 302-308.

Kim T., Kato S. and Murakami S. (2001), "Indoor cooling/heating load analysis based on coupled simulation of convection, radiation and HVAC control", *Building and Environment*, Vol. 36, pp. 901-908.

Krühne H. and Fitzner K. (2000), "Protection of non-smoking persons against cigarette smoke by airflow", *Proc. Roomvent 2000*, Vol. I, pp. 179-184, Ed. Awbi H.B., Elsevier Science Ltd.)

Kuwahara R., Akabayashi S.I., He P., Mizutani K. and Sato H. (2000), "An experimental and numerical study of the relationship between ventilation efficiency and air supply/exhaust system of an atrium space", *Proc. Roomvent 2000*, Vol. II, pp. 905-911, Ed. Awbi H.B., Elsevier Science Ltd.

Lam C.K.G. and Bremhorst K. (1981), "A modified form of the $k-\epsilon$ model for predicting wall turbulence", *ASME J. Fluid Eng.*, Vol. 103, pp, 456-460.

Laufer J. (1951), "Investigation of turbulent flow in a two-dimensional channel", *NACA TN 1053.*

LaVerne A.A. (1970), "Non specific Air Pollution Syndrome (NASP): Preliminary report", *Behav. Neuropsychiatry*, Vol. 2, pp. 19-21.

Launder B.E. and Kato M, (1993), "The modelling of flow-induced oscillations in turbulent flow around a square cylinder", *ASME Fluid Eng. Conf.*, Vol. 157, pp189-199.

Launder B.E., Morse A., Rodi W. and Spalding D.B. (1972),"The prediction of free shear flows - A comparison of the performance of six turbulence models", *Proc. Of NASA Conference on free Shear Flows*, Langley.

Launder B.E. and Sharma B.I. (1974),"Application of the energy dissipation model of turbulence to the calculation of flow near a spinning disc", *Letters heat and mass transfer*, Vol. 1, pp. 131-138.

Launder B.E. and Spalding D.B. (1974), "The numerical computation of turbulent

flows", *Computational methods applied to mechanical engineering*, Vol. 3, pp. 269-289.

Leonard B.P., (1974),"Energy cascade in large eddy simulation of turbulent fluid flows", *Adv. Geophys.*, Vol. 18 A, pp. 237-248.

Leonard B.P., (1979), "A stable and accurate convective modelling procedure based on quadratic upstream interpolation", *Computational methods applied to mechanical engineering*, Vol. 19, pp. 59-99.

Lesieur M. and Metais O. (1996), "New trend in large eddy simulation of turbulence", *Annual review of Fluid Mechanics*, Vol. 28, pp. 45-82.

Lilly D.K. (1992), "A proposed version of the Germano subgrid scale closure", *Physics of Fluids*, A 4, pp. 633-635.

Lin Z., Chow T.T., Fong K.F. and Chen Q., (1999), "Validation of CFD model for research into application of displacement ventilation to Hong Kong buildings", *Proc. of the* 3rd *Int. Symp. on HVAC*, Shenzhen, China, 17-19 Nov., Vol. II, pp. 602-613.

Liu Y., Tucker P.G., Jouvray A. and Carpenter P.W. (2003), "Computation of a non-isothermal complex geometry flow using non-linear URANS and zonal LES modelling", *Proceedings of the* 3rd *International Symposium on Turbulence and Shear Flow Phenomena*, Vol. 1, pp. 87-91, Ed. Kasagi N., Eaton J.K., Friedrich R., Humphrey J.A.C., Leschziner M.A. and Miyauchi T., Sendai, Japan, June, 2003.

Lo Iaconno G. (2003), "Numerical Study of particle motion in a turbulent ribbed duct", *PhD Thesis*, Fluid Dynamics Research Centre, University of Warwick, U.K.

Lu W. (1995), "Modelling of airflow and aerosol particle movement in buildings", *PhD*

Thesis, De Montfort University, UK.

Lu W. and Howarth A.T. (1999), "CFD modeling and measurement of aerosol particle distributions in ventilated multizone rooms", *ASHRAE Transaction*, Vol. 105, Part 2, pp. 116-127.

Lumley J.L. (1970), "Toward a turbulent constitutive relation", *J. of Fluid Mech.*, Vol. 41, Part 2, pp. 413-434.

Lumley J.L. (1975),"Pressure strain correlation", *Physics of fluids*, Vol. 18, pp. 750.

McGrattan K.B., Baum H.R. and Rehm R.G. (1998),"Large eddy simulation of smoke movement", *Fire safety journal*, Vol. 30, pp. 161-178.

McQuiston F.C. and Parker J.D. (1994),"Heating ventilating and air conditioning", J. Wiley & Sons, Fourth Ed. , 1994.

Melikov A.K. and Nielsen P.V. (1989), "Local thermal discomfort due to draft and vertical temperature difference in rooms with displacement ventilation", *AHSRAE Trans.* Vol. 95, Part. 2, pp. 1050-1057.

Menon S. and Kim W.W. (1996), "High Reynolds number flow simulations using the localized dynamic subgrid-scale model", 34^{th} Aerospace Sciences Meeting, *AIAA paper* 96-0425, Reno.

Molhave L. (1989), "The sick buildings and other buildings with indoor climate problems", *Environ. Int.*, Vol. 15, pp. 65-74.

Mompean G. (1998), "Numerical simulation of a turbulent flow near a right angled corner using the Speziale non-linear model with RNG $k - \epsilon$ equations", *Computers and*

Fluids, Vol. 27, No. 7, pp. 847-859.

Müller D. and Davidson L. (2000), "Comparison of different subgrid turbulence models and boundary conditions for large-eddy-simulation of room air flows", *Proc. Roomvent 2000*, Vol. I, pp. 301-306, Ed. Awbi H.B., Elsevier Science Ltd.

Mundt E., (2000), "Particles and displacement ventilation", *Proc. Roomvent 2000*, Vol. II, pp. 737-742, Ed. Awbi H.B., Elsevier Science Ltd.

Nazaroff W.W., Ligock M.P., Ma T and Cass G.R. (1990),"Particle deposition in a museum: comparison of modelling and measurement results", *Aerosol science and technology*, Vol. 13, pp. 332-348.

Nielsen P.V., Restivo A. and Whitelaw J.H. (1978), " The velocity characteristics of ventilated rooms", *J. of Fluid Engineering*, Vol. 100, pp. 291-298.

Nielsen P.V. (1990), "Specification of a two dimensional test case", ISSN 0902-7513 R9040, Aalborg University, Denmark.

Nielsen P.V., Filhojm C., Topp C., Davidson L. (2000), "Model experiments with low Reynolds number effects in a ventilated room", *Proc. Roomvent 2000*, Vol. I, pp. 185-190, Ed. Awbi H.B., Elsevier Science Ltd.

Park H.J. and Holland D. (2000), "The effect of location of a convective heat source on displacement ventilation: CFD study", *Proc. Roomvent 2000*, Vol. II, pp. 705-710, Ed. Awbi H.B., Elsevier Science Ltd.

Patankar S.V. (1980), "Numerical heat transfer and fluid flow", McGraw-Hill, New York.

Patankar S.V. and Spalding D.B. (1972),"A calculation procedure for heat mass and momentum transfer in three dimensional parabolic flows", *Int. J. of Heat and Mass Transfer*, Vol. 15, pp. 1787-1806.

Peltier L.J., Zajaczkowski F.J. and Wyngaard J.C. (2000), "A hybrid RANS/LES approach to large eddy simulation of high Reynolds number wall bounded turbulence", *Proc. ASME FEDSM'00*, ASME 2000 Fluid engineering division summer meeting, Boston, USA, FEDSM2000-11177.

Peng S-H. (1998), "Modelling of turbulent flow and heat transfer for building ventilation", *PhD thesis*, Chalmers University of technology, Gothenburg, Sweden.

Peng S-H., Davidson L. and Holmberg S. (1996), "Performance of two-equation turbulence models for numerical simulation of ventilated rooms", *Proc. Roomvent 1996*, Vol. 2, pp. 153-160.

Peng S-H., Davidson L. and Holmberg S. (1997), "A modified low Reynolds number $k-\omega$ model for recirculating flows", *ASME J. of fluid engineering*, Vol. 119, pp. 867-875.

Peng S-H. and Davidson L. (2000), "The potential of large eddy simulation techniques for modelling indoor air flows", *Proc. Roomvent 2000*, Vol. I, pp. 295-300, Ed. Awbi H.B., Elsevier Science Ltd.

Peng S-H. and Davidson L. (2001), "Large eddy simulation for turbulent buoyant flow in a confined cavity", *Int. J. of Heat and Fluid Flow*, Vol. 22, pp. 323-331.

Peng S-H. and Davidson L. (2002), "On a subgrid-scale heat flux model for large eddy simulation of turbulent thermal flow", *Int. J. of Heat and Mass Transfer*, Vol. 45, pp.

1393-1405.

Pollock D.D. (1991),"Thermocouples: Theory and properties", CRC press.

Pope S.B. (1975), "A more general effective-viscosity hypothesis", *J. of Fluid Mechanics*, Vol. 72, pp. 331-340.

Pope S.B. (2000), "Turbulent flows", *Cambridge University Press*, 2000.

Prandtl L. (1925),"Bericht uber Untersuchungen zur ausgebildeten Turbulenz", ZAMM 5 pp. 136.

Quemere and Sagaut (2002), "Zonal multi-domain RANS/LES simulations of turbulent flows", *Int. J. for numerical methods in fluids*, Vol. 40, pp. 903-925.

Rauer P. (1996), "Untersuchung der Deckenverschmutzung im Bereich Induktiver Decken-Zuluftdurchlasse", Diploma Thesis, FH Koln, Germany.

Recknagel H., Sprenger E. and Schamek E.R. (1999), "Taschenbuch fur Heizung + Klimatechnik", Munchen, Germany.

Reynolds O. (1895), "On the dynamical theory of incompressible viscous fluids and the determination of the criterion", *Phil. trans. of the Royal Soc. of London*, Series A, Vol. 186, pp. 123.

Rodi W. and Spalding D.B. (1970),"A two-parameter model of turbulence and its application to free jets", *Warme und Stroffubertragung*, Vol.3, pp. 20.

Rodi W. (1975), "The prediction of free turbulent boundary layers by the use of a two-equation model of turbulence", Ph.D. thesis, University of London, UK.

Rodi W., Mansour N.N. and Michelassi V. (1993), "One equation near wall turbulence modelling with the aid of direct simulation data", *J. of Fluid Engineering*, Vol. 115, pp. 196-205.

Rodi W., Ferziger J.H. Breuer M. and Pourquie M. (1997),"Status of large eddy simulation: Results of a workshop", *ASME Trans.*, Vol. 119, pp. 248-262.

Rogallo R. and Moin P. (1994), "Numerical simulation of turbulent flow", *Annual review of fluid mechanics*, Vol. 16. pp. 99-137.

Rollet-Miet P., Laurence L. and Ferziger J. (1999), " LES and RANS of turbulent flow in bundles", *Int. J. of heat and fluid flows*, Vol. 46, pp. 241-254.

Rokni M. (1997), "Improved modeling of turbulent forced convective heat transfer in straight ducts", *ASME HTD*, Vol. 346, pp. 141-149.

Rokni M. (1998), "Numerical investigation of turbulent fluid flow and heat transfer in ducts", Ph.D. thesis, Lund Institute of Technology, Sweden, ISSN 1104-7747.

Rokni M. (2000), "Algebraic stress model for heat transfer in ducts", *Numerical Heat Transfer, Part B*, Vol. 37, pp. 331-363.

Rokni M. (2000-b), *Personal Communication*, February, 2000.

Runchal A.K. (1987), "CONDIF: A modified central-difference scheme for convective flows", *Int. J. for numerical methods in engineering*, Vol. 24, pp. 1593-1608.

Rydock J.P., Hestad T., Haugen H. and Skaret J.E. (2000), "An isothermal air curtain for isolation of smoking areas in restaurants", *Proc. Roomvent 2000*, Vol. I, pp. 663-668, Ed. Awbi H.B., Elsevier Science Ltd.

Sagaut P., Troff B., Le T.H. and La P.L. (1996), "Large eddy simulation of turbulent flow past a backward facing step with a new mixed scales SGS model", *IMACS-COST Conf. Computational Fluid Dynamics three-Dimensional Complex Flow*, Lausanne, Switzerland, Sept. 1995, pp. 13-15.

Schlichting H. and Gersten K., (2000), "Boundary layer theory", 8^{th} Revised and Enlarged Edition, Springer-Verlag.

Shaw C.Y., Zhang J.S., Said M.N., Vaculik P.E. and Magee R.J. (1993-a), "Effect of air diffuser layout on the ventilation conditions of a workstation - Part I: Air distribution patterns", *ASHRAE Transactions*, Vol. 99, Part II.

Shaw C.Y., Zhang J.S., Said M.N., Vaculik P.E. and Magee R.J. (1993-b),"Effect of air diffuser layout on the ventilation conditions of a workstation - Part II: Air change efficiency and ventilation efficiency", *ASHRAE Transactions*, Vol. 99, Part II.

Shaw C.Y. (2000), "Evaluating seven diffuser layouts: Ventilation for Workstations", *ASHRAE Journal*, pp.52-59.

Shih T-H., Liou W.W., Shabbir A. Yang Z. and Zhu J. (1995), "A new $k-\epsilon$ eddy viscosity model for high Reynolds number turbulent flows", *Computers and Fluids*, Vol. 24, pp. 227-238.

Shur M., Spalart P.R., Strelets M. and Travin A. (1999), "Detached eddy simulation of an aerofoil at high angle of attack", *Proc. of the* 4^{th} *int. symp. on engineering turbulence modelling and measurements*, pp. 669-678, Corsica, France.

Sinai Y.L., Owens M.P. and McLaughlin A. (2000), "Case study: CFD modelling of HVAC in the Greenwich millenium dome", *Proc. Roomvent 2000*, Vol. II, pp. 1165-

1170, Ed. Awbi H.B., Elsevier Science Ltd.

Smagorinsky J. (1963), "General circulation experiments with the primitive equations. I. The basic experiment", *Monthly Weather Review*, Vol. 91, No. 3, pp. 99-165.

Spalart P.R. (1999), "Strategies for turbulence modelling and simulations", *Int. J. of Heat and Fluid Flow*, Vol. 21, pp. 252-263.

Spalart P.R., Jou W-H., Strelets M. and Allmaras S. (1997),"Comments on the feasibility of LES for wings and on a hybrid RANS/LES approach", 1^{st} *AFORS Int. Conf. on DNS/LES in Advances in DNS/LES*, Eds. Liu C. and Liu Z., Greyden Press.

Spalding D.B. (1961), "A single formula for the law of the wall", *ASME Transactions, Series A., J. of Applied Mechanics*, Vol. 28, pp. 444-458.

Spalding D.B. (1972)," A novel finite difference formulation for the differential expressions involving both first and second derivative", *Int. J. for Numerical Methods in Engineering*, Vol. 4, pp. 551-561.

Speziale C.G. (1982), "On turbulent secondary flows in pipes of non-circular cross section", *Int. J. Engineering Science*, Vol. 20, pp. 863.

Speziale C.G. (1987), "On non-linear k-l and k-ϵ models of turbulence", *J. Fluid Mech.*, Vol. 178, pp. 459-475.

Speziale C.G. (1998), "Turbulence modeling for time-dependent RANS and VLES: A review", *AIAA journal*, Vol 36. No. 2, pp. 173-184.

Speziale C.G. and Xu X-H. (1995), "Towards the development of second-order closure models for non-equilibrium turbulent flows", 10^{th} *Symp. on Turbulent Shear Flow*,

Pennsylvania State University, pp. 23.7-23.12.

Srebric J., Chen Q. and Glicksman L.R. (1999), " Validation of a zero-equation turbulence model for complex indoor airflow simulation", *ASHRAE Trans.*, Vol. 105, Part 2, pp. 414-427.

Srebric J. and Chen Q. (2001), " A method of test to obtain diffuser data for CFD modelling of room airflow", *ASHRAE Trans.*, Vol. 107, Part II, pp. 108-116.

Sundell J. (1994), "On the association between building ventilation characteristics, some indoor environemental exposures, some allergic manifestations and subjective symptom reports", *Indoor Air Supplement*, No. 2/94.

Sundell J. (1996), "What we know and what we don't know about sick building syndrome", *ASHRAE Journal*, Vol. 38.

Svidt K., Heiselberg P. and Nielsen P.V. (2000), "Characterization of the airflow from a bottom hung window under natural ventilation", *Proc. Roomvent 2000*, Vol. II, pp. 755-760, Ed. Awbi H.B., Elsevier Science Ltd.

Sykes J.M. (1989), "Sick building Syndrome", *Building Services Eng. Res. Technol.* Vol. 10, pp.1-11.

Tennekes H. and Lumley J.L. (1972), "A first course in turbulence", Cambridge, MA: MIT Press.

Thangam S. and Speziale C.G. (1992), "Turbulent flow past a backward-facing step: A critical evaluation of two-equation models", *AIAA Journal*, Vol. 30, No. 5, pp. 1314-1320.

Timmer H. and Zeller M. (2000), "Simulation of particle deposition near ceiling induction outlet", *Proc. Roomvent 2000*, Vol. I, pp. 95-100, Ed. Awbi H.B., Elsevier Science Ltd.

Toro E.F. (1999),"Riemann solvers and numerical methods for fluid dynamics: A practical introduction", 2^{nd} Edition, Springer.

Tritton D.J. (1988), "Physical Fluid Dynamics", Oxford University Press, Second ed., 1988.

Trzeciakiewicz Z., Lipska B., Popiolek Z. and Mierzwinski S. (2000), "Comparison of experimental and numerical test results of the airflow in a room with displacement ventilation", *Proc. Roomvent 2000*, Vol. II, pp. 719-724, Ed. Awbi H.B., Elsevier Science Ltd.

Tucker P.G. (1998), "Assessment of geometric multilevel convergence robustness and a wall distance for flows with multiple internal boundaries", *Applied Math. Modelling*, Vol. 22, pp. 293-311.

Tucker P.G. (2000), "Prediction of turbulent oscillatory flows in complex systems", *Int. J. for numerical methods in fluids*, Vol. 33, pp. 869-895.

Tucker P.G. (2001), "Computation of unsteady internal flows", Kluwer Academic Publishers, 2001.

Tucker P.G. (2001-b), "Novel multigrid orientated solution adaptive time step approaches", *Int. J. for numerical methods in fluids*, Vol. 40, pp. 507-519.

Tucker P.G. (2004), "DES computations for flows with mild separation using more dissipative solvers", *Submitted for* 42^{nd} *Aerospace science meeting and exhibit*, Reno, Nevada.

Tucker P.G. and Davidson L. (2003), "Zonal $k-l$ based large eddy simulations", 41^{st} *AIAA aerospace science meeting and exhibit*, Reno, Nevada, AIAA-2003-0082.

Tucker P. G., Liu Y., Chung Y-M. and Jouvray A. (2003), "Computation of an unsteady complex geometry flow using novel non-linear turbulence models", *International journal for numerical methods in fluids*, Vol. 43, No. 9, pp. 979-1001.

Turner J.S. (1973), "Buoyancy effects in fluids", Cambridge University Press.

Van Driest (1956),"On turbulent flow near a wall", *Journal of the Aeronautical Sciences*, Vol. 23, pp. 1007.

Versteeg H.K. and Malalasekera W. (1995), "An introduction to computational fluid dynamics", Longman, 1995.

von Karman T. (1931), *Technical Report NACA, TM 611.*

WHO (World Health Organization) (1983), "Indoor air pollutants: Exposure and health effects", EURO reports and studies 78, WHO, Geneva.

Wilcox D.C. (1995), "Turbulence modelling for CFD", DWC Industries, Inc., La Canada, California.

Wolfshtein M. (1969), "The velocity and temperature distribution in one-dimensional flow with turbulence augmentation and pressure gradient", *Int. J. of heat and mass transfer*, Vol. 12, pp. 301-318.

Xing H., Hatton A. and Awbi H.B. (2001), " A study of the air quality in a room with displacement ventilation", *Building and Environment*, Vol. 23, pp. 809-820.

Xin S. and Le Quere P. (1995), "Direct numerical simulation of two-dimensional chaotic natural convection in a differentially heated cavity of aspect ratio 4", *J. Fluid Mechanics*, Vol. 304, pp. 87-118.

Xu W. and Chen Q. (2001-a), "A two-layer turbulence model for simulating indoor airflow; Part I. Model development", *Energy and Buildings*, Vol. 33, pp. 613-625.

Xu W. and Chen Q. (2001-b), "A two-layer turbulence model for simulating indoor airflow; Part II. Applications", *Energy and Buildings*, Vol. 33, pp. 627-639.

Yakhot V. and Orzag S.A. (1986), "Renormalization group analysis of turbulence. I. Basis theory", *J. of Scientific Computing*, Vol. 1, pp. 3-51.

Yakhot V., Orzag S.A., Thangam S., Gatski T.B. and Speziale C.G. (1992), " Development of turbulence models for shear flow by a double expansion techniques", *Phys. Fluids A*, Vol. 4 (7), pp. 1510.

Yap C.R. (1987), "Turbulent heat and momentum transfer in recirculating and impinging flows", *PhD Thesis*, University of Manchester, U.K.

Yoon J., Lee K. and Lee J. (2000), "Computer simulation of the indoor environments with cooling and heating systems: The great hall in the Inchon international airport terminal", *Proc. Roomvent 2000*, Vol. II, pp. 1195-1200, Ed. Awbi H.B., Elsevier Science Ltd.

Yoshizawa A. (1993), "Bridging between eddy viscosity type and second order models using a two-scale DIA", 9^{th} *Int. Symp. on turbulent shear flow*, pp. 23.1.1-23.1.6, Kyoto.

Yuan X., Chen Q., Glicksman L.R., Hu Y. and Yang X. (1999), "Measurements and

computations of room airflow with displacement ventilation", *ASHRAE Trans.*, Vol. 105, Part 1., pp. 340-352.

Yuan X., Chen Q. and Glicksman L.R. (1999), "Models for the prediction of temperature difference and ventilation effectiveness with displacement ventilation", *ASHRAE Trans.*, Vol. 105, Part 1, pp. 353-367.

Zajaczkowski F.J. and Peltier L.J. (2001)," Energy containing range modelling of fully developed channel flow using a hybrid RANS/LES technique", *Proc. of the* 3^{rd} *Int. conference on DNS/LNS*, Arlington, Texas.

Zeng J., Shaw C.Y., Magee R.J. and Sander D. (2000), "Study on ventilation performance and indoor air quality of a portable classroom: field measurement and numerical simulation", *Proc. Roomvent 2000*, Vol. II, pp. 1001-1006, Ed. Awbi H.B., Elsevier Science Ltd.

Zhang W. and Chen Q. (2000), "Large eddy simulation of indoor airflow with a filtered dynamic subgrid scale model", *Int. J. of Heat and Mass Transfer*, Vol. 43, pp. 3219-3231.

Appendix A

An assessment of a range of tubulence models when predicting room ventilation

Any pages, tables, figures or photographs, missing from this digital copy, have been excluded at the request of the university.

Appendix B

Typical calibration certificate of the DANTEC anemometers

DANTEC
Measurement Technology
DK-2740 Skovlunde • Denmark
Phone: +45 4482 3816 FAX: +45 4284 8136

Calibration certificate.

Low Velocity Transducer 54R10

Date 980805 Certificate no. R10-0761
Initials PRN Probe serial no. 0761

The instrument with serial number as above contains the following calibrated items:

Test object:	Velocity sensor.	Test conditions:	
Ranges:	0-1 m/s, 0-5 m/s	Atmospheric air	
Calibrated:	980805	Temperature:	24,7°C
Procedure:	5900F227	Atm. press.:	101,6 kPa
Uncertainty:	±2%OR ±0,02 m/s on reference velocity.	Rel. humidity:	61%

Calibration results:

Reference velocity [m/s]	Indicated velocity [m/s]	Correction [m/s]
0,098	0,110	-0,012
0,145	0,151	-0,006
0,205	0,207	-0,002
0,294	0,290	+0,004
0,430	0,432	-0,002
0,636	0,650	-0,014
0,974	1,011	-0,037
2,18	2,32	-0,14
3,24	3,50	-0,26
4,90	5,00	-0,10

Test object:	Thermistor.	Test conditions:	
Range.	0-45°C	Atmospheric air	
Calibrated:	980805	Temperature:	24,7°C
Procedure:	5900F227	Velocity:	0,43 m/s
Uncertainty:	±0,2°C on reference temperature.		

Calibration results:

Reference temperature [°C]	Indicated temperature [°C]	Correction [°C]
24,8	24,6	0,2

Traceability of DANTEC LVFA Windtunnel to DANAK. 9055P2933
Orig.930123/TSV
Rev.970304/TSV

Calibrations in the DANTEC LVFA windtunnel 435-1010 are carried out in accordance with Nordtest Method NT VVS 018. The windtunnel calibrations are traceable to national accredited laboratories[1] through the following instruments or transfer standards:

Velocity 0 to 5 m/s.....: Micromanometer 435-1002.
Traceable to micromanom. 435-1050.
Traceable to DTI, Århus. Accreditation no 200.

Barometric pressure.....: Barometer 435-1008.
Traceable to elektr. baron. 435-1040.
Traceable to DTI, Århus. Accreditation no. 200.

Air temperature.....: Electronic thermometer 435-1001.
Traceable to DTI, Århus. Accreditation no. 200.

Relative humidity.....: Hygrometer 435-1009.
Not traceable.

DC voltage.....: Digital voltmeter 435-1004.
Traceable to AREPA, Silkeborg. Accreditation no. 22.

The measurement capability is calculated from the following table:

Velocity 0.1 to 0.7 m/s.....: ±0.02 m/s.

Velocity 0.7 to 5 m/s.....: ±0.02 m/s ±0.02 U.

Approved signature.....: Jenny Dam

Printed name/initials.....: Jenny Dam /JDM.

Approved signature.....: Per Ravn.

Printed name/initials.....: Per Ravn /PRN.

Approved signature.....: Toni Stannow.

Printed name/initials.....: Toni Stannow /TSV.

[1] In Denmark represented by DANAK, a member of the EOTC.

File: 9529331.DOC

Appendix C

Wall temperature for cases 01 to 06

Designation	x	y	z	Case 01	Case 02	Case 03
T1	900	2250	3000	25.07	23.32	21.30
T2	3000	2250	3000	25.06	23.38	21.40
T3	1950	1500	3000	25.40	23.58	21.58
T4	900	750	3000	27.55	25.54	24.30
T5	3900	2250	2250	25.22	23.46	21.56
T6	3900	2250	750	25.19	23.39	21.49
T7	3900	1500	1500	24.83	23.17	21.30
T8	3900	750	750	24.59	22.76	20.86
T9	3000	2250	0	25.12	23.42	21.44
T10	900	2250	0	24.90	23.10	21.10
T11	1950	1500	0	24.82	23.08	21.05
T12	3000	750	0	24.58	22.60	20.64
T13	900	750	0	24.67	22.68	20.67
T14	0	2250	750	24.83	23.21	21.20
T15	0	2250	2250	24.89	23.01	21.98
T16	0	1500	1500	25.13	23.40	21.35
T17	0	750	750	24.99	22.68	20.29
T18	0	750	2250	24.37	23.01	20.78
T19	900	0	750	24.15	21.99	19.96
T20	900	0	2250	25.32	23.50	21.50
T21	1950	0	1500	24.57	22.67	20.66
T22	3000	0	750	24.11	22.39	20.50
T23	900	3000	750	25.26	23.50	21.55
T24	900	3000	2250	25.04	23.28	21.32
T25	1950	3000	1500	25.07	23.31	21.28
T27	3000	3000	2250	25.41	23.73	21.75

Table C.1: Surface temperature in the room for the displacement ventilation layout. Dimensions in *mm*.

Designation	x	y	z	Case 04	Case 05	Case 06
T1	900	2250	3000	23.76	20.77	21.38
T2	3000	2250	3000	23.77	20.94	21.83
T3	1950	1500	3000	24.06	21.22	22.07
T4	900	750	3000	27.54	24.19	25.68
T5	3900	2250	2250	23.80	21.08	21.82
T6	3900	2250	750	23.76	21.03	21.66
T7	3900	1500	1500	23.54	20.82	21.93
T8	3900	750	750	23.92	20.65	22.24
T9	3000	2250	0	23.58	21.01	21.89
T10	900	2250	0	23.83	20.72	21.60
T11	1950	1500	0	23.49	20.65	21.54
T12	3000	750	0	23.40	20.49	21.44
T13	900	750	0	23.26	20.60	21.48
T14	0	2250	750	23.52	20.78	21.66
T15	0	2250	2250	23.54	20.65	21.55
T16	0	1500	1500	23.85	21.00	21.90
T17	0	750	750	23.13	20.18	21.10
T18	0	750	2250	23.74	20.65	21.69
T19	900	0	750	23.29	20.48	21.62
T20	900	0	2250	23.93	21.10	22.01
T21	1950	0	1500	23.48	20.78	21.92
T22	3000	0	750	21.93	20.49	21.61
T23	900	3000	750	23.91	21.15	22.05
T24	900	3000	2250	23.74	20.87	21.69
T25	1950	3000	1500	23.68	20.93	21.85
T27	3000	3000	2250	24.09	21.34	22.25

Table C.2: Surface temperature in the room for the mixed ventilation layout. Dimensions in *mm*.

Appendix D

Velocity and airflow temperature of the Dantec anemometers

Designation	x	y	z	Velocity (m/s)	Temperature (C)
D1	600	150	325	0.0949	22.74
D2	600	2850	325	0.0349	24.60
D3	600	150	2675	0.0925	21.56
D4	600	2850	2675	0.0452	23.88
D7	1600	1600	1800	0.1680	24.10
D8	1600	2850	1800	0.0486	22.20
D10	1600	1600	700	0.0683	21.39
D13	2700	1600	700	0.0585	23.33
D14	2700	2850	700	0.0632	22.61
D15	3600	1600	200	0.0529	24.34
D16	3100	950	1200	0.0375	24.12
D18	3600	950	2700	0.0482	24.59

Table D.1: Location, mean temperature and velocity of the Dantec anemometers for Case 02 (dimensions in mm).

Designation	x	y	z	Velocity (m/s)	Temperature (C)
D1	600	150	325	0.1191	18.84
D2	600	2850	325	0.0420	22.50
D3	600	150	2675	0.2131	18.53
D4	600	2850	2675	0.0384	22.14
D7	1600	1600	1800	0.2329	22.12
D8	1600	2850	1800	0.0602	19.51
D10	1600	1600	700	0.0787	19.50
D13	2700	1600	700	0.0488	21.47
D14	2700	2850	700	0.0577	19.79
D15	3600	1600	200	0.0452	22.66
D16	3100	950	1200	0.0357	21.93
D18	3600	950	2700	0.0449	22.22

Table D.2: Location, mean temperature and velocity of the Dantec anemometers for Case 03 (dimensions in mm).

Designation	x	y	z	Velocity (m/s)	Temperature (C)
D1	600	150	325	0.0739	24.19
D2	600	2850	325	0.0508	24.75
D3	600	150	2675	0.0662	24.13
D4	600	2850	2675	0.1169	23.97
D7	1600	1600	1800	0.1443	24.38
D8	1600	2850	1800	0.0660	24.04
D11	1600	2850	700	0.0642	23.73
D13	2700	1600	700	0.0453	23.92
D14	2700	2850	700	0.0844	24.34
D15	3600	1600	200	0.0473	24.89
D17	3100	950	1800	0.0446	24.26
D19	2400	950	2700	0.0744	24.96

Table D.3: Location, mean temperature and velocity of the Dantec anemometers for Case 04 (dimensions in mm).

Designation	x	y	z	Velocity (m/s)	Temperature (C)
D1	600	150	325	0.0664	21.33
D2	600	2850	325	0.2012	20.26
D3	600	150	2675	0.0926	20.99
D4	600	2850	2675	0.1739	20.20
D7	1600	1600	1800	0.0778	21.49
D8	1600	2850	1800	0.1006	20.92
D11	1600	2850	700	0.092	20.73
D13	2700	1600	700	0.0483	20.87
D14	2700	2850	700	0.0778	21.49
D15	3600	1600	200	0.0458	22.27
D16	3100	950	1200	0.0478	21.46
D18	3600	950	2700	0.0559	21.70

Table D.4: Location, mean temperature and velocity of the Dantec anemometers for Case 05 (dimensions in mm).

Designation	x	y	z	Velocity (m/s)	Temperature (C)
D1	600	150	325	0.0762	22.16
D2	600	2850	325	0.0503	22.48
D3	600	150	2675	0.1146	21.89
D4	600	2850	2675	0.2473	21.19
D7	1600	1600	1800	0.1692	22.12
D8	1600	2850	1800	0.0951	21.83
D11	1600	2850	700	0.0906	21.71
D13	2700	1600	700	0.0580	21.53
D14	2700	2850	700	0.0588	22.62
D15	3600	1600	200	0.0447	23.23
D17	3100	950	1800	0.0473	22.46
D19	2400	950	2700	0.1227	22.13

Table D.5: Location, mean temperature and velocity of the Dantec anemometers for Case 06 (dimensions in mm).